VYSOKÉ UČENÍ TECHNICKÉ V BRNĚ

BRNO UNIVERSITY OF TECHNOLOGY

FAKULTA STROJNÍHO INŽENÝRSTVÍ

ÚSTAV PROCESNÍHO A EKOLOGICKÉHO INŽENÝRSTVÍ

FACULTY OF MECHANICAL ENGINEERING

INSTITUTE OF PROCESS AND ENVIRONMENTAL ENGINEERING

COMPUTATIONAL MODELING OF TURBULENT SWIRLING DIFFUSION FLAMES

POČÍTAČOVÉ MODELOVÁNÍ TURBULENTNÍHO VÍŘIVÉHO DIFÚZNÍHO SPALOVÁNÍ

DIZERTAČNÍ PRÁCE

DOCTORAL THESIS

AUTOR PRÁCE — Ing. JIŘÍ VONDÁL

AUTHOR

VEDOUCÍ PRÁCE — doc. Ing. JIŘÍ HÁJEK, Ph.D.

SUPERVISOR

BRNO 2012

Abstract

The ability to predict local wall heat fluxes is highly relevant for engineering purposes as these fluxes are often the main results required by designers of fired heaters, boilers and combustion chambers. The aim of this work is to provide reliable data measured by an innovative method for the case of swirling diffusion natural gas flames and consequently utilize the data for validation of Computational Fluid Dynamic simulations represented by commercial solver ANSYS Fluent® 12.1. The subject is a large-scale combustion chamber with a staged-gas industrial type low-NO_x burner at two thermal duties, 745 kW and 1120 kW. Attention is paid to the evaluation of boundary conditions via additional measurement or simulation, such as wall emissivity and wall temperature. Several in-house software codes were created for computational support. Remarkable results were obtained for low firing rate where prediction reached accuracy up to 0.2 % in total extracted heat and better than 16 % in local wall heat flux in individual sections. However, for high firing rate the accuracy significantly decreases. Consequently close attention was paid to the confined swirling flow phenomena downstream of the swirl generator. There were identified several problematic points in the prediction capabilities of utilized computationally capable, industry-standard models.

Keywords

CFD, combustion, swirling flow, turbulence, heat transfer, radiation, experiment.

Abstrakt

Schopnost predikovat tepelné toky do stěn v oblasti spalování, konstrukce pecí a procesního průmyslu je velmi důležitá pro návrh těchto zařízení. Je to často klíčový požadavek pro pevnostní výpočty. Cílem této práce je proto získat kvalitní naměřená data na experimentálním zařízení a využít je pro validaci standardně využívaných modelů počítačového modelování turbulentního vířivého difúzního spalování zemního plynu. Experimentální měření bylo provedeno na vodou chlazené spalovací komoře průmyslových parametrů. Byly provedeny měření se pro dva výkony hořáku – 745 kW a 1120 kW. Z měření byla vyhodnocena data a odvozeno nastavení okrajových podmínek pro počítačovou simulaci. Některé okrajové podmínky bylo nutné získat prostřednictvím dalšího měření, nebo separátní počítačové simulace tak jako například pro emisivitu, a nebo teplotu stěny. Práce zahrnuje několik vlastnoručně vytvořených počítačových programů pro zpracování dat. Velmi dobrých výsledků bylo dosaženo při predikci tepelných toků pro nižší výkon hořáku, kde odchylky od naměřených hodnot nepřesáhly 0.2 % pro celkové odvedené teplo a 16 % pro lokální tepelný tok stěnou komory. Vyšší tepelný výkon však přinesl snížení přesnosti těchto predikcí z důvodů chybně určené turbulence. Proto se v závěru práce zaměřuje na predikce vířivého proudění za vířičem a identifikuje několik problematických míst v použitých modelech využívaných i v komerčních aplikacích.

Klíčová slova

CFD, spalování, vířivé proudění, turbulence, přestup tepla, radiace, experiment.

Bibliographic citation

VONDÁL, J. *Computational Modeling of Turbulent Swirling Diffusion Flames.* Brno: Brno University of Technology, Faculty of Mechanical Engineering, 2012. 221 p. Supervisor doc. Ing. Jiří Hájek, Ph.D..

Statement of originality

I hereby declare that this thesis is my own work written under supervisory of doc.Ing. Jiří Hájek, Ph.D. Utilized sources and resources are properly mentioned and acknowledged.

In Brno, May 15th, 2012 .....

Ing. Jiří Vondál

Acknowledgments

I gratefully acknowledge the support and help of my supervisor doc. Ing. Jiří Hájek, Ph.D. whose patient encouragement and sage advice supported me in completing this thesis. I am also thankful for the help with measurements to my colleagues Ing. Vít Kermes, Ph.D., Ing. Petr Bělohradský, Ph.D. and Ing. Jakub Broukal.

Last but not least, I would like to thank to prof. Ing. Petr Stehlík, CSc. for the opportunity he gave me and support during the studies.

Dedication

This thesis is dedicated to my wife Olga, son Vojtěch and my parents who offered me unconditional support through all my studies.

Contents

1. Introduction

Emissions are studied namely to ensure compliance with legislative regulations (e.g. [1]). One of the common emission reduction techniques is swirling combustion. Swirl-stabilised flames are very popular, especially in the so-called power burners that are widely used in power and process industries [2]. They combine the wide range of operating conditions with stable flame and low emission levels. The basic idea is to introduce swirl motion to the stream of air, fuel or both. This not only improves stability of the flame but also intensifies mixing.

However, it has been recognized for long time that the prediction of swirling diffusion flames using moment turbulence closures is extremely problematic, in spite of partial successes i.e. predictions of in-flame properties reported in [3–5]. Recent progress achieved using large-eddy simulations coupled with advanced chemistry models is on one hand very promising but on the other hand it is still far from being applicable to industrial problems due to excessive computational requirements, tractable only using supercomputing facilities due to huge dimensions of the combustors (on the order of 10 m) and the need to resolve fine features like gas nozzles with diameters on the order of 1 mm.

Industry primarily requires predictions of wall heat fluxes (typically for membrane walls or tubes). In spite of that, combustion modeling research almost exclusively focuses on the details of flame core structure and wall heat loads are typically disregarded. The present work thus focuses on validation of computationally manageable Reynolds-averaged Navier-Stokes (RANS) models by accurately measured local wall heat fluxes. The experiments were performed at a modern experimental facility of the Institute of Process and Environmental Engineering, FME, BUT.

1.1 Motivation

Our institute is equipped with the experimental facility containing industrial size combustion chamber. This allows us to test not only new fuels from renewable sources but new combustion equipment such as low-NO_x burners as well. Since we want to provide deeper insight into the process of combustion at the facility the suitable tool is Computational fluid dynamic (CFD) simulations. Even though it has been developing for many years there are still many concerns for use in specific areas such as combustion.

Testing facility was designed with accurate heat flux measurement and therefore this work benefits from it. It is the first step to verify ability of the computational software to accurately predict wall heat fluxes. This ability is highly demanded among design engineers. The local wall heat fluxes are crucial in the design of process or power industry equipment. It is required by material and stress analysts and designers who needs to know real heat loads of the walls. Other area is in already built plants for failure analysis, retrofit design and life cycle analysis.

1.2 Work objective

First task is to provide set of accurate and well documented measurements focused primarily on local wall heat fluxes (heat transfer rates) in a water cooled combustion chamber equipped with natural gas turbulent swirling diffusion flame burner. Accuracy of the measurements and exact operating conditions have to be reported. This will serve as a basis for validation of simulations.

When reliable data are gathered the focus will move to simulations. The models shall be examined and the best settings found with respect to pre-defined computational resources. Results will be helpful in industrial scale combustor simulations and providing guidelines for model selection.

1.3 State of art in swirling non-premixed combustion

Numerous detailed in-flame measured data are available for a range of swirl burners. In fact, a number of research groups have performed coordinated efforts to characterize several swirling diffusion gas flames by various experimental methods. One of the most notable projects was the TECFLAM cooperation performed by five institutes in Germany, which yielded numerous publications (e.g. [6–9]) and a validation database (presently available upon request). The burner used in these works (see Fig. 1.1) had a thermal duty of 150 kW and the swirl number at the burner orifice was 0.9. Other sets of data were collected for gas turbine combustors, e.g. [3, 10–12] on flames up to 35 kW (in the referenced works). Another remarkable project is the Sydney swirl burner experimental database [13–16] (see Fig. 1.2) which represents unconfined turbulent swirling gas combustion. Thermal duty varied from 11.1 kW for swirling methane flame up to 167.1 kW for swirling methane/hydrogen flame.

Many other burner geometries were investigated worldwide, covering various fuel injection systems and swirl generation systems, see e.g. [17–21]. The thermal duties of burners in all these studies ranged from several kilowatts up to about hundred kilowatts, i.e. they were all laboratory-scale experiments. It is also important to note that without exception all these studies focused on detailed in-flame measurements and paid little or no attention to the heat transfer to combustion chamber walls (in cases with non-adiabatic walls). Other problem is in focus of studies on chamber flow and no one is concerned about the flow through a swirler. When there exists simulations of the flow through burner and combustion chamber e.g. work of [22] a little or no attention is paid to the section of swirl generator. This is omitted even though it has impact on a flow field predicted in a chamber.

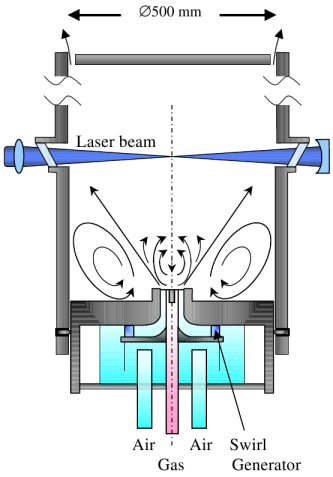

Figure 1.1: Schematic drawing of the TECFLAM swirl burner from [7]

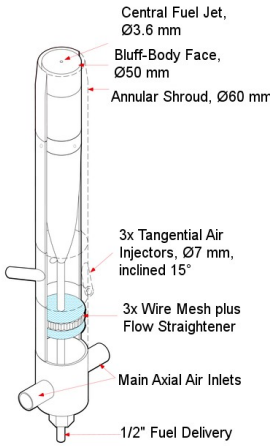

Figure 1.2: Schematic drawing of the Sydney burner from [15]

Several recent theoretical and modeling studies of in-flame phenomena affecting the heat transfer deals with turbulence radiation interaction (TRI) which reportedly has large effect on

heat flux predictions. Existence of the interaction has been proved experimentally e.g. in [23] and is subject of intensive study e.g. by Coelho [24, 25] or Li [26, 27]. Interaction is responsible for significant deviation of mean radiation quantities when TRI is included from those predicted from mean parameters due to strong nonlinear dependence on the temperature and species concentrations. It is responsible for decreased flame peak temperature and increased intensity of radiative heat transfer. The mean spectral radiation intensity in methane flames could be increased by TRI from 10 % to 50 % when compared to the mean values with no TRI assumed [25]. To capture this phenomena the scalar fields are crucial but often they are not available and have to be e.g. generated stochastically according [28]. Therefore high demand for computing resources is typical and often decoupled simulation is performed where RTE is solved in postprocessing stage. Limited resources restrict practical use of the TRI but it has to be considered when results of the averaged simulation are interpreted.

Studies focused on the wall heat flux within a combustion chamber are rare. Heat flux measurements reported in the literature are either spot measurements or global heat transfer rates. Spot measurements however, mostly provide just the thermal irradiation flux, not the actual radiative or total heat transfer rate.

Recent broad overview of modeling approaches and discussion of previous results from the literature in [29] is focused on radiation phenomena in industrial furnaces. The author concentrates on mathematical modeling of radiative heat transfer. He analyzes and compares several models for spectral modeling of absorbing and emitting flue gases. He suggests using wide band correlated-k method (WBCK) with only three gray gases and points out its higher accuracy over weighted-sum-of-gray-gases model (WSGGM). However, its main drawback is increased demand on CPU since three additional radiative heat transfer equations are solved which in the reported case results in approximately. 18 % increase of total computational time.

Measurement of combustion chamber wall heat loss together with acoustic analysis is discussed in the work of Sengissen [17] in experimental laboratory-scale 125 kW combustion chamber. However, only total heat flux from flame side to the cooling air in a cooling channel was measured since there was not a segmental design of the enclosure. Total wall heat flux was approximately 28 % (35 kW) of the total burner firing rate. Calculation of wall heat flux based on LES simulation was also utilized, but only as a postprocessing step with a rather strong simplifications. Impact of the heat losses on the flame was observed to be limited but it significantly changed acoustics of the chamber.

Directly with heat fluxes deals work focused on high-temperature air combustion with honeycomb regenerative burner [30] which utilizes point measurement with water-cooled sensor called “Gardon gauge”. It measures incident radiation heat flux received by the spot of size about 25 mm. Application of this heat flux measurement method is in the detection of fouling and slugging. The paper [31] reviews several methods of the heat flux measurement e.g. by disc sensors, inserted thermocouples and guarded cylinder concepts. But it still relies on the spot measurement. For another review of heat flux sensors and description of their principles see [32]. Described are sensors suitable for the combustion applications within a range of 10 to 7.1×10^5 W/m2.

The practical measurement from real-world industrial application is referred in [33]. The work deals with gas-fired, regenerative glass furnace and for measurement utilizes two gauges – hemispherical ellipsoidal radiometer and circular foil heat flux gauge. The measurements by the

gauges have deviation about 12 % when compared to each other. Comparison to the CFD simulation is provided as well.

The radiation effect on combustion was tested by [34] in a large-scale steam cracking furnace. Three radiation models were tested (Rosseland, P-1 and discrete ordinates method). Conclusion is drawn that Rosseland model is less accurate than the other two and should not be used for similar cases of combustion as in [34]. P-1 and DOM predict similar results in this study and are equivalent. However, no comparison to measurement is provided and all the work relies on simulated data with WSGGM for radiative properties.

Literature review suggests that there are unresolved issues in the total wall heat flux predictions. Only a limited number of studies uses accurate measurements of total wall heat flux to validate simulations while none of them uses local heat loads from segmentally designed combustion chambers. Local heat fluxes are mostly evaluated through spot measurement such as in [33].

Simulations will always form a compromise between accuracy and availability of computational resources. The only viable option for turbulence modeling in the simulation of industrial size applications are still moment closure turbulence models due their reasonable requirements for computational power. In the radiative heat transfer modeling the DOM has been reported as sufficiently reliable and new promising models of radiative properties were developed (e.g. WBCK). However, their availability in commercial codes is limited. These models are more CPU demanding which leads usually to utilizing the most popular but less accurate WSGGM.

1.4 Swirling flow generation in combustors

Swirling air flow is a key feature in many types of combustors. Tangential flow component is generated in an aerodynamic element called swirler (swirl generator, flame holder), which is often designed in the form of axial guide vanes. Such design is typical in low-NO_x diffusion burners with staged gas and/or air supply, e.g. as in [35]. The swirler is a key burner design component that significantly influences the flow pattern in combustion chambers. Current industrial practice in the CFD modeling of swirling flow combustors tends to include swirler into the computational domain since detailed measured data of inlet velocity profiles for swirling combustion air are generally unavailable. Another reason for this practice is that the swirler is rather part of the combustion chamber than a separated element in air supply duct. This is also a major difference for laboratory experiments, where swirler is placed However, it has long been a well-recognized fact that reliable predictions of turbulent swirling non-premixed flames are very difficult [36] especially for practical cases where application of LES methods is not feasible. Therefore there is a need for validation of RANS-based industry-standard codes in the prediction of flow through swirl generators. Measured data on flow through axial swirlers are unfortunately scarce. One of the rare recent experimental works that has been selected as the basis for one part of this thesis is the work of [37]. The swirler used in that work is similar to a typical flame holder in a staged-gas low-NO_x burner.

Several research works dealing with the flow prediction in axial swirlers may be found (e.g. [38]), but they mainly focused on the downstream of the sudden expansion within a combustion chamber. Flow in the swirler was not subject of their interest and in fact method of swirl generation was irrelevant for their study.

1.5 Summary

Turbulent swirling diffusion flames are topic of many ongoing researches. Several large projects with detail inflame measurement were previously described. Even though there are issues which do not receive attention they deserves. One of the issues is accurate segmental measurement of total wall heat fluxes which is afterward utilized for validation of CFD simulations. Another issue is flow prediction through the swirl generator. Both issues are further dealt with in this thesis along with other related topics such as identification of boundary conditions for CFD simulations or proper data acquisition during a measurement.

2. Measurements at the large-scale combustor facility

2.1 Experimental facility overview

The construction of the semi-industrial experimental combustion facility for burners up to 2 MW enables variable length adjustment of the combustion chamber and accurate heat flux and emission measurements. The main feature distinguishing the test facility at Brno University of Technology from others is the ability to measure local heat transfer rates to the cooled walls, which is enabled by the segmental design of the combustion chamber.

Several measurements previously performed at the same testing facility, although with different objectives than in this work, were described in [2, 39, 40].

Figure 2.1: Industrial-scale combustor

Flame ignition and stabilization is performed by a small (25 kW) premixed natural-draft pilot burner. Its thermal duty was included in the total thermal duty. The inner wall was black-painted for improved surface emissivity (see Fig. 2.2).

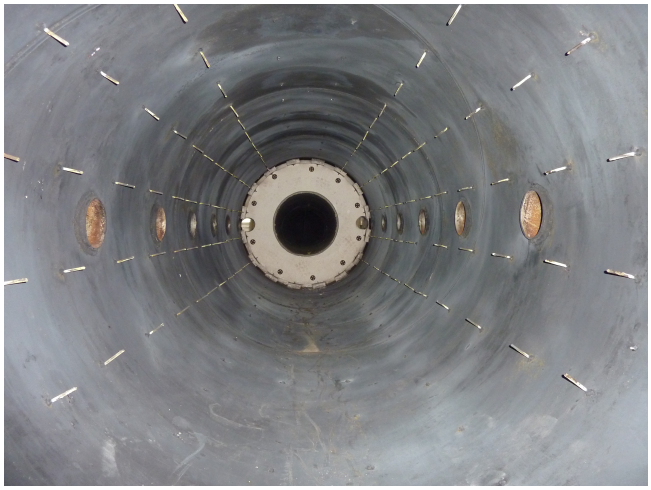

Figure 2.2: Insight into the combustion chamber from the burner side

2.1.1 Combustion chamber and burner geometry

There are up to seven water cooled segments of the combustion chamber, see Fig. 2.1 and 2.6. All internal segments are of diameter 1 m and length 0.5 m and have the same flame-facing area of 1.57 m^2, whereas the first and seventh section have length 0.4 m (area 1.26 m^2) and 1 m (area 3.14 m^2), respectively. The last three segments are removable which allows adjustment of the combustion chamber length.

The burner was a low-NO_x design with staged gas supply (Fig. 2.3 and 2.4) and axial swirl generator, fired by natural gas. Burner geometry was possible to adjust thanks to the design made with the six adjustable geometrical parts, namely (for details see Appendix A and [41]) :

- Diameter of swirl generator
- Pitch angle of the swirl generator's blade
- Number of secondary nozzles
- Secondary nozzle diameter
- Secondary nozzles head angle
- Tangential direction of secondary nozzles
- Secondary nozzles axial position
- Secondary nozzles radial position
- Secondary gas stage throttling

Geometry settings of the burner and a few other parameters were derived from the set of measurements as described in [39] and [40]. The primary parameter was stability of the flame and low emissions. The final assemble consists of swirl generator with diameter 240 mm made of 8 vanes with pitch angle of 35° acting as a flame holder. Gas inlet includes twelve primary nozzles and eight secondary nozzles. Eight of the primary nozzles have diameter 2.6 mm and the other four 3.0 mm. All the primary nozzles are drilled in a nozzle head located on the burner axis. Secondary gas injection is performed by four additional nozzle heads located in regular intervals around annular air channel which surrounds the primary nozzle head. Each

of the four secondary nozzle heads has two nozzles with a diameter of 3.3 mm and head angle of 20°. Secondary nozzle angle is 0° which means that it faces directly to the axis of the chamber and toward the center of the burner. Axial position is 0 mm therefore with the lowest possible extension to the chamber and radial position is 0 mm as well which states for the closest radial position to the axis of chamber and the burner. Throttling element had diameter of opening 5.5 mm. This settings were utilized in all the measurement in this thesis.

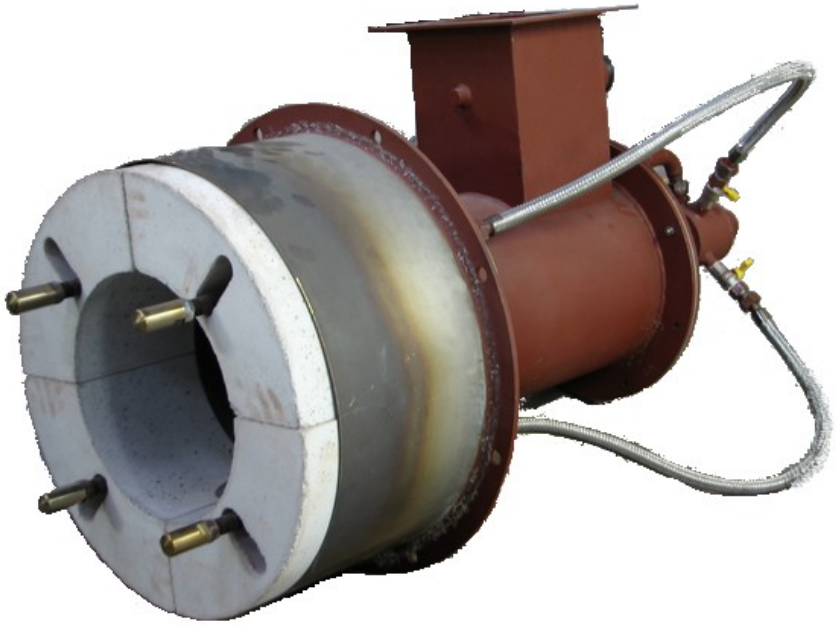

Figure 2.3: Gas staged burner

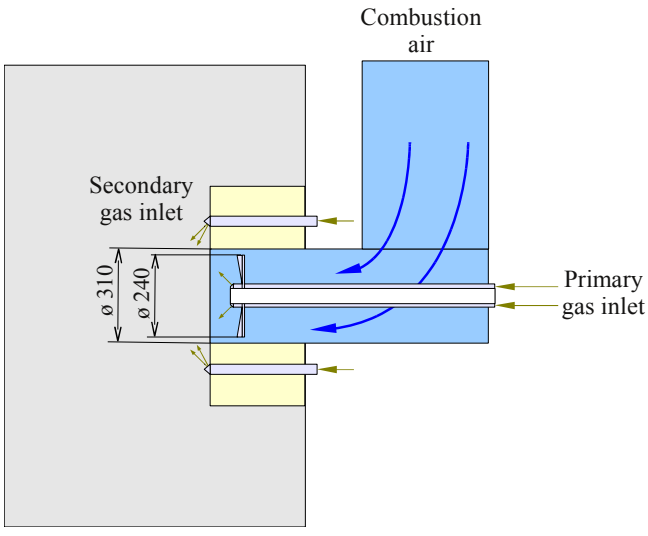

Figure 2.4: Swirl burner with two gas stages

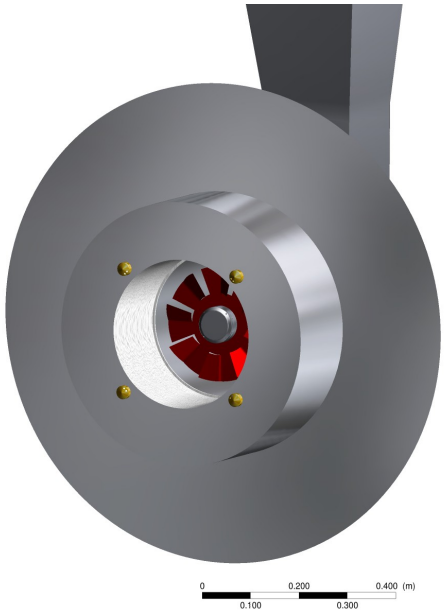

Figure 2.5: Model of the swirl burner

2.1.2 Instrumentation and Data Acquisition System

Inlet and outlet temperature and water flow rate data are collected at every section by an automatic data acquisition system. The total firing rate of the burner is calculated from the gas flow rate measured by rotary flow meter and adjusted by pressure and temperature readings to normal conditions. The excess air ratio is calculated from oxygen concentration in the exhaust gases.

All the data from sensors are collected in the central operator work station. The data acquisition system is industry standard with 1-second interval except for the flow meters which have approximately 6-second interval. Water flow is measured by turbine flow meters equipped with optical sensor sensing 10 000 impulses per 1 m^3 of water. Flow of the fuel (natural gas) is measured by positive displacement, rotary type flow meter and conversion to the standard conditions is made based on temperature and pressure measurement. All the data are visualized on a monitoring PC via Control Web® system.

All temperature sensors are of type platinum resistance temperature detector (RTD) Pt100 placed in a steel sheath. The accuracy indicated by manufacturer is better than +/- 0.3 ℃. List of all relevant sensors for heat flux measurement is in Table 1.

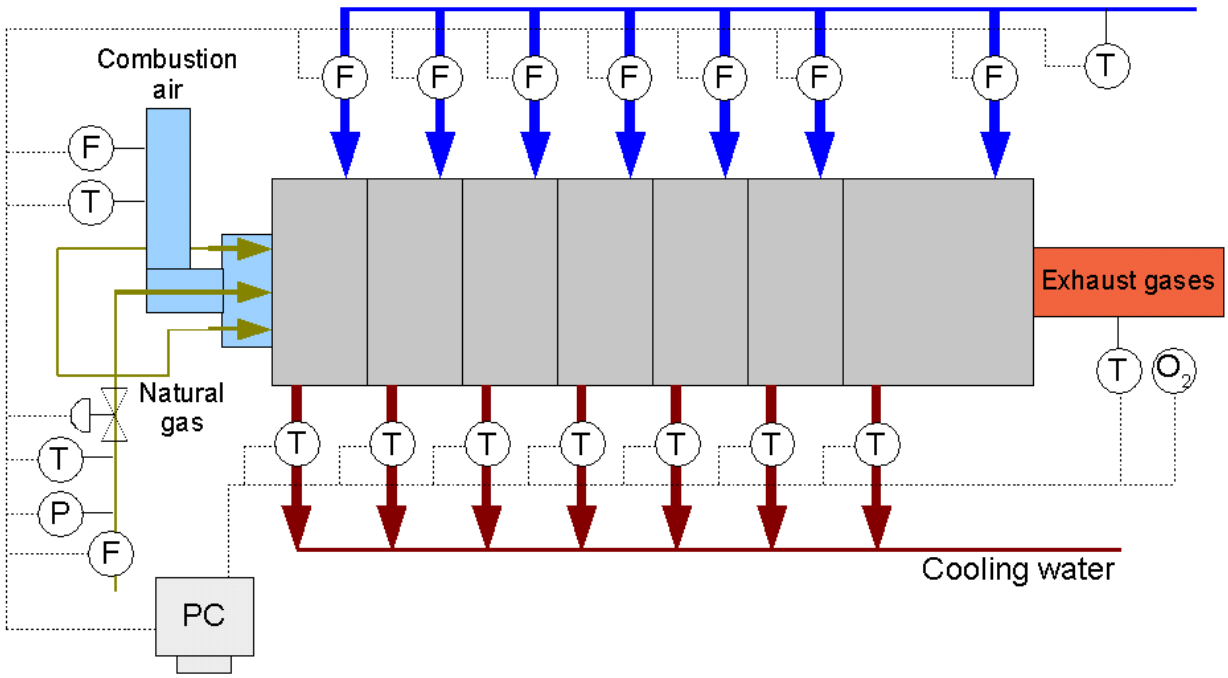

Figure 2.6: Combustion chamber and main parts of the data acquition system

Table 1: List of sensors at the testing facility important for the heat flux measurement

Measured properties	Sensor type
Cooling water thermometer at the duplicators' inlet	Pt100, PTP50J RAWET
Cooling water flow meter at the duplicators' inlet	XN-RK 04 L300 G2 Q10-BH E K10
Natural gas flow meter	Roots Dresser G100
Natural gas temperature sensor	Pt100 T1002 EEx IIC JSP Nová Paka
Gas pressure gauge	DMK331 EEx ia IIC T6
Flue gas thermometer	Thermoelectr. K 9999, L= 300 mm
Combustion air pressure gauge	Testo 1645 connected to Testo 350XL
Flue gas pressure gauge	Testo 745 connected to Testo 350 XL
Gas analyzer	Testo 350XL
Turbine anemometer	Testo 0635 9440

2.2 Inflame temperature measurement and sensor verification

Besides of optical inflame measurement methods, which would be prohibitively expensive for such a large combustion chamber as well as difficult to set up and operate, it is possible to apply more traditional and cost effective approach. It is based on thermocouples utilizing principle of voltage production under the exposition to a temperature gradient. Among a variety of existing types of thermocouples, it is advantageous to use bare fine-wire thermocouples, as small size of the hot junction allows fast response characteristic.

Platinum – platinum-rhodium thermocouple of type R was utilized. It consists of two wires – one is from pure Platinum and the other from platinum-rhodium alloy containing 13 % rhodium. Different wire sizes can be used. For this test the wire of the diameter 0.8128 mm was used. (see Fig. 2.7)

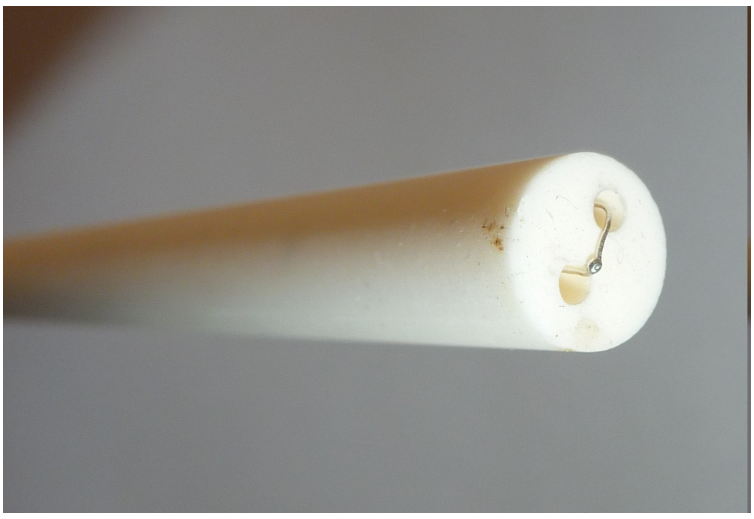

Figure 2.7: Detail of ceramic tip and thermocouple hot junction

2.2.1 Data acquisition and processing

Thermocouple was connected to the Omega iSeries® DPi8 monitor. Besides displaying the instantaneous temperature value, the monitor is also able to communicate over serial port RS232 with PC. Software supplied with the Omega meter was found very buggy and was replaced by my own code attached in appendix K. It is simple, but efficient and is able to run on Linux operating system booted even from live CD. The data are plotted on standard output from where it can be redirected into a file or processed. Usually we used redirection into a text file and online display by plotting software Gnuplot [42]. Another software code I created (see Appendix L) implement data processing, perform filtration and optionally compare measured data to the validation data.

The main feature of the software is correction of corrupted data (missing data in time steps) and proper filtering of obtained data which contain noise. Several filters were tested, including Backward moving average, Central moving average, Exponential moving average and Gaussian filtering. The most appropriate was found Gauissian filter which is in fact modification of moving average and is based on Gaussian distribution of weights [43] defined as:

$$G(x)=\frac{1}{\sigma\sqrt{2\pi}}e^{-\frac{x^2}{2\sigma^2}}. \tag{1}$$

The truncation of Gaussian distribution was chosen in 3σ and therefore we capture 99.7 % of area under the distribution. Filtration is applied to a data set in window covering $2N$+1 data points. Therefore we need the same number of weights (G'_n) which are used for the averaging. The sum of all weights is equal to 1. Weights are calculated as follows [43]:

$$G'_n=\frac{e^{-\frac{\left(\frac{3n}{N}\right)^2}{2}}}{\sum_{n=-N}^{N}e^{-\frac{\left(\frac{3n}{N}\right)^2}{2}}}. \tag{2}$$

The filtration works as a moving average, which means that we put a window over the data set so that i-th data point (s_i) is in the center of the window. Then we apply the weights to 2N+1 data points around the central data point and we get new, filtered, value:

$$s_i'=\sum_{n=-N}^{N}G'_n s_{i+n}. \tag{3}$$

Comparison of the filtered values to the measured raw data is in the Figure 2.8.

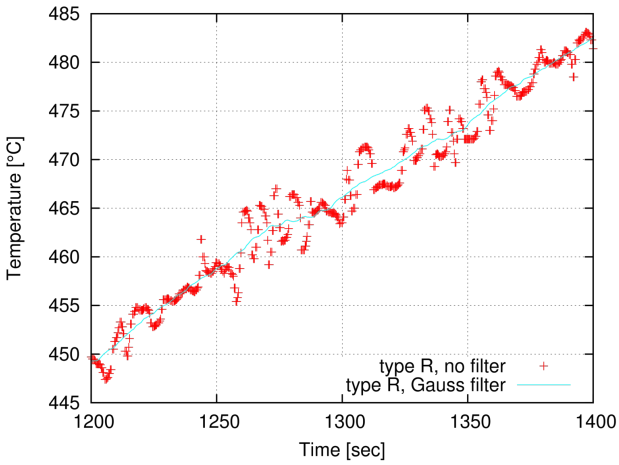

Figure 2.8: Comparison of Gaussian filtration of measured data to the raw measuerd data

2.2.2 Comparative verification

I cooperated on verification tests with my colleague Ing. Jakub Broukal and staff from the Heat Transfer and Fluid Flow Laboratory who provided us with additional sensors and access to a muffle furnace.

Three commercial K-type thermocouples were used to verify measured temperature inside the muffle furnace (see Fig. 2.9). Data logging was set up with the frequency of 3 Hz which is sufficient since our transducer (Omega iSeries) has maximum frequency of 2 Hz. Electric muffle furnace with proportional temperature control was utilized.

Our R-type thermocouple was placed into the furnace in ceramic support tube with just hot junction exposed. We tried to achieve the same conditions for the hot junction as will be during the inflame measurement. Other (reference) thermocouples were placed into the insulation material Sibral to eliminate radiation losses. The furnace was heated up to 900 ℃ within two hours with one time period of 5 minutes and one of 10 minutes to ensure temperature stabilization at the temperature 530 ℃ and 732 ℃ respectively (see Fig. 2.10). Continuous data acquisition was performed for all thermocouples. There was a short break in measurement at the 500 ℃. Data from the K-type thermocouples were downloaded to computer since it was not possible to examine the data during the measurement. After a while the measurement was resumed. The furnace was continuously heated up even during the break in data acquisition.

Results at the Fig. 2.10 show that R-type thermocouple constantly underestimates temperature. There is also dynamic relationship of the deviation (see Fig. 2.11 and Table 2) to the rate of temperature increase. The faster is temperature increase in the furnace the bigger is difference between R-type and K-type thermocouples. It can be seen that at the beginning (about the time 300 s) the rate of change is highest (0.45 ℃/s) and so is the difference (90 ℃). During the time the rate of change slows down and the difference between thermocouples decreases.

Table 2: Deviation of temperature over the time and specific temperature range

Time [s]	Temperature of K no. T1 [℃]	Rate of change [℃/s]	Temperature difference [℃]	Temperature difference [%]
300	292.6	0.45	90	30.8
1000	480.5	0.17	72.4	15.1
1750	530.6	0	38.6	7.3
3650	714.2	0.12	33.7	4.7
4600	744.7	0	24	3.2
7300	948.4	0.06	12.8	1.3

While the size of the hot junction (0.8128 mm) of the R-type thermocouple was of the same order as K-type, this dynamic lagging must be caused by another factor than internal heat capacity of the junction. One reason can be that the ceramic tip has much larger heating capacity (about 750 J/kg-K, density about 4900 kg/m^3) than the Sibral insulation (about 970 J/kg-K, density 100 kg/m^3) where the K thermocouples are placed and its influence on the platinum junction is more significant than we expected. Another trend that may be observed in temperature difference is that with increasing temperature the difference decreases. The same trend is even for K thermocouples. T2's deviation from T1 and T3 decreases with increasing temperature. Other explanation may be that the radiation losses are responsible for the difference since the reference thermocouples were placed in Sibral while our R-type was without any radiation shield.

Figure 2.9: Calibration of thermocouple in muffle furnace

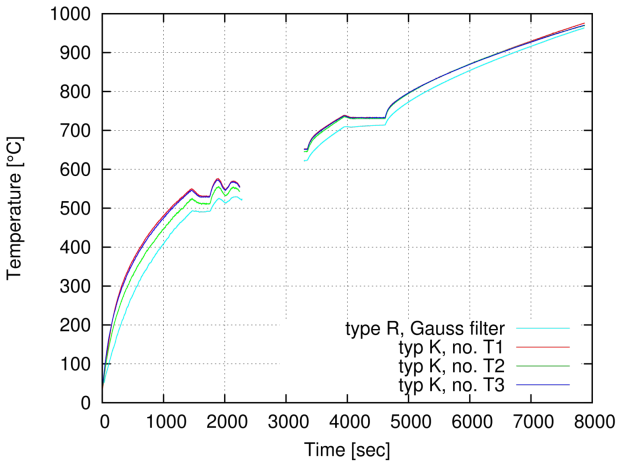

Figure 2.10: Temperature measured by four different thermocouples

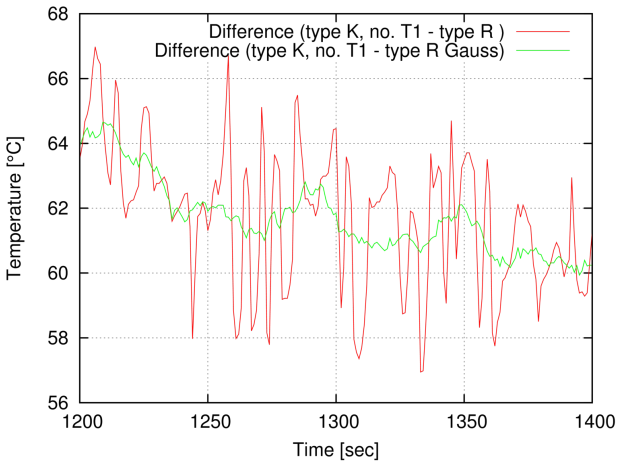

Figure 2.11: Temperature difference between type R and type K (no. T1) thermocouples

Even though there is the problem with deviation dependence on the temperature, the overall agreement at higher temperatures is very good, i e. difference is less than 5 %. There might be slow response due to the ceramic tip influencing the junction, but the Omega transducer is able to deliver only 2 values per second therefore this is the highest frequency it can operate on. The tip influence might be viewed as the physical averaging of the temperature fluctuations. For proper measurement of turbulence effect on temperature and its fluctuation this influence would have to be removed, but it doesn't impact the averaged value.

2.2.3 In-situ measurement

With the verified system of high temperature measurement we could proceed to the inflame environment. To be able to position the thermocouple into the flame directly, high temperature resistant support had to be constructed. Design of the water-cooled support created Ing. Vít Kermes, Ph.D. The probe consists of water cooled double wall shell (see Fig. 2.13) which carries a ceramic tube inside (see Fig. 2.12). The ceramic tube has two holes inside for each wire to be electrically insulated from each other. Omega monitor was mounted at the end of water cooled support. To suppress temperature influence of the probe around the sensor, the ceramic tube is extended from the water cooled shell by 150 mm. All the equipment is attached to the chamber by a flange of the inspection window (see Fig. 2.14). Cooling system of the support was connected to the cooling circuit of the combustion chamber.

For radial positioning, scale was created on the water-cooled support pipe. When inserted into the combustion chamber, whole body of the sensor is positioned by sliding it into the flange. Uncertainty is estimated based on the created scale which is +/- 0.5 mm, measured ceramic tip overhang +/- 0.5 mm and reading of the scale during the measurement which is +/- 0.5 mm as well. The total uncertainty is :

$$\delta Q = \sqrt{\delta a^2 + \delta b^2 + \delta c^2} = \sqrt{3 \cdot 0.5^2} = 0.87\ mm \tag{4}$$

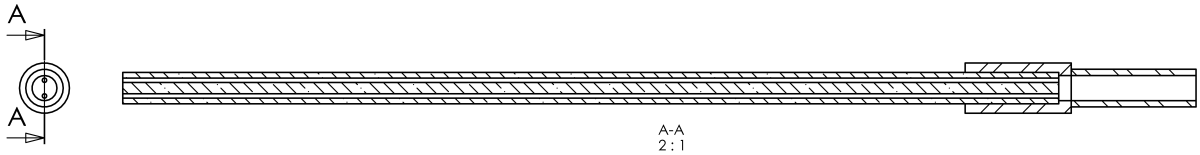

Figure 2.12: Ceramic insulation pipe from thermocouple support

Measurement was performed at three axial positions and five radial position i.e. 15 measurement points in total. Drawback of the change of axial location was requirement of operator to lower down the firing rate of the chamber for security reason, unbolt inspection window, move thermocouple and it's support and increase the firing rate to the original value. After such a change a stabilization period needs to follow. Only way to overcome such a process would be to employ another thermocouple with all the accessories.

Experiment was carried out with the gas staged burner at the firing rate 745 kW. Fuel was natural gas and the oxidizer was air. Stochiometric coefficient was 1.1.

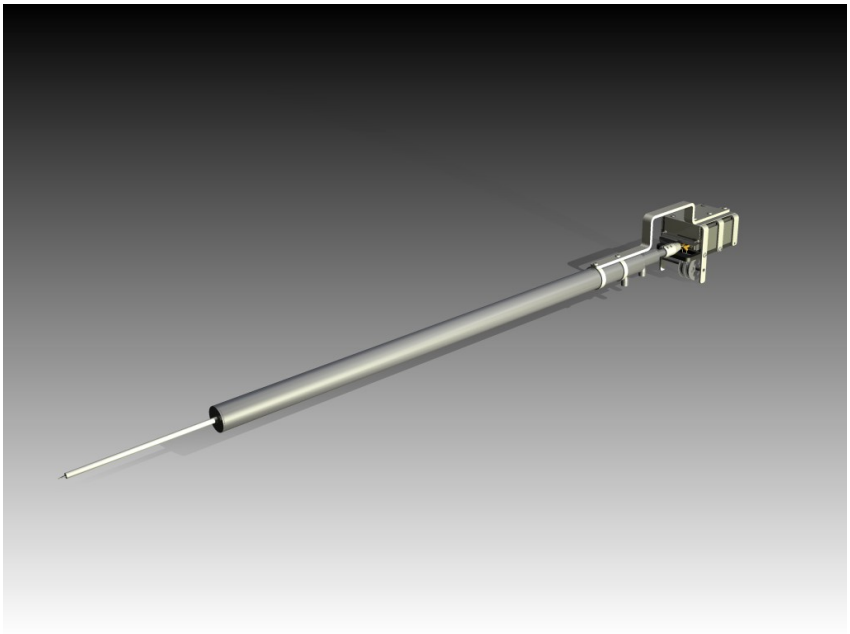

Figure 2.13: Visualization of thermocouple assembly

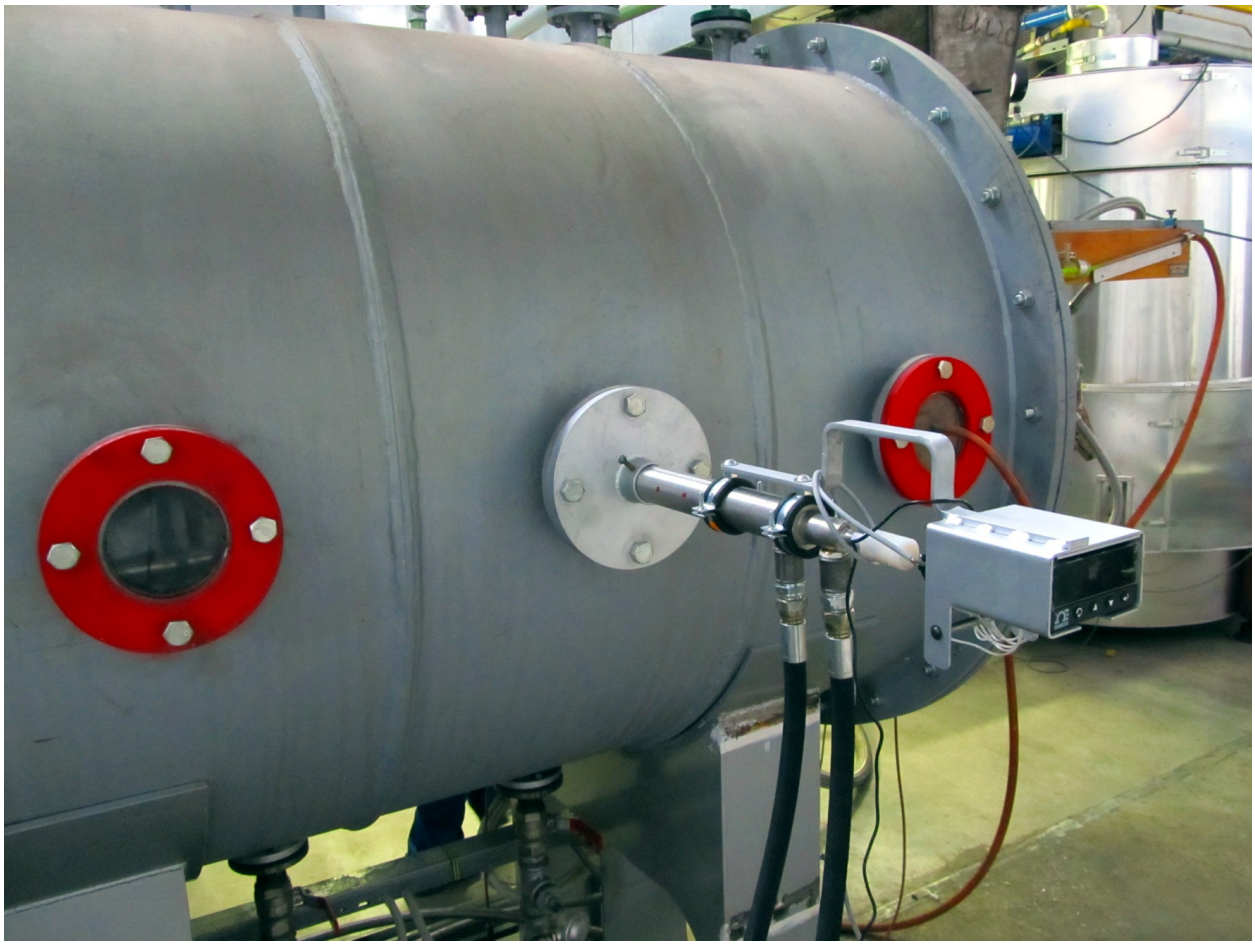

Figure 2.14: Inflame temperature measurement equipment

Measured data from all radial positions at the Section 2 are shown in Fig. 2.15. The step changes in temperature correspond to radial position changes. The highest temperature is in the middle of the chamber (r/D = 0.5). Temperature decrease behind the peak value at the position r/D = 0.59 (see Table 3) is the consequence of preparation for axial position switch. Tables 3 up to 5 show measuring records from individual sections of the chamber.

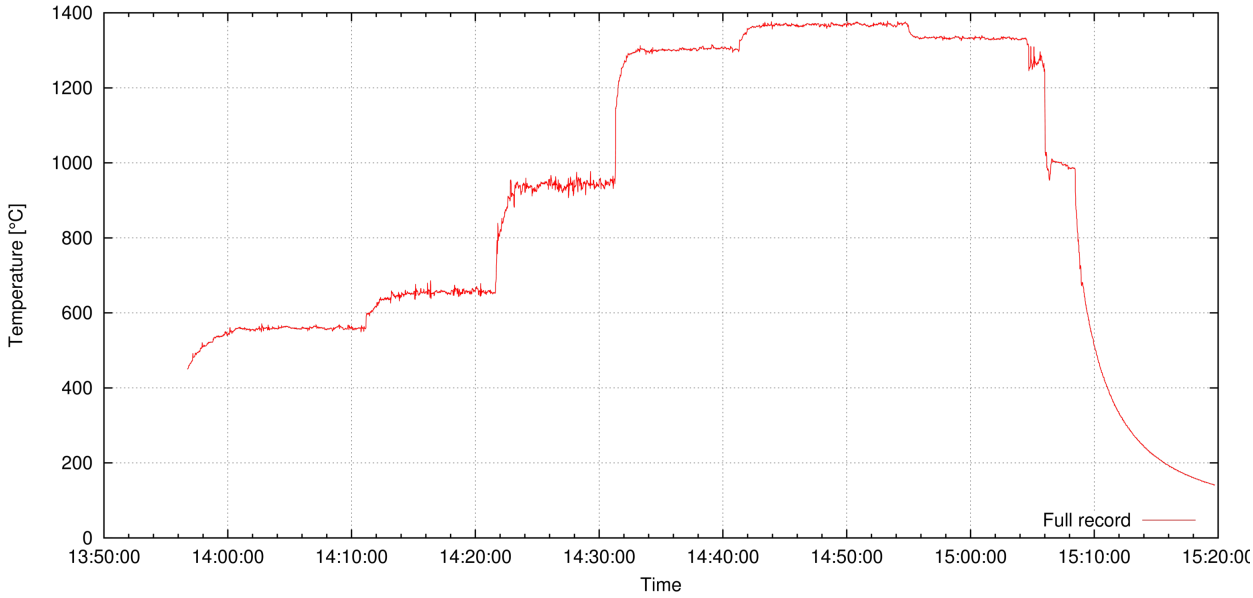

Figure 2.15: Measured data at Section 2

Table 3: Measured data at Section 2

Radial position (from the wall) [mm]	r/D [-]	Temperature [℃]	RMS [-]
91	0.09	560.0	2.7
191	0.19	654.9	5.3
291	0.29	940.0	9.8
391	0.39	1302.6	3.4
500	0.5	1368.4	2.9
591	0.59	1332.6	2.3

Table 4: Measured data at Section 4

Radial position (from the wall) [mm]	r/D [-]	Temperature [℃]	RMS [-]
91	0.09	809.6	6.2
191	0.19	937.3	7.3
291	0.29	1081.1	7.1
391	0.39	1187.4	6.6
500	0.5	1206.1	6.3
591	0.59	1132.5	6.7

Table 5: Measured data at Section 6

Radial position (from the wall) [mm]	r/D [-]	Temperature [℃]	RMS [-]
191	0.19	839.8	3.8
291	0.29	876.2	3.5
391	0.39	906.0	4.4
500	0.5	908.8	4.3
591	0.59	891.7	5.8

Results show the highest temperature in the Section 2 (close to the burner) in the middle of the chamber. For comparison the flue gas temperature was 850 ℃ and the corresponding adiabatic temperature would be 1787 ℃. 2-D contour plot was created from measured data in software Gnuplot see Fig. 2.16. The smooth colors were achieved by interpolation and the contour was mirrored to get symmetric picture of the chamber between section 2 and 6.

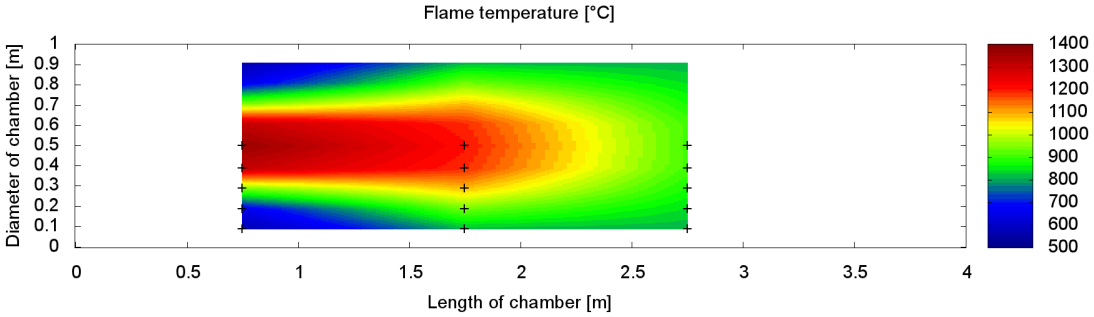

Figure 2.16: Inflame temperature visualization based on measured data with marked positions of measurement

2.3 Chemical Species Concentration Measurement

There are several methods available for species concentration measurement. It differs in the scope and complexity. Among the most detailed and advanced methods are Rammann spectroscopy and Laser-induced fluorescence. These methods allow direct inflame measurement. Both of them are based on the principle of excitation of molecules to higher energy levels. While Raman spectroscopy detects non-elastic scattering effects, the Laser-induced fluorescence method detects wavelength of emitted photons after the de-excitation. Besides there are many others method derived from the same theoretical background e.g. Rayleigh scattering, or non-linear Coherent Anti-Stokes Raman Scattering and Degenerate Four-Wave Mixing. Overview of the methods is more in-depth described in [44].

At the testing facility there are utilized portable emission analyzer Testo 350XL. It is equipped with several chemical and temperature sensors, such as non-dispersive infrared (NDIR) for CO_2 detection and electrochemical sensors for other gases (O_2, CO, NO, NO_2, SO_2, H_2S). This is intended for flue gas measurement in the stack. The position of the probe is just behind the combustion chamber in the exhaust (see Figure 2.6). The most important is the Oxygen sensor from which the flow rate of combustion air is calculated.

2.4 Heat Flux Measurement

The local heat loads to tubes (in fired heaters), to membrane walls (in boilers), or combustion chamber walls (cooled as well as refractory-lined), are key parameters required by designers from CFD combustion analysts. Wall heat fluxes and wall temperatures are required to be uniform and their peaks to lay below certain hard limit values given by material strength considerations. Measurement of local heat loads in industrial conditions is possible only using special heat flux probes that cannot provide reliable detailed data covering the whole heat transfer area, but only a limited number of discrete points. An overview of available instrumentation is provided e.g. in [32] and [45]. The best way to measure local heat fluxes clearly would be different – to measure directly the heat absorbed by walls on the heated medium side (e.g. steam or water). Such segmental design is naturally impracticable in industrial furnaces, but actually quite common in laboratory reactors (except for the missing heat-transfer related instrumentation), see e.g. [46], [47], [48], [49]. Additionally, industrial units typically have only rough estimates of the instantaneous total heat transfer rate (e.g. ± 4 % in [31]). Thanks to the fact that fouling and slagging are absent in gas combustion, the measured heat flux data are more reliable than in e.g. pulverised fuel combustors. Even though, the accuracy of available measurement methods is on the order of several percent. E.g. for the measurements of thermal irradiation flux are often used ellipsoidal radiometers (accuracy ± 5 %) and water-cooled circular foil heat flux radiometers (accuracy ± 2 %) [33]. The latter ± 2 % accuracy is about the best we can achieve with heat flux metering probes. As reported in [33], differences of values measured by these two methods may however reach up to 12 %, thus further decreasing the credibility of point heat flux measurements.

Our facility utilizes measurement based on heat absorbed by the cooling water. Heat flux is measured in each section via the temperature increase of the cooling water. This measurement is easy and industry standard procedures exist.

2.4.1 Geometry of water-cooled duplicator

When we want to measure temperature of the chamber's wall more advanced methods have to be employed. For the analysis only indirect evaluation was adopted. It consists of knowledge of duplicator's internal geometry, the flow rate through the duplicator and inlet and outlet temperatures of cooling water. From these facts the water-side wall temperature can be estimated.

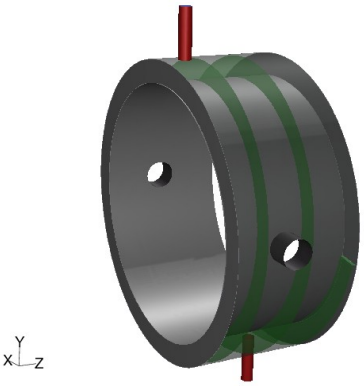

Figure 2.17: Geometry of the duplicator

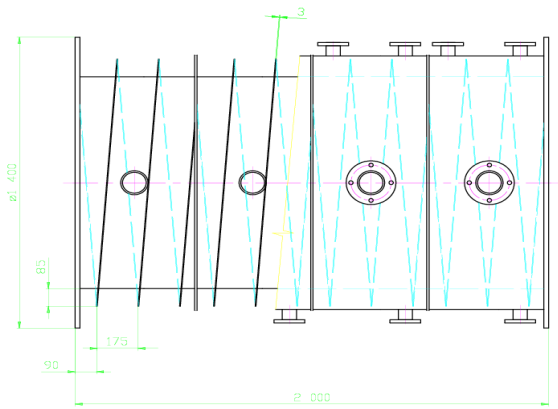

Figure 2.18: Side view of the duplicator

The geometry of the duplicator is shown in the Figure 2.17 and the side view in the Figure 2.18. It consists of the inlet pipe at the top and the outlet pipe at the bottom, two inspection windows at sides and helical baffle. Role of the helical baffle is in the heat transfer enhancement via an increase of water flow velocity. Flow conditions are affected unpredictably for analytical methods of heat transfer calculation due to the gap left between helical baffle and outer shell for thermal expansion. It causes a short circuit and therefore the velocity cannot be determined. Discussion and prediction of flow inside the duplicator is further investigated by CFD modeling in Chapter 3.8.1.

2.5 Emissivity measurement

The emissivity (or emittance according NIST [50]) of the material at the flame facing wall may affect radiation transport of heat. Therefore verification of surface emissivity has been done. The measuring device was infrared thermometer IR-364 with build-in contact temperature measurement sensor. It is equipped with 30:1 optics (distance-to-spot ratio). The measurement relies on the relation of temperature measured by infrared thermometer to the temperature measured by contact measurement.

Accuracy improvement was achieved by heating up the measured steel plate above the temperature 150 ℃ up to 300 ℃. This eliminates influence of surrounding radiation reflected on the measured surface. Since heating up part of the testing chamber would be complicated the plate of the size 0.150 m x 0.1 m was fabricated and utilized for measurement. One side was painted with the black paint. The same is used in the combustion chamber. The other side

was left as it was – rusted steel which simulates damaged surface of combustion chamber after the approx. one-year usage with various types of aggressive fuels.

The plate was heated up in a electric furnace up to the temperature of 300 ℃. Then taken out and the temperature was measured both in contact and non-contact way at the same time. Several such a measurements were done with different emissivity setup for infrared measurement. The Figure 2.19 shows temperature difference between the contact and infrared measurement according:

$$\Delta t = t_{Contact} - t_{Infrared} \tag{5}$$

It says that when the difference Δt is close to zero the temperature of infrared measurement corresponds to the contact measurement and that emissivity settings of the infrared measurement agrees with the emissivity of the surface. The Figure 2.19 shows that for black painted side of plate is the emissivity almost 1 since the temperature difference is close to zero for the value while for rusted side is about 0.945 (zero temperature difference). In a literature [50] is emissivity for sheet steel with rough oxide layer from 0.8 up to for rough steel plate equal to 0.97 (the same also with black paint). Therefore I decided to utilized throughout this thesis the value of 0.9 unless stated otherwise.

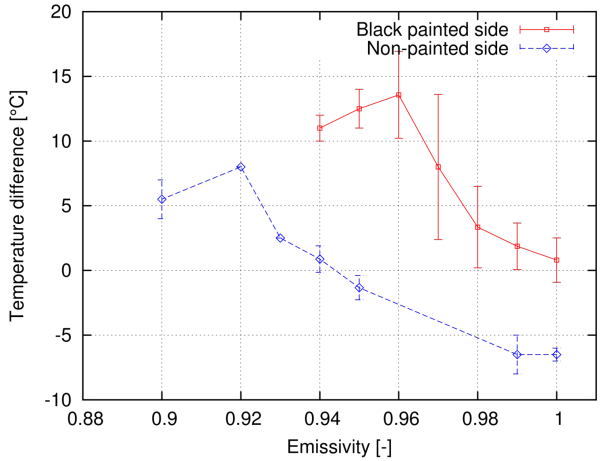

Figure 2.19: Temperature difference between contact and infrared measurement on black painted and non-painted side of the testing steel plate

Several other methods for emissivity measurements are described in literature and possibly could provide more reliable information. E.g. periodic radiometry [51] which can be used at room temperature and is focused on eliminating other influences such as reflective radiative flux. It uses basic principle of modulating temperature of the examined material. While emitted radiative flux is proportional to modulation, reflective flux remains constant.

2.6 Heat loss of combustion chamber

Infrared camera has been used to determine amount of heat lost via outside shell and not transferred into the water or flue gas. Measurement and data evaluation were carried out by Ing. Petr Trávníček from Mendel University in Brno. He used area averaging according to the

Figure 2.20. From the averaged surface temperature and the ambient temperature (14.8 ℃) could be calculated total heat loss consisting of convection loss term:

$$Q_k = \alpha_k \Delta t \, A \tag{6}$$

where heat transfer coefficient is calculated according:

$$\alpha_k = 9{,}7 \cdot \sqrt[3]{\frac{\Delta t}{T_1}} \tag{7}$$

The radiation loss term can be calculated according:

$$Q_s = \sigma \epsilon \left(t_1^4 - t_2^4 \right) A \tag{8}$$

It was confirmed that heat loss from the shell of the combustion chamber does not exceed 6 kW which was less than 0.7 % of the total burner duty 745 kW. For the settings of the burner and measurement details see Chapter 2.1 and 2.9.

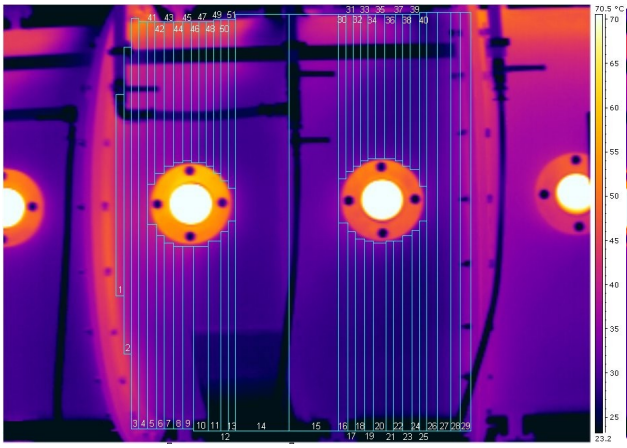

Figure 2.20: Area based evaluation of the surface temperature

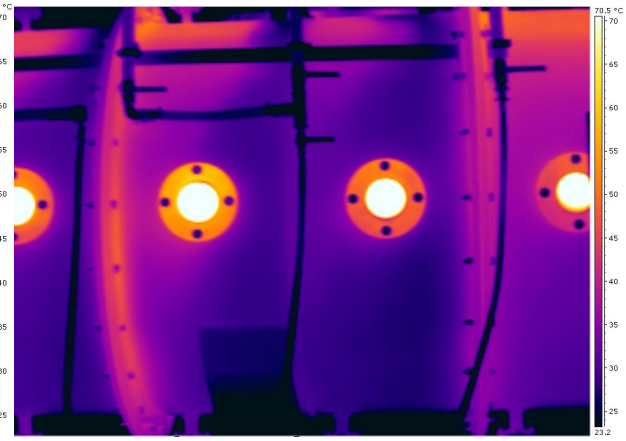

Figure 2.21: Heat loss evaluation

2.7 Measurement uncertainty and its propagation in calculated data

Using the information from sensor manufacturers, the uncertainty of derived parameters can be calculated. To do this, the theory of uncertainty propagation [44] was utilized. E.g. the standard deviation σ_P of product P of uncorrelated variables A and B which have standard deviations σ_A and σ_B may be calculated from the following formula:

$$\left(\frac{\sigma_P}{P} \right)^2 = \left(\frac{\sigma_A}{A} \right)^2 + \left(\frac{\sigma_B}{B} \right)^2 . \tag{9}$$

Equation 9 is general form of uncertainty propagation in summations. Other forms are introduced in following chapters.

2.7.1 Uncertainty in wall heat flux measurement

The accuracy of the measurement of heat transfer rate in a segmental experimental combustion chamber with water cooling may be determined using the calorimetric equation

$$Q = \dot{m}\, c_p \Delta T / A \,, \tag{10}$$

where Q is the heat transfer rate [kW/m^2], m is mass flow rate of the cooling water [kg/s], c_p is specific heat capacity [kJ/kg-K], ΔT is temperature difference [K] and A is the heat exchanging surface area of a section [m^2]. By applying the theory of error propagation [44] we can easily show that for the variance of calculated heat flux holds the following relation:

$$\left(\frac{\sigma_Q}{Q}\right)^2 = \left(\frac{\sigma_{\dot{m}}}{\dot{m}}\right)^2 + \frac{\sigma^2_{T_{in}} + \sigma^2_{T_{out}}}{\Delta T^2} \,. \tag{11}$$

In order to see what measures may be taken in the operation of an experimental facility to minimize measurement errors, we have to use standard deviations of the readings on mass flow meters and temperature sensors. These standard deviations are often proportional to the measured value, for example $m_{true} = m_{measured} \pm 0.005\, m_{measured}$ and in some cases they are relatively constant in the working range, e.g. $T_{true} = T_{measured} \pm 0.3$ K (these are the values relevant for the present work). Thus the first term on the right side of equation (11) is typically independent of the operating conditions, but the denominator in the second term is inversely proportional to the cooling water mass flow rate. Consecutively, we can easily decrease the error of measured heat flux by reducing flow rate of the cooling water.

However, uncertainty of the measurement due to sensors inaccuracy is not the only source of deviation. More problematic are systematic errors which are hard to determine.

2.7.2 Uncertainty in gas and water flow rate measurements

All the data from flow rate sensors are collected in the central operator work station. The water flow meters have longer sensing interval due to the nature of impulse measurements which is at our typical flow rate (about 5 m^3/h) approximately 7-second. Water flow is measured by turbine flow meters XN-RK 04 L300 G2 Q10-BH E K10 equipped with optical sensor sensing 10 impulses per 1 m^3 of water. Measurement uncertainty proposed by the producer is in Figure 2.22.

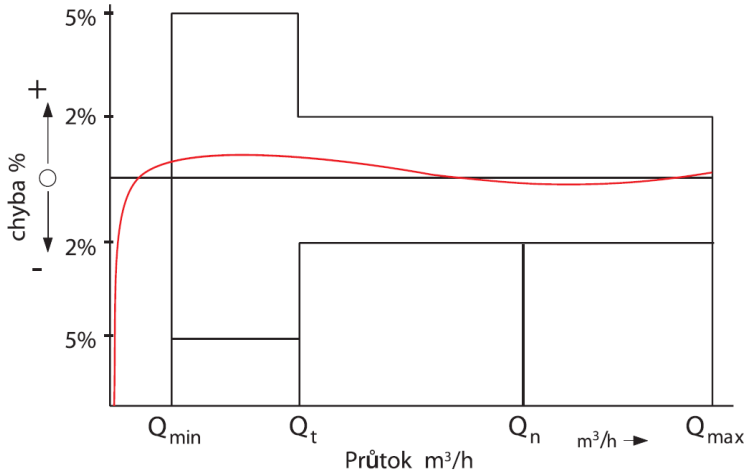

Figure 2.22: Measurement error of water flow rate meter XN-RK 04 L300 G2 declared by the producer (picture from www.sensusesaap.com)

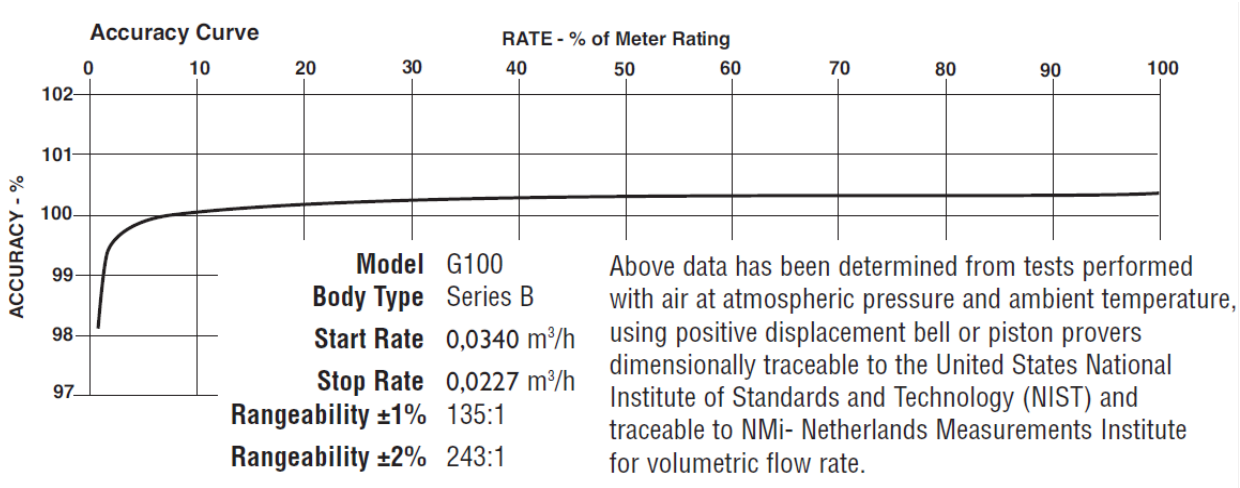

Figure 2.23: Accuracy of rotary gas flow meter as declared by the manufacturer (picture from www.dresser.com/index.cfm/go/list-products/productline/G-Rated-Meter/)

Flow rate of the fuel (natural gas) is measured by positive displacement, rotary type flow meter Roots Dresser G100 and conversion to the standard conditions is made based on temperature (Pt100 T1002 EEx IIC JSP Nová Paka) and pressure (DMK331 EEx ia IIC T6) measurement of the natural gas. Measurement error from the manufacturer is displayed in Figure 2.23.

2.7.3 Uncertainty in air flow rate measurement

An additional procedure for the measurement of air flow rate has been implemented to provide verification of the primary method. The primary indirect measurement based on oxygen concentration in the flue gas has a long response time and rather large uncertainty as documented in Chapter 2.9, Table 8. The calculation of air flow rate is in the primary method based on the measured O_2 content in flue gas and measurement of natural gas flow rate, which itself depends on the readings of three sensors as described in previous chapter.

The second method of flow rate measurement which provides verification for the first one employs a vane anemometer located directly in combustion air pipe which has inner diameter of 246 mm. Information from the anemometer is also automatically collected by the data acquisition system. The uncertainty provided by manufacturer is ±0.1 m/s and ±1.5 % of measured value. The readings from the vane anemometer are however biased due to natural non-uniformity of flow profile in the pipe and further due to slight non-symmetry of velocity profile at the location of measurement. This is caused by a 90° turn of the pipe, which precedes the probe by approximately 12 diameters. In order to provide a reliable correction function for the vane anemometer, the turbulent flow in the air supply pipe has been modeled using ANSYS Fluent® software system for several flow rates spanning the range corresponding to admissible burner duties. The results displayed in Figure 2.24 show that the following linear correction function is appropriate:

$$\dot{m}_{air} = 0.972\, S\, \nu_{anem}\, \rho - 0.015\,, \tag{12}$$

where $\dot{m}_{air}$ [kg/s] is total air flow rate through the duct, S [m^2] is cross-sectional area, ρ [kg/m^3] is air density and v_{anem} [m/s] is the velocity measured by the anemometer. In the simulations was applied no-slip condition at the walls and wall roughness height equal to 0.1 mm. Table 6 provides a comparison of the corrected values from the anemometer with data based on the flue gas O_2 measurements.

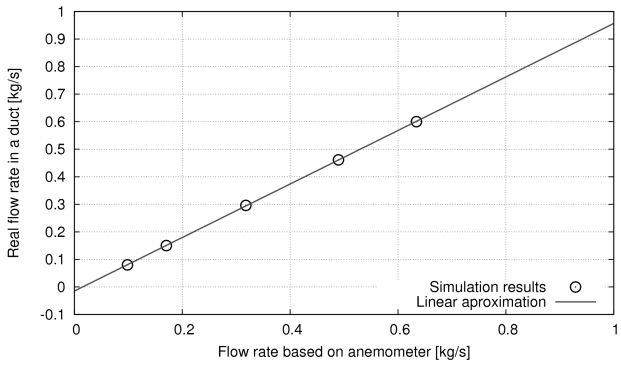

Figure 2.24: Vane anemometer air flow rate

Table 6: Mass flow rate of air in the supply air duct

Predicted by flue gas analyzer	kg/s	0.283	0.377	0.428	0.510	0.548
Predicted by anemometer	kg/s	0.273	0.393	0.434	0.512	0.585
Relative deviation	%	−3.49	4.31	1.38	0.57	6.74

Suggested correction in air flow rate measurement with turbine anemometer could improve reliability of air flow measurement due to requirement for regular replacement of oxygen sensor and inclination for unpredictable failure. This improvement has not been implemented yet since it require adjustment of control system in a operator's workstation.

2.7.4 Uncertainty in temperature measurement

All temperature sensors are of type RTD Pt100 and are placed in a steel sheath. The accuracy indicated by manufacturer is better than ± 0.3 ℃. Gas temperature sensor is Pt100 T1002 EEx IIC JSP Nová Paka and cooling water temperature sensors Pt100, PTP50J RAWET.

2.8 Experimental data processing and analysis

Measured data are displayed during measurement on the computer screen of the operator's PC for monitoring by the operator. In order to save instantaneous data the operator can make a snapshot of all the measured data into a separate structured text file. However, for complex analysis is required the continuous data record.

Data acquisition system was initially designed for a emissions measurements. All the data were collected with low frequency less than 0.5 Hz and were filtered out by the system. Therefore the acquisition system has been modified to fit our needs. All the records from every sensor are written in one-second interval with no filtration into separates text files. We can subsequently process the data with our own filters with known behavior.

In my work the stability of measured data is crucial as I needed to monitor wall heat flux trends and stabilization. Usually there are fluctuations and instabilities present due to the measurement nature which are necessary to be filtered out. Therefore I implemented data processing and data averaging into a stand-alone platform independent software written in C++ language (see Appendix H) with wxWidgets [52] - the widget toolkit for creating graphical user interface. The software takes benefit of object oriented programming, classes and inheritance. Functions and classes are designed to be transferable into other projects – e.g. text file import, data correction or moving average.

Implemented averaging is currently backward moving average with adjustable time range for in-situ heat flux monitoring which reveals overall trends. Post-processing data evaluation is based on standard average over a specified time range – typically around 15 minutes.

The chart panel is taken from other project [53] published under the wxWindows license [54]. It offers ability to display measured heat-fluxes as they develop during the experiment in graphical form (see Fig. 2.25). Graphics based on wxWidgets utilizes wxAUI style which stands for “Advanced User Interface” library. It allows user to use floating frames to arrange workplace to suit one's needs.

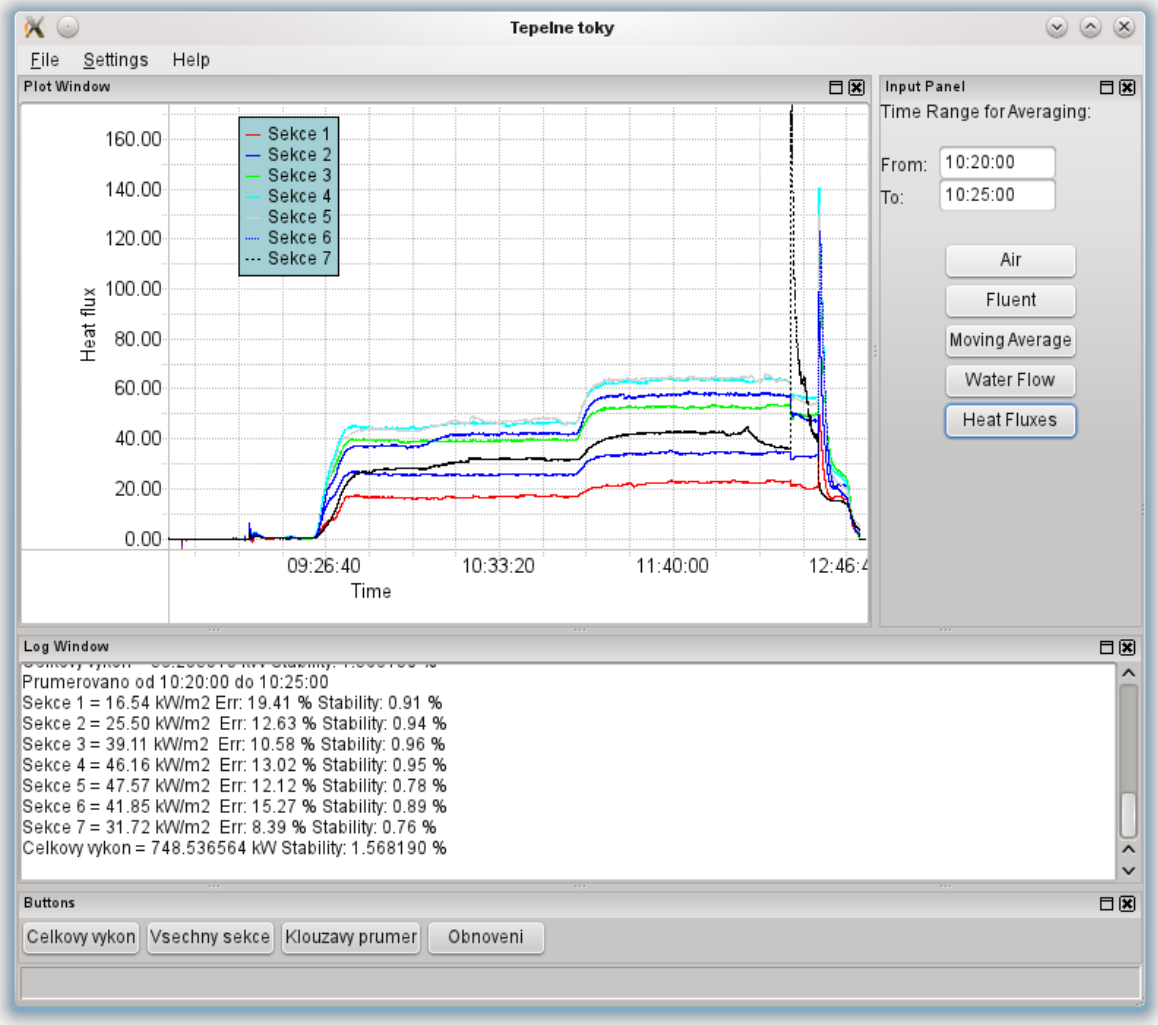

Figure 2.25: Graphical frontend of the developed software for measured data processing

Operator has the possibility to view trends in wall heat fluxes, evaluate stabilization and see estimation of measured heat flux errors. There is possibility to use backward moving average with adjustable size of filtration window. Such a function filters out fluctuations and reveals main trends. All the information helps the operator to decide how to proceed with experiment e.g. to lower cooling water flow to improve accuracy of measurement.

Other functions are implemented for data post-processing. It is aimed at easy evaluation of boundary conditions from experiments and direct export to the form suitable for CFD analysis. Exported data are summarized in following Table 7. All the data can be averaged over specified time range.

Table 7: Exported data from software TepToky

Natural gas flow rate	[kg/s]	measured
Natural gas flow rate	[m^3/s]	normal conditions – calculated based on flow rate, temperature and pressure of the gas
Methane flow rate	[kg/s]	computed methane equivalent of natural gas flow rate, based on heating values
Temperature of the natural gas	[℃]	measured
Combustion air flow rate	[kg/s]	computed from oxygen content in flue gas and natural gas flow rate
Combustion air flow rate	[kg/s]	measured by vane anemometer
Combustion air flow rate	[m^3/h]	measured by vane anemometer
Temperature of combustion air	[℃]	measured
Oxygen concentration in flue gas	[%]	measured
Saturation pressure of water in air	[Pa]	computed

Usual procedure in postprocessing of an experiment record is to graphically evaluate experiment, i.e. examine suitable time ranges for averaging. After that the averaging over the desired time interval is performed. Text output is written into the log window of the program from where it can be copied and saved for further needs. Default is to write heat fluxes in every section with uncertainty evaluated according to the Chapter 2.7. Example of text output from the software is bellow (currently available in Czech version only):

```
Soubor: 2009_05_28
Soubor:
/home/jura/Dokumenty/VUT/zkusebna/Data/2009_05_28_Gas_stage_moje
_2/
Cas_file: 2009_05_281333456909
pd = 2420.412097
rho_vv = 1.208231

**********Data pro Fluent**********
Prumerovano od 11:40:00 do 12:00:00
Prutok plynu = 0.022239 kg/s (pro fluent)
Prutok plynu = 0.022703 kg/s (namereny)
Prutok plynu = 112.113177 Nm3/h (namereny)
Teplota plynu =  20.58 °C
Prutok vzduchu = 0.434925 kg/s (analyzator)
Prutok vzduchu = 0.480518 kg/s (vrtulka)
Prutok vzduchu = 1431.733765 m3/h (vrtulka)
Teplota vzduchu = 20.55 °C
Mnozstvi kysliku ve spalinach (O2) = 2.19 % Fluctuation: 0.02 %

**********Pr  toky vody**********
```

```
Sekce 1: 3.070 m3/hod = 0.8505 kg/s hustota = 997.15 kg/m3
výstupní teplota = 28.69
Sekce 2: 3.261 m3/hod = 0.9024 kg/s hustota = 996.31 kg/m3
výstupní teplota = 34.96
Sekce 3: 3.146 m3/hod = 0.8696 kg/s hustota = 995.03 kg/m3
výstupní teplota = 43.47
Sekce 4: 3.575 m3/hod = 0.9879 kg/s hustota = 994.79 kg/m3
výstupní teplota = 44.95
Sekce 5: 3.267 m3/hod = 0.9023 kg/s hustota = 994.37
kg/m3výstupní teplota = 47.50
Sekce 6: 3.107 m3/hod = 0.8585 kg/s hustota = 994.60 kg/m3
výstupní teplota = 46.10
Sekce 7: 3.423 m3/hod = 0.9443 kg/s hustota = 993.12 kg/m3
výstupní teplota = 54.61
Celkem: 22.849 m3/hod = 6.3162 kg/s hustota = 995.14 kg/m3
výstupní teplota = 42.82
Teplota na vstupu do sekcí: 20.69 °C

Sekce 1 = 22.65 kW/m2 Err: 5.33 % Stability: 0.01 %
Sekce 2 = 34.29 kW/m2  Err: 3.02 % Stability: 0.01 %
Sekce 3 = 52.71 kW/m2  Err: 1.93 % Stability: 0.01 %
Sekce 4 = 63.77 kW/m2  Err: 1.82 % Stability: 0.00 %
Sekce 5 = 64.35 kW/m2  Err: 1.66 % Stability: 0.00 %
Sekce 6 = 58.03 kW/m2  Err: 1.74 % Stability: 0.00 %
Sekce 7 = 42.60 kW/m2  Err: 1.35 % Stability: 0.00 %
Celkovy vykon = 1115.274538 kW Stability: 0.001179 %
```

The benefit of this application is in its direct and fast data processing to a form suitable for the set-up of boundary condition in CFD analysis and calculation of measurement uncertainty for all the calculated and measured data. Tedious repetitive data handling in a spreadsheet application can be avoided and significant amount of time is saved.

2.9 Results of wall heat flux measurements

Total of four long term experiments were carried out at the testing facility focused on wall heat flux measurement. Two at the firing rate 745 kW (referred as Case 1) and other two at 1120 kW (referred as Case 2). All the experiments utilizes the excess air ratio 1.1 and the same burner geometry. Repetitive measurements were performed to verify repeatability of experiments.

Based on my recommendation the cooling water flow through each duplicator was reduced to the minimum. It improved uncertainty of the heat flux measurement by 50 %, e.g. from uncertainty 16.1 % for original flow rate to the 8.4 % at the lowered flow rate. The reason is that due to lower flow rate the outlet temperature increases and so the difference between outlet and inlet temperature increases. Based on the calculation of propagation of uncertainty (see Chapter 2.7.1) the heat flux measurement uncertainty is inversely proportional to the temperature difference. The fact significantly improved measurement results.

Main operating parameters characterizing the two cases for all four runs are summarized in Table 8. Note that natural gas utilized during experiment was for CFD simulation purposes substituted by methane and the flow rates were corrected to compensate the difference in heating values. Mass flow rates through particular gas stages were not measured since we do not have flow meters there, but are rather calculated in CFD simulation. Model of the entire gas-staged fuel piping system was created earlier in our research group which I used for flow rate calculations.

Table 8: Operating conditions in the Case 1 (745 kW)

		Measurement A	Error estimate [%]	Measurement B	Error estimate [%]	Average
Total thermal duty	[kW]	745.7	1.62	748.0	2.7	746.9
Natural gas flow rate	[kg/s]	0.01517	1.62	0.01522	2.7	0.01520
Calculated methane mass flow rate	[kg/s]	0.01486	1.62	0.01492	2.7	0.01489
Air mass flow rate	[kg/s]	0.289	9.8	0.290	10.1	0.290
Fuel temperature	[℃]	20.11	1.5	12.5	2.6	16.31
Air temperature	[℃]	19.23	1.5	4.26	1.9	11.75
Total extracted heat flux	[kW]	438.5	4.3	437.8	5.27	438.1
Mass flow rate at primary gas stage	[kg/s]					3.84E-3
Mass flow rate at secondary gas stage	[kg/s]					1.10E-2

Table 9: Operating conditions in the Case 2 (1120 kW)

		Measurement A	Error estimate [%]	Measurement B	Error estimate [%]	Average
Total thermal duty	[kW]	1115.0	1.6	1124.2	2.4	1119.6
Natural gas flow rate	[kg/s]	0.02270	1.6	0.02286	2.4	0.02278
Calculated methane mass flow rate	[kg/s]	0.02224	1.6	0.02240	2.4	0.02232
Air mass flow rate	[kg/s]	0.435	9.8	0.438	10	0.436
Fuel temperature	[℃]	20.58	1.5	13.08	2.3	16.83
Air temperature	[℃]	20.55	1.4	8.53	1.6	14.54
Total extracted heat flux	[kW]	591.5	3.3	596.7	4.2	594.1
Mass flow rate at primary gas stage	[kg/s]					5.79E-3
Mass flow rate at secondary gas stage	[kg/s]					1.65E-2

The measured heat flux densities are summarized in Table 10, which includes the average of measured values from the two data sets available for each of the Cases 1 and 2. These average values (and corresponding averaged operating conditions) were used in simulations reported in the following sections. The table also includes mean fluctuations observed in the measurement during the period of steady operation, i.e. standard deviation of the measured data. Additionally provided are also error estimates calculated by error propagation theory according to accuracy of the involved sensors. Those measurements were also introduced by Vondál [55, 56] included in Appendix D and E.

Table 10: Measured heat fluxes – averaged values from two measurements

	Case 1 (745 kW)			Case 2 (1120 kW)		
	Heat flux	Mean fluctuation	Error estimate	Heat flux	Mean fluctuation	Error estimate
	[kW/m^2]	[kW/m^2]	[%]	[kW/m^2]	[kW/m^2]	[%]
Section 1	17.25	0.15	8.4%	21.88	0.21	6.4%
Section 2	25.57	0.16	4.8%	34.05	0.27	3.5%
Section 3	40.17	0.14	2.9%	53.28	0.26	2.3%
Section 4	46.41	0.15	2.8%	63.58	0.24	2.0%
Section 5	47.87	0.16	2.6%	65.45	0.27	1.9%
Section 6	42.33	0.17	2.8%	58.9	0.29	2.0%
Section 7	31.4	0.21	0.02	42.74	0.19	1.6%

2.10 Summary

Modern industrial-scale facility allows us to accurately measure local wall heat fluxes with uncertainty of measured data better than 8.5 %. The method of propagation of uncertainty was utilized to identify error estimate of measured data. The acquisition system is able to collect data with frequency 1 Hz except for the cooling water flow measurement with the frequency 0.17 Hz. Other measuring technique is in development – i.e. inflame temperature measurement which shows us promising results. Wall emissivity was identified to be about 0.9 based on the measurement of the wall sample with identical coating with the chamber.

The data processing and evaluation with my in-house software allows us to quickly use measured data for CFD analysis. Underlying features of the software was introduced and the software is included on CD-ROM.

3. Gas combustion modeling and simulation

This chapter introduces the basics of the mathematical modeling underlining computation fluid dynamics. Due to the focus of this work are also summarized modeling approaches for reactive flows with radiative heat transfer. Attention is also payed to the proper setup of CFD case such as boundary conditions and material properties. Focus is on effects of particular models and settings on wall heat flux predictions. Several comparisons of predicted wall heat fluxes with two measured cases (firing rate 745 kW and 1120 kW) are provided. All discussed models and methods are either available in ANSYS Fluent® commercial solver or source code is given for its implementation via User defined function (UDF).

3.1 Governing equations

Fluid flow can be described by a system of equations. Basic conservation laws must be satisfied. These include conservation of mass, momentum (Newton's second law $F = ma$) and energy. Entire CFD field is based on the mentioned equations. However, analytical solution is unavailable except for several simple cases of laminar flows (e.g. laminar boundary layer flow past a flat plate [57, 58]). Any flow can be simulated numerically (the equations are valid for all flows) but solution of real world turbulent flows is still beyond nowadays capability due excessive demands on computational resources. The published studies utilizing so-called direct numerical simulation (DNS) are only for low-Reynolds flows resolved in a small domain. In practical cases averaging must be applied to filter out small scale turbulence eddies which have to be approximated by modeling such as well-known Reynolds-averaged Navier-Stokes (RANS) equations or Large Eddy Simulations (LES).

Transport of any fluid flow quantity can be expressed in a conservative form of general Eulerian transport equation:

$$\frac{\partial(\rho\phi)}{\partial t}+\frac{\partial(\rho\phi u_i)}{\partial x_i}=\frac{\partial}{\partial x_i}\left(\Gamma\frac{\partial\phi}{\partial x_j}\right)+S_\phi\,, \tag{13}$$

where first expression on the left is the rate of accumulation of Φ in a fluid element, second is net rate of flow of Φ out of fluid element (convective term). On the right side is the rate of increase of Φ due to diffusion and the rate of increase of Φ due to sources. The notation uses the so-called Einstein summation convention. throughout Chapter 3.

Continuity equation

Conservation of mass is expressed in the continuity equation:

$$\frac{\partial\rho}{\partial t}+\frac{\partial(\rho u_j)}{\partial x_j}=0\,. \tag{14}$$

Conservation of momentum

From Newton's second law $F = ma$ can be derived momentum transport equation which says that body forces and surface forces are balanced with inertia:

$$\frac{\partial(\rho u_i)}{\partial t}+\frac{\partial(\rho u_i u_j)}{\partial x_j}=-\frac{\partial p}{\partial x_i}+\frac{\partial \tau_{ji}}{\partial x_j}+\rho f_i\,. \tag{15}$$

Conservation of energy

The following equation describes the transport of specific enthalpy:

$$\frac{\partial(\rho h)}{\partial t}+\frac{\partial(\rho h u_j)}{\partial u_j}=-\frac{\partial p}{\partial t}+\frac{\partial}{\partial x_j}\left(\lambda\frac{\partial T}{\partial x_j}\right)+\frac{\partial(\tau_{jl}u_j)}{\partial u_l}+S_h\,. \tag{16}$$

Conservation of species

The transport equation for species reads:

$$\frac{\partial(\rho Y_k)}{\partial t}+\frac{\partial(\rho u_i Y_k)}{\partial x_i}=\frac{\partial}{\partial x_i}(\rho D\frac{\partial Y_k}{\partial x_i})+S_k\,. \tag{17}$$

3.2 Geometry and computational grid

The geometry of the modeled flow domain includes several meters of air supply duct, the burner, and combustion chamber. It was necessary to include the air duct as the air enters the burner from a side and the burner does not include a honeycomb that would homogenize the flow. In preliminary cold-flow computations it was confirmed that due to this asymmetry the air flow is far from axially symmetrical. The predicted flame is inclined due to the air maldistribution downwards, but the effect of buoyancy was in the predicted flames observed to have a greater effect, as it again lifts the flame above burner axis already 1 m after the burner. The burner geometry does not include the actual nozzle holes drilled through nozzle heads and the gas enters the computational domain at the nozzle orifices instead. This was considered a reasonable trade-off between accuracy and CPU costs. Additionally, the diameter of nozzles has been increased in order to eliminate unrealistic exit velocities due to nozzle area reduction after discretization. Specifically, the diameters have been increased by 18% as corresponds to the discretization of a circle by an inscribed regular hexagon. Grid was created with great care to ensure high quality. Most of the volume of computational domain was meshed by hexahedral cells and only in the vicinity of nozzles were used tetrahedral elements. Total number of grid cells was approximately 1,300,000. Whole model can be seen in the Figure 3.1 and the mesh in Figure 3.2.

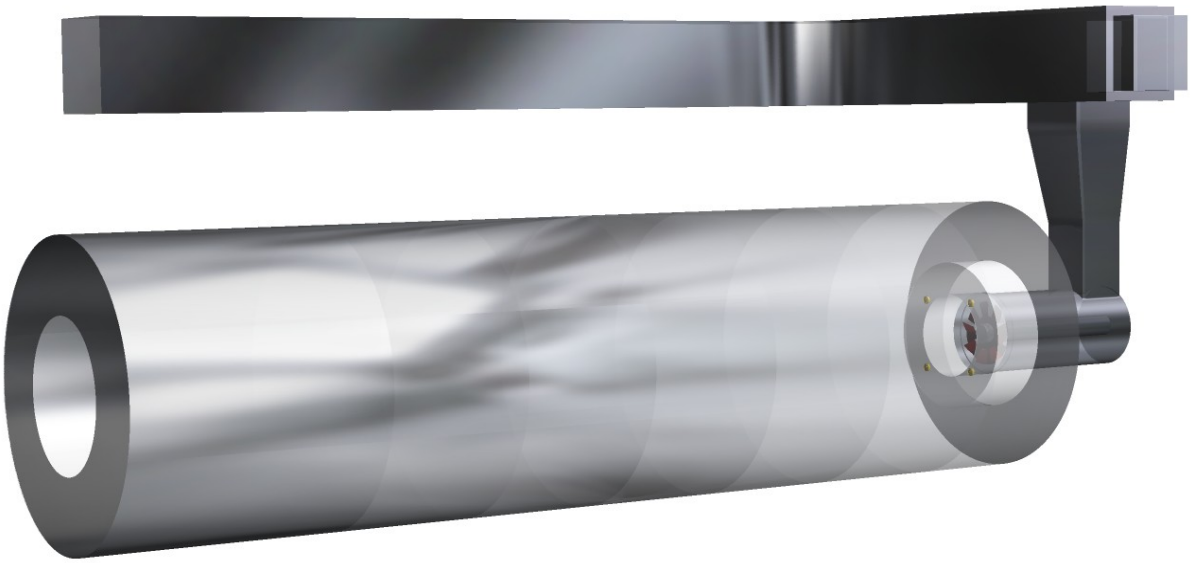

Figure 3.1: Model of combustion chamber

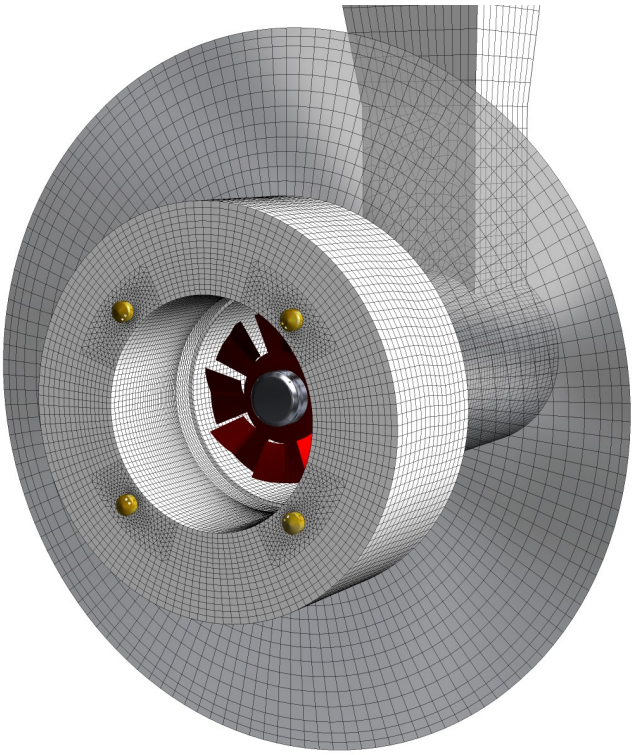

Figure 3.2: Mesh around the burner inside the combustion chamber

3.3 Turbulence modeling

Turbulence is the major concern in modeling of swirling diffusion flames. Turbulence is the main reason why simulation of this type of flames is so difficult. Swirling flows generally (i.e. including nonreacting flows e.g. in cyclones) pose a challenging problem for CFD simulations and the additional complexity caused by large density variations, turbulence-modified chemical reaction rates and radiative heat transfer make the simulations even more challenging.

The objective of this work is to analyze the performance of CFD models that have acceptable computational requirements and thus can be applied in the industrial practice. Therefore the considered turbulence models comprise a selection of turbulence modeling approaches that are available in most commercial CFD codes.

The first group of models is applicable to the calculation of time-averaged (Reynolds-averaged) flow field properties. This group of models includes so-called moment turbulence closures and they are collectively classified as Reynolds-averaged Navier-Stokes models (RANS).

When turbulent fluctuations are too severe and simulations using RANS models do not converge, it is possible to include accumulation terms into the model equations and simulate the problem as transient. The resulting models are collectively denoted as unsteady RANS models (URANS).

The last subsection related to turbulence deals with wall boundary conditions in turbulent flows as an important part of the simulation methods.

3.3.1 RANS models

Reynolds-averaged Navier-Stokes equation (momentum transport equation) has the following form:

$$\frac{\partial(\rho\overline{u_i}\,\overline{u_j})}{\partial x_j}=-\frac{\partial p}{\partial x_i}+\frac{\partial}{\partial x_j}\left[\mu\left(\frac{\partial\overline{u_i}}{\partial x_j}+\frac{\partial\overline{u_j}}{\partial x_i}\right)-\rho\overline{u_i'u_j'}\right]. \tag{18}$$

An important new term produced by the averaging operation is the last one on the right side. This one and similar terms in the remaining governing Navier-Stokes equations are the so-called Reynolds stresses, which have to be modeled (approximated). Widely utilized is so-called Boussinesq hypothesis, which models the effect of turbulence on the time-averaged flow field by increased viscosity and relates Reynolds stresses to the viscous stresses (i.e. assumes gradient transport of turbulence):

$$-\rho\overline{u_i'u_j'}=\mu_t\left(\frac{\partial u_i}{\partial x_j}+\frac{\partial u_j}{\partial x_i}\right)-\frac{2}{3}\mu_t\frac{\partial u_l}{\partial x_l}\delta_{ij}-\frac{2}{3}\rho k\,\delta_{ij}, \tag{19}$$

where k is turbulence kinetic energy and μ_t is the turbulent viscosity defined as:

$$\mu_t=C_\mu\rho\frac{k^2}{\epsilon}, \tag{20}$$

where C_μ is a model constant and ε is the dissipation of turbulence kinetic energy.

Two prominent models that make use of the Bussinesq hypothesis and prevail in the industrial practice are the k-ε model and the k-ω model. Both of them use two transport equations for turbulence properties. They are briefly summarised in the following paragraphs.

k-ε model

The most popular for turbulence modeling is probably the standard k-ε model [59]. Transport equation for turbulence kinetic energy k has form [60]:

$$\frac{\partial k}{\partial t}+\frac{\partial (u_j k)}{\partial x_j}=\frac{\partial u_i \tau_{ij}}{\partial x_j}-\epsilon+\frac{\partial}{\partial x_j}\left[\left(\nu+\frac{\nu_t}{\sigma_k}\right)\frac{\partial k}{\partial x_j}\right], \tag{21}$$

and equation for rate of energy dissipation ε is:

$$\frac{\partial \epsilon}{\partial t}+\frac{\partial (u_j \epsilon)}{\partial x_j}=C_{1\epsilon}\frac{\epsilon}{k}\frac{\partial u_i \tau_{ij}}{\partial x_j}-C_{2\epsilon}\frac{\epsilon^2}{k}+\frac{\partial}{\partial x_j}\left[\left(\nu+\frac{\nu_t}{\sigma_\epsilon}\right)\frac{\partial \epsilon}{\partial x_j}\right], \tag{22}$$

where $C_{\varepsilon 1}$, $C_{\varepsilon 2}$, C_μ, σ_k, σ_ε are (empirical) closure coefficients.

The model is derived only for regions of fully developed turbulence, therefore it is not valid through the wall boundary layers. Boundary conditions of the k-ε model equations therefore require some additional modeling by so-called wall functions as discussed below.

k-ω model

The k-ω model as proposed by Wilcox [60] uses the following equations:

$$\frac{\partial k}{\partial t}+\frac{\partial (u_j k)}{\partial x_j}=\frac{\partial u_i \tau_{ij}}{\partial x_j}-\beta' k\omega+\frac{\partial}{\partial x_j}\left[\left(\nu+\sigma'\frac{k}{\omega}\right)\frac{\partial k}{\partial x_j}\right], \tag{23}$$

$$\frac{\partial \omega}{\partial t}+\frac{\partial (u_j \omega)}{\partial x_j}=\frac{\partial u_i \tau_{ij}}{\partial x_j}-\beta\omega^2+\frac{\sigma_d}{\omega}\frac{\partial k}{\partial x_j}\frac{\partial \omega}{\partial x_j}+\frac{\partial}{\partial x_j}\left[\left(\nu+\sigma\frac{k}{\omega}\right)\frac{\partial \omega}{\partial x_j}\right], \tag{24}$$

where α, β, β', σ, σ', σ_d are closure coefficients. One of the advantages of this model is its validity even in low-Re regions, most importantly in the wall-adjacent boundary layer. Therefore no wall functions are needed. However, the k-ω model has certain limitations in inner region and was improved by Menter [61] by blending with the k-ε model. This more advanced variation of the model is called Shear stress transport k-ω model (SST k-ω).

Reynolds stress model (RSM)

The Bussinesq gradient-transport hypothesis can be dropped in the domain of RANS models only by modeling and solving transport equation for each of the Reynolds stresses. This approach is called second order closure and the implementation in the ANSYS Fluent® software is based on the work [62]. The model is more computationally demanding than the preceding two-equation models since it solves transport equations for the Reynolds stresses and energy dissipation rate which yields seven additional partial differential equations. Note

that RSM is again valid only in fully developed turbulent flows and thus requires special treatment near the walls similarly as the k-ε model.

RSM is recommended for highly swirling and cyclone flow due its ability to capture swirl, rotation and rapid changes in flow. It has advantage over the one or two equation models in its ability to account for anisotropy of the Reynolds stresses.

3.3.2 URANS models

Unsteady Reynolds-averaged Navier-Stokes models are obtained from the RANS models by simply adding accumulation terms to the governing equations. A generic transport equation integrated over a control volume then reads:

$$\int_V \frac{\partial(\rho\phi)}{\partial t} dV + \oint \partial(\rho\phi u_i)\cdot dA_i = \oint (\Gamma \frac{\partial\phi}{\partial x_j})\cdot dA_i + \int_V S_\phi dV \tag{25}$$

From a physical viewpoint the concept of URANS is strange because it uses time-averaged Navier-Stokes equations for unsteady calculations, which is contradictory. However, it proves to be a useful tool in strongly unsteady turbulent flows such as von Kármán vortex street.

3.3.3 Wall functions

At the end of this chapter that discusses turbulence models, it is necessary to mention the treatment of the boundary layers in models that are not valid through the low-Re regions near walls. Near-wall velocity field and convective heat transfer both depend strongly on the turbulence model. In the case of combustion, where approximately 90 % of heat is transferred via radiation, boundary model doesn't influence heat flux significantly, but it may impact the flow pattern in the combustion chamber.

The law of the wall as described e.g. in [60] is based on assumption that variation of the local shear stress τ variation with the distance from the wall is small. Therefore the surface shear stress τ_ω can be used instead. Then the velocity scale (also known as friction velocity) is:

$$u_\tau \equiv \sqrt{\frac{\tau_\omega}{\rho}}\,. \tag{26}$$

Based on measurements [63] the law of the wall was derived in following form:

$$\frac{U}{u_\tau} = \frac{1}{\kappa}\ln\frac{u_\tau y}{\nu} + C\,, \tag{27}$$

where C is constant reflecting wall roughness. Following dimensionless velocity and distance from the wall are often used in reporting results of modeling:

$$u^+ \equiv \frac{U}{u_\tau} \text{ and } y^+ \equiv \frac{u_\tau y}{\nu}\,.$$

3.3.4 Effect of turbulence models on wall heat flux

Four RANS turbulence models described in previous sections and available in ANSYS Fluent® were investigated for their influence on wall heat flux predictions. Namely it was realizable k-ε,

RNG k-ε, SST k-ω and RSM turbulence model. Solver settings were kept the same for all of the test cases as specified in Table 11 and 12. Simulations were run in unsteady mode since combustion in such a complex geometry is physically transient phenomena. Time step was chosen according the convergence to allow the solver performing from ten to twenty iterations per time step. The new method for WSGGM absorption coefficient calculation was utilized (for details see Chapter 3.6.1).

Table 11: Solver settings of all cases

Model	Settings
Turbulence model	realizable (or RNG) k-ε or SST k-ω or RSM
Radiation model	Discrete ordinates
Species transport	EDM with global one step mechanism
Pressure-velocity coupling	SIMPLEC
Skewness correction	1
Time step [s]	0.002

Table 12: Discretization scheme of all cases

Variable	Scheme
Pressure	PRESTO!
Density	QUICK
Momentum	QUICK
Turbulent Kinetic Energy	First Order Upwind
Specific Dissipation Rate	First Order Upwind
CH_4	First Order Upwind
O_2	First Order Upwind
CO_2	First Order Upwind
H_2O	First Order Upwind
Energy	First Order Upwind
Discrete Ordinates	First Order Upwind

Comparison has been made for both measured cases (see Chapter 2.9). The first one for the Case 1 with firing rate 745 kW and the second for the Case 2 with firing rate 1120 kW. All the boundary conditions remain identical except for mass flow inlets i.e. combustion air inlet and all the fuel inlets.

Turbulence model comparison for the Case 1 (745 kW)

Results show negligible effect of turbulence model on overall heat transfer which differs by less than 5 % from measured value. This is given by fact that all fuel has enough time to completely mix with oxygen, burn and release heat no matter what turbulence model is used.

After that it is just upon the radiative properties of gas and walls how much heat is transferred into walls and how much is carried out of the chamber by the gas. Turbulence may only affect location where within the chamber is the heat released.

Presented results are the best that were achieved so far. Overall heat flux for the SST k-ω model deviates just by 0.3 % from the measured value. The profile of wall heat fluxes along the axial length of chamber fits well to the measured profile – see Fig 3.3 and Table 13 and 14.

Surprisingly the worst predictions give one of the modern turbulence models realizable k-ε. The overall transferred heat into wall has acceptable deviation of 5.0 %. However the profile of the heat flux is inaccurate. First five sections are underestimated (up to 19 %) while the last seventh section is overestimated by 25 %.

Table 15 shows interlink between volume-averaged temperature inside the combustor, extracted heat into the cooling water and area-weighted averaged temperature at the outlet. These variables are bounded by law of conservation of energy. Any disproportional change could only mean imbalance in calculation or increased emissions carrying out unburned species with chemical form of energy. In fact the energy imbalance does occur during calculation and is monitored by my own UDF attached in Appendix I. It is the highest for the RSM turbulence model and reaches no more than 1.4 % of the total firing rate. Therefore I assume it to be negligible.

The peak temperature (in Table 15 referred as maximum temperature) is primarily dependent on chemistry (see Chapter 3.4) and less on turbulence model. It is well known fact that Eddy dissipation model overestimates the peak flame temperature. There exists methods how to flatter the temperature e.g. see Table 22 which however doesn't affect the wall heat flux.

Displayed values in Figure 3.3 and Tables 13 and 14 are averaged over at least 2 seconds of physical time in simulation. Whereas the data in Table 15 are instantaneous.

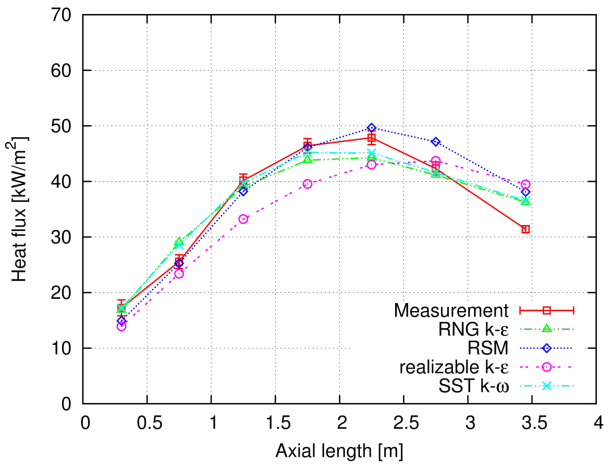

Figure 3.3: Turbulence model comparison and its effect on predicted wall heat flux

Table 13: Turbulence model comparison via wall heat fluxes for Case 1

	Measurement		RNG k-ε		RSM	
	Wall heat flux	Error estimate	Wall heat flux	Deviation from measurement	Wall heat flux	Deviation from measurement
	[kW/m²]	[%]	[kW/m²]	[%]	[kW/m²]	[%]
Section 1	17.25	8.4	16.8	−2.3	14.9	−13.6
Section 2	25.57	4.8	29.0	13.5	25.3	−1.2
Section 3	40.17	2.9	39.1	−2.8	38.2	−4.9
Section 4	46.41	2.8	43.8	−5.5	46.1	−0.7
Section 5	47.87	2.6	44.3	−7.6	49.7	3.7
Section 6	42.33	2.8	41.2	−2.7	47.1	11.4
Section 7	31.4	2	36.3	15.5	38.1	21.4

Table 14: Turbulence model comparison via wall heat fluxes for Case 1

	realizable k-ε		SST k-ω	
	Wall heat flux	Deviation from measurement	Wall heat flux	Deviation from measurement
	[kW/m²]	[%]	[kW/m²]	[%]
Section 1	13.9	−19.3	17.2	0.0
Section 2	23.4	−8.5	28.6	11.7
Section 3	33.2	−17.3	39.7	−1.1
Section 4	39.5	−14.8	45.2	−2.6
Section 5	43.0	−10.1	45.1	−5.7
Section 6	43.7	3.2	41.6	−1.8
Section 7	39.5	25.7	36.5	16.4

Table 15: Predictions of four different turbulence models – instantaneous values of Case 1

	Volume averaged temperature [℃]	Maximum temperature [℃]	Area weighted average of temperature at outlet [℃]	Absorption coefficient [m⁻¹]	Total wall heat flux [kW]
RNG k-ε	905.0	2032.6	883.2	0.3	433.5
RSM	901.1	1817.9	817.0	0.3	450.5
realizable k-ε	888.9	2039.0	924.5	0.3	416.1
SST k-ω	875.8	1907.9	884.9	0.31	439.3

Turbulence model comparison for the Case 2 (1120 kW)

Even at higher firing rate the results confirm accurate predictions of total extracted heat, see Figure 3.4 and Table 16 and 17 (averaged data). Good agreements show realizable k-ε turbulence model with deviation just 0.12 %. The highest deviation from measured total extracted heat indicated RSM turbulence model (3.8 %). In contrary the local wall heat fluxes monitored by separate sections shows higher deviations than in preceding simulations of Case 1. In the case of SST k-ω turbulence models deviation reaches up to 41 % in last, seventh section when compared to the measurement. All the turbulence models, but one, amplified previously observed trend in overprediciton of local wall heat fluxes in the last section. Only exception was RSM turbulence model which gives consisting deviation in all the sections for both cases 1 and 2 (compare Table 13 and 16).

Obvious underprediction of the local wall heat fluxes in the first four sections and significant overprediction in the last two sections indicates low turbulence mixing of fuel and oxidizer. Turbulence models seems to have problems with the swirling flow enhanced mixing and heat release therefore takes longer time than in reality.

The results in Table 18 shows that RSM turbulence model predicts the highest volume-averaged temperature in the combustion chamber and therefore also the highest extracted heat. All the maximum temperatures are lower than in previous Case 1 (see Table 15). Such a decrease may be caused by more intensive mixing eliminating fuel rich areas and truncating the peak temperatures. It shows potential for lower NO_x emissions.

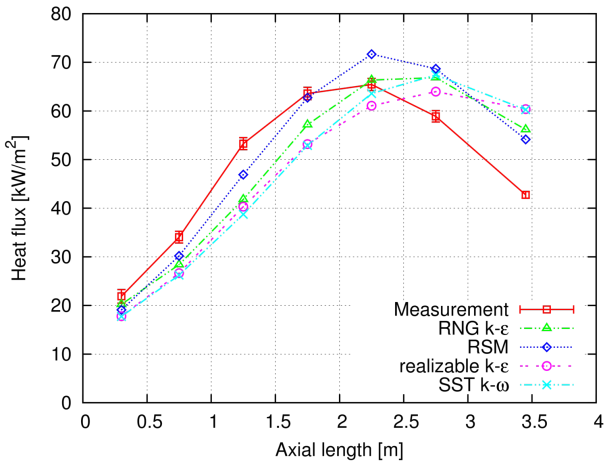

Figure 3.4: Turbulence model comparison for the Case 2

Table 16: Turbulence model comparison via wall heat fluxes for Case 2

	Measurement		RNG k-ε		RSM	
	Wall heat flux	Error estimate	Wall heat flux	Deviation from measurement	Wall heat flux	Deviation from measurement
	[kW/m²]	[%]	[kW/m²]	[%]	[kW/m²]	[%]
Section 1	17.25	8.4	16.8	−7.5	14.9	−12.8
Section 2	25.57	4.8	29.0	−16.6	25.3	−11.3
Section 3	40.17	2.9	39.1	−21.5	38.2	−11.9
Section 4	46.41	2.8	43.8	−10.1	46.1	−1.3
Section 5	47.87	2.6	44.3	1.4	49.7	9.5
Section 6	42.33	2.8	41.2	13.5	47.1	16.6
Section 7	31.4	2	36.3	31.5	38.1	26.7

Table 17: Turbulence model comparison via wall heat fluxes for Case 2

	realizable k-ε		SST k-ω	
	Wall heat flux	Deviation from measurement	Wall heat flux	Deviation from measurement
	[kW/m²]	[%]	[kW/m²]	[%]
Section 1	13.9	−18.7	17.2	−18.9
Section 2	23.4	−21.8	28.6	−22.9
Section 3	33.2	−24.3	39.7	−27.3
Section 4	39.5	−16.4	45.2	−16.8
Section 5	43.0	−6.7	45.1	−2.8
Section 6	43.7	8.6	41.6	14.5
Section 7	39.5	41.3	36.5	41.0

Table 18: Predictions of four different turbulence models – instantaneous values of Case 2

	Volume averaged temperature [℃]	Maximum temperature [℃]	Area weighted average of temperature at outlet [℃]	Absorption coefficient [m⁻¹]	Total wall heat flux [kW]
RNG k-ε	949.9	1955.6	938.3	0.29	593.4
RSM	964.4	1930.2	918.8	0.28	617.0
realizable k-ε	915.9	1953.7	1011.2	0.29	577.9
SST k-ω	928.2	1957.8	992.6	0.29	583.4

3.3.5 Summary

The most accurately predicts local wall heat fluxes in the Case 1 the SST k-ω turbulence model along with new implementation of WSGGM and domain-based mean beam length. Overall heat flux deviates by 0.3 %. However it still tends to overpredicts heat fluxes in the last section. In this case it is over 16 %. Very good results gives RNG k-ε model as well with deviation of total heat fluxes at 1 % and maximum local deviation no more than 15.5 %.

Predictions for the Case 2 shows higher deviations from measured values. Total extracted heat is still in good agreement (from 0.12 % to 3.8 %) but the local wall heat fluxes in last section tend to significantly overpredicts measured data (from 26.7 % to 41 %). I assign this behavior to the problematic predictions of swirling flow affecting mixing and therefore even heat release. However such a problems are only amplified for higher firing rates with more intensive swirl and higher velocity through the swirl generator.

3.4 Chemistry modeling of methane combustion

An extensive recent review of turbulent combustion modeling may be found in [64]. There are discussed both premixed and non-premixed combustion models within the domain of RANS approaches. Another excellent reference is the book [65]. Effect of the flame acoustics on the heat release from the flame and on the burning was reviewed in [66]. This work discussed also turbulence-chemistry interaction and scales at which these phenomena occur. The main conclusion was that single-scale turbulent combustion modeling can be used only when combustion time-scale is of the same magnitude as turbulent time scale.

3.4.1 Eddy Dissipation Model

Need for a simple and widely applicable model for nonpremixed turbulent combustion was partially satisfied by the so-called eddy dissipation model (EDM) introduced by Magnussen and Hjertager [67]. It is based on assumption "mixed is burned". The reaction rates are assumed to be controlled by turbulence and Arhenius chemical kinetics is omitted. The resulting model therefore has moderate computational requirements.

EDM should be used only with one-step or two-step (global) mechanism. More complex chemical mechanisms are inapplicable due to the equal reaction rates applied to all reactions. The net rate of production of species due to reactions [68] reads:

$$R_{i,r} = \nu`_{i,r} M_{\omega,i} A \rho \frac{\epsilon}{k} min_R \left( \frac{Y_R}{\nu`_{R,r} M_{\omega,R}} \right). \tag{28}$$

Combustion of methane described by one-step reaction mechanism represents the simplest model of oxidizing methane as follows:

$$CH_4 + 2O_2 \rightarrow CO_2 + H_2O$$

This mechanism neglects all the intermediate species. The most significant of them is perhaps CO, the oxidation of which is rather slow [69]. Therefore two-step mechanism can be utilized to capture the effect of CO oxidation:

$$CH_4 + 3/2O_2 \rightarrow CO + 2H_2O$$

$$CO+1/2O_2 \rightarrow CO_2$$

One or two step reaction mechanisms inevitably overpredict the peak flame temperature. Therefore [70] suggested to remedy this effect by increasing specific heat of the mixture species by adjusting polynomial coefficients of the main species.

3.4.2 Effect of settings in eddy dissipation model

Simulations were run to check influence of constant A in the net rate of production of species due to reactions, in equation 28 as suggested by [71]. Original value of constant $A = 4$ recommended in [68] was changed according to the value $A = 0.6$ as proposed in [71]. The authors in the work argue that this modification partially compensates the use of simple global reaction mechanism and lowers the peak flame temperature.

Simulation was transient with settings as follows in Table 19 and 20:

Table 19: Solver settings

Model	Settings
Turbulence model	realizable k-ε
Radiation model	Discrete ordinates
Species transport	EDM with global two step mechanism
Pressure-velocity coupling	SIMPLEC
Skewness correction	1
Time step	0.02 s

Table 20: Discretization scheme of equations

Variable	Scheme
Pressure	PRESTO!
Density	QUICK
Momentum	QUICK
Turbulent Kinetic Energy	First Order Upwind
Specific Dissipation Rate	First Order Upwind
CH_4	First Order Upwind
O_2	First Order Upwind
CO_2	First Order Upwind
CO	First Order Upwind
H_2O	First Order Upwind
Energy	First Order Upwind
Discrete Ordinates	First Order Upwind

Present simulations showed that there was decrease in overall wall heat flux by less than 3 % see Tab. 21 where the average values of the total heat flux and positive and negative variation in the averaged data are shown. The most significant changes were observed in first 4 sections (close to the burner) meanwhile rest of the section had similar values as the baseline case with default value of the parameter A.

While decrease of the A-constant caused only 3% decrease in wall heat fluxes the maximum temperature in the chamber decreased by 26 % (see Table 22). It is due to decrease in reaction rate which flattens the temperature peaks and makes the temperature field more uniform.

Table 21: Effect of constant A on the wall heat fluxes – averaged values over more than 10 000 iterations

	A = 4			A = 0.6		
	Wall heat flux [kW/m^2]	Average positive deviation [kW/m^2]	Average negative deviation [kW/m^2]	Wall heat flux [kW/m^2]	Average positive deviation [kW/m^2]	Average negative deviation [kW/m^2]
Section 1	23.28	0.52	−0.47	18	0.39	−0.41
Section 2	41.88	1.16	−1.07	35.27	0.79	−0.81
Section 3	57.23	1.33	−1.45	53.67	1.02	−1.14
Section 4	59.2	1.15	−1.26	58.02	1.24	−1.48
Section 5	53.23	0.99	−0.96	53.86	1.2	−1.25
Section 6	44.27	0.96	−1.06	46.52	1.09	−1.06
Section 7	33.5	1.03	−1.1	35.84	0.87	−0.96
Total	525.53 kW			512.24 kW		

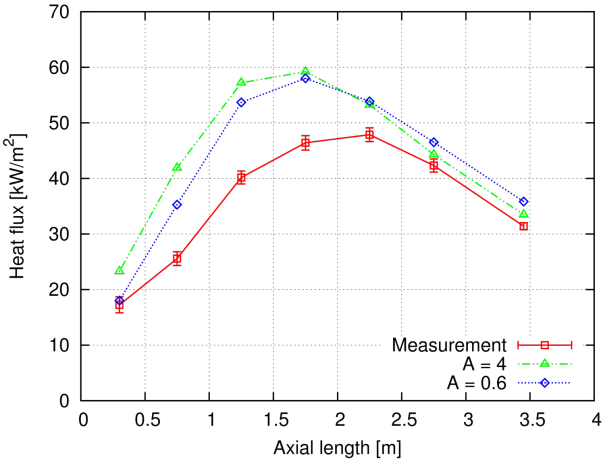

Figure 3.5: Effect of constant A on wall heat fluxes

Table 22: Effect of constant A on the temperature field in the chamber – instantaneous values

	Volume averaged temperature [℃]	Maximum temperature [℃]	Area weighted average of temperature at outlet [℃]	Absorption coefficient [m^{-1}]	Total wall heat flux [kW]
A = 0.6	755.62	1424.32	692.75	2.17	512.47
A = 4	751.62	1930.71	700.95	2.19	525.53

3.4.3 Eddy dissipation concept

Eddy Dissipation Concept (EDC) [72] model is extension of Eddy Dissipation Model. It allows for use of detail chemical mechanisms.

Even though it allows to use advanced chemical mechanism it was found to be challenging task. When I tested two mechanisms Leeds [73] and Smooke [74] both of them predicted extinction of the flame which is clearly unphysical behavior. I used global two step mechanism of Westbrook and Dryer (WD) [75] refined by [76] to be able to maintain the flame:

$CH_4 + 1.5O_2 \longrightarrow CO + 2H_2O$

$CO + 0.5O_2 \longrightarrow CO_2$

$CO_2 \longrightarrow CO + O_2$

3.4.4 Flamelets

The third option of chemistry model is a steady strained laminar flamelet approach as documented e.g. in [77] and described in detail in [68]. This model is based on geometry of the flame. It assumes that all reactions are fast enough to allow the length scale of reaction zone to be smaller than Kolmogorov length scale. Consequently the flame can be assumed as an ensemble of one-dimensional, thin, isotropic, laminar flame structures – so called flamelets.

Implementation consists of creating look-up table with pre-calculated steady state governing equations for scalars prior to the CFD calculation itself. In case of non-premixed combustion the scalar is mixture fraction.

A chemical reaction mechanism for flamelet chemistry model was GRI-Mech 3.0. It is compilation of 325 elementary reactions with rate coefficients expressions and thermochemical parameters obtained from [78].

3.4.5 Comparison of chemistry models and effect on wall heat fluxes

Two separate sets of simulations were compared. First EDM and EDC with SST k-ω turbulence model and new WSGGM for absorption coefficient calculations as described in Chapter 3.6.1. with domain-based mean beam length calculation. All the simulations were run as transient with fixed time step of 0.002 s.

For EDM the chemistry involved was global one-step mechanism as described in Chapter 3.4.1. For EDC the chemistry was reversible two-step WD mechanism described in previous Chapter 3.4.3. Solver settings and discretization for simulation with EDM is in Table 19 and 20.

Table 23: Solver settings

Model	Settings of EDM simulation	Settings of EDC simulation
Turbulence model	SST k-ω	SST k-ω
Radiation model	Discrete ordinates	Discrete ordinates
Species transport	EDM with global one step mechanism	EDC with global two step mechanism
Pressure-velocity coupling	SIMPLEC	SIMPLEC
Skewness correction	1	1
Time step [s]	0.002	0.002

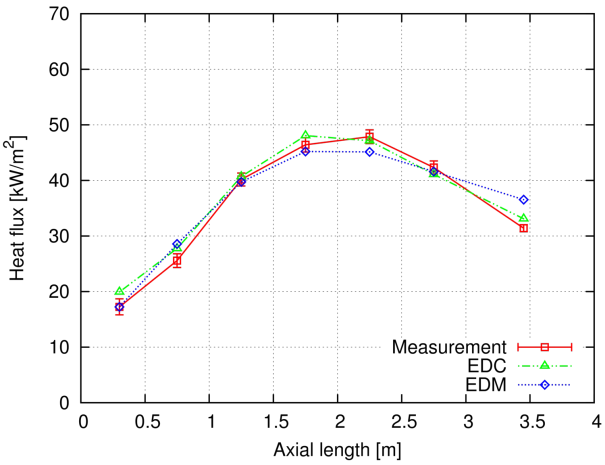

Figure 3.6: Wall heat flux predictions of EDM and EDC models compared to measured data

Table 24: Eddy dissipation model vs. Eddy dissipation concept comparison

	Volume averaged temperature [℃]	Maximum temperature [℃]	Area weighted average of temperature at outlet [℃]	Absorption coefficient [m^{-1}]	Total wall heat flux [kW]
EDM	898.01	1990.74	809.35	0.31	440.02
EDC	875.8	1907.87	884.89	0.31	439.3

Results show only small change in prediction of wall heat fluxes. The total extracted heat changed only by 0.2 % and the highest difference is in first section (15 %) followed by the last seventh section (9 %). Overall small change is consequence of similar global chemistry mechanisms.

The second comparison was of EDM and Flamelet chemistry. Different turbulence model was utilized i.e. realizable k-ε and mean beam length calculation based on cells dimensions in contrary to previous case with EDC. Summary of the solver settings is in Table 25:

Table 25: Solver settings

Model	Settings of EDM simulation	Settings of Flamelet simulation
Turbulence model	realizable k-ε	realizable k-ε
Radiation model	Discrete ordinates	Discrete ordinates
Species transport	EDM with global one step mechanism	Flamelet chemistry with GRI-Mech 3.0 reaction mechanism
Pressure-velocity coupling	SIMPLEC	SIMPLEC
Skewness correction	1	1
Time step [s]	0.002	0.002

Results in a Figure 3.7 show significant overprediction of wall heat flux in fifth and sixth section by 29.9 % and 31.3 % respectively when compared to measurement and 12 % and 13.8 % when compared to the EDM model. The total extracted heat was overpredicted by the prediction with Flamelet chemistry model by 19.8 % while in the case of EDM by 17.6 %. Most of the heat flux overpredictions when compared to the measurement are due to utilized cell-based mean beam length calculations in WSGGM model as will be explained in Chapter 3.6.2. However comparison to the EDM model gives good picture of model predictions.

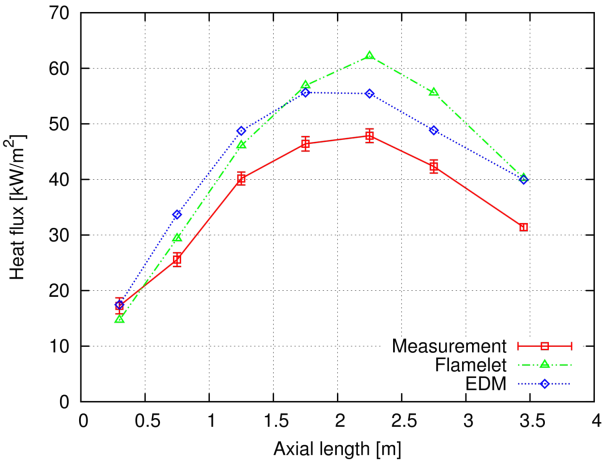

Figure 3.7: Wall heat flux of EDM and Flamelet models compared to the measured data

Table 26: Eddy dissipation model vs. Flamelets chemical mechanism comparison

	Volume averaged temperature [℃]	Maximum temperature [℃]	Area weighted average of temperature at outlet [℃]	Absorption coefficient [m^{-1}]	Total wall heat flux [kW]
Flamelet	681.41	1897.35	573.56	2.2	524.81
EDM	695.84	2045.93	683.47	2.32	515.3

3.4.6 Summary

Chemistry models for combustion modeling vary in complexity and demand for computational power. The least demanding and the most simple is Eddy dissipation model from the family of Eddy break-up models. It allows for global one or two step mechanisms only. It is computationally efficient and suitable for fast reaction rates. Extension is Eddy dissipation concept which allows to use more complex reactions. However it was not implemented successfully with the advanced mechanisms for the swirling combustion problem of this thesis. During computation it suffered of flame extinctions. On the contrary it was successfully implemented with the global mechanism of refined Westbrook and Dryer (WD). There was only 0.2 % change in total extracted heat when compared to the EDM mechanism and slightly lower deviations (15 % in the firs and just 5 % in the last) when compared to measurement in particular sections.

The flamelet chemistry model utilized reactions from GRIMech 3.0 project. It predicts higher heat flux rates in fifth and seventh section by 12 % and 13.8 % when compared to the EDM chemistry model.

In my opinion the EDM model is the most efficient for such a complex geometry with swirl stabilized combustion of natural gas since it delivers acceptable accuracy with the lowest computational demand.

3.5 Radiation in confined combustion environment

Radiation is the main source of energy transport in combustion systems. In the examined combustor it is responsible for up to 90 % of heat transfer. The rest is transported by convection and only for a fraction is responsible conduction.

3.5.1 Thermal radiation modeling

In the modeling of fluid flow where all surfaces have similar temperature then radiative heat transport may be omitted since significantly more energy is transferred either by convection or conduction. However, as soon as temperature differences in the modeled domain are significant, then radiation has to be modeled.

Spectral radiative intensity is the rate of energy transferred by radiation per unit area, unit time, unit wavelength and unit solid angle, which may be mathematically written [29] as:

$$I_{\eta}=\frac{d^{4}E}{dA\ dt\ d\eta\ d\Omega}\ . \tag{29}$$

An important concept is the blackbody, which is characterized by absorbing and emitting the maximum amount of energy possible. All real bodies have temperature-dependent spectral ability to absorb and emit radiation (emissivity).

The transport of radiation in absorbing medium is defined by Radiative transport equation (RTE). It specifies change of spectral radiative intensity over vector $\vec{s}$ due to scattering, absorbtion and emission:

$$\frac{dI_\eta(\vec{s})}{ds} = -\beta_\eta I_\eta(\vec{s}) + \kappa_\eta I_{b,\eta} + \frac{\sigma_{s,\eta}}{4\pi}\int_{4\pi} I_\eta(\vec{s}\,')\Phi_\eta(\vec{s}\,' \rightarrow \vec{s})\, d\Omega\,, \tag{30}$$

where β_η is the spectral extinction coefficient, κ_η is spectral absorption coefficient, $\sigma_{s,\eta}$ is scattering coefficient and $\Phi(\vec{s}\,' \rightarrow \vec{s}\,)$ is the scattering phase function from incoming direction $\vec{s}\,'$.

A number of solution methods for the RTE have been developed. They may be classified into three basic groups:

- Zonal methods
- Ray tracing methods
- Differential methods

In the zonal methods every cell in the domain is treated as separate zone and radiative transfer is evaluated for each of them. In the ray tracing methods a number of radiation beams is followed until they are totally absorbed, while RTE is solved along every ray. The zonal methods and the ray tracing methods are utilized in CFD only for benchmark cases since they are too computationally demanding.

The differential methods have an important advantage over the previously mentioned methods in that the solution algorithm is similar to that for other (flow-related) variables. The RTE is approximated by a set of partial differential equations. There are several methods for differential approach e.g. P1, six-flux model [79], Rosseland diffusion model [80] and discrete ordinates method [50]. The most advanced and widely utilized in combustion simulations is the discrete ordinates method. In this method, the total solid angle is discretized into a certain selectable number of directions and the approximated RTE is solved for each of them.

Basic comparison of radiation effects during methane-air combustion is shown in [81]. This work summarized the impact of radiation and its effect on temperatures and species.

3.5.2 Emissivity effect on wall heat fluxes

Emissivity influences radiative transport of energy with linear dependency. Based on equation for radiation power

$$P = \epsilon \sigma S T^4 \tag{31}$$

Even though the emissivity of the wall was experimentally investigated in Chapter 2.5 I decided to estimate influence of emissivity on local wall heat fluxes. CFD modeling was utilized to predict wall heat fluxes for three emissivities 0.6, 0.8 and 0.9. Settings of the ANSYS Fluent® solver was according Table 27 and 28. Modeling of absorption coefficient was via standard WSGGM with cell-based calculation of mean beam length. Constant settings and identical computational procedure has been kept for all three cases.

Table 27: Solver settings

Model	Settings of EDM simulation
Turbulence model	SST k-ω
Radiation model	Discrete ordinates
Species transport	EDM with global one step mechanism
Pressure-velocity coupling	SIMPLEC
Skewness correction	1
Time step [s]	0.002

Table 28: Discretization scheme of equations

Variable	Scheme
Pressure	PRESTO!
Density	QUICK
Momentum	QUICK
Turbulent Kinetic Energy	First Order Upwind
Specific Dissipation Rate	First Order Upwind
CH_4	First Order Upwind
O_2	First Order Upwind
CO_2	First Order Upwind
H_2O	First Order Upwind
Energy	First Order Upwind
Discrete Ordinates	First Order Upwind

Results are shown in the Figure 3.8. There is obvious that emissivity has little impact in the first three sections while the rest of the chamber is influenced much more. In fourth and seventh section the wall heat fluxes for the case with the emissivity 0.6 decreases by 14 % when compared to the emissivity 0.9. Total extracted heat decreased by 12 % which is much less than would be expected from emissivity comparison which was changed by 33 %. It was also observed, that adjusting emissivity by 25 % (ε = 0.6 to 0.8) changes total extracted heat by 5.6 % and radiation-to-total wall heat flux ratio changes by 2.8 % (84.8 % and 87.6 %).

Those results reveals more complicated interactions in radiative heat transfer. The role of wall emissivity is suppressed by much stronger effect of emissivity and absorptivity of the gas.

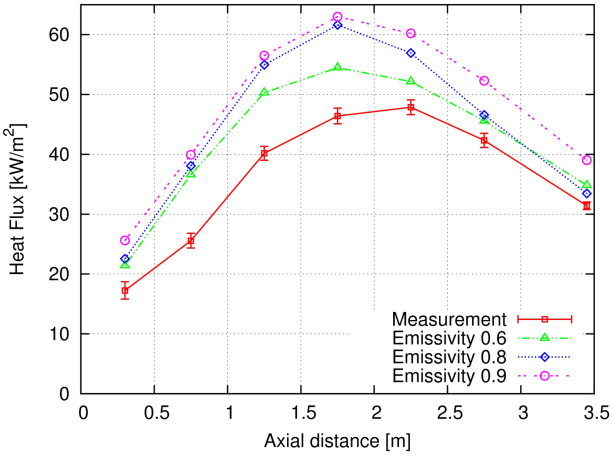

Figure 3.8: Wall emissivity influence on wall heat flux

3.6 Modeling of absorption coefficient

In the ambient temperature usually we assume air as a transparent medium while at the higher temperature absorption of gases becomes more significant and must be included in calculation. Absorptivity is interlinked with two other material characteristics – transmissivity and reflectivity:

$$\alpha+\tau+\rho=1\,. \tag{32}$$

Since absorption of a photon (or electromagnetic wave) is followed by a rise of energy in the receiving atoms or molecules, it obeys the principles of quantum mechanics. The theory reveals that only certain discrete energy levels are possible for each atom and molecule. E.g. for OH molecule these correspond to 0.1×10^{13}, 1.7×10^{13}, and 2.5×10^{13} rotations per second [82]. No other spin velocity is possible for this particular molecule. This fact can be utilized for optical diagnostics of gas composition and mainly to define absorptivity and emissivity which are wavelength-dependent.

In the case of methane-air combustion the main absorbing species are the molecules of water (H_2O) and carbon dioxide (CO_2). Other important radiating species in combustion systems are CO, OH and NO but their concentrations are typically low. Transmissivity is described by Beer-Lambert law:

$$\tau_\eta=\frac{I_\eta}{I_{0\eta}}=e^{-\kappa_\eta L}\,, \tag{33}$$

which defines ratio of transmitted intensity as a function of path length and wavelength dependent absorption coefficient. Spectral absorptivity then may be calculated as follows:

$$\alpha_\eta=1-\tau_\eta=1-e^{-\kappa_\eta L}\,. \tag{34}$$

Radiative heat loss according to [83] with main contributors H_2O, CO_2, CO, and CH_4 can be calculated from:

$$q_R = -4\sigma K_P\left(T^4 - T_\infty^4\right), \tag{35}$$

where $K_P = \sum_i^{i=4} P_i K_i$, $i = \mathrm{H_2O}, \mathrm{CO_2}, \mathrm{CO}, \mathrm{CH_4}$, is called the Planck mean absorption coefficient, p_i is partial pressure of a specie and K_i is Planck mean absorption coefficient of a specie. Data for calculation of emissivity of a two-component gas mixture CO_2-H_2O can be found in [84] and [29].

Compromise in accuracy between simplified gray gas model and narrow band model for absorption coefficient identification represents weighted-sum-of-grey-gases model (WSGGM) first published in [85]. The applicability of WSGGM with any solution method e.g. Discrete ordinates, P-1, etc. was documented in [86]. The mean absorption coefficients for any species may be calculated from line spectrum by method published in [87]. It utilizes measured and calculated data of the project started at Air Force Cambridge Research Laboratories known as HITRAN. Currently it is being developed at the Atomic and Molecular Physics Division, Harvard-Smithsonian Centre for Astrophysics [88].

According to [50] Planck-mean absorption coefficients for all major species show monotonic decrease with rising temperature. Nevertheless many recent works including e.g. [89] utilize absorption coefficient based on the tool RADCAL [90] which doesn't show decrease until 1000 K.

Detailed comparison of WSGG model to the correlated k-distribution model (CK) and WBCK model can be found in [24]. It shows that WBCK model is significantly more accurate over WSGGM and is not as CPU intensive as CK. Overall error due to WSGGM may reach up to 30 % when combined with DO method. However author utilized WSGG model with the cell-based mean beam length evaluation which might cause the deviation as explained bellow.

Significant difference between cell-based and domain-based WSGGM was observed by Ströhle [29]. The term cell- and domain-based describes the way how the path length (or mean beam length) is determined. He shows that cell-based WSGGM significantly over-predicts both the total wall heat fluxes and radiative source term when compared to domain-based WSGGM and non-grey wide band correlated-k method (WBCK).

For the computations a new WSGGM was tested, adopted from [91]. When compared to the standard WSGGM utilized in ANSYS Fluent® based on the work of [92] it predicts the wall heat fluxes more accurately and is suitable even for oxy-fuel combustion. This model was chosen for my calculation because is very easy to implement and gives promising results for wall heat flux predictions.

3.6.1 Modification of standard absorption coefficient calculation

Based on the work of [91] the new weighted sum of gray gases model was adopted. It improves the standard WSGGM utilized in Fluent®. Authors derived new coefficients according the data from exponential wide band model (EWBM). The new model even extends WSGGM usability to the area of oxy-fuel combustion. It claims to predict emissivity of a gas with better accuracy when compared to the EWBM predictions.

The emissivity is calculated as:

$$\epsilon = \sum_{i=0}^{I} a_{\epsilon,i} T_g \left(1 - e^{-k_i P L}\right), \tag{36}$$

where coefficients are:

$$a_{\epsilon,i}(T) = \sum_{j=1}^{\mathcal{J}} b_{\epsilon,i,j} \left(\frac{T_g}{T_{ref}}\right)^{j-1} ; \; i = 1, \ldots, I; \; a_{\epsilon,i} > 0,$$

$I = 4$, $\mathcal{J} = 4$, $T_{ref} = 1200$ K,

$k_0 = 0$ – represents windows in the spectrum; $a_{\epsilon,0} = 1 - \sum_{i=1}^{I} a_{\epsilon,i} > 0$,

P – sum of partial pressures of all of the participating gases (atm),

$L = 3.6 \frac{V_{domain}}{A_{domain}}$ – is mean beam length. (37)

The overall gray gas (effective) absorption coefficient than reads:

$$\bar{k}_a = -\frac{1}{L} \ln\left(1 - \epsilon\right) \cdot \tag{38}$$

Source code of User defined function (UDF) for ANSYS Fluent® is in appendix J. It is written in C programming language with built-in Fluent macros.

3.6.2 Comparison and Effect on Wall Heat Flux

Numerical simulations were performed to compare three procedures of absorption coefficient and mean beam length evaluations. The first is standard ANSYS Fluent® WSGGM model based on the work of [92] with cell-based mean beam length calculation. It means that the length is calculated based on a cell size. This procedure is straight forward and easy to evaluate, but its drawback is in strong mesh-dependency. On the other hand the domain-based procedure is mesh independent, but requires the evaluation of domain size which must be specified by a convention. The one utilized by [91] is defined by equation 37. Last case in comparison utilizes domain-based method as well and adopts new WSGGM coefficients as described in previous Chapter 3.6.1 and appendix J. Solver settings identical for all the cases can be found in Table 29 and 30. Only difference between cases is in calculation of mean beam length and absorption coefficient.

Table 29: Solver settings of all cases

Model	Settings
Turbulence model	realizable k-ε
Radiation model	Discrete ordinates
Species transport	EDM with global one step mechanism
Pressure-velocity coupling	SIMPLEC
Skewness correction	1
Time step [s]	0.002

Table 30: Discretization scheme of all cases

Variable	Scheme
Pressure	PRESTO!
Density	QUICK
Momentum	QUICK
Turbulent Kinetic Energy	First Order Upwind
Specific Dissipation Rate	First Order Upwind
CH_4	First Order Upwind
O_2	First Order Upwind
CO_2	First Order Upwind
H_2O	First Order Upwind
Energy	First Order Upwind
Discrete Ordinates	First Order Upwind

Predicted wall heat fluxes of all the models can be seen in a Figure 3.9. Domain-based evaluation of mean beam length significantly reduces wall heat fluxes. It is due to lowered emissivity of the gas (see Table 31) which is interlinked with the absorption coefficient via equation 38. Total extracted heat was reduced by 13.5 % in the case of standard WSGGM and even by 19.2 %. in the case of new, modified WSGGM. Highest change in local wall heat flux was in the section 3 i.e. 23.6% reduction in standard WSGGM when compared to the cell-based variant. Table 31 shows that due to lower transport of energy to walls is increased averaged temperature inside the chamber and accordingly also temperature of the flue gas. However maximum temperature value inside the chamber remains the same.

Interesting point is in the last (seventh) section where no matter what model is used remains roughly the same wall heat flux. Reason may be in the side wall attached to the last section which has assigned zero wall heat flux boundary condition and in the outlet defined as a constantly emitting black body at the given temperature 776.8 ℃. The temperature was obtained from measurement of the flue gas. This constant conditions seems to attenuate influence of other factors on the last section.

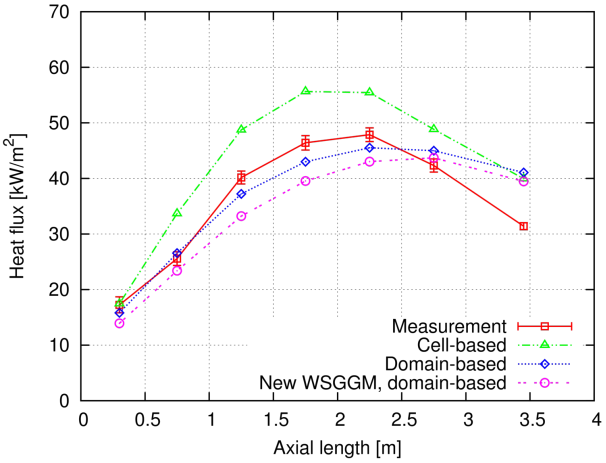

Figure 3.9: Comparison of different methods for absorption coefficient calculation

Table 31: CFD predictions of data in the chamber's volume

	Volume averaged temperature [℃]	Maximum temperature [℃]	Area weighted average of temperature at outlet [℃]	Absorption coefficient [m^{-1}]	Total wall heat flux [kW]
Cell-based	695.84	2045.93	683.47	2.32	515.3
Domain-based	829.24	2040.82	875.04	0.44	445.7
Domain-based, new WSGGM	888.93	2039.04	924.47	0.3	416.13

3.7 Effect of convergence criteria on the wall heat fluxes

One of the biggest issues of numerical computations is convergence and stability. In the present case of combustion calculation we focus on the stabilization of heat fluxes. Figure 3.10 shows convergence history of heat flux for all 7 sections of the combustion chamber. One can see that after application of the QUICK discretization scheme in the momentum equations (at 9000 iterations), the calculation became strongly unstable with the amplitude of heat flux fluctuations up to 6 kW/m^2. This problem prevailed even after modification of relaxation factors and with other higher-order schemes.

The primary reason for the observed instability was found in the physics of the flow. [93] explains that in swirl combustion are present several types of fluctuations and instabilities, e.g. flame wobble and precessing vortex core are present. Measured instabilities in the heat fluxes (naturally smoothed out by the averaging and damping effect of the steel walls and cooling water) are also displayed in Figure 3.11. It is important to note that the RANS modeling approach cannot properly account for these fluctuations but it was not discarded based on the reasoning presented in the Introduction and Chapter 3.3.

Figure 3.13 displays instantaneous results from iterations 8900, 13 000, 16 000 and 19 000 as snapshots from the iteration history shown in Figure 3.10. The changes in reported heat fluxes are well visible.

A more reliable value (than instantaneous) of the heat fluxes was obtained through simple averaging of the results over certain range of iterations. Rate of fluctuation was calculated via non-symmetric error bars defined as follows:

$$q' = q - \bar{q}, \text{ for } q' > 0: \ \sigma_{up} = \frac{1}{n}\sum_{0}^{n} q', \text{ for } q' < 0: \ \sigma_{down} = \frac{1}{n}\sum_{0}^{n} q' \tag{39}$$

where q is instantaneous heat flux, $\bar{q}$ is the average, q' is fluctuation and σ is mean deviation.

A comparison of measured and average heat fluxes from the histories shown in Figure 3.10 (averaged from 9 500 up to 19 000 iterations) is shown in Figure 3.12, including non-symmetric error bars defined in equation (39). The figure includes also averages obtained using two other RANS models, namely realizable k-ε model and a second-order Reynolds-stress model.

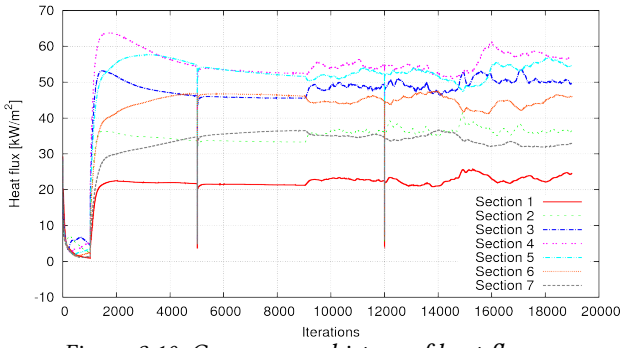

Figure 3.10. Convergence history of heat fluxes

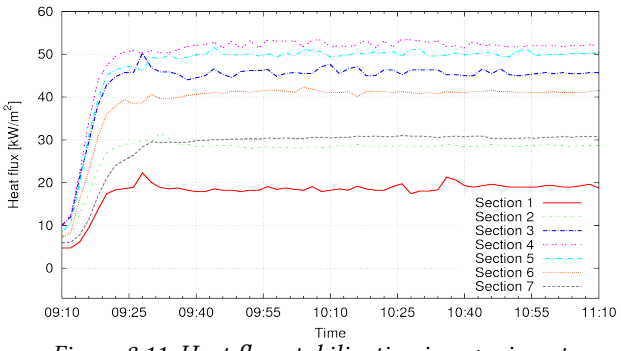

Figure 3.11. Heat flux stabilization in experiment

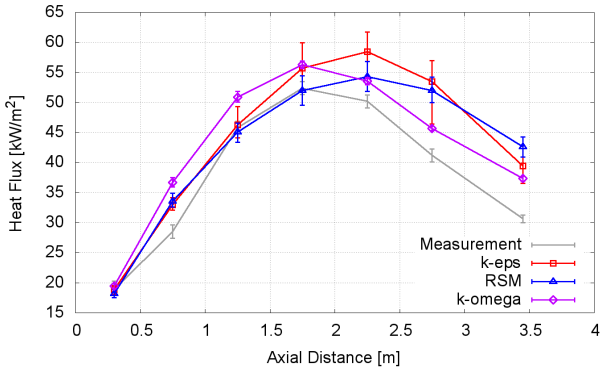

Figure 3.12. Heat fluxes averaged over 9 500 iterations

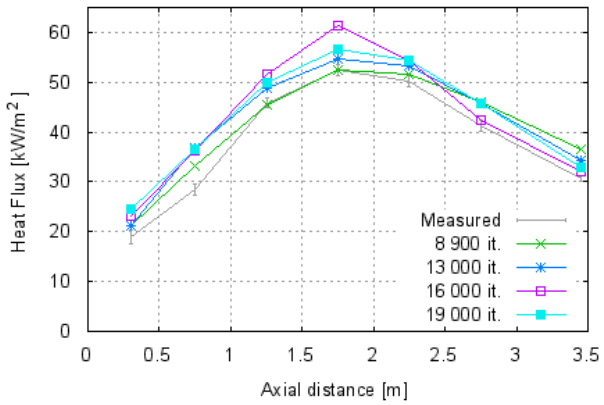

Figure 3.13. Comparison of instantaneous heat fluxes at different iterations (SST k-ω)

Due to instabilities in RANS simulations it was decided to extend simulations with time variable. Transient simulation can capture instabilities and specially for swirling flows can aid to converge the case. This is called unsteady Reynolds-Averaged Navier-Stokes (URANS) and

was introduced in Chapter 3.3.2. If not stated, the URANS is utilized in simulations in this thesis.

3.8 Boundary conditions

Boundary conditions are an all-important factor in CFD model set-up. Most conditions were easy to evaluate thanks to the measuring instrumentation of the facility – e.g. natural gas flow rate and temperature, air flow rate and temperature, etc. Besides these, some boundary conditions were much harder to evaluate accurately and these were deemed to be responsible for a significant part of the observed deviations of predictions from measurements. Wall temperature on the water side and wall emissivity on the flame side were two of these hard-to-determine parameters. This topic is also covered in Appendix C [94].

3.8.1 Wall temperature

Heat transfer through the cooled walls depends on one hand on hot-side properties (radiation contributes by about 90 %) and on the other hand it is influenced by heat transfer coefficient and surface temperature on the water-side. Boundary condition of the first kind (Dirichlet i.e. constant wall temperature) is utilized in all combustion simulations in this thesis therefore water-side temperature has to be determined reliably. Joint simulation of combustion and water-side flow would be highly computationally demanding and benefits would not outweigh the costs of such a simulation.

At the facility we are able to measure inlet and outlet cooling water temperature. However there is no access into the inner wall and therefore no possibility to measure wall temperature directly. Indirect method of evaluation of water-side wall temperature had to be utilized. The wall temperature depends on heat transfer coefficient on the water side under specified heat flux. Since the inlet and outlet water temperature is measured and geometry of duplicator is known, I could use CFD simulation to obtain the water-side wall temperature.

Even though designers of the duplicator incorporated helical fin to increase water velocity and to eliminate dead zones, there is still opportunity for boiling to occur in areas with low water velocity. It can significantly increase the heat transfer coefficient and affect calculated wall temperature. Boiling can occur only in locations with low water velocity (considering inlet water temperature was usually about 20 ℃ and outlet about 30 ℃). Due to low outlet temperature and high modeling complexity of boiling, I analyzed the flow without a boiling model. Propensity to boiling will still be visible in the results, if computation predicts zones with temperatures exceeding the boiling point.

Computational model of a single cooling section has been created to study the heat transfer on the water side in detail, assuming no boiling and a uniform heat flux from the flame side. The turbulence model utilized in simulation was realizable k-ε with so called enhanced wall function. A lot of details from real duplicator was modeled – e.g. gap between the helical fin and the outer shell which causes short-circuit of water flow. Mesh had 385 000 hexahedral elements. Helical fin is modeled as a thin wall (represented by just a face in the mesh). ANSYS Fluent® allows to associate thickness to the face for the purpose of heat conduction, therefore I did so by inputting 3 mm. In default only 1-D heat conduction is assumed in such a thin walls, but since the fin is attached to the hot steel plate facing the flame, shell conduction has been enabled. This allows to take into account heat conduction in all directions.

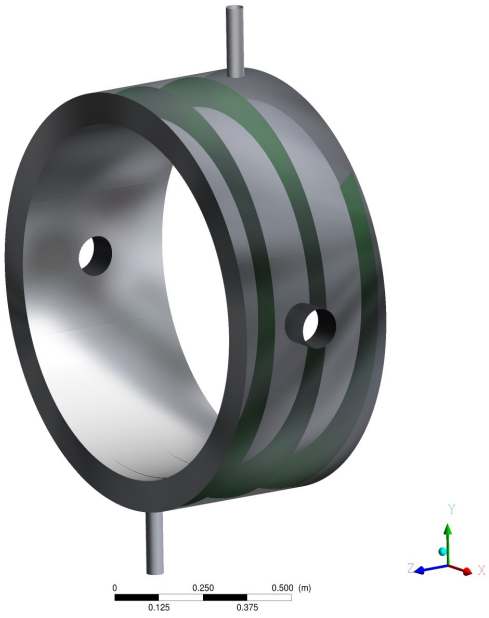

Figure 3.14: Geometry of duplicator

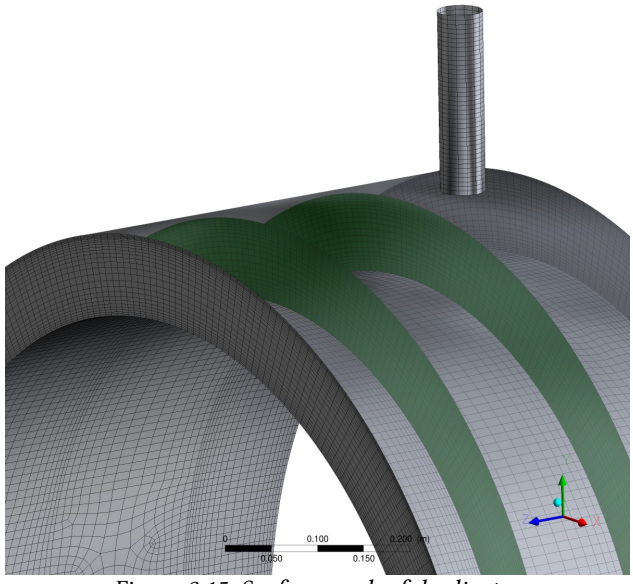

Figure 3.15: Surface mesh of duplicator

Material data for water density were defined using piecewise-linear function. The same way of input data was used also for specific heat and the gravity was taken into account. The material of walls was identified as steel with thermal conductivity 45 W/m-K. Boundary conditions for mass flow inlet and walls (see Table 32) were obtained from measurement specified in Chapter 2.9 as a Case 1 (firing rate 745 kW) from measurement 1 (not averaged).

Table 32: Input data for simulation

	Water flow rate [kg/s]	Wall heat flux [kW/m^2]
Section 2	0.9314	25.51
Section 5	0.9438	48.11

Steady state simulations have been performed with realizable k-ε turbulence model. Non-equilibrium wall functions have been applied. All the computations were done with pressure-based solver with SIMPLEC pressure-velocity coupling and second order discretization scheme in all equations.

Table 33: Results obtained from the surface of combustor's wall

	Area weighted average of temperature [℃]	Maximum temperature [℃]
Section 2	67.94	107.03
Section 5	109.41	137.85

Contours of calculated water-side surface temperature are shown in Figure 3.16. The highest temperatures are incorrect due to the missing boiling model but they indicate possible local boiling. Therefore temperatures above the boiling point (124.2 ℃ at 236.4 kPa) [95] served only to identify locations of local boiling. Real values lay in between the boiling point and the

displayed value due to increased heat transfer coefficient caused by boiling [96]. Area weighted averages from the calculated values over the heat-exchanging surface are shown in Table 33.

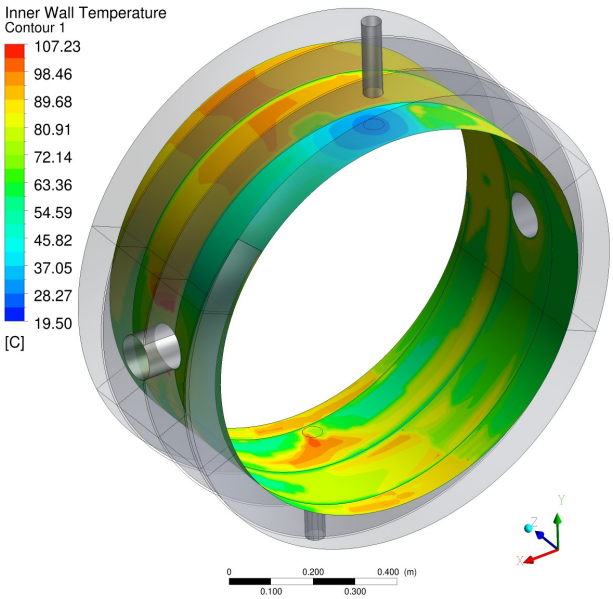

Figure 3.16. Contours of surface temperature [°C] in Section 2

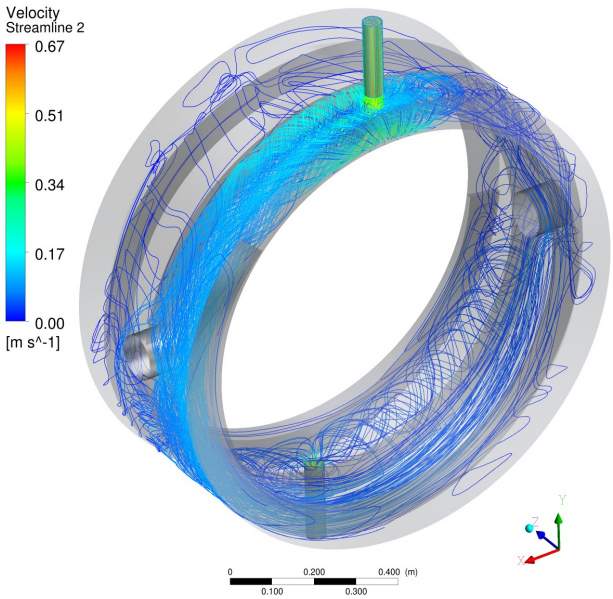

Figure 3.17: Streamlines illustrating flow in the duplicator in Section 2

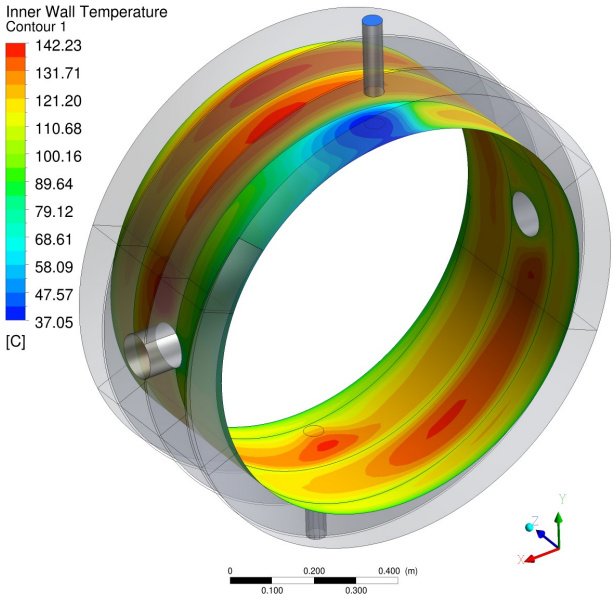

Figure 3.18. Contours of surface temperature [°C] in Section 5

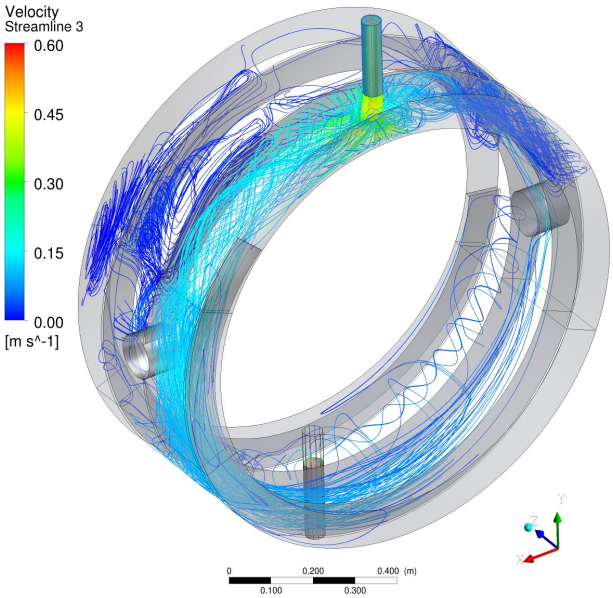

Figure 3.19: Streamlines illustrating flow in the duplicator in Section 5

The uneven distribution of temperature is mainly caused by short-circuit through the gap between fin and shell, where water heads toward the outlet pipe in the shortest way. This is illustrated by the streamlines at the Fig. 3.17 and 3.19.

From the maximum temperatures in Table 33 is obvious that in Section 2 it is unlikely that boiling will occur since maximum temperature is bellow boiling point of water at the given pressure. However in Section 5 it might occur

3.8.2 Wall emissivity

Emissivity of the heat exchanging surface of the combustion chamber was measured by IR thermometer coupled with a thermocouple probe. This measurement is described in Chapter 2.5. The effect on wall heat fluxes was also investigated in Chapter 3.5.2. It was decided based on the measurement and on literature review that the value of emissivity utilized throughout this thesis will be 0.9. This value corresponds for partly rusted steel plate.

3.9 Review of relevant materials properties

Properties of various materials are important input data for CFD modeling. Typical concerns include e.g. heat conductivity, density and fluid viscosity. Moreover the properties have to be available for a wide range of temperatures. The focus should also be aimed at radiative properties, because radiation is responsible for about 90 % of the heat transfer in combustion chambers. The required parameters are wall emissivity and gas absorption coefficient. Note that it is common to neglect scattering since its effect is mostly minuscule.

The preferable choice is often empirical relationship since it provides relialbe approximation. When empirical data are not available, then another method e.g. based on kinetic theory may be utilized. Overview of common methods used to model material properties is given in the following sections.

3.9.1 Thermal conductivity

Thermal conductivity of steel is tabulated and a constant value (e.g. 45 W/m-K corresponding to carbon steel) is mostly reported. Its dependence on temperature is rather weak and is often neglected. On the other hand conductivity of gases could be evaluated through following options:

- Constant value valid only in a narrow temperature range,
- Empirical polynomial – function of temperature,
- Computed from kinetic theory.

The empirical relationship is mostly the preferred option.

3.9.2 Density

Density is a key parameter especially in compressible gas flows. In flows with low pressure gradients and velocities below Mach number 0.6, it is however common to neglect compressibility and utilize so-called ideal incompressible gas. The exit velocity of gas fuel at burner nozzle orifices can often reach near this value and therefore it is better to use ideal compressible gas approximation. Equation for real gases would have to be employed near

condensation and critical point and at very high pressures where occur significant deviations from the theory of ideal gases.

3.9.3 Viscosity

For viscosity in the field of combustion may be used either kinetic theory, power-law, Sutherland's law or experimentally derived polynomial function. A formula based on kinetic theory is defined [97] as:

$$\mu = 2.67 \cdot 10^{-6} \frac{\sqrt{M_w T}}{\sigma^2 \Omega_\mu}, \tag{40}$$

$$\Omega = \Omega_\mu(T') \text{ where } \quad T' = \frac{T}{\epsilon / k_B}$$

σ and ε/k_B are Lennard-Jones parameters.

The power-law with the three coefficients may be used as an alternative viscosity model:

$$\mu = \mu_0 \left(\frac{T}{T_0} \right)^n, \tag{41}$$

and third option is the Sutherland's law [98], which is defined as:

$$\mu = \mu_0 \left(\frac{T}{T_0} \right)^{3/2} \frac{T_0 + S}{T + S}, \tag{42}$$

3.9.4 Specific heat capacity

Specific heat capacity is crucial for calculations involving significant enthalpy variation. Moreover the selected level of approximation has great impact on the predicted temperature. Therefore in combustion problems it must be defined as temperature dependent. The same types of modeling methods may be used as in the case of viscosity or density i.e. polynomial function or kinetic theory.

Polynomial function is based on measured data and should be preferred option. If empirical measurements are missing for some important constituent, one may utilize a formula based on kinetic theory [97]:

$$c_{p,i} = \frac{1}{2} \frac{R}{M_{w,i}} (f_i + 2). \tag{43}$$

The model is based on molecular composition and motion, if stands for the number of modes of energy storage (degrees of freedom).

3.9.5 Properties of gas mixture

All of the material properties of gases discussed above in Chapter 3.9 apply to single species. When gas mixture is utilized, its properties have to be calculated from the data of the involved species or measured experimentally. Several methods were introduced for calculation of gas mixture properties. Commonly utilized is mixing law which has options such as volume-weighted, mass-weighted or ideal-gas mixing law [97]. The formula of volume-weighted mixing law applied to composition-dependent density is the following:

$$\rho = \frac{1}{\sum_i \frac{Y_i}{\rho_i}} \,. \tag{44}$$

Mass-weighted mixing law applied to composition-dependent non-ideal gas viscosity has simple form:

$$\mu = \sum_i Y_i \mu_i \,. \tag{45}$$

And the last, ideal-gas mixing law as applied to the thermal conductivity yields:

$$k = \sum_i \frac{X_i k_i}{\sum_j X_j \phi_{ij}} \,, \tag{46}$$

where $\phi_{ij} = \frac{\left[1 + \left(\frac{\mu_i}{\mu_j}\right)^{1/2} \left(\frac{M_{w,j}}{M_{w,i}}\right)^{1/4}\right]^2}{\left[8\left(1 + \frac{M_{w,i}}{M_{w,j}}\right)\right]}$.

3.9.6 Absorptivity of the gas

Absorptivity of the gas is one of the key parameter for the radiative heat transfer and was already described in Chapter 3.6.

3.10 Summary

Several aspects of gas combustion modeling and simulations were shown in this chapter. Focus was on models and properties of the simulation influencing the wall heat flux predictions. In the Table 34 is in descending order summarize effect on total wall heat flux. The maximum change in total wall heat flux represents e.g. in emissivity of walls change of total extracted head between emissivity 0.6 and 0.9.

Table 34: Influence of solver models or material properties on total extracted heat

Parameter	Maximum change in total wall heat flux [%]
Absorption coefficient/mean beam length	19.2
Emissivity of walls	12
Turbulence model	7.6
Chemistry model	1.8

From the Table 34 can be seen that the most sensitive is the total wall heat flux to the mean beam length calculation which decrease heat flux by 19.2 % when changed from cell-based to domain-based method. Significant is also emissivity of walls which can be however identified from literature or measured. Turbulence models has surprisingly a little effect (just 7.6 % change). The highest deviation (7.6 %) was between RSM and realizable k-ε turbulence model.

4. Swirling flow prediction and modeling

Modeling of the combustion chemistry via simple eddy dissipation model, which utilizes the strategy mixed-is-burned relies on the accurate turbulence prediction more than any other chemistry model. The reason is that turbulence is the driving factor for mixing and therefore also for chemistry and heat release. The importance of the turbulence modeling is therefore amplified.

4.1 Introduction

Following discussion of swirling flows and more details were already introduced in my previous work [35, 99] which are attached in Appendix G and F.

Swirl-stabilised non-premixed flames are frequently used in industrial burners, but they present one of the most difficult problems to predict computationally. Only with the advances in large eddy simulations (LES), successful predictions of in-flame properties were reported [3–5]. The LES approach is unfortunately still too computationally expensive for the simulation of large-scale fired heaters due to their huge dimensions (on the order of 10 m) and the need to resolve fine features like gas nozzles with diameters on the order of 1 mm. The only viable alternative for practical predictions in the present as well as for a number of years to come thus consists of models based on first or second-order turbulence closures.

The key question in predicting swirling diffusion flames is, whether the prediction of swirl using geometry of swirl generator is dependable. In the literature, only scarce instances may be found of measurements suitable for the validation of such swirl generation predictions [37, 100]. In most cases of advanced predictions of swirling flows including those mentioned above, boundary conditions on the inlet are typically specified using measured velocities and velocity fluctuations. Predictions validated by experimental data are almost nonexistent in peer-reviewed journals. Occasionally, swirl is even specified by geometric swirl number, i.e. by inclination of swirl generator vanes (helixes) [101]. Neither of these approaches is however suitable for most cases of practical predictions of swirl-stabilised gas and liquid fuel burners, due to the large variety of swirl generator designs used by burner vendors and due to the unavailability of detailed measurements.

For the quantitative description of the relative strength of tangential momentum is used a nondimensional swirl number (S), which is defined as the ratio of axial flux of tangential momentum over axial flux of axial momentum [36]. In most cases published works provide values of swirl number calculated on the basis of swirl generator geometry as proposed by [102]. The geometric swirl number must however be used thoughtfully, as it is suitable only for specific swirler geometries, e.g. when guide vanes cover the whole cross-section of air flow tube and there are no short-cut currents. In spite of this, number of authors provides geometry-based swirl number as the only information about swirl intensity, e.g. [103], [100]. Swirl number calculated from measured velocity profiles is encountered less frequently in the literature, e.g. in [104] or [105], but it is essential in the case of this work, as measured data are necessary for the validation of predictions.

There are two basic types of swirling flow – low swirl flows typically with swirl number lower than 0.6 and strongly swirling flows with higher value of swirl number. Precessing vortex core is encountered mainly in the case of strong swirl flows, with the exception of flow through

sudden expansion (which is the case also in most burners), where PVC has been observed even with lower swirl numbers [106].

4.2 Experimental data for validation of CFD simulation

Since I was aware of the importance of the swirling generation and propagation on the combustion process the investigation was initiated to find capabilities of the utilized software ANSYS Fluent®. The task was to identify published experiment with the same swirler to ours'. However only experiment with guide vane swirler was found while the burner at our facility is equipped with combination of bluff-body and guide vane swirl generator (see Fig. 4.1 and 4.2). The combustion air flows partly around our swirler since the duct has bigger diameter than the swirler and partly through the swirler and along the guide vanes.

In our case after the swirler there is about one diameter long constant cross-section channel followed by the sudden change of diameters from supply air round duct into combustion chamber itself. Similar concept adopt many works e.g. [37, 38, 100, 107]. However in the first stage we focused on the flow field prediction just behind the swirler and before a sudden expansion. Our aim is to see ability of the solver to predict flow through guide vanes.

After a literature survey the most proper source of measured validation data was found in a work of [37]. They utilized axial guide vane swirler. The geometry of experimental setup was further clarified in personal communications with one of the authors [108]. Measured data were in a suitable form however many details necessary for validation of the CFD simulation were missing. The main problem was with uncertain geometry specification, which was cleared by personal communication [108] Nevertheless doubts still remains since the authors had just a few records about the measurement which took place several years ago. This is common problem among many published articles with experimental data. Nearly none of them provide complete geometry specification, which would allow to create reliable model for CFD computation.

The measurements were performed for a vane swirl generator by optical method (particle image velocimetry, PIV). Geometry of the computational domain including the swirl generator is displayed in Figure 4.3 and swirler itself in Figure 4.4. Inclination of the guide vanes in the present case is 45°. The experimental work was focused on analyzing flow features in a sudden expansion and its deeper analysis by proper orthogonal decomposition (POD), but they measured also velocity components just above the expansion ($x/D = -0.44$) in order to determine accurately the amount of swirl in the expanding flow. These velocity measurements above the expansion were used in the present work to validate computational predictions. Working medium was water.

Figure 4.1: Swirler from the testing facility

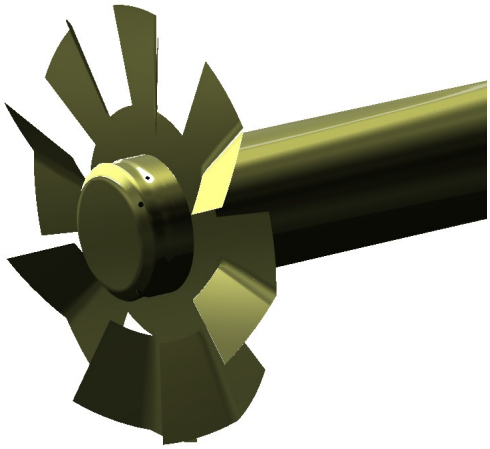

Figure 4.2: Model of swirler from the testing facility

Figure 4.3: Sudden expansion chamber with swirler [37]

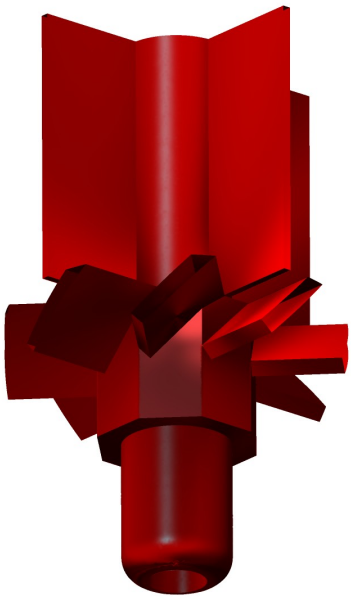

Figure 4.4: Detail of axial guide vane swirl generator from the sudden expansion chamber [37]

4.3 Geometry of the water tunnel with swirler

Adopted geometry was in closed-loop water flow circuit. Honeycomb was placed before working section followed by the channel of diameter 40 mm where the axial eight guide vane swirler is placed with inclination angle of 45° (see Figure 4.3, 4.4 and 4.5). Guide vanes were modeled with a real thickness. In the middle of swirler body is a hole of the diameter 7 mm through which the flow can bypass the swirler.

Between the swirler and sudden expansion is the length 102 mm (x/D = 2.55). The sudden expansion itself broadens inlet diameter of 40 mm into swirling chamber's diameter of 100 mm (d/D = 2.5). Length of the chamber is 73 mm. Outflow is realized with gradual contraction and free outlet to the collection tank.

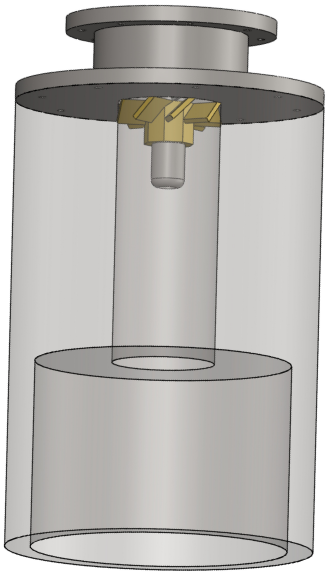

Figure 4.5: Geometry of the expansion chamber with axial guide vane swirler

4.4 Mesh

The aim was to investigate ability of software ANSYS Fluent® to predict generating of the swirl by guide vanes and the swirling flow decay. Four turbulence models available in the software were tested in combination with a grid independence study. Four meshes were created. The first was with the use of symmetry – only quarter was modeled and meshed by structured hexahedral mesh. The other three meshes were created for the full 3-D geometry. These were unstructured tri-element meshes converted to polyhedral by the solver. Resulting numbers of elements are summarized in Table 35.

Table 35: List of created meshes

Mesh type	Number of cells	Type of cells
Quarter geometry	1 137 865	Hexahedral
Low density, full geometry	899 007	Polyhedral
Mid density, full geometry	1 721 600	Polyhedral
High density, full geometry	2 764 345	Polyhedral

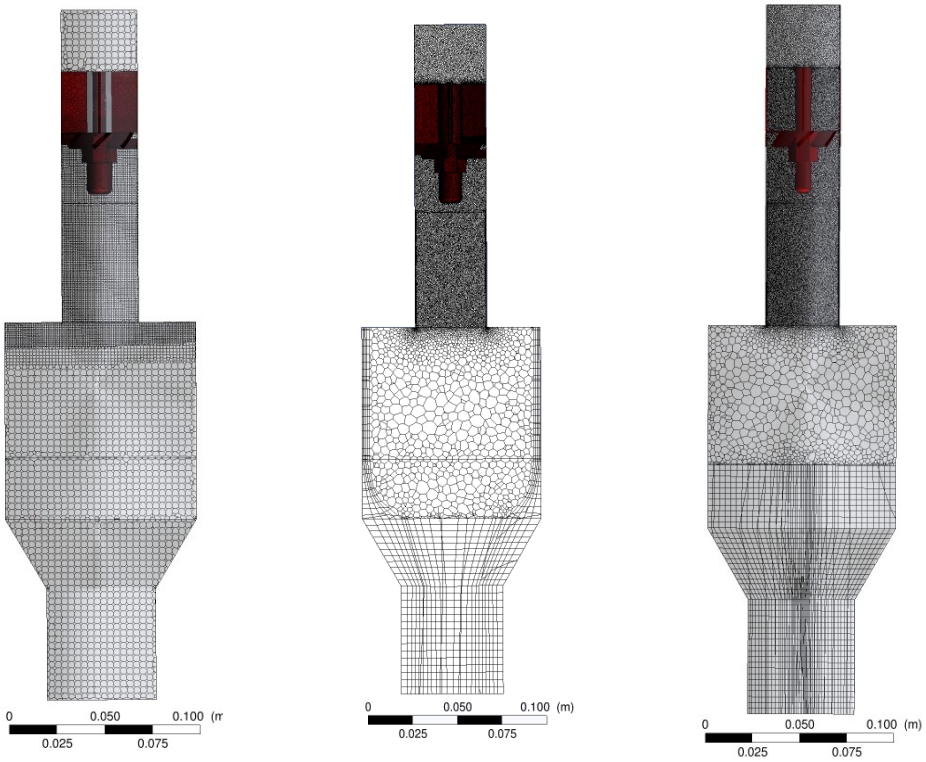

Figure 4.6: Computational grid - a) 899 007; b) 1 721 100; c) 2764 345

4.5 Computational set-up

This work is aimed at the flow field just after the axial guide vane generator. Several Reynolds-averaged turbulence closures (RANS) are applied and compared. Unsteady formulation was found to be necessary due to large fluctuations (U-RANS). Computations are done in ANSYS Fluent® v12 code using frequently used moment-closure turbulence models, specifically RNG k-ε, realizable k-ε, SST k-ω and Reynolds Stress Model (RSM).

Fluid utilized in the experiment was water. Properties of water assumed in simulations were the following:

- density 998.2 kg/m^3
- viscosity $9.982 \cdot 10^{-4}$ Pa-s

Inlet (bulk) velocity was 0.25 m/s. For the inlet boundary condition it was converted to mass flow rate 0.3135938 kg/s. Outlet was defined as pressure outlet with zero outlet pressure. Other

boundary conditions were walls defined with no-slip condition and zero roughness height (hydraulic smooth wall).

Set of four turbulence models were tested. Namely the SST k-ω, realizable k-ε, RNG k-ε and RSM. No heat transfer was assumed. Solver settings is in Table 36. Discretization scheme describes Table 37.

Table 36: Solver settings of all cases

Model	Settings
Turbulence model	realizable (or RNG) k-ε or SST k-ω or RSM
Pressure-velocity coupling	SIMPLEC
Skewness correction	1
Time step [s]	0.01

Table 37: Discretization scheme of all cases

Variable	Scheme
Pressure	PRESTO!
Momentum	Second Order Upwind
Turbulent Kinetic Energy	Second Order Upwind
Turbulent Dissipation Rate	Second Order Upwind

All the cases are first calculated with the steady state procedure and the with first order discretization scheme for all equations. When residua reaches the convergent criteria the discretization scheme was changed according the Table 37.

4.6 Results

Since we wanted to compare predicted data with the validation data from the paper of [37] it was necessary to make the same control plane at the x/D = −0.05. At this plane the line was created and data from the line were exported. All the results are averaged values over several seconds of physical time.

4.6.1 Flow fields predictions

Three turbulence models were tested for ability to predict flow field in three-dimensional domain. Figures 4.7 to 4.10 bellow show comparison of results from the three meshes and three turbulence models. The Figure 4.7 shows results for the mesh with 899 007 cells, Figure 4.9 for the mesh with 1 721 100 and Figure 4.10 for 2 764 345 cells. For axial velocity profiles is predicted decrease in the center by all the models however only SST k-ω and RNG k-ε turbulence model on a rough mesh predicted reversed flow. Since the results were not confirmed on a finer meshes it might be rejected as scatty results.

Problem in predictions of axial velocity is caused on one hand by radial momentum transport from the swirl effect and on the other hand in contrary by jet penetration downstream from the short-circuit through the center of guide vane swirler. Effect of the jet can be seen on Figure 4.8. There is also visualized backflow from the chamber penetrating the inlet pipe.

Other effect is caused by guide vanes which generates vortex shedding. Those vortices are then pushed toward the wall by radial transport of momentum, travel downstream and influence near wall velocity profile. Those vortices are visible at Figure 4.8 as well.

Radial velocity profile near the axis is predicted well by all the models. However at the near-wall region strongly deviates from the measured data. It might be caused by vortex shedding mentioned earlier which affects flow field near wall and RANS turbulence models cannot describe it.

Near-axis tangential velocity and its gradient is in all cases underpredicted. While in the near wall region is tangential velocity significantly overpredicted. This leads us to hypothesis that swirling tangential momentum is pushed toward the wall while in the center of the stream dominates non-swirling jet, penetrating further downstream.

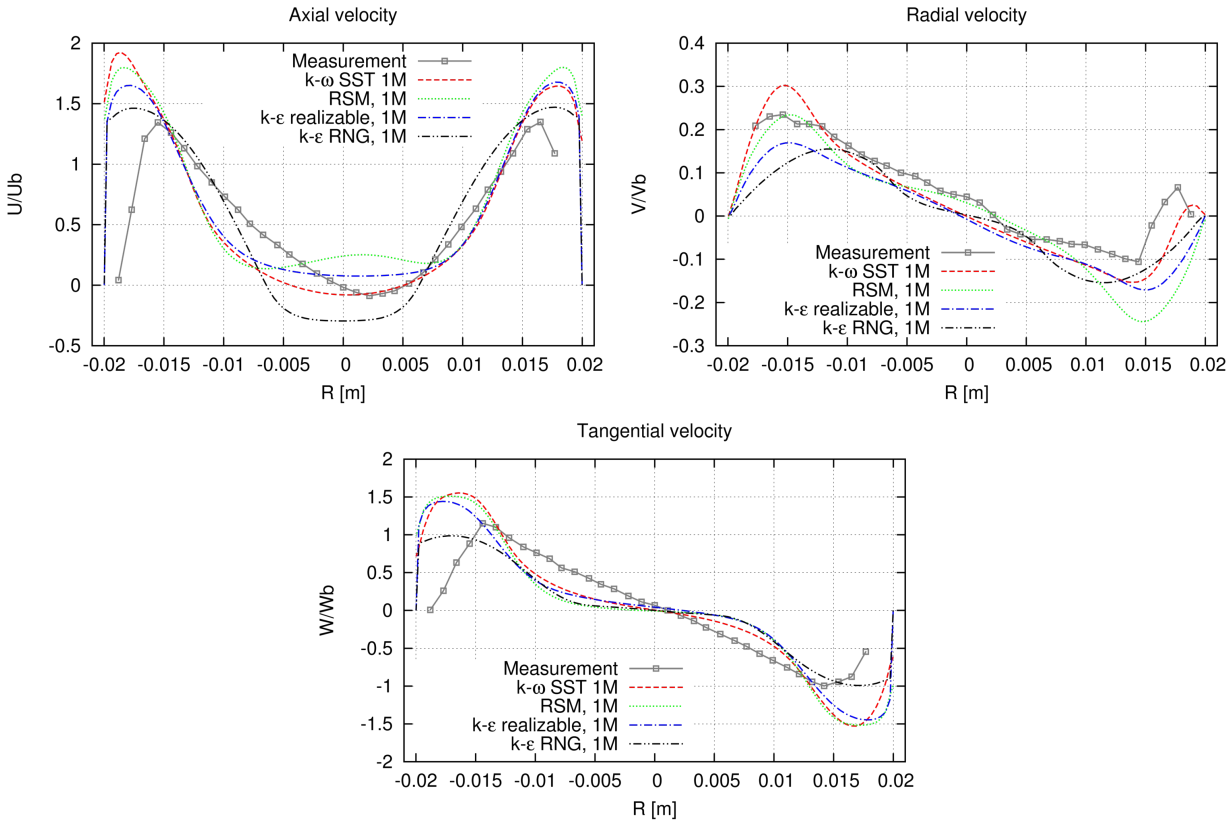

Figure 4.7: Profiles of axial, radial and tangential velocity in the lowest density mesh for four turbulence models

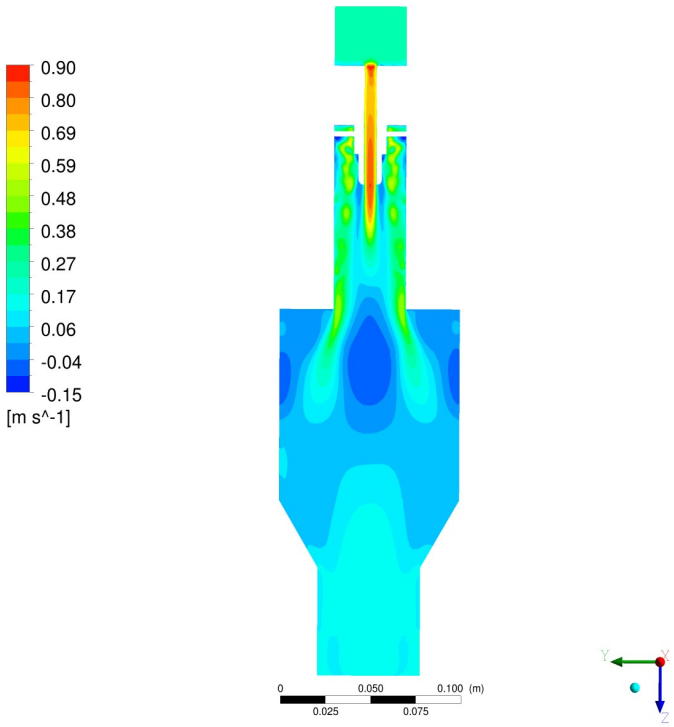

Figure 4.8: Contour of a mean axial velocity on a rough mesh with SST k-o turbulence model

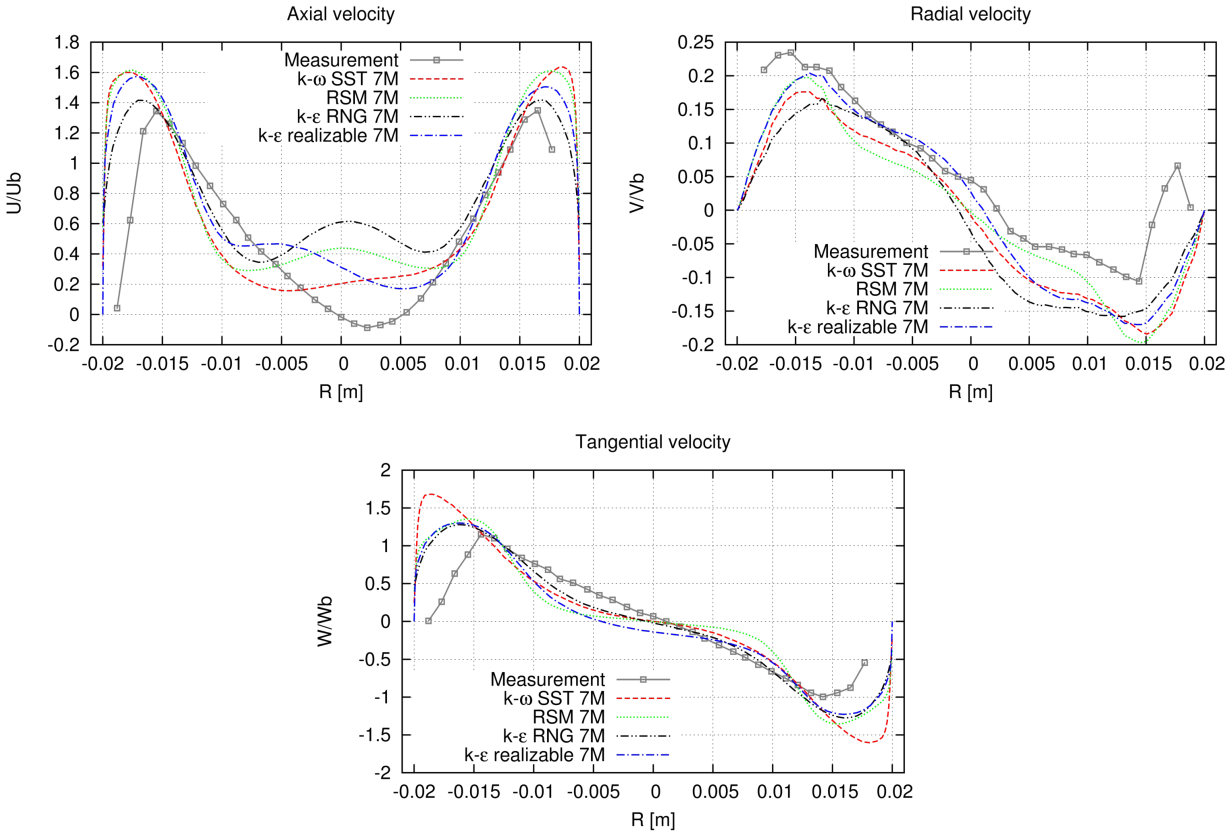

Figure 4.9: Profiles of axial, radial and tangential velocity in the medium density mesh for four turbulence models

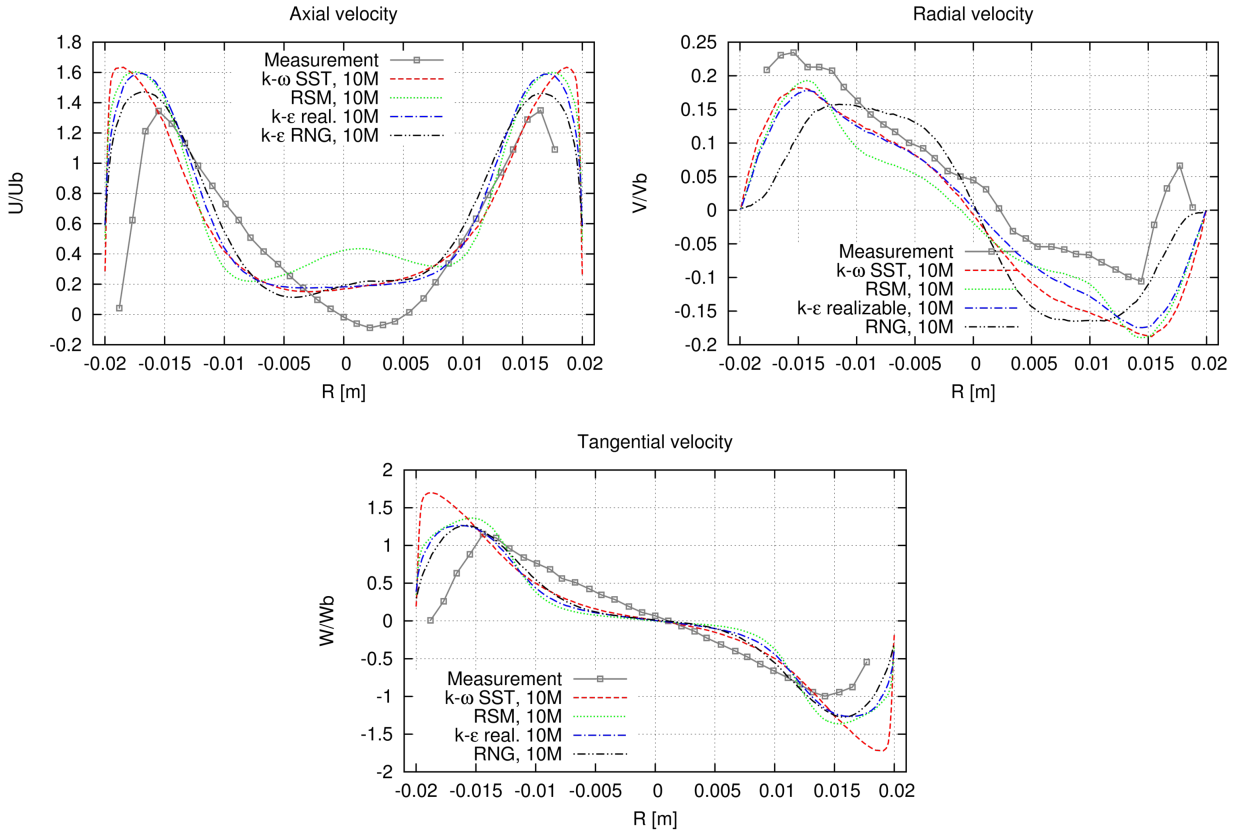

Figure 4.10: Profiles of axial, radial and tangential velocity in the highest density mesh for four turbulence models

It is shown that none of the models is able to predict the solid body rotation of the core swirling flow, which is observed in the measured data. Moreover the SST k-ω model shows an unexpected behavior in the tangential momentum transport behind the swirler, as monitored by the swirl number. Discussion of the results is confronted with previously published observations on this topic. The aim is to critically evaluate the applicability of computations to determine inlet boundary conditions for swirling air in industrial combustors.

4.6.2 Frequency analysis of the swirling flow

Swirl flow is often accompanied by periodical instabilities in a flow field. Broad attention is paid to such a phenomena in previously mentioned review [93]. Even though usual tool to study instabilities in the swirling flow is LES as it use spatial averaging I could observe periodical instabilities with URANS which use time averaging. Unsteady vortices are obviously not filtered out as would be expected. Therefore I decided to study dominant frequencies in the domain.

Periodograms (autocorrelation function) were generated for me by a provided scripts for computing periodograms i.e. Siegel's test routine in Matlab® [109]. Dominant frequency was revealed for three turbulence models.

Facet averaged data of axial velocity at the specified point was recorded for at least 20 seconds. These point data served to capture significant frequencies. Results are in Figure 4.11. Horizontal axis shows number of time steps. In order to calculate frequency in (Hz) is

necessary to multiply the number by time step size (in this case 0.01 s) and make inverse of the result. Significant frequency is for the case of SST k-ω 44 time steps i.e. 2.27 Hz. For the realizable k-ε turbulence model it is 15 time steps i.e. 6.67 Hz and for RSM turbulence model it is 27 time steps i.e. 3.7 Hz. These frequencies are much lower than frequencies associated with the precessing vortex core (275 Hz in [110]) or general oscillations observed in combustion systems (from 24 Hz [93]).

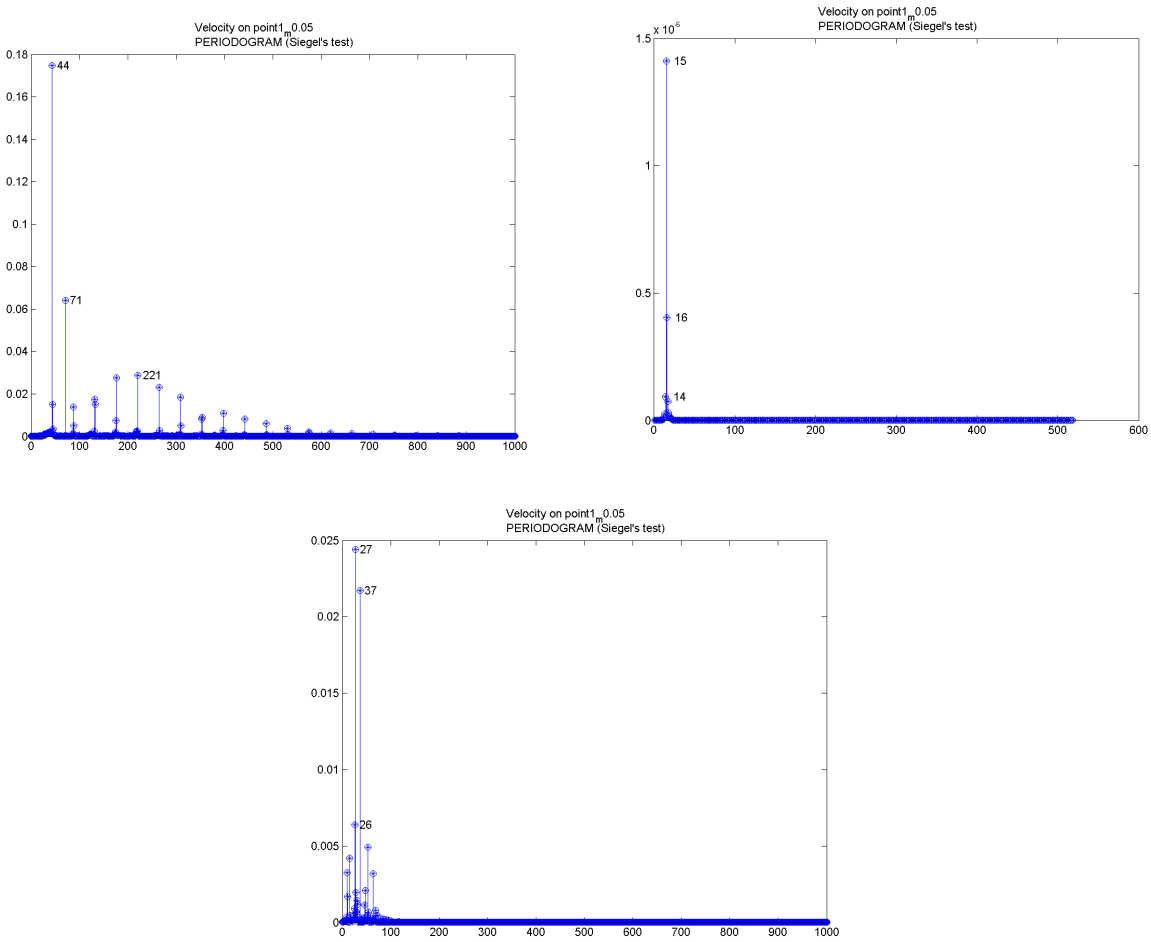

Figure 4.11: Frequency analysis at point 1 for SST k-ω, realizable k-ε and RSM turbulence model

4.7 Summary

In a literature I was not able to find any well documented measurement with the axial guide vane swirl generator combined with bluff-body as our swirler utilized in the burner.

Results show that prediction of swirling flow in the given geometry is problematic. One key factor is combination of jet-like flow combined with guide vane swirl generator influenced flow. When interaction of these two flows is involved turbulence models fail to predict velocity flow fields in the near-wall region no matter what turbulence model is utilized from common set of commercially available turbulence models.

Frequency analysis revealed that the lowest frequency of oscillation (2.27 Hz) predicts SST k-ω turbulence model while the highest (6.67 Hz) predicts realizable k-ε turbulence model.

5. Conclusions

This thesis was focused on phenomena of heat transfer within combustion chamber with turbulence swirling diffusion flame. The fuel was natural gas converted for the purpose of CFD simulation to the equivalent flow rate of methane. Oxidizer was air at ambient conditions. Measurements were performed at experimental facility with industry-size combustor. The facility is equipped with modern data acquisition system. Key feature distinguishing this experimental facility from others is segmental design with accurate wall heat flux measurement. Measurement of local wall heat fluxes was performed for two firing rates 745 kW and 1120 kW. Measurement uncertainty of the local wall heat fluxes was calculated as better than 8.4 % in (Section 1) for the Case 1 (firing rate 745 kW). All the other parameters (flow rates, temperatures, pressure, etc.) were acquired as well. Calculated uncertainty was usually better than 2 % for all parameters but for air mass flow rate, where it reaches 9.8 % for the Case 1. Such a data was then utilized for validation of CFD predictions.

Introduced and described was also my own software for measured data processing and graphical interpretation which was used to prepare raw data from measurement for direct input to the simulation software as boundary conditions. It was designed in object oriented C++ code.

Promising new setup for inflame measurement was also presented. It consists of our own platinum – platinum-rhodium type R thermocouple (welded at our institute), water-cooled stainless steel support body, ceramic tube and transmitter. Comparative measurement in muffle furnace was performed with commercial K-type thermocouples. The highest deviation was observed at the lower temperatures (30 % at 300 ℃) while at higher temperatures the agreement of our R-type thermocouple to the K-type was much better (7.3 % at 530 ℃ and 1.3 % at 950 ℃). Even though the test conditions were complicated it shows promising results for high temperature measurement.

For CFD simulations setup it is important to properly identify boundary conditions. One of hard to determine value for boundary condition is emissivity of the combustion chamber's wall. Therefore I decided to perform measurement and determine emissivity value experimentally. Through comparison of infrared thermometer and contact temperature sensor it was found that emissivity of the steel plate is close the value of 0.9, which is recommended for surfaces similar to the combustion chamber wall. Another boundary condition broadly investigated in this thesis was water-side wall temperature of the combustion chamber wall. CFD simulation was performed to resolve flow and heat transfer rate inside the duplicator. Heat load of the walls was taken from the measurement of Case 1. Averaged water-side wall temperature was 67 ℃ for Section 2 and 109 ℃ for Section 5. It was confirmed that presumed temperature of 80 ℃ is acceptable compromise and it was decided to keep the settings.

Settings of various industry-standard models utilized for combustion and underlying physical phenomena were investigated. Boundary conditions were set according to processed data from measurements. Simulations focused on effects of individual models and their settings on total and local wall heat flux predictions. Investigated models were turbulence models, chemistry models and radiative properties of involved materials. Their effect on wall heat flux was assessed and it was found that predictions are most sensitive to the evaluation of mean beam length which is related to the absorption coefficient of the gas in combustion chamber. Different evaluation of such a parameter may change the total wall heat flux prediction by 19.2 %. Therefore it is essential to properly choose this parameter.

Predictions of wall heat fluxes for the Case 1 with lower firing rate was found to be very accurate. Total wall heat flux was predicted with deviation from measurement by just 0.3 %. Predicted local wall heat fluxes deviated the most in last (seventh) section by 16 %. However, in other sections the deviations were around 5 %. In the Case 2 with the higher firing rate predictions of total extracted heat was very good as well. Predictions deviated from measurement by just 0.1 %. However, the turbulence models were found to be limiting factor in such simulations since deviation in local heat flux measured at individual sections reached up to 27 %. The whole profile of heat fluxes was shifted toward the outlet of the combustion chamber. First four sections were underestimated while last three sections were overestimated. Such profile shift was predicted by all turbulence models. This reveals problems in swirling flow predictions and swirl generation in the guide vane swirl generator which was included in computational model.

Prediction difficulties of swirling flow are discussed in the last chapter of this thesis with focus on effect of turbulence models. Well documented measurement with the swirl generator similar to ours was utilized from literature. First of all a grid independence study has been performed on prepared computational models. Even though the model included sudden expansion chamber my attention was paid to the first measuring plane between swirl generator and sudden expansion. This plane captured velocity fields affected by generated swirling flow. Decay of swirl and momentum transport can be monitored without additional geometrical disturbances. The aim was to verify ability of turbulence model to predict flow field generated by the guide vanes swirl generator. Results confirms that utilized turbulence models have problem to accurately predict such a flow. The main problem seems to be in interaction of the jet at the center of swirl generator and swirling flow generated by the guide vanes.

In appendixes are provided additional data such as author's own publications and software codes. Included are works related to the topic of this thesis and one article based on patented technology invented by author of this thesis in cooperation with colleagues from Masaryk university, Brno, Czech Republic.

5.1 Benefits of this thesis for scientific community and industry

This thesis implements innovative method for local wall heat fluxes measurement with improved measurement uncertainty. Open source code for data processing might be implemented in other facility focused on heat flux measurement based on cooling water control (flow rate and temperatures). Promising results were shown in the inflame measurement. It can lead to an industry applicable device capable to measure in furnace.

In the field of CFD predictions optimal setup was found for low firing rates, which lead to predictions of both total and local wall heat fluxes with good accuracy. Results are directly applicable to industry computations since the simulation setup utilizes computationally manageable models able to resolve simulations in complex geometry of the burner and the combustion chamber. For example typical solution takes just few days on workstations with twelve CPU cores.

Problematic behavior was observed in the predictions of all investigated turbulence models, which was amplified in higher firing rates. More work is necessary to resolve this issue. Users of the models in industry projects should be aware of problematic behavior and keep attention in related simulations.

All the created software are provided along with source code. All the software created in C/C++ is platform independent and can be used on variety of operation systems.

References

[1] *Directive 2001/80/EC of the European Parliament and of the Council on the limitation of emissions of certain pollutants into the air from large combustion plants* [online]. 23 October 2001. S.l.: [Accessed 30 November 2009]. Available from: http://eur-lex.europa.eu/LexUriServ/LexUriServ.do?uri=CELEX:32001L0080:EN:HTML.

[2] KERMES, V. et al. Testing of gas and liquid fuel burners for power and process industries. In: *Energy*. October 2008, Vol. 33, no. 10, pp. 1551–1561. DOI 10.1016/j.energy.2008.07.013. 10th Conference Process Integration, Modelling and Optimisation for Energy Saving and Pollution Reduction, Ischia Isl, ITALY, JUN 24-27, 2007.

[3] FUREBY, C. et al. An experimental and computational study of a multi-swirl gas turbine combustor. In: *Proceedings of the Combustion Institute*. January 2007, Vol. 31, no. 2, pp. 3107–3114. DOI 10.1016/j.proci.2006.07.127.

[4] SADIKI, A. et al. Unsteady methods (URANS and LES) for simulation of combustion systems. In: *International Journal of Thermal Sciences*. August 2006, Vol. 45, no. 8, pp. 760–773. DOI 10.1016/j.ijthermalsci.2005.11.001.

[5] JAMES, S. et al. Large eddy simulations of turbulent flames using the filtered density function model. In: *Proceedings of the Combustion Institute*. January 2007, Vol. 31, no. 2, pp. 1737–1745. DOI 10.1016/j.proci.2006.07.160.

[6] LANDENFELD, T. et al. Laser-diagnostic and numerical study of strongly swirling natural gas flames. In: *Symposium (International) on Combustion*. 1998, Vol. 27, no. 1, pp. 1023–1029. DOI 10.1016/S0082-0784(98)80502-X.

[7] MEIER, W. et al. Investigations in the TECFLAM swirling diffusion flame: Laser Raman measurements and CFD calculations. In: *Applied Physics B: Lasers and Optics*. 15 November 2000, Vol. 71, no. 5, pp. 725–731. DOI 10.1007/s003400000436.

[8] SCHMITTEL, P. et al. Turbulent swirling flames: Experimental investigation of the flow field and formation of nitrogen oxide. In: *Proceedings of the Combustion Institute*. 2000, Vol. 28, no. 1, pp. 303–309. DOI 10.1016/S0082-0784(00)80224-6.

[9] BÖCKLE, S. et al. Laser-diagnostic multi-species imaging in strongly swirling natural gas flames. In: *Applied Physics B: Lasers and Optics*. 15 November 2000, Vol. 71, no. 5, pp. 741–746. DOI 10.1007/s003400000392.

[10] WEIGAND, P. et al. Investigations of swirl flames in a gas turbine model combustor: I. Flow field, structures, temperature, and species distributions. In: *Combustion and Flame*. January 2006, Vol. 144, no. 1-2, pp. 205–224. DOI 10.1016/j.combustflame.2005.07.010.

[11] MEIER, W. et al. Investigations of swirl flames in a gas turbine model combustor: II. Turbulence-chemistry interactions. In: *Combustion and Flame*. January 2006, Vol. 144, no. 1-2, pp. 225–236. DOI 10.1016/j.combustflame.2005.07.009.

[12] MEIER, W. et al. Reaction zone structures and mixing characteristics of partially premixed swirling CH4/air flames in a gas turbine model combustor. In: *Proceedings of the Combustion Institute*. January 2005, Vol. 30, no. 1, pp. 835–842. DOI 10.1016/j.proci.2004.08.065.

[13] RANGA DINESH, K.K.J. et al. Modelling of instabilities in turbulent swirling flames. In: *Fuel*. January 2010, Vol. 89, no. 1, pp. 10–18. DOI 10.1016/j.fuel.2009.06.024.

[14] AL-ABDELI, Y.M. et al. Time-varying behaviour of turbulent swirling nonpremixed flames. In: *Combustion and Flame*. July 2006, Vol. 146, no. 1-2, pp. 200–214. DOI 10.1016/j.combustflame.2006.03.009.

[15] MASRI, A.R. et al. The compositional structure of swirl-stabilised turbulent nonpremixed flames. In: *Combustion and Flame*. April 2004, Vol. 137, no. 1-2, pp. 1–37. DOI 10.1016/j.combustflame.2003.12.004.

[16] KALT, P.A.M. et al. Swirling turbulent non-premixed flames of methane: Flow field and compositional structure. In: *Proceedings of the Combustion Institute*. 2002, Vol. 29, no. 2, pp. 1913–1919. DOI 10.1016/S1540-7489(02)80232-2.

[17] SENGISSEN, A.X. et al. LES and experimental studies of cold and reacting flow in a swirled partially premixed burner with and without fuel modulation. In: *Combustion and Flame*. July 2007, Vol. 150, no. 1-2, pp. 40–53. DOI 10.1016/j.combustflame.2007.02.009.

[18] HUANG, R.F. and YEN, S.C. Aerodynamic characteristics and thermal structure of nonpremixed reacting swirling wakes at low Reynolds numbers. In: *Combustion and Flame*. December 2008, Vol. 155, no. 4, pp. 539–556. DOI 10.1016/j.combustflame.2008.01.001.

[19] SOLERO, G. and COGHE, A. Effect of injection typology on turbulent homogeneous mixing in a natural gas swirl burner. In: *Experimental Thermal and Fluid Science*. March 2000, Vol. 21, no. 1-3, pp. 162–170. DOI 10.1016/S0894-1777(99)00067-9.

[20] HÜBNER, A.W. et al. Experiments on a rotating-pipe swirl burner. In: *Experimental Thermal and Fluid Science*. April 2003, Vol. 27, no. 4, pp. 481–489. DOI 10.1016/S0894-1777(02)00251-0.

[21] TUMMERS, M.J. et al. Hysteresis and transition in swirling nonpremixed flames. In: *Combustion and Flame*. February 2009, Vol. 156, no. 2, pp. 447–459. DOI 10.1016/j.combustflame.2008.10.027.

[22] WEGNER, B. et al. Assessment of unsteady RANS in predicting swirl flow instability based on LES and experiments. In: *International Journal of Heat and Fluid Flow*. erven 2004, Vol. 25, no. 3, pp. 528–536. DOI 16/j.ijheatfluidflow.2004.02.019.

[23] PORTSCHT, R. Studies on Characteristic Fluctuations of the Flame Radiation Emitted by Fires. In: *Combustion Science and Technology*. 1975, Vol. 10, no. 1, pp. 73. DOI 10.1080/00102207508946659.

[24] COELHO, P.J. Numerical simulation of radiative heat transfer from non-gray gases in three-dimensional enclosures. In: *Journal of Quantitative Spectroscopy and Radiative Transfer*. 1 August 2002, Vol. 74, no. 3, pp. 307–328. DOI 10.1016/S0022-4073(01)00249-7.

[25] COELHO, P.J. Numerical simulation of the interaction between turbulence and radiation in reactive flows. In: *Progress in Energy and Combustion Science*. August 2007, Vol. 33, no. 4, pp. 311–383. DOI 10.1016/j.pecs.2006.11.002.

[26] LI, G. and MODEST, M.F. Application of composition PDF methods in the investigation of turbulence-radiation interactions. In: *Journal of Quantitative Spectroscopy and Radiative Transfer*. 15 April 2002, Vol. 73, no. 2-5, pp. 461–472. DOI 10.1016/S0022-4073(01)00218-7.

[27] LI, G. and MODEST, M.F. Importance of Turbulence-Radiation Interactions in Turbulent Diffusion Jet Flames. In: *Journal of Heat Transfer*. October 2003, Vol. 125, no. 5, pp. 831–838. DOI 10.1115/1.1597621.

[28] JENG, S.-M. et al. Nonluminous Radiation in Turbulent Buoyant Axisymmetric Flames. In: *Combustion Science and Technology*. 1984, Vol. 40, no. 1-4, pp. 41–53. DOI 10.1080/00102208408923797.

[29] STRÖHLE, J. *Spectral Modelling of Radiative Heat Transfer in Industrial Furnaces*. Aachen, Germany: Shaker Verlag GmbH, Germany, 2004. ISBN 3832224920.

[30] KOBAYASHI, H. et al. Performance of High Temperature Air Combustion Boiler with Low NOx Emission. In: *JSME International Journal Series B Fluids and Thermal Engineering*. 2002, Vol. 45, no. 3, pp. 481–486. DOI 10.1299/jsmeb.45.481.

[31] VALERO, A. and CORTÉS, C. Ash fouling in coal-fired utility boilers. Monitoring and optimization of on-load cleaning. In: *Progress in Energy and Combustion Science*. 1996, Vol. 22, no. 2, pp. 189–200. DOI 10.1016/0360-1285(96)00004-4.

[32] ARAI, N. et al. A review of measurements of heat flux density applicable to the field of combustion. In: *Experimental Thermal and Fluid Science*. May 1996, Vol. 12, no. 4, pp. 452–460. DOI 10.1016/0894-1777(95)00136-0.

[33] HAYES, R.R. et al. Crown incident radiant heat flux measurements in an industrial, regenerative, gas-fired, flat-glass furnace. In: *Experimental Thermal and Fluid Science*. 14 March 2001, Vol. 24, no. 1-2, pp. 35–46. DOI 10.1016/S0894-1777(00)00055-8.

[34] HABIBI, A. et al. Impact of radiation models in CFD simulations of steam cracking furnaces. In: *Computers & Chemical Engineering*. November 2007, Vol. 31, no. 11, pp. 1389–1406. DOI 10.1016/j.compchemeng.2006.11.009.

[35] VONDÁL, J. and HÁJEK, J. Experimental and numerical investigation of swirling non-premixed gas flames in industrial-scale furnace. In: *Proceedings of the 9th European Conference on Industrial Furnaces and Boilers*. Estoril, Portugal: 26 April 2011.

[36] GUPTA, A.K. et al. *Swirl Flows*. S.l.: Abacus Press, 1984. ISBN 0-85626-175-0.

[37] MAK, H. and BALABANI, S. Near field characteristics of swirling flow past a sudden expansion. In: *Chemical Engineering Science*. December 2007, Vol. 62, no. 23, pp. 6726–6746. DOI 10.1016/j.ces.2007.07.009.

[38] WANG, P. et al. Large eddy simulation and experimental studies of a confined turbulent swirling flow. In: *Physics of Fluids*. 2004, Vol. 16, no. 9, pp. 3306. DOI 10.1063/1.1769420.

[39] BĚLOHRADSKÝ, P. et al. Design and analysis of experiment for low-NOx burners design for process industries. In: *8th European Conference on Industrial Furnaces and Boilers*. Vilamouria, Portugal: 25 March 2008.

[40] KERMES, V. et al. Influence of burner geometry with staged gas supply on the formation of nitrogen oxides. In: *8th European Conference on Industrial Furnaces and Boilers*. Vilamouria, Portugal: 25 March 2008.

[41] HÁJEK, J. et al. Numerical and experimental analysis of turbulent swirling diffusion gas flames. In: *11th Conference on Process Integration, Modelling and Optimisation for Energy Saving and Pollution Reduction*. Prague, Czech Republic: August 2008.

[42] WILLIAMS, T. and KELLEY, C. *Gnuplot* [online]. S.l.: 2010. Available from: http://www.gnuplot.info/documentation.html.

[43] BURGER, W. and BURGE, M. *Principles of digital image processing: fundamental techniques*. S.l.: Springer, 2009. ISBN 9781848001909.

[44] BRAEMBUSSCHE, V. Den (Ed.). *Measurement Techniques in Fluid Dynamics: An Introduction*. Rhode Saint Genése: von Karman Institute for Fluid Dynamics, 2001.

[45] PAIST, A. et al. Probes for measuring heat transfer parameters and fouling intensity in boilers. In: *Fuel*. 1 September 2002, Vol. 81, no. 14, pp. 1811–1818. DOI 10.1016/S0016-2361(02)00114-X.

[46] NEMODA, S. et al. Experimental and numerical investigation of gaseous fuel combustion in swirl chamber. In: *International Journal of Heat and Mass Transfer*. October 2005, Vol. 48, no. 21-22, pp. 4623–4632. DOI 10.1016/j.ijheatmasstransfer.2005.04.004.

[47] BARREIROS, A. et al. Prediction of the near burner region and measurements of NOx and particulate emissions in heavy fuel oil spray flames. In: *Combustion and Flame*. February 1993, Vol. 92, no. 3, pp. 231–240. DOI 10.1016/0010-2180(93)90035-2.

[48] BUTLER, B.W. et al. Radiation heat transfer in a laboratory-scale, pulverized coal-fired reactor. In: *Experimental Thermal and Fluid Science*. July 1994, Vol. 9, no. 1, pp. 69–79. DOI 10.1016/0894-1777(94)90010-8.

[49] SAARIO, A. et al. Heavy fuel oil combustion in a cylindrical laboratory furnace: measurements and modeling. In: *Fuel*. March 2005, Vol. 84, no. 4, pp. 359–369. DOI 10.1016/j.fuel.2004.10.002.

[50] MODEST, M.F. *Radiative Heat Transfer*. New York: McGraw-Hill, 1993. ISBN 0-07-042675-9.

[51] ESPECEL, D. and MATTEÏ, S. Total emissivity measurements without use of an absolute reference. In: *Infrared Physics & Technology*. December 1996, Vol. 37, no. 7, pp. 777–784. DOI 10.1016/S1350-4495(96)00017-5.

[52] SMART, J. wxWidgets Cross-Platform GUI Library. In: [online]. 2011. [Accessed 12 March 2012]. Available from: http://www.wxwidgets.org/.

[53] RONDINI, D. wxMathPlot. In: *wxMathPlot Scientific Plotting for wxWidgets* [online]. 2008. [Accessed 12 March 2012]. Available from: http://wxmathplot.sourceforge.net/.

[54] SMART, J. and ROEBLING, R. wxWindows Library Licence, Version 3.1. In: [online]. [Accessed 12 March 2012]. Available from: http://www.wxwidgets.org/about/licence3.txt.

[55] VONDÁL, J. and HÁJEK, J. Experimental data of the local wall heat flux for combustion codes validation in non-premixed swirling gas flames. In: *Proceedings of the ASME-ATI-UIT 2010 Conference on Thermal and Environmental Issues in Energy Systems*. Sorrento, Italy: 16 May 2010. pp. 931–936.

[56] VONDÁL, J. et al. Local wall heat fluxes in swirling non-premixed natural gas flames in large-scale combustor: Data for validation of combustion codes. In: *Chemical Engineering Transactions*. 28 August 2010, Vol. 21, no. 2, pp. 1123–1128. DOI 10.3303/CET1021188.

[57] BLASIUS, H. Grenzschichten in flüssigkeiten mit kleiner reibung. In: *Z. Math. Phys.* Vol. 1908, no. 56, pp. 1–37.

[58] LIAO, S.-J. An explicit, totally analytic approximate solution for Blasius' viscous flow problems. In: *International Journal of Non-Linear Mechanics*. July 1999, Vol. 34, no. 4, pp. 759–778. DOI 10.1016/S0020-7462(98)00056-0.

[59] LAUNDER, B.E. and SPALDING, D.B. *Lectures in Mathematical Models of Turbulence*. London: Academic Press, 1972. ISBN 72083798.

[60] WILCOX, D.C. *Turbulence Modeling for CFD*. 3rd. S.l.: Dcw Industries, Incorporated, 2006. ISBN 1928729088.

[61] MENTER, F.R. Two-equation eddy-viscosity turbulence models for engineering applications. In: *AIAA Journal*. August 1994, Vol. 32, pp. 1598–1605. DOI 10.2514/3.12149.

[62] LAUNDER, B.E. et al. Progress in the Development of a Reynolds-Stress Turbulence Closure. In: *Journal of Fluid Mechanics* [online]. 1975, Vol. 68, no. 3. [Accessed 15 March 2010]. Available from: http://www.scopus.com/inward/record.url?eid=2-s2.0-0347154273&partnerID=40&md5=5054361960135cd8d545dc63d51e05b4.

[63] COLES, D.E. and HIRST, E.A. In: *Computation of Turbulent Boundary Layers-1968 AFOSR IFP-Stanford Conference* [online]. 1969, Vol. 2. Available from: www.scopus.com.

[64] VEYNANTE, D. and VERVISCH, L. Turbulent combustion modeling. In: *Progress in Energy and Combustion Science*. March 2002, Vol. 28, no. 3, pp. 193–266. DOI 10.1016/S0360-1285(01)00017-X.

[65] WARNATZ, J. et al. *Combustion: Physical and Chemical Fundamentals, Modelling and Simulation, Experiments, Pollutant Formation*. Berlin: Springer, 1996. ISBN 3-540-60730-7. 536.4.

[66] PETERS, N. Multiscale combustion and turbulence. In: *Proceedings of the Combustion Institute*. 2009, Vol. 32, no. 1, pp. 1–25. DOI 10.1016/j.proci.2008.07.044.

[67] MAGNUSSEN, B.F. and HJERTAGER, B.H. On mathematical modeling of turbulent combustion with special emphasis on soot formation and combustion. In: *Symposium (International) on Combustion*. 1977, Vol. 16, no. 1, pp. 719–729. DOI 10.1016/S0082-0784(77)80366-4.

[68] FLUENT. *FLUENT 6.3.26, User`s Guide*. 2006. S.l.: Fluent Inc., Lebanon, USA.

[69] LAW, C.K. *Combustion Physics*. 1. S.l.: Cambridge University Press, 2006. ISBN 0521870526.

[70] ROSE, J.W., SPIERS, H.M. and COOPER, J.R. (Eds.). *Technical data on fuel*. 7th. New York: Wiley, 1977. ISBN 0470992395.

[71] YIN, C. et al. Mathematical Modeling and Experimental Study of Biomass Combustion in a Thermal 108 MW Grate-Fired Boiler. In: *Energy & Fuels*. 1 March 2008, Vol. 22, no. 2, pp. 1380–1390. DOI 10.1021/ef700689r.

[72] GRAN, I.R. and MAGNUSSEN, B.F. A Numerical Study of a Bluff-Body Stabilized Diffusion Flame. Part 2. Influence of Combustion Modeling And Finite-Rate Chemistry. In: *Combustion Science and Technology*. 1996, Vol. 119, no. 1-6, pp. 191–217. DOI 10.1080/00102209608951999.

[73] HUGHES, K.J. et al. Development and testing of a comprehensive chemical mechanism for the oxidation of methane. In: *International Journal of Chemical Kinetics*. 2001, Vol. 33, no. 9, pp. 513–538.

[74] SMOOKE, M.D. (Ed.). *Reduced Kinetic Mechanisms and Asymptotic Approximations for Methane-Air Flames: A Topical Volume*. 1. S.l.: Springer, 1991. ISBN 3540542108.

[75] WESTBROOK, C.K. and DRYER, F.L. Simplified Reaction Mechanisms for the Oxidation of Hydrocarbon Fuels in Flames. In: *Combustion Science and Technology*. 1981, Vol. 27, no. 1-2, pp. 31–43. DOI 10.1080/00102208108946970.

[76] ANDERSEN, J. et al. Global Combustion Mechanisms for Use in CFD Modeling under Oxy-Fuel Conditions. In: *Energy Fuels*. 2009, Vol. 23, no. 3, pp. 1379–1389. DOI 10.1021/ef8003619.

[77] BRAY, K.N. and PETERS, N. Laminar Flamelets in Turbulent Flames. In: LIBBY, P.A. and WILLIAMS, F.A. (Eds.), *Turbulent Reacting Flows* [online]. S.l.: London : Academic, 1994. pp. 63–114. ISBN 0124479456. Available from: http://trove.nla.gov.au/work/9880780.

[78] SMITH, G.P. et al. GRI-Mech 3.0. In: [online]. [Accessed 25 April 2012]. Available from: http://www.me.berkeley.edu/gri_mech.

[79] BRUCATO, A. et al. Estimating radiant fields in flat heterogeneous photoreactors by the six-flux model. In: *AIChE Journal*. 2006, Vol. 52, no. 11, pp. 3882–3890.

[80] ROSSELAND, S. *Theoretical astrophysics...* [online]. Oxford: Clarendon Press, 1936. [Accessed 17 March 2010]. Available from: http://openlibrary.org/b/OL6341918M/Theoretical_astrophysics...

[81] BIDI, M. et al. Numerical analysis of methane-air combustion considering radiation effect. In: *Energy Conversion and Management*. December 2008, Vol. 49, no. 12, pp. 3634–3647. DOI 10.1016/j.enconman.2008.07.010.

[82] Basic Quantum Mechanics. In: *Engine Research Center - UW-Madison* [online]. [Accessed 17 July 2009]. Available from: http://www.erc.wisc.edu/bqm.php.

[83] PARK, J. et al. Addition Effects of H2 and H2O on Flame Structure and Pollutant Emissions in Methane–Air Diffusion Flame. In: *Energy & Fuels*. 1 November 2007, Vol. 21, no. 6, pp. 3216–3224. DOI 10.1021/ef700211m.

[84] JEONG, S. et al. Computer modeling of the continuous annealing furnace. In: *Journal of Mechanical Science and Technology*. 1 March 1991, Vol. 5, no. 1, pp. 16–21. DOI 10.1007/BF02945146.

[85] HOTTEL, H.C. *Radiative Transfer*. New York: McGraw-Hill, 1967. QC175.2.H62.

[86] MODEST, M.F. The Weighted-Sum-of-Gray-Gases Model for Arbitrary Solution Methods in Radiative Transfer. In: *Journal of Heat Transfer*. 1991, Vol. 113, no. 3, pp. 650–656. DOI 10.1115/1.2910614.

[87] DENISON, M.K. and WEBB, B.W. A Spectral Line-Based Weighted-Sum-of-Gray-Gases Model for Arbitrary RTE Solvers. In: *Journal of Heat Transfer*. November 1993, Vol. 115, no. 4, pp. 1004–1012. DOI 10.1115/1.2911354.

[88] ROTHMAN, L.S. et al. The HITRAN 2008 molecular spectroscopic database. In: *Journal of Quantitative Spectroscopy and Radiative Transfer*. June 2009, Vol. 110, no. 9-10, pp. 533–572. DOI 10.1016/j.jqsrt.2009.02.013.

[89] KONTOGEORGOS, D.A. et al. Assessment of simplified thermal radiation models for engineering calculations in natural gas-fired furnace. In: *International Journal of Heat and Mass Transfer*. December 2007, Vol. 50, no. 25-26, pp. 5260–5268. DOI 10.1016/j.ijheatmasstransfer.2007.06.011.

[90] GROSSHANDLER, W.L. RADCAL: A narrow-band model for radiation calculations in a combustion environment. In: *NIST Technical Note*. 1993, .

[91] YIN, C. et al. New Weighted Sum of Gray Gases Model Applicable to Computational Fluid Dynamics (CFD) Modeling of Oxy−Fuel Combustion: Derivation, Validation, and Implementation. In: *Energy & Fuels*. 16 December 2010, Vol. 24, no. 12, pp. 6275–6282. DOI 10.1021/ef101211p.

[92] SMITH, T.F. et al. Evaluation of Coefficients for the Weighted Sum of Gray Gases Model. In: *Journal of Heat Transfer*. November 1982, Vol. 104, no. 4, pp. 602–608. DOI 10.1115/1.3245174.

[93] SYRED, N. A review of oscillation mechanisms and the role of the precessing vortex core (PVC) in swirl combustion systems. In: *Progress in Energy and Combustion Science*. 2006, Vol. 32, no. 2, pp. 93–161. DOI 10.1016/j.pecs.2005.10.002.

[94] VONDÁL, J. and HÁJEK, J. Boundary Condition Evaluation and Stability Issues in Swirling Flame Gas Combustion. In: *ThermaComp2009* [online]. Naples, Italy: 10 September 2009. pp. 314–317. Available from: http://www.thermacomp.com/uploads/ThermaComp2009_Proceedings_web.pdf.

[95] WAGNER, W. et al. The IAPWS Industrial Formulation 1997 for the Thermodynamic Properties of Water and Steam. In: *Journal of Engineering for Gas Turbines and Power*. 2000, Vol. 122, no. 1, pp. 184, 150.

[96] INCROPERA, F.P. *Fundamentals of Heat and Mass Transfer*. 6th ed. New York: John Wiley & Sons, 2007. ISBN 0-471-45728-0. 536.

[97] ANSYS ACADEMIC RESEARCH, RELEASE 12.1. *Help System, Users's Guide*. 2009. S.l.: ANSYS, Inc.

[98] SUTHERLAND, W. The viscosity of gases and molecular force. In: *Philosophical Magazine*. Vol. 1893, no. 36, pp. 507–531.

[99] VONDÁL, J. and HÁJEK, J. Prediction of flow through swirl generator and validation by measured data. In: *Journal of Physics: Conference Series*. 2011, Vol. 318, no. 2, pp. 022026. DOI 10.1088/1742-6596/318/2/022026.

[100] FERNANDES, E.C. et al. An analysis of unsteady highly turbulent swirling flow in a model vortex combustor. In: *Experiments in Fluids*. 2006, Vol. 40, no. 2, pp. 177–187. DOI 10.1007/s00348-005-0034-4.

[101] SO, R.M.C. et al. Jet characteristics in confined swirling flow. In: *Experiments in Fluids*. 1985, Vol. 3, no. 4, pp. 221–230.

[102] CLAYPOLE, T.C. and SYRED, N. The effect of swirl burner aerodynamics on NOx formation. In: *Symposium (International) on Combustion*. 1981, Vol. 18, no. 1, pp. 81–89. DOI 16/S0082-0784(81)80013-6.

[103] CORTÉS, C. and GIL, A. Modeling the gas and particle flow inside cyclone separators. In: *Progress in Energy and Combustion Science*. jen 2007, Vol. 33, no. 5, pp. 409–452. DOI 16/j.pecs.2007.02.001.

[104] KHEZZAR, L. Velocity measurements in the near field of a radial swirler. In: *Experimental Thermal and Fluid Science*. March 1998, Vol. 16, no. 3, pp. 230–236. DOI 10.1016/S0894-1777(97)10027-9.

[105] COGHE, A. et al. Recirculation phenomena in a natural gas swirl combustor. In: *Experimental Thermal and Fluid Science*. September 2004, Vol. 28, no. 7, pp. 709–714. DOI 10.1016/j.expthermflusci.2003.12.007.

[106] RANGA DINESH, K.K.J. and KIRKPATRICK, M.P. Study of jet precession, recirculation and vortex breakdown in turbulent swirling jets using LES. In: *Computers & Fluids*. erven 2009, Vol. 38, no. 6, pp. 1232–1242. DOI 10.1016/j.compfluid.2008.11.015.

[107] AHMED, S.A. and NEJAD, A.S. Swirl effects on confined flows in axisymmetric geometries. In: *Journal of Propulsion and Power*. March 1992, Vol. 8, no. 2, pp. 339–345. DOI 10.2514/3.23483.

[108] BALABANI, S. *Personnal communication*. 4 October 2010. S.l.: .

[109] VESELÝ, V. *Computing periodogram and detecting significant periodicities using fisher's and siegel's test*. Brno, Czech Republic: Masaryk University of Brno, 1999.

[110] SELLE, L. et al. Joint use of compressible large-eddy simulation and Helmholtz solvers for the analysis of rotating modes in an industrial swirled burner. In: *Combustion and Flame*. April 2006, Vol. 145, no. 1-2, pp. 194–205. DOI 10.1016/j.combustflame.2005.10.017.

[111] Bash (Unix shell) - Wikipedia, the free encyclopedia. In: [online]. [Accessed 1 March 2012]. Available from: http://en.wikipedia.org/wiki/Bash_(Unix_shell).

Nomenclature

Physical constants

g	standard acceleration of gravity (9.80665 m/s^2)
R_u	universal gas constant (8314.51 J/(kmol-K))
σ	Stefan–Boltzmann constant (5.67051 × 10^{-8} W/(m^2-K^4))

Variables

A	area [m^2]
c_p	specific heat capacity [kJ / kg-K]
C_μ	model constant
D_i	diffusion coefficient of species i [m^2/s]
h	specific enthalpy [J/kg]
$I_{b\eta}$	Planck function [J/(m-s)]
I_η	transmitted spectral radiative intensity [J/(m-s)]
$I_{0\eta}$	received spectral radiative intensity [J/(m-s)]
k	turbulence kinetic energy [m^2/s^2]
K_p	Planck mean absorption coefficient [1/m]
K_η	spectral absorption coefficient [1/m]
m	mass [kg]
$\dot{m}$	mass flow rate [kg/s]
M_w	molar weight [kg/kmol]
p	pressure [Pa] = [kg/(m-s^2)]
p_0	reference pressure [Pa]
Q	heat transfer rate [kW/m^2]
Q_{rad}	radiation source term in enthalpy equation [J/(m^3-s)]
Re	Reynolds number [–]
r	radius [m]
$R_{i,r}$	net rate of production of species i due to reaction r [kg/(m^3-s)]
s	direction (for radiation) [m]
S	effective temperature [K] (Sutherland constant), swirl number
S_Φ	source term of general variable
t	time [s]
T	temperature [K]
T_0	reference temperature [K]
u	mixture specific internal energy [J/kg]
u'_i	fluctuating component of velocity vector [m/s]
u_i	velocity vector [m/s]
V	volume [m^3]
Y	species mass fractions [kg$_\alpha$/kg]
x, y, or z	Cartesian spatial coordinates [m]

Greek-letter variables

α_η	spectral absorptivity
β_η	spectral extinction coefficient
ε	molecular dissipation rate of turbulence kinetic energy [m2/s3]
Φ	scattering phase function
κ	Kármán constant
μ	dynamic viscosity [kg/(m-s)]
μ_0	reference value of dynamic viscosity [kg/(m-s)]
μ_t	apparent turbulent viscosity [kg/(m-s)]
ν	kinematic viscosity [m^2/s]
ω	specific dissipation rate [s-1]
ρ	mass density [kg/m^3]
$\sigma_{s,\eta}$	scattering coefficient [1/m]
τ	viscous stress tensor [$kg/(m\text{-}s^2)$]
τ_η	spectral transmittance
τ_ω	surface share stress [$kg/(m\text{-}s^2)$]

Subscripts

i, j, or k	cartesian vector or tensor component
η	spectral

Abbreviations

CFD	Computational fluid dynamics
CK	Correlated k-distribution model
CPU	Central processing unit
DNS	Direct numerical simulation
EWBM	Exponential wide band model
LDA	Laser Doppler anemometry
LDV	Laser Doppler velocimetry
LES	Large-eddy simulation
LIF	Laser-induced fluorescence
PDPA	Phase Doppler particle analysis
PIV	Particle image velocimetry
PLIF	Planar laser-induced fluorescence
RANS	Reynolds-averaged Navier Stokes
RNG	Re-normalisation group
RSM	Reynolds stress model
RTD	Resistance temperature detectors
RTE	Radiative transfer equation
SST	Shear stress transport
TRI	Turbulence radiation interaction
URANS	Unsteady Reynolds-averaged Navier Stokes
WBCK	Wide band correlated-k method
WSGGM	Weighted-sum-of-grey-gases model

List of Figures

Appendix A Numerical and experimental analysis of turbulent swirling diffusion gas flames

This appendix contains author's paper published at 11th Conference on Process Integration, Modelling and Optimisation for Energy Saving and Pollution Reduction held in Prague on August 2008.

Bibliographic citation:

HÁJEK, J., VONDÁL, J., ŠARLEJ, M. and STEHLÍK, P. Numerical and experimental analysis of turbulent swirling diffusion gas flames. In: *11th Conference on Process Integration, Modelling and Optimisation for Energy Saving and Pollution Reduction*. Prague, Czech Republic: August 2008.

Numerical and experimental analysis of turbulent swirling diffusion gas flames

Jiří Hájek, Jiří Vondál, Marek Šarlej, Petr Stehlík
Institute of Process and Environmental Engineering, Faculty of Mechanical Engineering,
Brno University of Technology (UPEI VUT) Technická 2, 616 69 Brno, Czech Republic
Tel.: +420 541 142 373, Fax: +420 541 142 372, Email: hajek@fme.vutbr.cz

The computational prediction of turbulent swirling diffusion flames poses a well known, difficult and challenging problem that has been studied by many researchers. The objective of the present article is to provide an experimental and computational study of swirling diffusion gas flames using a different approach to validation of the predictions. Detailed description of the experiment, the testing facility, measuring procedure and instrumentation is provided. List of adjustable components of the staged gas burner is also given with operation ranges of these parameters. Attention is paid to the way steady state conditions are achieved and identified in the experiments. Obtained measured results are analysed with regard to the propagation of uncertainty. The particular experiment and its settings chosen to be modelled by a CFD approach is described as well. Boundary conditions as well as key sub-models for turbulence and chemistry are specified. Finally 4 numerically successful simulations are reported. The results show an unexpectedly large deviation of predicted wall heat fluxes from the real experimental values.

1 Introduction

Turbulent swirling diffusion flames belong among the most popular in industrial practice, while their prediction using Reynolds-Averaged Navier-Stokes (RANS) equations poses a very difficult task. This work reports highly reliable experimental data of local heat fluxes along the combustion chamber and uses them to validate numerical combustion simulations. The investigation has been performed in a large-scale experimental combustion chamber with a low-NO_x natural gas burner with staged gas supply and firing capacity of 1.2 MW.

Intensity of the swirling motion at burner outlet is a very important design parameter and for its specification are used several alternative swirl number definitions [1, 2]. As documented in [3] and manifested in recent publications (e.g. [4]), a formula that gradually became the most popular defines swirl number as the ratio of axial flux of tangential momentum to the axial flux of axial momentum.

The prediction of swirling flames using Reynolds-averaged Navier-Stokes (RANS) models has proven to be fairly difficult. Conclusions obtained e.g. by International Flame Research Foundation (IFRF) in their research of swirling pulverised coal burners [5] or by Barreiros et al. in research of fluid fuel burners [6] and again recently by German and Mahmud for gas fuels [7] confirm the preceding statement. The reasons of significant discrepancies between RANS model predictions and measurements in swirling flames are not very clear, especially as the predictions of non-swirling flames are much more reliable [8].

It is nevertheless a matter of fact that really reliable predictions of swirling flames appeared only recently and in all cases they were based on Large-eddy simulations (LES), see e.g. [9-11]. Therefore they entail computational requirements several orders of magnitude higher than RANS models. That is also the reason why the investigated burners had in all but few exceptional cases very simple designs. To the authors' knowledge, only in facilities like the Center for turbulence research at the Stanford University, where computational resources

are top-level (including the world's fastest supercomputer Blue Gene with over 200.000 processors), researchers have attempted to simulate industry-relevant applications [12].

The target of research of swirling diffusion gas flames at UPEI VUT thus is not an accurate prediction of in-flame properties. Instead, the focus is on utilising the length-wise segmental design of the combustion chamber with accurate monitoring of local heat loads for tuning of RANS models. It is expected that in this way, it will be possible to gain control over the simulated flame length. The reasons for mildly optimistic expectations are found in good experiences of other authors in solving similar problems (see e.g. [6] or [13]), even though those works have been concerned with in-flame properties and not wall heat fluxes.

2 Measurement

Experimental analysis of turbulent swirling diffusion flames has been performed in order to provide a solid ground for the validation of numerical predictions. The experimental work was previously documented in [14, 15, 16]. The information included in this text has however different objective than those other works and concentrates on factors, related to the validation of numerical predictions.

2.1 The experimental facility

Experiment was performed on a water-cooled horizontal combustion chamber (1 m internal diameter and 4 m length, maximum admissible burner capacity about 1.8 MW) with low-NO_x burner firing natural gas. Shell of the combustion chamber is divided into seven sections, six of which are 0.5 m long and the seventh (nearest to the exhaust) section has 1 m. Each of the sections has separate water inlet and outlet and is equipped by a water flow meter and temperature sensors, serving to measure the heat transfer rate. Hot water from the combustor is cooled in a cooling tower placed outside of the testing facility.

Each section of the combustion chamber is equipped by two inspection windows opposite to each other. Also both ends of the chamber have two inspection windows for optical flame inspection.

The gas supply is connected to a medium-pressure natural gas main and reduced to the approx. 45 kPa. Gas pressure, temperature and flow rate is measured and employed to calculate gas mass flow rate. Small and simple auxiliary burner is used for flame ignition and stabilisation, which is firing about 20 kW of total gas supply.

2.2 Description of the burner

The low-NOx gas burner used in the experiments is equipped with staged gas supply, has single air stream, swirl generator (flame holder), primary gas choke (orifice plate) secondary jets the position of which is adjustable in axial, radial and tangential direction. The burner was used to perform a total of 146 measurements with different burner's setting. Adjustable components were as follows:

- Burner duty
- Diameter of swirl generator
- Pitch angle of the swirl generator's blades
- Diameter of primary gas choke
- Air equivalence ratio
- Pitch angle of secondary nozzles
- Tangential direction of secondary nozzles
- Radial position of secondary nozzles
- Axial position of secondary nozzles

2.3 Instrumentation

This section describes only sensors employed for the measurement of heat fluxes, which play a key role in this article.

All temperature probes used to measure cooling water temperature are thermocouples Pt100 PTP50J RAWET with transmitter 4-20 mA and stainless well. Temperature is measured at a common supply pipe which provides water to all sections of the combustion chamber and also at the outlet of each section. The accuracy of all thermocouples is within class B as defined by the standard IEC 60751 [17].

Water flow rate in every section is measured by a multi-jet flow meter XN-RK 04 L300 G2 Q10-BH E K10 equipped by a pulse generator. The same flow rate meter is placed in a common pipe bringing water to all sections, to measure the total water flow rate.

Gas pressure is measured using rotary natural gas meter Roots Dresser G100 and to determine gas pressure, ceramic pressure sensor DMK331 EEx ia IIC T6 is used. Temperature of gas is measured by a thermocouple probe Pt100 T1002 EEx IIC JSP Nová Paka. The recorded values were employed to calculate volumetric flow rate at normal conditions. For details see [14].

All measured data were collected by an automatic data acquisition system which uses either digital (receives pulses e.g. from water flow rate meter) or analogue (current transmitter devices, e.g. gas pressure meter) signals.

2.4 Scope of experiments

The 146 settings of the burner were used to determine sensitivity of various parameters in response to any combination of the independent variable factors. During the test, settings were given by a statistically developed plan of measurements [16]. Adjustable components had the following ranges:

- Burner duty [kW] 745; 930; 1120
- Diameter of swirl generator [mm] 240; 260; 280
- Pitch angle of the swirl generator's blades [°] 35; 45; 55
- Diameter of primary gas choke [mm] 5.5; 6; 6.5
- Air equivalence ratio [-] 1.1; 1.15; 1.2
- Pitch angle of secondary nozzles [°] 20; 30; 40
- Tangential direction of secondary nozzles [°] 0; 22.5; 45
- Radial position of secondary nozzles [mm] 0; 25; 50
- Axial position of secondary nozzles [mm] 0; 40; 80

Most changes were done manually, as they required interruption of fuel firing, dismounting of the burner and replacement of various parts. Due to these interruptions during experiments it was necessary to pay attention to stabilization of the operating conditions. This requirement was fulfilled by tracking the flue gas temperature in the exhaust duct. After achieving steady state conditions, one set of data was collected manually and three sets of data were saved by the data acquisition system.

The single setup of the burner that has been used for validation of computational models in this work, has the following specifications:

- Burner duty [kW] 745
- Diameter of swirl generator [mm] 240
- Pitch angle of the swirl generator's blades [°] 35
- Diameter of primary gas choke [mm] 5.5
- Air equivalence ratio [-] 1.1
- Pitch angle of secondary nozzles [°] 20
- Tangential direction of secondary nozzles [°] 0

- Radial position of secondary nozzles [mm] 0
- Axial position of secondary nozzles [mm] 0

2.5 Error analysis

Total heat fluxes on the walls of the combustion chamber were calculated from the following measured data:

- inlet water temperature
- outlet water temperature
- water flow rate

All measured data were accompanied by unknown measurement errors that are however assumed to lie within accuracy intervals given by the manufacturers of the respective sensors. The temperature measurements were performed by thermocouples with accuracy of class B [17], the maximum error of which is defined by ±(0.3+0.005|t|). The water flow rate meter has error estimate based on the flow rate and it is accurate to within ±0.5% of the measured value.

In order to determine the maximum error of total heat flux measurement using the specified sensors, it is necessary to consider the equation used for its calculation from the primitive measured parameters. The equation reads:

$$Q = \dot{m} \cdot c \cdot \Delta t = \dot{V} \cdot \rho \cdot c \cdot \left(t_{out} - t_{in}\right) \tag{1}$$

where m [kg/s] is water mass flow rate
c [J/kg-K] specific heat capacity
t [°C] temperature and
ρ [kg/m3] is water density

Using the concept of propagation of uncertainty [18] based on equation (1) with a single concrete set of data resulting from the above-described settings leads for each section to error estimates, displayed in Table 1.

Table 1 Calculated maximum errors in measured heat fluxes

Section	Heat flux [kW/m^2]	Maximum absolute error [kW/m^2]	Maximum relative error [%]
s1	21.3	2.74	16.1
s2	32.97	2.82	5.5
s3	48.45	2.83	3.7
s4	50.17	2.99	3.8
s5	46.15	2.9	4
s6	36.6	2.91	5.1
s7	30.27	1.56	1.8

2.6 Heat flux curve fitting

The aim was to develop procedure which would offer simple approximation of the heat flux distribution over the chamber length by function with a small number of coefficients.

To perform the fit of all measured heat fluxes within each section, heat fluxes [kW/m] were calculated from the total heat transfer rates calculated from equation (1). Length of each chamber section appears in Figure 1 as the width of the bars. Position of the calculated heat

flux value (which is an average in each section) was assumed to lie in the middle of the sections and a function was sought that would to fit these points as well as possible. Objective function to be optimised was the integral of the function over each section and it was required to be the same as the integral of the constant average value.

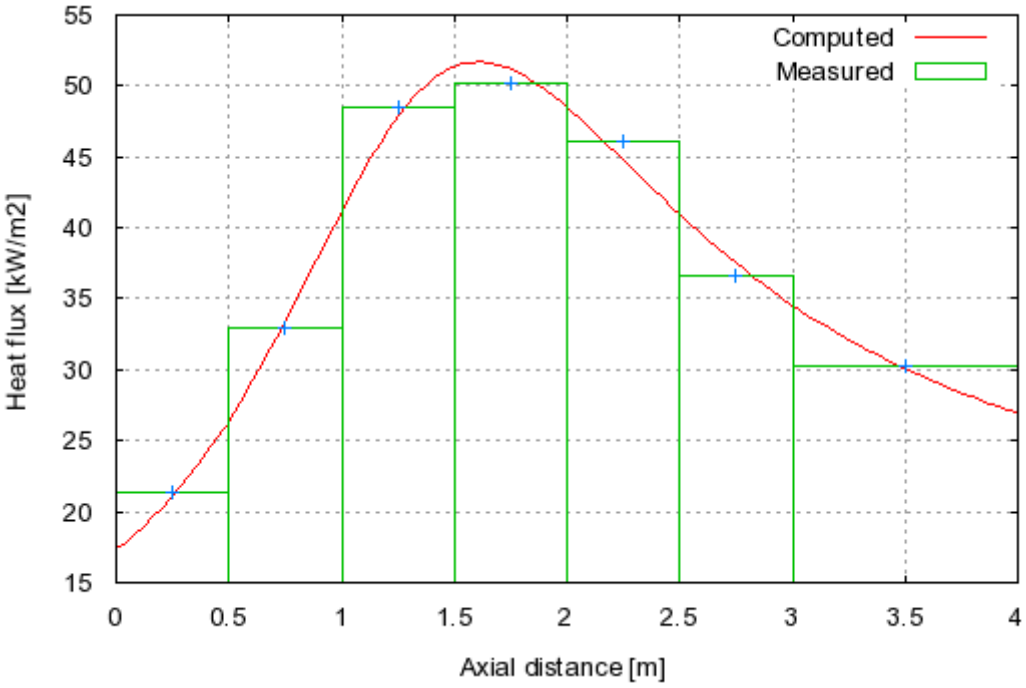

Figure 1 Curve fitting of the measured heat flux along the combustion chamber

For a preliminary selection of approximation function was found helpful an on-line tool [19]. It is equipped with "function finder" feature allowing users to find appropriate function for inserted points. It's only criteria is sum of squares of residuals therefore results had to be checked for singular points or non-physical behaviour. Based on results from the on-line tool [Philips 2008] was chosen a function NIST MGH09 with five coefficients.

$$y = \frac{a\left(x^2 + bx\right)}{x^2 + c + d} + e \tag{2}$$

Due to the big amount of data to be processed, a script in Bash [20] has been used to pass the intended data to the Gnnuplot software [21] where built in curve fitting tool could be used. Initial value for all coefficients was taken from the results of the online tool. The fitted function was describes approximate heat flux on the combustion chamber walls. Integration of the function (2) over the chamber's length yields expressions shown in equation (3) and (4). For the integration procedure see e.g. [18]. Namely, when $4\mathrm{d} - c^2 > 0$, then:

$$q = \int_{x_1}^{x_2} y = \left[\begin{array}{l} (a+e)\,x - \frac{ac}{2} \cdot \ln\left|x^2 + cx + d\right| + a\frac{c^2 - 2\mathrm{d}}{2} \cdot \frac{2}{\sqrt{4\mathrm{d} - c^2}} \cdot actg\frac{2\mathrm{x} + c}{\sqrt{4\mathrm{d} - c^2}} + \\ + \frac{ab}{2} \cdot \ln\left|x^2 + cx + d\right| - \frac{abc}{2} \cdot \frac{2}{\sqrt{4\mathrm{d} - c^2}} \cdot actg\frac{2\mathrm{x} + c}{\sqrt{4\mathrm{d} - c^2}} \end{array} \right]_{x_1}^{x_1} \tag{3}$$

When the opposite is true ($4\mathrm{d} - c^2 < 0$), then the following equation holds:

$$q = \int_{x_1}^{x_2} y = \left[\begin{array}{l} (a+e)x - \frac{ac}{2} \cdot \ln\left|x^2 + cx + d\right| + a\frac{c^2 - 2\mathrm{d}}{2} \cdot \frac{1}{\sqrt{c^2 - 4\mathrm{d}}} \cdot \ln\left|\frac{2\mathrm{x} - c - \sqrt{c^2 - 4\mathrm{d}}}{2\mathrm{x} + c + \sqrt{c^2 - 4\mathrm{d}}}\right| + \\ + \frac{ab}{2} \cdot \ln\left|x^2 + cx + d\right| - \frac{abc}{2} \cdot \frac{1}{\sqrt{c^2 - 4\mathrm{d}}} \cdot \ln\left|\frac{2\mathrm{x} - c - \sqrt{c^2 - 4\mathrm{d}}}{2\mathrm{x} + c + \sqrt{c^2 - 4\mathrm{d}}}\right| \end{array} \right]_{x_1}^{x_2} \quad (4)$$

where q [kW/m] is the heat flux
a,b,c,d,e [-] coefficients of function y
x [m] axial coordinate in the combustion chamber

A statistics of the errors of the approximation fit is shown in Table 2 below.

Table 2 Summary of errors in the fitting function

	RSS	s1	s2	s3	s4	s5	s6	s7	all
	[-]	[%]	[%]	[%]	[%]	[%]	[%]	[%]	[%]
Average error	4.94	3.34	2.01	1.99	1.73	1.2	1.82	3.41	2.21
Minimal error	0.04	0.1	0.07	0	0.09	0.05	0.04	0.07	0
Maximal error	42.05	41.84	6.56	5.99	5.71	3.41	8.2	10.72	41.84

3 Computations

Computations were performed to validate several mathematical models with the measured axial profile of heat fluxes. This is a unique evaluation, as revealed by the literature review, included in the Introduction. All computations were performed using CFD (Computational Fluid Dynamics) software FLUENT, v. 6.3.26 [22] from company ANSYS, Inc.

3.1 Geometry and computational grid

For the computational analysis, a model of the chamber with supply air duct has been developed. All the geometry was modelled with maximum care and attention to detail; only few details were deemed unimportant and therefore neglected. The modelled geometry and a photograph of the burner testing facility are shown in Figures 2 and 3.

Figure 2 Photograph of the burner testing facility

The geometry model was meshed by a combination of hexahedra and tetrahedral, with large majority of hexahedra. The total number of finite volume cells in the resulting computational grid was 1,156,788. Thus, for reasonable computational times it was necessary to run the simulations on a parallel machine, in this case a cluster with 22 CPUs, 2 GB per CPU of operating memory and fast interconnect Myrinet.

The diameter of each gas nozzle has been adjusted to compensate non-ideal approximation of the round orifice by the cells of mesh. Every jet has been meshed with four deformed quadrilateral cells so that the circumference was approximated by eight edges. That would lead to area decrease of about 10 %. This effect has been eliminated by enlarging the diameter of each jet as follows:

- Primary jet 1 – from 2.6 mm to 2.74 mm
- Primary jet 2 – from 3 mm to 3.16 mm
- Secondary jet – from 3.3 to 3.48 mm

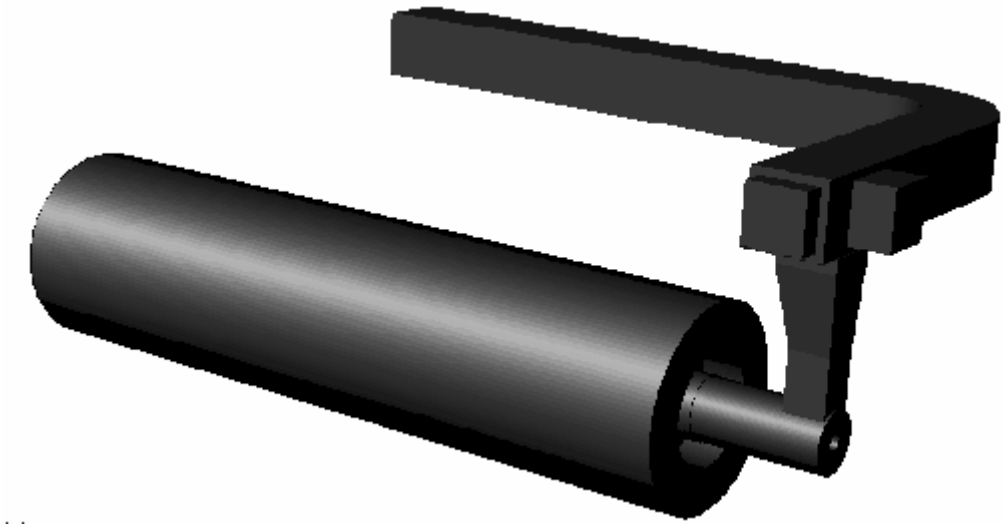

Figure 3 Computational model geometry

3.2 Boundary conditions

For proposed model, there were a total of 4 different types of boundary conditions. Namely mass flow inlets (gas and air), pressure outlet, cooled walls of the segmental combustion chamber and adiabatic walls approximating all other walls. The inputs for the calculation were based on the measured flow rate of gas and O_2 concentration measured in the exhaust. From these values and using several simplifying assumptions (e.g. assuming simple composition of air), it is possible to determine very precisely the air mass flow rate.

Distribution of gas between the primary and secondary stages was controlled by the applied choke. It would be technically possible to calculate the distribution of mass flow rate based on manual evaluation of pressure drops in all elements of the gas distribution elements in the burner using tables (e.g. [23]), but this could be quite inaccurate due to the close neighbourhood of the local flow resistances. Therefore a CFD model of the gas distribution system within the burner was simulated beforehand in order to determine the gas distribution to the primary and secondary nozzles.

3.3 Applied turbulence and chemistry models

It is well known that models assuming homogeneous isotropic turbulence (like two-equation models) are unable to work well in swirling flows with significant orthotropic turbulence effects. Moreover, the reported predictions of swirling flames using any RANS approach appear to be biased in a varying degree as discussed in the Introduction. The two applied turbulence models were selected as they represent viable tools for engineering applications. Large-Eddy modelling of the present system would most likely be adequate, but extremely computationally demanding.

The applied turbulence models included the well-known k-ε model [24] in its realizable variant [25] and also a second-order closure, also called Reynolds Stress Model (RSM) [26]. All the model equations are well described in the FLUENT program documentation [22].

Fast chemistry model was the first approach adopted for simulation of the combustion reactions. Combustion of methane is in this model represented by a single step global reaction, the rate of which is controlled solely by turbulent mixing [27]. The underlying assumption is thus that mixed = burned, or that chemical reaction rates are much faster than the mixing.

The second option of chemistry model was a steady strained laminar flamelet approach as documented e.g. in [28] and described in detail in [22]. This model allows for greater precision in predicting non-equilibrium chemistry and should perform better than the simple eddy-dissipation model.

4 Results and discussion

The simulations revealed that the simulated burner with air supply duct and combustion chamber is essentially an unsteady problem. Convergence of steady-state models was in some cases very hard if impossible to attain. The most important parameter from the point of view of this study, i.e. wall heat fluxes, typically displayed oscillatory character with large amplitude (on the order of 10 kW/m^2).

It was therefore impossible to successfully conclude calculation in steady state with RSM and EDM (eddy-dissipation model). On the other hand, laminar flamelet chemistry appeared to have a stabilising effect on the simulations and it was thus possible to complete successfully both combinations of laminar flamelets with k-ε model and RSM. Further to that, unsteady simulation combining k-ε model and laminar flamelets was conducted to provide a more rigorous representation. The obtained results are included in Figure 4.

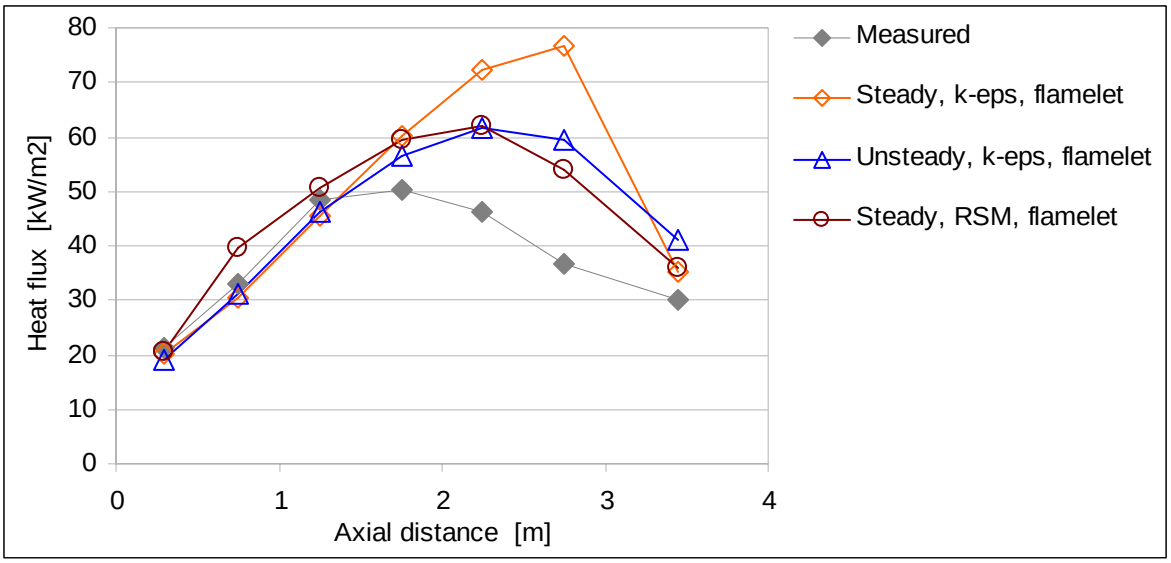

Figure 4 Measured and predicted heat fluxes in sections of the combustion chamber (burner is at the left side)

It is apparent that all predictions over-estimate the total heat transfer rate, absorbed by the cooled walls (numerical values show increase by about 20% to 30%). Also, the flames predicted by these models are in all cases longer than in the measured profile.

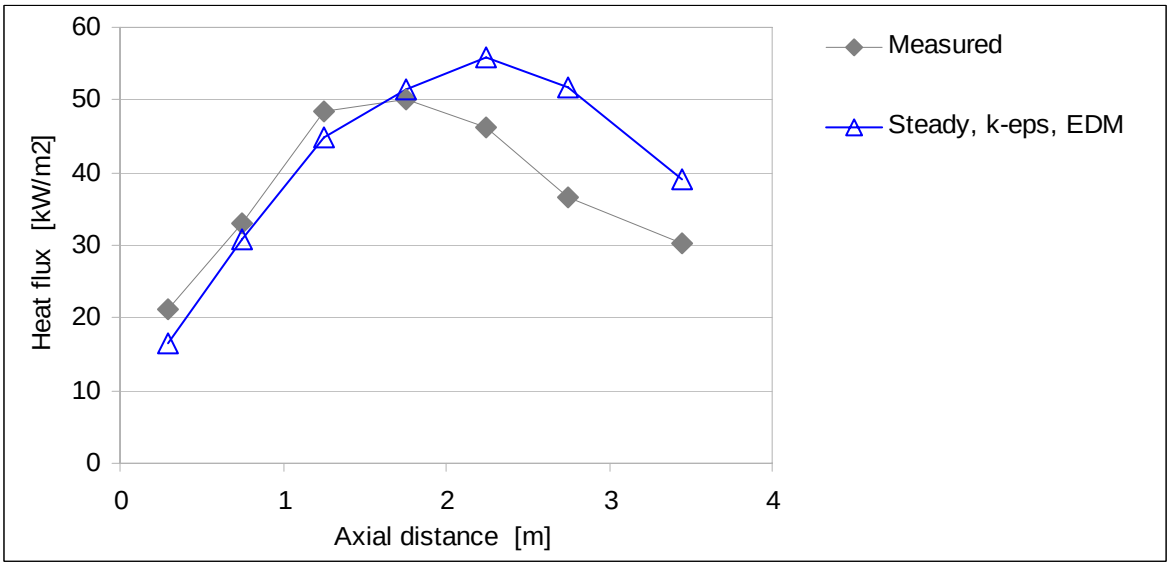

Figure 5 Measured and predicted heat fluxes in sections of the combustion chamber (burner is at the left side), eddy-dissipation model for the chemistry

Figure 5 shows the predicted wall heat fluxes using the simple EDM chemistry model, coupled with the two-equation k-ε model. In this case the prediction is qualitatively better than in the case of laminar flamelets (total heat transfer greater than measurement by 11%). The predicted flame length is however still substantially greater than in the measured profile.

Unsteady computations with the same model settings were attempted as well, but due to limited hardware resources it was not feasible to obtain a sufficiently large data set for time averaging. The results have a character of instantaneous profiles and they are hard to compare with the average values obtained in the measurements. The variability of heat fluxes in the unsteady computations was similar to that, reported above for not converging steady-state

formulations (on the order of 10 kW/m^2).

5 Conclusions

The reported work provides a rigorous validation of several mathematical models, relevant to practical CFD analysts, in an equally relevant combustion application, i.e. swirling diffusion flames. High-quality experimental data for model validation are provided that have been obtained in a new burner testing facility. Accuracy of the measured heat fluxes is also rigorously determined. Calculated heat flux profiles are not in a good agreement with the measurements, which has been expected, but the size of the deviations is quite great. This has implications for the predictions of various industry-relevant applications, as swirl-stabilised burners prevail in a large number of applications.

6 Acknowledgement

We gratefully acknowledge financial support of the Ministry of education, youth and sports of the Czech Republic within the framework of research plan No. MSM 0021630502 "Waste and Biomass Utilization focused on Environment Protection and Energy Generation".

7 References

[1] Hagiwara A., Bortz S. and Weber R. Theoretical and experimental studies on isothermal, expanding swirling flows with application to swirl burner design, Results of the NFA 2-1 investigation, IFRF document No. F 259/a/3, 1986

[2] Weber R., Dugué J. and Horsman H. The effect of combustion on Swirling and expanding flows, Results of the NFA 3-1 investigation, IFRF document No. F 59/a/6, 1989

[3] Weber R., Dugué J. Combustion accelerated swirling flows in high confinements. Progress in Energy and Combustion Science, Vol 17, pp. 349-367, 1992

[4] Weigand P., Meier W., Duan X.R., Stricker W., Aigner M. Investigations of swirl flames in a gas turbine model combustor I. Flow field, structures, temperature, and species distributions. Combustion and Flame, Vol. 114, pp. 205-224, 2006

[5] Weber R., Peters A.A.F., Breithaupt P.P. and Visser B.M. Mathematical modeling of swirling flames of pulverized coal: What can combustion engineers expect from modeling? Journal of Fluids Engineering, Vol 117, pp. 289-297, 1995

[6] Barreiros, A., Carvalho M.G., Costa M. and F.C. Lockwood. Prediction of the near burner region and measurements of NO_x and particulate emissions in heavy fuel oil spray flames. Combustion and Flame, Vol. 92, pp. 231-240, 1993

[7] German A.E. and Mahmud T. Modelling of non-premixed swirl burner flows using a Reynolds-stress turbulence closure. Fuel, Vol. 84, pp. 583-594, 2005

[8] Pfuderer D.G., Neuber A:A:, Fruchtel G., Hassel E.P. and Janicka J. Turbulence modulation in jet diffusion flames: Modeling and experiments. Combustion and Flame, Vol. 106, pp. 301-317, 1996

[9] Sadiki A., Maltsev A., Wegner B., Flemming F., Kempf A., Janicka J.. Unsteady methods (URANS and LES) for simulation of combustion systems. International Journal of Thermal Sciences, Vol. 45, pp. 760-773, 2006

[10] Fureby C., Grinstein F.F., Li G. and Gutmark E.J. An experimental and computational study of a multi-swirl gas turbine combustor. *Proceedings of the Combustion Institute*, Vol. 31(2), pp. 3107-3114, January 2007

[11] James S., Zhu J. and Anand M.S. Large eddy simulations of turbulent flames using the filtered density function model. *Proceedings of the Combustion Institute*, Vol. 31(2), pp. 1737-1745, January 2007

[12] Akselvoll K., Pierce C and Moin P. Large Eddy Simulations of Combustor Flows, Center for Turbulence Research [online]. [cit. 2007-05-07], URL: <http://www.stanford.edu/group/ctr/gallery.html>

[13] Frassoldati A., Frigerio S., Colombo E., Inzoli F. and Faravelli T. Determination ofNO x emissions from strong swirling confined flames with an integrated CFD-based procedure. Chemical Engineering Science, Vol. 60, pp. 2851-2869, 2005

[14] Kermes V., Skryja P. and Stehlík P., Up to date experimental facility for testing low-NOx burners, 10 th Conference on Process Integration, Modelling and Optimisation for Energy Saving and Pollution Reduction PRES 2007, Proceedings on CD ROM, Ischia Porto, Italy (June 24 – 27, 2007)

[15] Bělohradský P., Kermes V. and Stehlík P., Importance of experiments, empirical models and CFD for up to date burners design for process industries, 6th European Congress of Chemical Engineering ECCE 2007, Denmark (September 16 – 21, 2007)

[16] Bělohradský P., Kermes V., Stehlik P., Design and analysis of experiment for low-NOx burners design for process industries, 8th European Conference on Industrial Furnaces and Boilers – INFUB 2008, Vilamoura, Portugal (March 25 – 28, 2008)

[17] Industrial Platinum Resistance Thermometer Sensors. IEC Publication 60751, (1983).

[18] Rektorys, Karel. Přehled užité matematiky. 3. Prague: SNTL, 1973

[19] Phillips, James, R.. Online Curve Fitting and Surface Fitting Web Site. March 2008. 25 Mar 2008 <http://www.zunzun.com/>.

[20] BASH - Bourne Again SHell. Copyright © 2007 Free Software Foundation, Inc., 51 Franklin Street, Fifth Floor, Boston, MA 02110-1301, US. www.gnu.org/software/bash/

[21] Gnuplot. Copyright 1986 - 1993, 1998, 2004 Thomas Williams, Colin Kelley. www.gnuplot.info/

[22] FLUENT 6.3.26, 2006, *User`s Guide*, Fluent Inc., Lebanon, USA

[23] Idelčik, I.E.: *Handbook of hydraulic resistance*, druhé vydání, opravené a doplněné, Hemisphere Publishing Corporation, 1986.

[24] Launder, B.E, and Spalding D.B. “Lectures in mathematical models of turbulence”, Academic press, London/New York, 1972

[25] T.-H. Shih, W. W. Liou, A. Shabbir, Z. Yang, and J. Zhu. A New k-ε Eddy-Viscosity Model for High Reynolds Number Turbulent Flows - Model Development and Validation. *Computers and Fluids*, 24(3):227-238, 1995.

[26] B. E. Launder. Second-Moment Closure: Present... and Future? *International Journal of Heat and Fluid Flow*, 10(4):282-300, 1989.

[27] Magnussen, B.F. and Hjertager, B.H. ‘On mathematical models of turbulent combustion with special emphasis on soot formation and combustion’, *16th Symposium (International) on Combustion*, The Combustion Institute, 1985

[28] K. N. Bray and N. Peters. Laminar Flamelets in Turbulent Flames. In P. A. Libby and F. A. Williams, editors, *Turbulent Reacting Flows*, pages 63-114. Academic Press, 1994

Appendix B Experimental and numerical analysis of wall heat transfer in non- premixed gas combustor

This appendix contains author's paper published at 12th Conference on Process Integration, Modelling and Optimisation for Energy Saving and Pollution Reduction, PRES'09, held in Rome, 10 – 13 May 2009.

Bibliographic citation:

VONDÁL, J. and HÁJEK, J. Experimental and numerical analysis of wall heat transfer in non-premixed gas combustor. In: *Chemical Engineering Transactions*. 10 May 2009, no. 18, pp. 587–592. DOI 10.3303/CET0918095.

Experimental and numerical analysis of wall heat transfer in non-premixed gas combustor

Jiří Vondál, Jiří Hájek
Institute of process and environmental engineering, Brno University of Technology (UPEI VUT), Technická 2, 616 69 Brno, Czech Republic, tel. +420 541 142 374, vondal@upei.fme.vutbr.cz

Prediction of wall heat transfer in combustion chambers attracts attention of design engineers in process industry due its implications for the construction of combustors and boilers. Firstly, this paper addresses the reliability and accuracy of an experiment performed in a large-scale experimental combustion chamber equipped with staged-gas non-premixed 745 kW burner. The experiment serves as means to determine boundary conditions and validate predictions by computational fluid dynamics (CFD) software. Several accuracy issues of the used measuring gauges and instruments are discussed with focus on wall heat fluxes and stabilization of the measured data.
Second part of the paper presents CFD simulations of the combustor using Reynolds-averaged Navier-Stokes (RANS) models and validates them by the measured data. Overall model configuration, boundary conditions and key sub-models for turbulence and chemistry are summarised. Deviations of the predictions from the experiment are discussed and possible explanations are offered.

Introduction

Diffusion swirling gas combustion is a favoured solution in many industrial applications. Thus a lot of recent research work was focused on its analysis in several ways. Experiments seem to be an irreplaceable reliable method for verification of computational models. Most authors dealing with computational fluid dynamical (CFD) simulations of swirling diffusion flames use experimental data in their work for comparison e.g. German and Mahmud (2005) and Khelil et al. (2008). These papers however use detailed data describing the internal structure of the respective flames. Such a complete information is however rarely available.
Many experiments follow narrow particular objectives, e.g. to determine pollutant formation rates and species concentration fields, temperature field, or velocity field. The respective experiment set up is then suitable only for a specific objective, e.g. Kermes et al. (2008). The view adopted in this work is more practical and holistic as we are interested namely in the prediction of wall heat fluxes.
Numerical simulations presented in this paper use Reynolds-Averaged Navier-Stokes (RANS) equations. This approach is preferred in practical applications due its reasonable CPU requirements, unlike more advanced approaches as Large Eddy Simulations or Direct Numerical Simulations. However, numerous works show that the prediction of swirling diffusion gas flames using RANS equations is a difficult task, see e.g. Warnatz et al. (1996) or Weber et al. (1995). Therefore the correct use of RANS

models for practical swirling diffusion flames in a large-scale furnace with experimental validation is the main objective of the present work.

Experimental set-up

The measurements have been performed at a burner testing facility of the UPEI VUT Institute, which has been described in detail by Bělohradský et al. (2008), Kermes et al. (2008) and Kermes et al. (2007). The combustion chamber has 1 m internal diameter and is 4 m long, water cooled. The burner used in the experiments is a gas-staged 745 kW low-NO_x type (see Fig. 1). The shell of the chamber is divided into seven sections, enabling evaluation and monitoring of heat flux in each section. The length of the first six sections is 0.5 m and the last one is 1 m long.

Previous research in the facility was focused on parametric studies of the effect of burner parameters on pollutant formation as documented by Kermes et al. (2007). In the present work, the objective is heat transfer analysis, which required adjustments of the measuring procedures. The main difference is in the time scope because pollutants formation analysis is much less time consuming, since stabilization of the flue gas species composition is mainly related to the flame temperature (outlet flue gas temperature). Flue gas temperature has been a sufficient indicator of a steady state condition for the NO_x formation analysis, whereas it was observed that heat fluxes need much longer time for stabilization (see Fig. 2) and thus the outlet temperature could not be used as an indicator of stabilisation any more.

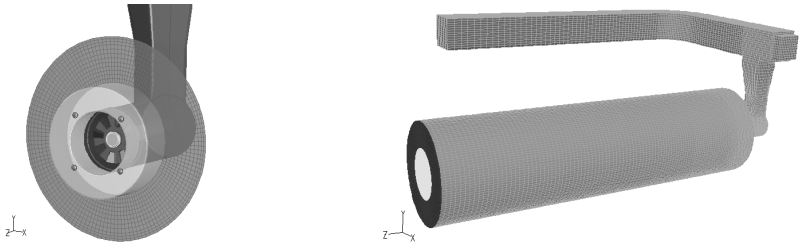

Figure 1: a) Gas-stage burner *b) Combustor*

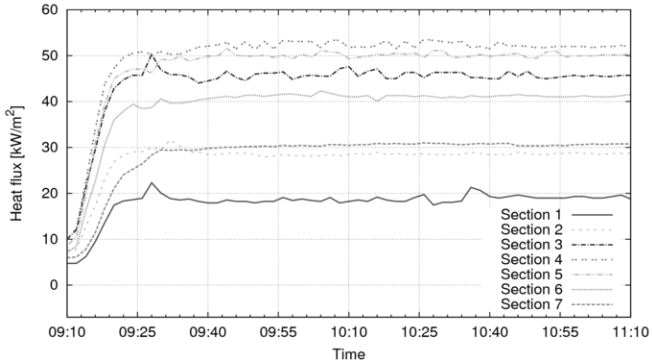

Figure 2: Heat fluxes during the long-term experiment

It was necessary to perform experiment with a stabilizing period long enough to achieve steady state condition in terms of the wall heat fluxes. Thus stable heat fluxes in each individual section had to be achieved in order to obtain reliable data. Fig. 2 shows start-up and stabilization process of the experiment.

Error analysis

The main focus of this paper is on the heat fluxes. Thus error analysis concentrates on three related quantities, namely inlet cooling water temperature, outlet cooling water temperature and cooling water flowrate.Calculations are based on the methodology of propagation of uncertainty according to Braembussche (2001). For the heat flux calculation is used the following simple equation:

$$Q = \rho V c_p \Delta t / A \tag{1}$$

where Q is heat flux rate [kW/m^2],
ρ is density [kg/m^3],
V is water flow rate [m^3/h],
c_p is specific heat [kJ/kg],
Δt is temperature difference [K] and
A is area of the section [m^2].

Therefore two basic equations for error propagation have to be used:

$$\Delta t = t_{out} - t_{in} \quad : \qquad \sigma_{\Delta t}^2 = a^2 \sigma_{t_{in}}^2 + b^2 \sigma_{t_{out}}^2 \tag{2}$$

$$Q = \rho V c_p \Delta t / A \quad : \qquad \left(\frac{\sigma_Q}{Q}\right)^2 = \left(\frac{\sigma_V}{V}\right)^2 + \left(\frac{\sigma_{\Delta t}}{\Delta t}\right)^2 \tag{3}$$

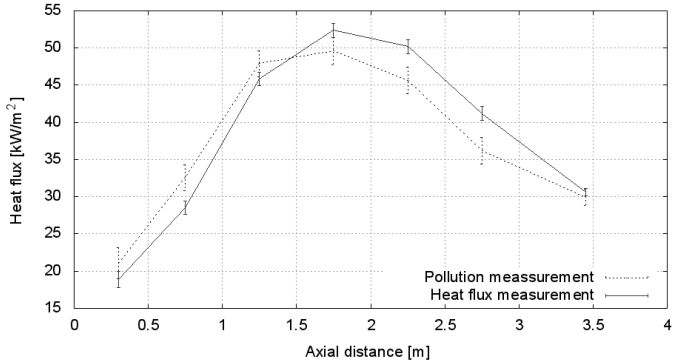

Figure 3: Comparison of two measurements with different objectives

Table 1 and Fig. 3 show the results of error analysis and also comparison of measurements. Objective of the first was pollutant emission analysis with a demand only on stabilisation of outlet flue gas temperature and emission levels and the other

focuses on stabilised heat fluxes. Finally an obvious and clearly observable, but very important fact needs to be stressed, namely that the uncertainty discussed above does not include deviations due to poorly stabilised wall heat loads.

Tab. 1: Heat fluxes from the two experiments focused on emission characteristics vs. wall heat loads

	Objective: Pollution measurement			Objective: Heat Fluxes		
	Q	Absolute Error	Relative Error	Q	Absolute Error	Relative Error
	kW/m^2	kW/m^2	%	kW/m^2	kW/m^2	%
Section 1	21.05	2.71	12.87	18.88	1.37	7.23
Section 2	32.59	1.92	5.88	28.53	1.11	3.88
Section 3	47.89	1.98	4.13	45.84	1.06	2.32
Section 4	49.59	2.09	4.21	52.39	1.08	2.05
Section 5	45.61	2.02	4.43	50.20	1.07	2.13
Section 6	36.17	1.99	5.51	41.19	1.11	2.70
Section 7	29.92	1.21	4.06	30.64	0.61	1.98

Computational set-up

The aim of the numerical study was the prediction of steady-state heat fluxes through the water-cooled walls of the combustion chamber. Since the case involves swirling non-premixed combustion, the problem is at the utmost limits of current state-of the art RANS models as discussed in the introduction and a proper validation is thus required.
For numerical analysis the meshed model consisted mostly of hexahedral cells (97 %). The total number of computational cells was 1,156,788. Simulation-relevant details were modelled including air supply ductwork, swirl generator and fuel jets (see Fig. 1a,b). The jet diameters were adjusted to compensate nozzle area reduction in the meshed model, as compared to the real cross-sectional area.
Four different types of boundary conditions have been used. Namely mass flow inlets (gas and air), pressure outlet, Dirichlet condition for walls of the segmental combustion chamber (constant cooling water temperature) and all other walls were approximated as adiabatic. The boundary condition used in the present simulations for the water-cooled segmental wall is slightly idealised. The assumption was made that cooling is highly efficient and temperature boundary layer can be neglected. Thus logarithmic average of the inlet and outlet temperature of each section was deemed adequate as an approximation of the wall temperature.
All computations performed were using RANS equations coupled with Eddy Dissipation Model (EDM) (Magnussen and Hjertager, 1977). For RANS coupled with Flamelet model see Hájek et al. (2008). Three different turbulence models were tested. The most computationally costly was the Reynolds Stress Model (RSM) (Fluent, 2006), but it displayed high unsteadiness when used with second order discretization scheme. Other two turbulence models were two-equation models: SST k-ω (Menter, 1994) and realizable k-ε (Shih et al., 1995). All models were used with the third order

discretization scheme QUICK (Leonard and Mokhtari, 1990) for momentum and density equations and Pressure Staggering Option (PRESTO!) (Patankar, 1980) for the pressure (continuity) equation.

Results and discussion

As can be seen in Fig. 4, the results show that all simulations overestimated the wall heat fluxes. RSM and k-ε overpredict the total heat flux by 10 %. These two models give similar results, acceptably agreeing with measured values in the first three sections, but strongly overestimating heat fluxes in the last three sections. This leads to a conclusion that EDM when used with k-ε or RSM models is unable to predict length of the flame accurately. This is in agreement with Warnatz et al. (1996) who show that EDM highly overpredicts the temperature in the end of the flame.
However, the k-ω model when coupled with EDM predicts qualitatively reasonably well the heat flux profile over the whole length of the chamber and fails only in the identification of absolute values. The overall difference of extracted heat is again 10 %.

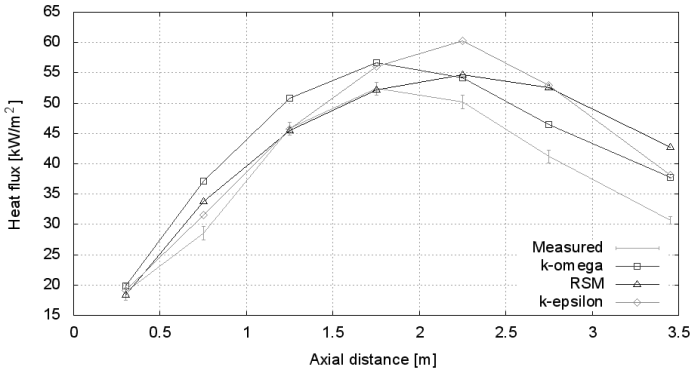

Figure 4: Turbulence model comparison

Conclusion

The reported work presents a rigorous method of identification of boundary condition values for numerical analysis. It points out the importance of correct experimental set-up and discusses achieved accuracy for the reported experiments. Error analysis is performed to increase reliability and credibility of the measurements.
The results of the CFD simulations are not completely satisfactory, but the k-ω turbulence model coupled with simple eddy-dissipation chemistry model predicts qualitatively well the overall profile of wall heat fluxes. This combination of models performs better than eddy-dissipation chemistry coupled with the RSM and the k-ε turbulence models.

Acknowledgement

The authors gratefully acknowledge financial support of the Ministry of Education, Youth and Sports of the Czech Republic within the framework of project No. 2B08048

″Waste as raw material and energy source″ and research plan No. MSM 0021630502 "Waste and Biomass Utilization focused on Environment Protection and Energy Generation".

References

Bělohradský, P., V. Kermes, and P. Stehlík, 2008, Design and analysis of experiment for low-NOx burners design for process industries, in 8th European Conference on Industrial Furnaces and Boilers, Vilamouria, Portugal.

Braembussche, V. D. (Ed.), 2001, Measurement Techniques in Fluid Dynamics: An Introduction, von Karman Institute for Fluid Dynamics, Rhode Saint Genése.

Fluent, 2006, FLUENT 6.3.26, User`s Guide,

German, A., and T. Mahmud, 2005, Modelling of non-premixed swirl burner flows using a Reynolds-stress turbulence closure, Fuel, 84(5), 583-594.

Hájek, J., J. Vondál, M. Šarlej, and P. Stehlík, 2008, Numerical and experimental analysis of turbulent swirling diffusion gas flames, in 11th Conference on Process Integration, Modelling and Optimisation for Energy Saving and Pollution Reduction, Prague, Czech Republic.

Kermes, Vít et al. (2008): „Testing of gas and liquid fuel burners for power and process industries“. V: *Energy*. 33 (10), s. 1551-1561.

Kermes, Vít; Skryja, Pavel; Stehlík, Petr (2007): „Up to date experimental facility for testing low-NOx burners“. V: *10th Conference on Process Integration, Modelling and Optimisation for Energy Saving and Pollution Reduction PRES 2007*. Ischia Porto, Italy s. 1-6.

Khelil, A., H. Naji, L. Loukarfi, and G. Mompean, 2008, Prediction of a high swirled natural gas diffusion flame using a PDF model, Fuel, 88(2), 374-381.

Leonard, B. P., and S. Mokhtari, 1990, ULTRA-SHARP nonoscillatory convection schemes for high-speed steady multidimensional flow, NASA; Institute for Computational Mechanics in Propulsion, Lewis Research Center, Case Western Reserve University.[online] Available from: http://purl.access.gpo.gov/GPO/LPS67518

Magnussen, B., and B. Hjertager, 1977, On mathematical modeling of turbulent combustion with special emphasis on soot formation and combustion, Symposium (International) on Combustion, 16(1), 719-729.

Menter, F. R., 1994, Two-equation eddy-viscosity turbulence models for engineering applications, AIAA Journal, 32, 1598-1605.

Patankar, S. V., 1980, Numerical Heat Transfer and Fluid Flow, Taylor & Francis, Great Britain.

Shih, T., W. W. Liou, A. Shabbir, Z. Yang, and J. Zhu, 1995, A new k-[epsilon] eddy viscosity model for high reynolds number turbulent flows, Computers & Fluids, 24(3), 227-238.

Warnatz, J., R. W. Dibble, and U. Maas, 1996, Combustion: Physical and Chemical Fundamentals, Modelling and Simulation, Experiments, Pollutant Formation, Springer, Berlin.

Weber, R., A. Peters, P. Breithaupt, and B. Visser, 1995, Mathematical-Modeling of Swirling Flames of Pulverized Coal - What Can Combustion Engineers Expect from Modeling, Journal of Fluids Engineering-Transactions of the Asme, 117(2), 289-297.

Appendix C Boundary condition evaluation and stability issues in swirling flame gas combustion

This appendix contains author's paper published at 1st International Conference on Computational Methods for Thermal Problems, held in Naples, Italy, 10 September 2009.

Bibliographic citation:

VONDÁL, J. and HÁJEK, J. Boundary Condition Evaluation and Stability Issues in Swirling Flame Gas Combustion. In: *ThermaComp2009* [online]. Naples, Italy: 10 September 2009. pp. 314–317. Available from:

http://www.thermacomp.com/uploads/ThermaComp2009_Proceedings_web.pdf

First International Conference on Computational Methods for Thermal Problems
ThermaComp2009, September 8-10, 2009, Napoli, Italy
N.Massarotti and P.Nithiarasu (Eds.)

BOUNDARY CONDITION EVALUATION AND STABILITY ISSUES IN SWIRLING FLAME GAS COMBUSTION

Jiří Vondál

Institute of process and environmental engineering, Brno University of Technology, Technická 2, 616 69 Brno, Czech Republic, vondal@upei.fme.vutbr.cz

Jiří Hájek

Institute of process and environmental engineering, Brno University of Technology, Technická 2, 616 69 Brno, Czech Republic, hajek@fme.vutbr.cz

ABSTRACT

Prediction of wall heat fluxes in combustion chambers attracts attention of design engineers in process industry due to its implications for the construction of combustors, boilers and similar devices. Furthermore, reliable experimental evaluation of the heat loads in large-scale experiment is rare. This work deals with stability issues observed in simulation of swirling diffusion gas flames and compares them to the real-world experiment and its instability. Steady and unsteady simulations using Reynolds-averaged Navier-Stokes (RANS) equations are discussed. The experimental facility has a sectional water cooled combustion chamber equipped with a staged-gas 745 kW low-NO_x type burner with axial-type swirl generator.

Key Words: *Combustion, CFD, Burner, Swirl, Heat Flux, Stability.*

1. INTRODUCTION

Swirl-stabilised flames are very popular, especially in the so-called power burners [1] that are widely used in power and process industries. However, it has been recognised for long time that the prediction of swirling diffusion flames using moment turbulence closures is extremely problematic [2, 3], in spite of partial successes [4]. Recent progress achieved using large-eddy simulations coupled with advanced chemistry models [5, 6] is on one hand very promising but on the other hand it is still far from being applicable to industrial problems due to excessive computational requirements, tractable only using supercomputing facilities.

Industry primarily requires predictions of wall heat fluxes (typically for membrane walls or tubes). In spite of that, combustion modelling research almost exclusively focuses on the details of flame core structure and wall heat loads are typically disregarded. The present work thus focuses on validation of computationally manageable Reynolds-Averaged Navier-Stokes (RANS) models by accurately measured local wall heat fluxes. The experiments were performed at a new experimental facility described in [1, 7]. The paper extends previous work reported in [8] which dealt with error analysis of the experimental data and reported several heat flux predictions. The target here is to identify some of the sources of deviation from experimental results.

2. EXPERIMENTAL FACILITY

Combustion chamber of the testing facility was designed for maximum firing capacity of 2 MW and consists of 7 water-cooled sections enabling separate heat flux monitoring. The wall material is steel covered with high-temperature black paint for increased emissivity. Industrial-type low-NO_x, natural gas burner with staged gas supply (8 primary and 8 secondary nozzles) and an axial-type swirl generator were employed for the experiment. The firing rate was adjusted to 745 kW.

3. IDENTIFICATION OF BOUNDARY CONDITIONS

Boundary conditions were an all-important factor in model set-up. Most conditions were easy to evaluate thanks to the measuring instrumentation of the facility – e.g. natural gas flow rate and temperature, air flow rate and temperature, etc. Besides these, some boundary conditions were much harder to evaluate accurately and these were deemed to be responsible for a significant part of the observed deviations from measurements [8]. Wall temperature on the water side was one these hard-to-determine parameters.

Heat transfer through the cooled walls depends on one hand on hot-side properties (radiation contributes by about 90%) and on the other hand it is influenced by heat transfer coefficient and surface temperature on the water-side. Local boiling was possible only in places with low water velocity (considering inlet water temperature was 21°C and outlet about 30°C), but water flow in each section was directed by a helical fin for minimization of such dead zones.

Computational model of a single cooling section has been created to study the heat transfer on the water side in detail, assuming no boiling and a uniform heat flux from the flame side. Contours of calculated water-side surface temperature are shown in Fig. 1. The highest temperatures were however incorrect due to the missing boiling model. Therefore temperatures above the boiling point (124.2 °C at 236.4 kPa) [9] served only to identify locations of local boiling. Real values lay in between the boiling point and the displayed value due to increased heat transfer coefficient caused by boiling [10]. Area weighted average from the calculated values over the heat-exchanging surface was 96 °C. Future work is necessary to adjust this value while taking the boiling into account. Currently all simulations presented in this work used an estimated value of 80 °C as the wall boundary condition.

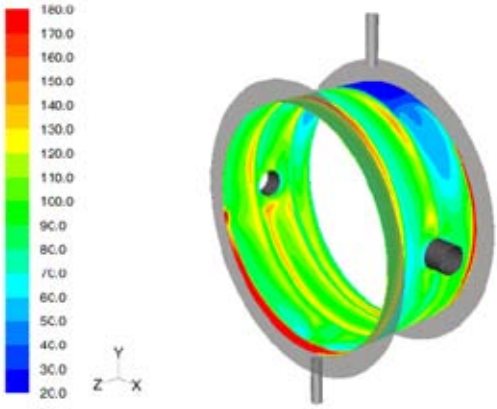

FIGURE 1. Contours of surface temperature [°C]

4. COMPUTATIONAL SET-UP

Modelling of the swirling diffusion flame was performed using several turbulence models and a simple fast chemistry model with one global reaction as implemented in commercial code FLUENT 6.3.26 [11]. Specifically the baseline model included turbulence model SST k-ω, discrete-ordinates radiation model with weighted-sum-of-gray-gases cell-based model for the absorption coefficient, one-step reaction mechanism and pressure-velocity coupling using so-called pressure-staggering option. During the computation, several stability issues were observed that are discussed in the next section. Standard computational procedures were followed, namely start up without radiation and switching to higher-order discretization scheme (QUICK) after the solution almost converged. This was performed firstly for the density and after several iterations also for the velocity. Increasing the order of discretization for velocity caused severe instability in the calculated heat fluxes (see Fig.2) but was crucial for accuracy.

5. STABILITY PHENOMENA

One of the biggest issues of numerical computations is convergence and stability. In the present case of combustion calculation we focus on the stabilization of heat fluxes. Fig. 2 shows convergence history of heat flux for all 7 sections of the combustion chamber. One can see that after application of the QUICK discretization scheme in the momentum equations (at 9000 iterations), the calculation became strongly unstable with the amplitude of heat flux fluctuations up to 6 kW/m^2. This problem prevailed even after modification of relaxation factors and with other higher-order schemes.

The primary reason for the observed instability was found in the physics of the flow. [12] explains that in swirl combustion several types of fluctuations and instabilities, e.g. flame wobble and precessing vortex core are present. Measured instabilities in the heat fluxes (naturally smoothed out by the averaging and damping effect of the steel walls and cooling water) are also displayed in Fig. 3. It is important to note that the RANS modelling approach cannot properly account for these fluctuations but it was not discarded based on the reasoning presented in the Introduction.

Fig. 4 displays instantaneous results from iterations 8900, 13000, 16000 and 19000 as snapshots from the iteration history shown in Fig. 2. The changes in reported heat fluxes are well visible.

A more reliable value (than instantaneous) of the heat fluxes was obtained through simple averaging of the results over certain range of iterations. Rate of fluctuation was taken into account via non-symmetric error bars defined as follows:

$$q' = q - \bar{q} \quad , \quad \text{for } q' > 0: \ \sigma_{up} = \frac{1}{n}\sum_{0}^{n} q' \quad , \quad \text{for } q' < 0: \ \sigma_{down} = \frac{1}{n}\sum_{0}^{n} q' \tag{1}$$

where q is instantaneous heat flux, $\bar{q}$ is the average, q' is fluctuation and σ is mean deviation.

A comparison of measured and average heat fluxes from the histories shown in Fig. 2 (averaged from 9 500 up to 19 000 iterations) is shown in Fig. 5, including non-symmetric error bars defined in

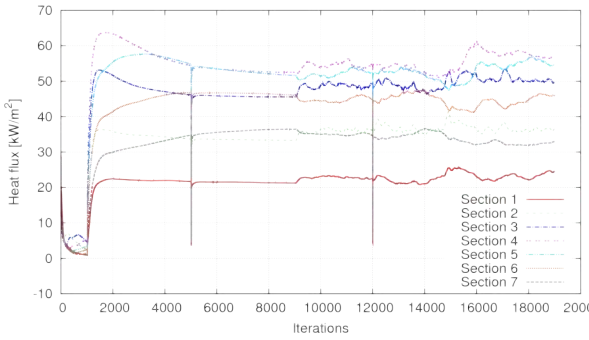

FIGURE 2. Convergence history of heat fluxes

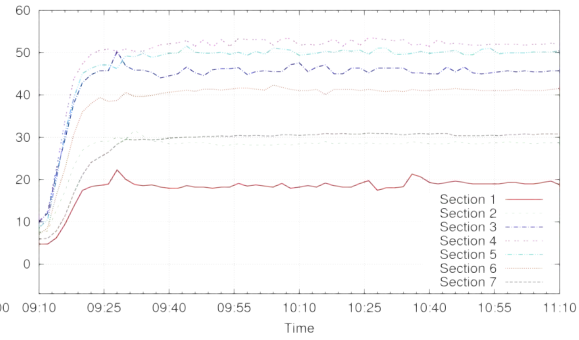

FIGURE 3. Heat flux stabilization in experiment

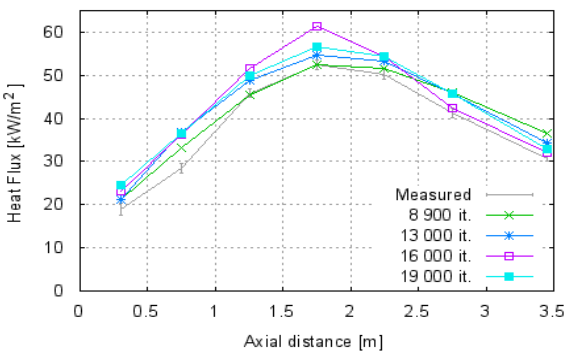

FIGURE 4. Comparison of instantaneous heat fluxes at different iterations (SST *k-ω*)

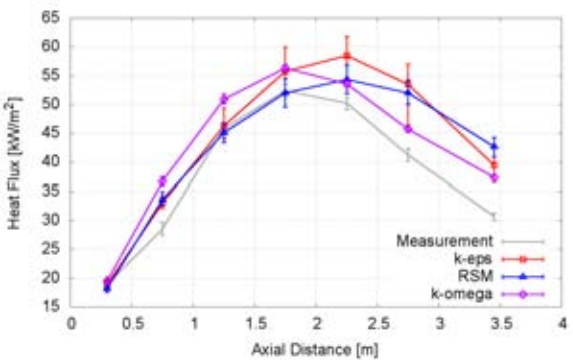

FIGURE 5. Heat fluxes averaged over 9 500 iterations

equation (1). The figure includes also averages obtained using two other RANS models, namely realizable k-ε model and a second-order Reynolds-stress model.

6. CONCLUSION

Measured data from a large-scale industrial-type swirl combustor were used to validate simulations. Thermal boundary condition at the cooled walls was analyzed in detail. The total deviation of the best computed result (SST k-ω) after averaging was 12.6 %, which is considered acceptable thanks to the complexity of the problem. Stability issues in calculated and measured heat transfer were studied and averaging method was described.

REFERENCES

[1] V. Kermes, P. Bělohradský, J. Oral, and P. Stehlík, "Testing of gas and liquid fuel burners for power and process industries," *Energy*, vol. 33, 2008, pp. 1551-1561.

[2] A. Khelil, H. Naji, L. Loukarfi, and G. Mompean, "Prediction of a high swirled natural gas diffusion flame using a PDF model," *Fuel*, vol. 88, 2008, pp. 374-381.

[3] A.E. German, T. Mahmud, "Modelling of non-premixed swirl burner flows using a Reynolds-stress turbulence closure", *Fuel*, vol. 84, 2005, pp. 583-594

[4] A. Frassoldati, S. Frigerio, E. Colombo, F. Inzoli, T. Farevelli, "Determination of NOx emissions from strong swirling confined flames with an integrated CFD-based procedure", *Chemical Engineering Science*, vol. 60, 2005, pp. 2851-2869

[5] C. Fureby, F.F. Grinstein, G. Li, E.J. Gutmark, "An experimental and computational study of a multi-swirl gas turbine combustor", *Proceedings of the Combustion Institute*, vol. 31, 2007, pp. 3107-3114

[6] S. James, J. Zhu, M.S. Anand, "Large eddy simulations of turbulent flames using the filtered density function model", *Proceedings of the Combustion Institute*, vol. 31, 2007, pp. 1737-1745

[7] V. Kermes, P. Skryja, and P. Stehlík, "Up to date experimental facility for testing low-NOx burners," *10th Conference on Process Integration, Modelling and Optimisation for Energy Saving and Pollution Reduction PRES 2007*, Ischia Porto, Italy: 2007, pp. 1-6.

[8] J. Vondál and J. Hájek, "Experimental and numerical analysis of wall heat transfer in non-premixed gas combustor", *Chemical Engineering Transactions*, vol 18, 2009, pp. 587-592

[9] W. Wagner, J. Cooper, A. Dittmann, J. Kijima, H. Kretzschmar, A. Kruse, R. Mareš, K. Oguchi, H. Sato, I. Stöcker, O. Šifner, Y. Takaishi, I. Tanishita, and J. Trübenbach, "The IAPWS Industrial Formulation 1997 for the Thermodynamic Properties of Water and Steam," *Journal of Engineering for Gas Turbines and Power*, vol. 122, 2000, pp. 184, 150.

[10] F.P. Incropera, *Fundamentals of Heat and Mass Transfer*, New York: John Wiley & Sons, 2007.

[11] Fluent, "FLUENT 6.3.26, User`s Guide," 2006.

[12] N. Syred, "A review of oscillation mechanisms and the role of the precessing vortex core (PVC) in swirl combustion systems," *Progress in Energy and Combustion Science*, vol. 32, 2006, pp. 93-161.

Appendix D Experimental data of the local wall heat flux for combustion codes validation in non-premixed swirling gas flames

This appendix contains author's paper published at ASME-ATI-UIT 2010 Conference on Thermal and Environmental Issues in Energy Systems, held in Sorrento, Italy, 16 – 19 May 2010.

Bibliographic citation:

VONDÁL, J. and HÁJEK, J. Experimental data of the local wall heat flux for combustion codes validation in non-premixed swirling gas flames. In: *Proceedings of the ASME-ATI-UIT 2010 Conference on Thermal and Environmental Issues in Energy Systems*. Sorrento, Italy: 16 May 2010. pp. 931–936.

ASME-ATI-UIT 2010 Conference on Thermal and Environmental Issues in Energy Systems
16 – 19 May, 2010, Sorrento, Italy

EXPERIMENTAL DATA OF THE LOCAL WALL HEAT FLUX FOR COMBUSTION CODES VALIDATION IN NON-PREMIXED SWIRLING GAS FLAMES

Jiří Vondál*, Jiří Hájek*

*Institute of process and environmental engineering, Brno University of Technology, Technická 2, 616 69 Brno, Czech Republic

ABSTRACT

The main purpose of this work is the measurement of local heat fluxes from confined non-premixed swirling gas flame absorbed into water cooled walls. Presented are two thermal duties 745 kW and 1120 kW fired in a large-scale combustion chamber. Measured data are intended for use as a benchmark. Its purpose is to validate computational fluid dynamics (CFD) codes against reliable and transparent measurements. The uniqueness of reported measurements is in the scale of the experimental facility and its ability to provide accurate data at above thermal duties. The data uncertainty is also discussed. The experimental facility is described including complete geometry of the burner and combustion chamber to enable use of the measured data by the other researchers. The entire geometry is made available in the STEP format.

INTRODUCTION

Study of flame structure is the subject of long-lasting interest of the combustion modeling community. Detailed in-flame measurements of temperature, velocity and species concentrations have served for the validation of all existing combustion models. Unlike the in-flame properties, wall heat fluxes have been used for model validation only rarely. Heat flux measurements reported in the literature are either spot measurements or global heat transfer rates. Spot measurements however mostly provide just the thermal irradiation flux, not the actual radiative or total heat transfer rate (e.g. in the study of industrial furnaces and boilers [1-3]). Likewise, global heat transfer rates calculated from the hot water (steam) production are insufficient for the validation of detailed predictions.

In contrast to that, the interest of engineering community focuses primarily on local heat fluxes and pollutant emissions. Emissions are studied namely to ensure compliance with legislative regulations (e.g. [4]), while heat fluxes are required to check proper furnace design and to ensure safe operation. It is thus apparent that the correct prediction of local heat fluxes on heat transfer surfaces is one of the most important aspects of practical combustion simulations that should receive adequate attention.

Swirling combustion

Our understanding of phenomena that are at work in swirling diffusion flames is quite advanced, as shows recent extensive review of dynamic instabilities in swirl combustion systems [5]. However, the computational fluid dynamics (CFD) modeling of swirling diffusion flames registered little success until the advances in large eddy simulations (LES) in the last decade. This was mainly due to the deficiencies of available first-order and second-order turbulence closures in characterizing the complex three-dimensional swirling and reacting flow structure [6-10].

Swirl-stabilized non-premixed flames are frequently used in industrial burners, but they present one of the most difficult problems to predict computationally. The effects affecting predictions are still under investigation.

Authors of recent works were focused on inflame detailed study e.g. turbulence and its relation to chemical kinetics [11], radiation and radiant properties of the species and precessing vortex core phenomena.

Only with the advances in large eddy simulations (LES), successful predictions of in-flame properties were reported [12-14]. The LES approaches are unfortunately still too computationally expensive for the simulation of large-scale fired heaters due to their huge dimensions (on the order of 10 m) and the need to resolve fine features like gas nozzles with diameters on the order of 1 mm. The only viable alternative for practical predictions are therefore models based on first order or second order turbulence closures.

Wall heat fluxes

The local heat loads to tubes (in fired heaters), to membrane walls (in boilers), or combustion chamber walls (cooled as well as refractory-lined), are key parameters required by designers from CFD combustion analysts. Wall heat fluxes and wall temperatures are required to be uniform and their peaks to lay below certain hard limit values given by material strength considerations. Measurement of local heat loads in industrial conditions is possible only using

special heat flux probes that cannot provide reliable detailed data covering the whole heat transfer area, but only a limited number of discrete points. An overview of available instrumentation is provided e.g. in [15] and [16]. The best way to measure local heat fluxes clearly would be different – to measure directly the heat absorbed by walls on the heated medium side (e.g. steam or water). Such segmental design is naturally impracticable in industrial furnaces, but actually quite common in laboratory reactors (except for the missing heat-transfer related instrumentation), see e.g. [10] and [17].

Thanks to the fact that fouling and slagging are absent in gas combustion, the heat flux data measured by probes are more reliable than in e.g. pulverized fuel combustors. Even though, the accuracy of available measurement methods is on the order of several percent. For the measurements of thermal irradiation flux are often used ellipsoidal radiometers (accuracy ± 5 %) and water-cooled circular foil heat flux radiometers (accuracy ± 2 %) [3]. The latter ± 2 % accuracy is about the best we can achieve with heat flux metering probes. As reported in [3], differences of values measured by these two methods may however reach up to 12 %, thus decreasing the credibility of point heat flux measurements.

Experiments

Experimental investigation is irreplaceable part of the research process in computational fluid dynamics. The computer codes and simulations are validated against well described experiments. Numerous detailed in-flame measured data are available for a range of swirl burners. In fact, a number of research groups have performed coordinated efforts to characterize several swirling diffusion gas flames by various experimental methods. One of the most notable projects was the TECFLAM cooperation performed by five institutes in Germany, which yielded numerous publications (e.g. [6,7,18,19]) and a validation database (presently available upon request). The burner used in these works had a thermal duty of 150 kW and the swirl number at the burner orifice was 0.9. Other sets of data were collected for gas turbine combustors, e.g. [12,20-22] on flames up to 35 kW (in the referenced works). Another remarkable project is the Sydney swirl burner experimental database [23,24] which represents the unconfined turbulent swirl gas combustion.

Many other burner geometries were investigated worldwide, covering various fuel injection systems and swirl generation systems, see e.g. [25-29]. The thermal duties of burners in all these studies ranged from several kilowatts up to about hundred kilowatts, i.e. they were all laboratory-scale experiments. It is also important to note that without exception all these studies focused on detailed in-flame measurements and paid little or no attention to the heat transfer to combustion chamber walls (in cases with non-adiabatic walls).

EXPERIMENTAL FACILITY

Geometry

The construction of the semi-industrial experimental facility for burners up to 2 MW was aimed at providing variable length of combustion chamber and accurate heat flux and emission measurements. The main feature distinguishing the test facility at Brno University of Technology from others is the ability to measure local heat transfer rates to the cooled walls, which is enabled by segmental design of the combustion chamber. There are up to seven water cooled segments of the combustion chamber, see Fig. 1 and 2. All internal segments have the same flame-facing area of 1.57 m^2, whereas the first and seventh section have 1.26 m^2 and 3.14 m^2, respectively. The last three segments are removable which allows adjustment of the combustion chamber length.

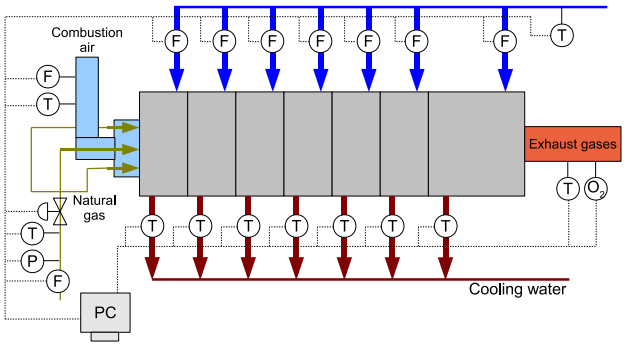

Figure 1: Combustion chamber and main parts of the data acquition system

Figure 2: Industrial-scale combustor

Inlet and outlet temperature and water flow rate data are collected at every section by an automatic data acquisition system and local heat flux is calculated. The total firing rate of the burner is calculated from the gas flow rate measured by rotary flow meter and adjusted by pressure and temperature readings to normal conditions. The excess air ratio is calculated from oxygen concentration in the exhaust gases.

The burner was a low-NOx design with staged gas supply (Fig. 3) and axial swirl generator, fired by natural gas. Swirl generator with diameter 240 mm consisting of 8 vanes acts as a flame holder. Gas inlet consists of twelve primary nozzles and eight secondary nozzles. Eight of the primary nozzles have diameter 2.6 mm and the other four 3.0 mm. All the primary nozzles are drilled in a nozzle head located on the burner axis.

Secondary gas injection is performed by four additional nozzle heads located in regular intervals around annular air channel which surrounds the primary nozzle head. Each of the four secondary nozzle heads has two nozzles with a diameter of 3.3 mm.

Flame ignition and stabilization is performed by a small (25 kW) premixed natural-draft pilot burner. Its thermal duty was included in the total thermal duty.

The burner performance was set at 745 kW (Case 1) and 1120 kW (Case 2) with excess air ratio 1.1. Several measurements previously performed at the same testing facility, although with different objectives than in this work, were described in [30-32].

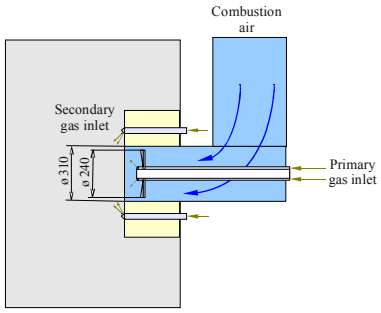

Figure 3: Swirl burner with two gas stages

MEASURED DATA

Measured data consists of a set of records from all the sensors at the facility. Data is automatically collected during the entire experiment. Four sets of data were collected. There were two performance levels 745 kW (Case 1) and 1120 kW (Case 2). Fig. 4 shows a record of the transient heat fluxes from Measurement 1 of the Case 1. The experiment consists of four distinct stages: start-up, warm-up, stabilization and stable state. The measurement procedure was kept the same for all runs. At the beginning the flame was ignited and brought to the desired power, then was the chamber heated up with air equivalence ratio higher than the target value due to safety reasons. In the stabilization period air flow rate was adjusted to the proper value and wall heat fluxes were monitored until reaching stable conditions. The last part was run at the desired conditions and data collected during this period are those, presented in this paper. The data displayed in the tables and graphs are averaged values over 5 minutes (Case 1) and 15 minutes (Case 2). Averaging was applied to remove random fluctuations in the measured values.

Each of the two regimes was measured twice to test them for repeatability. Operating conditions during stabilization time are shown in Tables 1 and 2. It can be seen that reproducibility is good even though conditions were slightly changed e.g. air temperature 19.3 °C vs 4.3 °C in Case 1

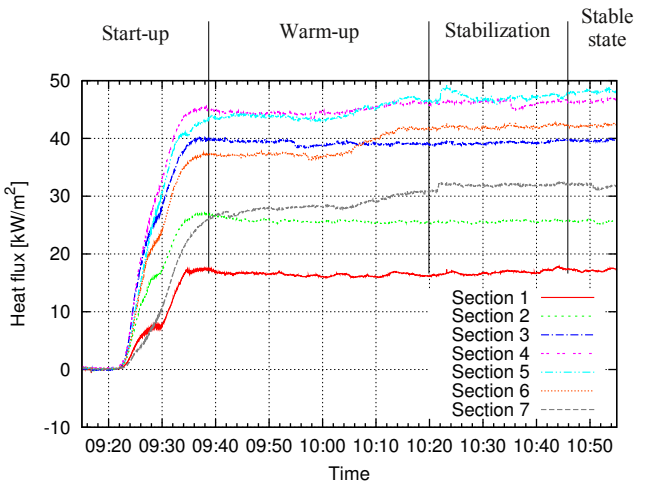

Figure 4: Section wall heat fluxes for Case 1

The deviation in the total extracted heat flux into the water was 0.16 % for the Case 1 and 0.88 % in the Case 2. The maximum load difference was in 3rd section 2.7 % for the Case 2 and 2.4 % in 5th section for the Case 1. The total extracted heat from flame (Q_{total}) was evaluated from natural gas flow rate, temperature and pressure. Equivalent methane mass flow (m_{CH4}) is calculated from natural gas flow rate using the ratio of heating values of natural gas and methane. Air flow was calculated based on oxygen concentration in exhaust gases and the fuel flow rate.

Table 1: Operation conditions of the Case 1

		Measurement 1	Error [%]	Measurement 2	Error [%]	Average
Q_{total}	[kW]	746	1.62	748	2.7	747
m_{CH4}	[kg/s]	0.015	1.62	0.015	2.7	0.015
m_{air}	[kg/s]	0.289	9.8	0.290	10.1	0.290
T_{fuel}	[°C]	20.1	1.5	12.5	2.6	16.3
T_{air}	[°C]	19.2	1.5	4.3	1.9	11.7
Q_{water}	[kW]	438	4.3	438	5.27	438
RH	[%]	42		90		66

Table 2: Operation conditions of the Case 2

		Measurement 1	Error estimate [%]	Measurement 2	Error estimate [%]	Average
Q_{total}	[kW]	1115	1.6	1124	2.4	747
m_{CH4}	[kg/s]	0.022	1.6	0.022	2.4	0.548
m_{air}	[kg/s]	0.435	9.8	0.438	10	3.567
T_{fuel}	[°C]	20.6	1.5	13.1	2.3	11.7
T_{air}	[°C]	20.6	1.4	8.5	1.6	10.2
Q_{water}	[kW]	592	3.3	597	4.2	397
RH	[%]	41		81		61

Measured heat fluxes (extracted heat rates in each of the seven sections along the combustion chamber) are shown in Table 3. The displayed data are averages from the two repeated measurements for each of the cases. The measured time period was the same as for operation conditions. Mean fluctuations during the averaging period are shown as well. All of the fluctuations are under 1 % of measured heat fluxes.

The fuel distribution among primary and secondary nozzles was determined from numerical simulation based on total fuel flow rate since only main fuel supply pipeline is equipped with flow meter. The fuel flow in the Case 1 was $3.84\ 10^{-3}$ kg/s for primary and $1.1\ 10^{-2}$ kg/s for secondary nozzles. In the Case 2 the distribution was $5.79\ 10^{-3}$ kg/s to the primary and $1.65\ 10^{-2}$ to the secondary nozzles.

Table 3: Measured heat fluxes

	Case 1			Case 2		
	Heat flux [kW/m²]	Mean fluctuation [kW/m²]	Error estimate [%]	Heat flux [kW/m²]	Mean fluctuation [kW/m²]	Error estimate [%]
Section 1	17.25	0.15	8.4%	21.88	0.21	6.4%
Section 2	25.57	0.16	4.8%	34.05	0.27	3.5%
Section 3	40.17	0.14	2.9%	53.28	0.26	2.3%
Section 4	46.41	0.15	2.8%	63.58	0.24	2.0%
Section 5	47.87	0.16	2.6%	65.45	0.27	1.9%
Section 6	42.33	0.17	2.8%	58.9	0.29	2.0%
Section 7	31.4	0.21	2.0%	42.74	0.19	1.6%

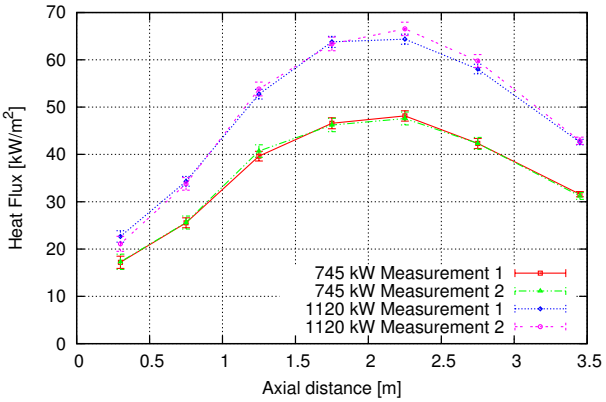

Figure 5: Comparison of measured heat fluxes in seven sections

Instrumentation and data acquisition system

All the data from sensors are collected in the central operator work station. The data acquisition system is industry standard with 1-second interval except for the flow meters which have approximately 6-second interval. Water flow is measured by turbine flow meters equipped with optical sensor sensing 10 000 impulses per 1 m^3 of water. Flow of the fuel (natural gas) is measured by positive displacement, rotary type flow meter and conversion to the standard conditions is made based on temperature and pressure measurement.

All temperature sensors are of type RTD Pt100 and are placed in a steel sheath. The accuracy indicated by manufacturer is better than +/- 0.3 °C.

Data accuracy

Using the information from sensor manufacturers, the accuracy of derived parameters was calculated. To do this, the theory of error propagation [33] was utilized. E.g. the standard deviation of product P of uncorrelated variables A and B which have standard deviations σ_A and σ_B may be calculated from the following formula:

$$\left(\frac{\sigma_P}{P}\right)^2 = \left(\frac{\sigma_A}{A}\right)^2 + \left(\frac{\sigma_B}{B}\right)^2 \quad .$$

Swirl number evaluation

Swirl number is an important parameter used to characterize the intensity of swirl in a flow. For definition see e.g. [20] which defines swirl number in radial coordinates. For evaluation in a CFD solver is however more suitable the following formulation:

$$S = \frac{\int_A \rho u w r \, dA}{R \int_A \rho u^2 \, dA} \quad ,$$

where u is axial velocity (m/s), w is circumferential velocity (m/s) , ρ is density (kg/m^3), r is radius (m), R is the maximum radius of the nozzle exit (m), A = surface area (m^2).

The grid was identical in all simulations, as noted above. The calculated swirl number however substantially differed between simulations employing the SST k-ω turbulence model ($S \approx 0.48$) and other alternatives using k-ε realizable model or RSM ($S \approx 0.74$). This may be caused partly by insufficiently fine grid in the vicinity of swirl generator. Grid independence study however has not been performed so far.

MODELING

Grid was created with great care to ensure high quality. Most of the volume of computational domain was meshed by hexahedral cells and only in the vicinity of nozzles were used tetrahedral elements. Total number of grid cells was approximately 1,300,000.

Commercial code ANSYS Fluent was utilized for simulation. Turbulence was modeled by two-equation turbulence models that prevail in current engineering applications of CFD in the area of reactive flows. These include namely the realizable $k-\varepsilon$ model [34]. For the description of chemical reactions and interaction with turbulence was used eddy-dissipation (ED) model [35] with a one-step global reaction.

Radiation was included using the discrete ordinates method and radiative gas properties were calculated by the weighted-sum-of-gray-gases method with data based on [36] and [37]. Emissivity of the walls was set at 0.9.

Boundary conditions were utilized according Tab. 1 and 2. Walls other than water cooled are assumed adiabatic.

The solutions were performed using a pressure-based solver option of FLUENT 6.3, with the SIMPLEC solution algorithm and generalized QUICK third-order scheme [38] for momentum and density, and pressure staggering option. The remaining model equations, namely the turbulence model equations, were discretized using first order differencing.

Steady solution was sought, but the solution did not converge even in most stabilizing numerical settings with first order upwind differencing and strong relaxation. Therefore a more rigorous treatment was adopted by adding time into the problem formulation. The resulting unsteady-RANS (URANS) simulations display smaller fluctuations and complete convergence is achieved in every time step with step size 0.002 s. In order to obtain results independent of the initial conditions at least 3 s of physical time were always simulated, as the residence time in the combustion chamber is about 2 s and only afterwards it was possible to start collecting data for statistics.

Wall heat fluxes predicted by the simulation are shown in the Fig. 6 and 7. There are significant deviation in all sections – from 14 % to 36 %, except for the first section in Case 1 where deviation is only 2 %.

CONCLUSIONS

Local wall heat fluxes were investigated in a cylindrical, water-cooled large experimental combustion chamber for nonpremixed swirling natural gas flames. Measured data are provided for two firing rates (745 kW and 1120 kW) together with a complete geometry of the fluid flow domain including air duct, staged-gas burner and combustion chamber. Error analysis is included to complete the data base. Wall heat fluxes during measurement for Case 1 are displayed in Fig. 4. Measured wall heat flux profiles over the chamber length for both cases are displayed in Fig. 5. This validation benchmark

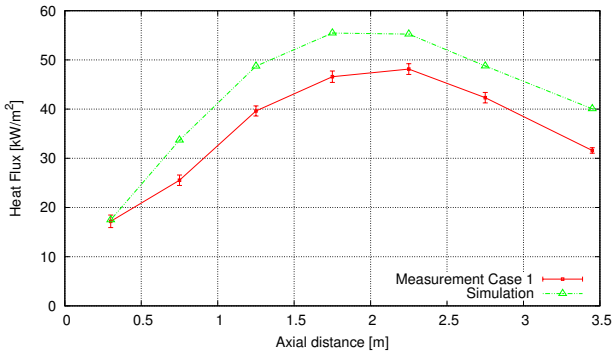

Figure 6: Measurement to simulation data comparison for Case 1

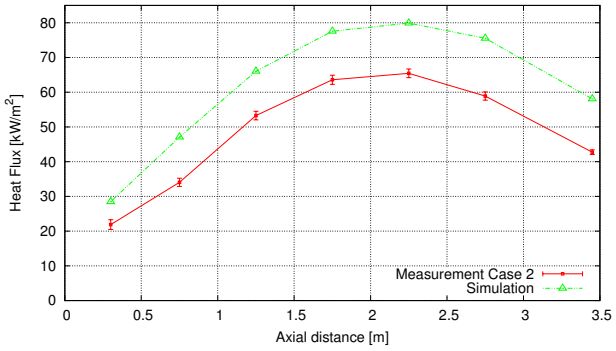

Figure 7: Measurement to simulation data comparison for Case 2

is provided to the research community as a basis for the validation of combustion models and codes using a problem which is both well documented and practically relevant. The article also includes two predictions that were performed. Wall heat fluxes predicted by the simulations are show in Fig. 6 and 7. It is shown that unsteady RANS computations are required to obtain well-converged results due to internal flow instabilities. The models included in the study over-predict total wall heat fluxes on the cooled wall by 17.5 % to 25.1 %, which shows that engineering simulations of swirling diffusion flames in large combustors using approaches commonly available at the present should be used and interpreted with caution.

ACKNOWLEDGMENTS

The authors gratefully acknowledge financial support of the Ministry of Education, Youth and Sports of the Czech Republic within the framework of research plan No. MSM 0021630502 "Waste and Biomass Utilization focused on Environment Protection and Energy Generation".

REFERECES

[1] H. Kobayashi, Y. Ito, N. Tsuruta, and K. Yoshikawa, "Performance of High Temperature Air Combustion Boiler with Low NOx Emission," *JSME International Journal Series B Fluids and Thermal Engineering*, vol. 45, 2002, pp. 481-486.

[2] J. Ströhle, *Spectral Modelling of Radiative Heat Transfer in Industrial Furnaces*, Aachen, Germany: Shaker Verlag GmbH, Germany, 2004.

[3] R.R. Hayes, S. Brewster, B.W. Webb, M.Q. McQuay, and A.M. Huber, "Crown incident radiant heat flux measurements in an industrial, regenerative, gas-fired, flat-glass furnace," *Experimental Thermal and Fluid Science*, vol. 24, Mar. 2001, pp. 35-46.

[4] *Directive 2001/80/EC of the European Parliament and of the Council on the limitation of emissions of certain pollutants into the air from large combustion plants* , 2001.

[5] N. Syred, "A review of oscillation mechanisms and the role of the precessing vortex core (PVC) in swirl combustion systems," *Progress in Energy and Combustion Science*, vol. 32, 2006, pp. 93-161.

[6] T. Landenfeld, A. Kremer, E. Hassel, J. Janicka, T. Schäfer, J. Kazenwadel, C. Schulz, and J. Wolfrum, "Laser-diagnostic and numerical study of strongly swirling natural gas flames," *Symposium (International) on Combustion*, vol. 27, 1998, pp. 1023-1029.

[7] W. Meier, O. Keck, B. Noll, O. Kunz, and W. Stricker, "Investigations in the TECFLAM swirling diffusion flame: Laser Raman measurements and CFD calculations," *Applied Physics B: Lasers and Optics*, vol. 71, Nov. 2000, pp. 725-731.

[8] S. Repp, A. Sadiki, C. Schneider, A. Hinz, T. Landenfeld, and J. Janicka, "Prediction of swirling confined diffusion flame with a Monte Carlo and a presumed-PDF-model," *International Journal of Heat and Mass Transfer*, vol. 45, Mar. 2002, pp. 1271-1285.

[9] A. German and T. Mahmud, "Modelling of non-premixed swirl burner flows using a Reynolds-stress turbulence closure," *Fuel*, vol. 84, Mar. 2005, pp. 583-594.

[10] S. Nemoda, V. Bakic, S. Oka, G. Zivkovic, and N. Crnomarkovic, "Experimental and numerical investigation of gaseous fuel combustion in swirl chamber," *International Journal of Heat and Mass Transfer*, vol. 48, Oct. 2005, pp. 4623-4632.

[11] R.R. Cao and S.B. Pope, "The influence of chemical mechanisms on PDF calculations of nonpremixed piloted jet flames," *Combustion and Flame*, vol. 143, Dec. 2005, pp. 450-470.

[12] C. Fureby, F. Grinstein, G. Li, and E. Gutmark, "An experimental and computational study of a multi-swirl gas turbine combustor," *Proceedings of the Combustion Institute*, vol. 31, Jan. 2007, pp. 3107-3114.

[13] A. Sadiki, A. Maltsev, B. Wegner, F. Flemming, A. Kempf, and J. Janicka, "Unsteady methods (URANS and LES) for simulation of combustion systems," *International Journal of Thermal Sciences*, vol. 45, Aug. 2006, pp. 760-773.

[14] S. James, J. Zhu, and M. Anand, "Large eddy simulations of turbulent flames using the filtered density function model," *Proceedings of the Combustion Institute*, vol. 31, Jan. 2007, pp. 1737-1745.

[15] N. Arai, A. Matsunami, and S.W. Churchill, "A review of measurements of heat flux density applicable to the field of combustion," *Experimental Thermal and Fluid Science*, vol. 12, May. 1996, pp. 452-460.

[16] A. Paist, A. Poobus, and T. Tiikma, "Probes for measuring heat transfer parameters and fouling intensity in boilers," *Fuel*, vol. 81, Sep. 2002, pp. 1811-1818.

[17] A. Barreiros, M.G. Carvalho, M. Costa, and F.C. Lockwood, "Prediction of the near burner region and measurements of NOx and particulate emissions in

heavy fuel oil spray flames," *Combustion and Flame*, vol. 92, Feb. 1993, pp. 231-240.

[18] P. Schmittel, B. Günther, B. Lenze, W. Leuckel, and H. Bockhorn, "Turbulent swirling flames: Experimental investigation of the flow field and formation of nitrogen oxide," *Proceedings of the Combustion Institute*, vol. 28, 2000, pp. 303-309.

[19] S. Böckle, J. Kazenwadel, T. Kunzelmann, and C. Schulz, "Laser-diagnostic multi-species imaging in strongly swirling natural gas flames," *Applied Physics B: Lasers and Optics*, vol. 71, Nov. 2000, pp. 741-746.

[20] P. Weigand, W. Meier, X. Duan, W. Stricker, and M. Aigner, "Investigations of swirl flames in a gas turbine model combustor: I. Flow field, structures, temperature, and species distributions," *Combustion and Flame*, vol. 144, Jan. 2006, pp. 205-224.

[21] W. Meier, X. Duan, and P. Weigand, "Investigations of swirl flames in a gas turbine model combustor: II. Turbulence-chemistry interactions," *Combustion and Flame*, vol. 144, Jan. 2006, pp. 225-236.

[22] W. Meier, X. Duan, and P. Weigand, "Reaction zone structures and mixing characteristics of partially premixed swirling CH4/air flames in a gas turbine model combustor," *Proceedings of the Combustion Institute*, vol. 30, Jan. 2005, pp. 835-842.

[23] K. Ranga Dinesh, K. Jenkins, M. Kirkpatrick, and W. Malalasekera, "Modelling of instabilities in turbulent swirling flames," *Fuel*, vol. 89, Jan. 2010, pp. 10-18.

[24] Y.M. Al-Abdeli, A.R. Masri, G.R. Marquez, and S.H. Starner, "Time-varying behaviour of turbulent swirling nonpremixed flames," *Combustion and Flame*, vol. 146, Jul. 2006, pp. 200-214.

[25] R.F. Huang and S.C. Yen, "Aerodynamic characteristics and thermal structure of nonpremixed reacting swirling wakes at low Reynolds numbers," *Combustion and Flame*, vol. 155, Nov. 2008, pp. 539-556.

[26] A. Sengissen, J. Van Kampen, R. Huls, G. Stoffels, J. Kok, and T. Poinsot, "LES and experimental studies of cold and reacting flow in a swirled partially premixed burner with and without fuel modulation," *Combustion and Flame*, vol. 150, Jul. 2007, pp. 40-53.

[27] G. Solero and A. Coghe, "Effect of injection typology on turbulent homogeneous mixing in a natural gas swirl burner," *Experimental Thermal and Fluid Science*, vol. 21, Mar. 2000, pp. 162-170.

[28] A.W. Hübner, M.J. Tummers, K. Hanjalic, and T.H. van der Meer, "Experiments on a rotating-pipe swirl burner," *Experimental Thermal and Fluid Science*, vol. 27, April. 2003, pp. 481-489.

[29] M. Tummers, A. Hübner, E. van Veen, K. Hanjalic, and T. van der Meer, "Hysteresis and transition in swirling nonpremixed flames," *Combustion and Flame*, vol. 156, Feb. 2009, pp. 447-459.

[30] P. Bělohradský, V. Kermes, and P. Stehlík, "Design and analysis of experiment for low-NOx burners design for process industries," *8th European Conference on Industrial Furnaces and Boilers*, Vilamouria, Portugal: 2008.

[31] V. Kermes, P. Bělohradský, and P. Stehlík, "Influence of burner geometry with staged gas supply on the formation of nitrogen oxides," *8th European Conference on Industrial Furnaces and Boilers*, Vilamouria, Portugal: 2008.

[32] V. Kermes, P. Bělohradský, J. Oral, and P. Stehlík, "Testing of gas and liquid fuel burners for power and process industries," *Energy*, vol. 33, Oct. 2008, pp. 1551-1561.

[33] V.D. Braembussche, ed., *Measurement Techniques in Fluid Dynamics: An Introduction*, Rhode Saint Genése: von Karman Institute for Fluid Dynamics, 2001.

[34] T. Shih, W.W. Liou, A. Shabbir, Z. Yang, and J. Zhu, "A new k-[epsilon] eddy viscosity model for high reynolds number turbulent flows," *Computers & Fluids*, vol. 24, Mar. 1995, pp. 227-238.

[35] B. Magnussen and B. Hjertager, "On mathematical modeling of turbulent combustion with special emphasis on soot formation and combustion," *Symposium (International) on Combustion*, vol. 16, 1977, pp. 719-729.

[36] A. Coppalle and P. Vervisch, "The total emissivities of high-temperature flames," *Combustion and Flame*, vol. 49, Jan. 1983, pp. 101-108.

[37] T.F. Smith, Z.F. Shen, and J.N. Friedman, "Evaluation of Coefficients for the Weighted Sum of Gray Gases Model," *Journal of Heat Transfer*, vol. 104, Nov. 1982, pp. 602-608.

[38] Fluent, "FLUENT 6.3.26, User`s Guide," 2006.

Appendix E Local wall heat fluxes in swirling non-premixed natural gas flames in large-scale combustor: Data for validation of combustion codes

This appendix contains author's paper published at 12th Conference on Process Integration, Modelling and Optimisation for Energy Saving and Pollution Reduction, PRES 2010, held in Prague, 28 August – 1 September 2010.

Bibliographic citation:

VONDÁL, J., HÁJEK, J. and KERMES, V. Local wall heat fluxes in swirling non-premixed natural gas flames in large-scale combustor: Data for validation of combustion codes. In: *Chemical Engineering Transactions*. 28 August 2010, Vol. 21, no. 2, pp. 1123–1128. DOI 10.3303/CET1021188.

CHEMICAL ENGINEERING TRANSACTIONS Volume 21, 2010
Editor J. J. Klemeš, H. L. Lam, P. S. Varbanov
 ISBN 978-88-95608-05-1 ISSN 1974-9791
DOI: 10.3303/CET1021188

Local Wall Heat Fluxes in Swirling Non-Premixed Natural Gas Flames in Large Scale Combustor: Data for Validation of Combustion Codes

Jiří Vondál, Jiří Hájek*, Vít Kermes
Institute of Process and Environmental Engineering, Faculty of Mechanical Engineering, Brno University of Technology, Technická 2,
616 69 Brno, Czech Republic,
hajek@fme.vutbr.cz

The main purpose of this work is the measurement of local heat fluxes (absorbed into water cooled walls) from confined non-premixed swirling gas flame. Presented are two thermal duties 745 kW and 1120 kW fired in a large-scale combustion chamber. Measured data are intended for use as a benchmark. Its purpose is to validate computational fluid dynamics (CFD) codes against reliable and transparent measurements. The uniqueness of reported measurements is in the scale of the experimental facility and its ability to provide accurate data at above thermal duties. The data uncertainty is also discussed. The experimental facility is described including complete geometry of the burner and combustion chamber to enable use of the measured data by other researchers. The entire geometry is made available in the STEP format.

1. Introduction

Study of flame structure is the subject of long-lasting interest of the combustion modelling community. Detailed in-flame measurements of temperature, velocity and species concentrations have served for the validation of all existing combustion models. Unlike the in-flame properties, wall heat fluxes have been used for model validation only rarely. Heat flux measurements reported in the literature are either spot measurements or global heat transfer rates. Spot measurements however mostly provide just the thermal irradiation flux, not the actual radiative or total heat transfer rate, e.g. in the study of industrial furnaces and boilers (Kobayashi et al., 2002; Ströhle, 2004; Hayes et al., 2001). Likewise, global heat transfer rates calculated from the total hot water (steam) production are insufficient for the validation of detailed predictions.
In contrast to that, the interest of engineering community focuses primarily on local heat fluxes and pollutant emissions. Emissions are studied namely to ensure compliance with legislative regulations, e.g. directive (EC 2001), while heat fluxes are required to check proper furnace design and to ensure safe operation. It is thus apparent that the correct prediction of local heat fluxes on heat transfer surfaces is one of the most important aspects of practical combustion simulations that should receive adequate attention.

Please cite this article as: Vondál J., Hájek J. and Kermes V., (2010), Local wall heat fluxes in swirling non-premixed natural gas flames in large scale combustor: Data for validation of combustion codes, Chemical Engineering Transactions, 21, 1123-1128 DOI: 10.3303/CET1021188

Swirl-stabilised non-premixed flames are frequently used in industrial burners, but they present one of the most difficult problems to predict computationally. Only with the advances in large eddy simulations (LES), successful predictions of in-flame properties were reported e.g. in (Fureby et al., 2007; Sadiki et al., 2006; James et al., 2007; Dinesh et al., 2010). The LES approach is unfortunately still too computationally expensive for the simulation of large-scale fired heaters due to their huge dimensions (on the order of 10 m) and the need to resolve fine features like gas nozzles with diameters on the order of 1 mm. The only viable alternative for practical predictions in the present as well as for a number of years to come thus consists of models based on first or second-order turbulence closures as eg. in (Khelil et al., 2009).

2. Testing facility

The construction of the semi-industrial experimental facility for burners up to 2 MW was aimed at providing variable length of combustion chamber and accurate heat flux and emission measurements. The main feature distinguishing the test facility at Brno University of Technology from others is the ability to measure local heat transfer rates to the cooled walls, which is enabled by segmental design of the combustion chamber. There are up to seven water cooled segments of the combustion chamber, see Figure 2. All internal segments have the same flame-facing area of 1.57 m^2, whereas the first and seventh section has 1.26 m^2 and 3.14 m^2, respectively. The last three segments are removable which allows adjustment of the combustion chamber length.

The burner was a low-NOx design with staged gas supply (Figure 1) and axial swirl generator, fired by natural gas. Swirl generator with diameter 240 mm consisting of 8 vanes acts as a flame holder. Gas inlet consists of twelve primary nozzles and eight secondary nozzles. Eight of the primary nozzles have diameter 2.6 mm and the other four 3.0 mm. All the primary nozzles are drilled in a nozzle head located on the burner axis.

Secondary gas injection is performed by four additional nozzle heads located in regular intervals around annular air channel which surrounds the primary nozzle head. Each of the four secondary nozzle heads has two nozzles with a diameter of 3.3 mm.

Flame ignition and stabilization is performed by a small (25 kW) premixed natural-draft pilot burner. Its thermal duty was included in the total thermal duty.

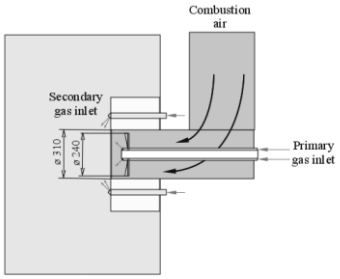

Figure 2: Swirl burner with two gas stages

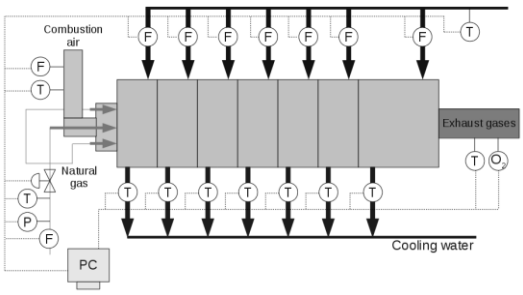

Figure 1: Combustion chamber and main parts of the data acquisition system

The burner performance was set to 745 kW (Case 1) and 1120 kW (Case 2) with excess air ratio 1.1. Measurements previously performed at the same testing facility, although with different objectives than in this work, were described e.g. in (Kermes et al. 2008).

3. Measurements

Each of the two studied regimes (Case 1 and 2) was measured twice to test repeatability. Operating conditions during stabilization time are shown in Table 1. It can be seen that reproducibility is good even though conditions were slightly changed e.g. air temperature 19.3 °C vs. 4.3 °C in Case 1. The deviation in the total extracted heat flux into the water was 0.16 % for the Case 1 and 0.88 % in the Case 2. The maximum load difference was in 3rd section 2.7 % for the Case 2 and 2.4 % in 5th section for the Case 1. The total extracted heat from flame (Q_{total}) was evaluated from natural gas flow rate, temperature and pressure. Equivalent methane mass flow rate (m_{CH4}) is calculated from natural gas flow rate using the ratio of heating values of natural gas and methane. Air flow was calculated based on oxygen concentration in exhaust gases and the fuel flow rate. The data displayed in the tables and graphs are averaged values over 5 minutes (Case 1) and 15 minutes (Case 2). Averaging was applied to remove random fluctuations in the measured values.

Measured heat fluxes (extracted heat rates in each of the seven sections along the combustion chamber) are shown in

Table 2. The displayed data are averages from the two repeated measurements for each of the cases. The averaging period was the same for measured data as for operating conditions. Mean fluctuations during the averaging period are shown as well. All of the fluctuations are under 1 % of measured heat fluxes.

Table 1: Operation conditions of the measurements

		Case 1				*Case 2*			
		Measurement 1	*Uncertainty [%]*	*Measurement 2*	*Uncertainty [%]*	*Measurement 1*	*Uncertainty [%]*	*Measurement 2*	*Uncertainty [%]*
Q_{total}	[kW]	746	1.62	748	2.7	1115	1.6	1124	2.4
m_{CH4}	[kg/s]	0.015	1.62	0.015	2.7	0.022	1.6	0.022	2.4
m_{air}	[kg/s]	0.289	9.8	0.290	10.1	0.435	9.8	0.438	10
T_{fuel}	[°C]	20.1	1.5	12.5	2.6	20.6	1.5	13.1	2.3
T_{air}	[°C]	19.2	1.5	4.3	1.9	20.6	1.4	8.5	1.6
Q_{water}	[kW]	438	4.3	438	5.27	592	3.3	597	4.2
RH	[%]	42		90		41		81	

The fuel distribution among primary and secondary nozzles was determined from numerical simulation of gas distributor based on total fuel flow rate since only the gas main is equipped with flow meter. Fuel flow rate in Case 1 was 3.84 10^{-3} kg/s for primary and 1.1 10^{-2} kg/s for secondary nozzles. In Case 2 the distribution was 5.79 10^{-3} kg/s to the primary and 1.65 10^{-2} to the secondary nozzles.

Using the information from sensor manufacturers, maximum error of heat fluxes was calculated and results are shown as uncertainties in

Table 2. To do this, the theory of error propagation (Braembussche, 2001) was utilized.

Table 2: Measured heat fluxes

	Case 1			*Case 2*		
	Heat flux [kW/m^2]	*Mean fluctuation [kW/m^2]*	*Uncertainty [%]*	*Heat flux [kW/m^2]*	*Mean fluctuation [kW/m^2]*	*Uncertainty [%]*
Section 1	17.25	0.15	8.4%	21.88	0.21	6.4%
Section 2	25.57	0.16	4.8%	34.05	0.27	3.5%
Section 3	40.17	0.14	2.9%	53.28	0.26	2.3%
Section 4	46.41	0.15	2.8%	63.58	0.24	2.0%
Section 5	47.87	0.16	2.6%	65.45	0.27	1.9%
Section 6	42.33	0.17	2.8%	58.9	0.29	2.0%
Section 7	31.4	0.21	2.0%	42.74	0.19	1.6%

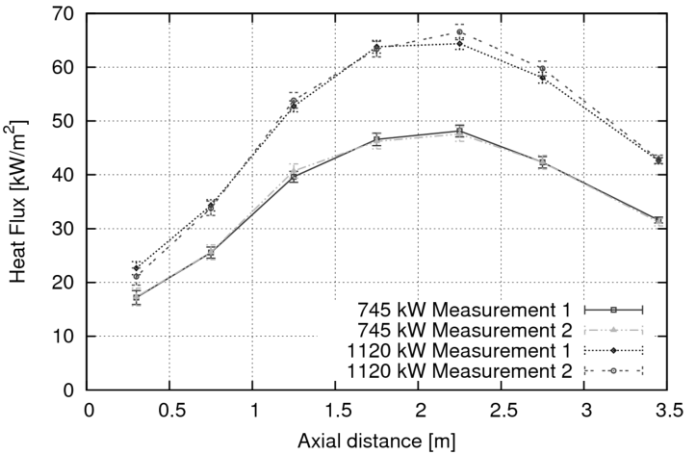

Figure 3: Comparison of measured heat fluxes in seven sections

Geometry of the flow domain in STEP format has been prepared for researchers interested in making their own computational analysis of the present flames. It will be provided upon request by the corresponding author.

4. Verification of air flow rate measurement

An additional procedure for the measurement of air flow rate has been implemented to provide verification of the primary method. The primary indirect measurement based on oxygen concentration in the flue gas has a long response time and rather large uncertainty as documented in Table 1. The calculation of air flow rate is in the primary method based on the measured O_2 content in flue gas and measurement of natural gas flow rate, which itself depends on the readings of three sensors as described above.

The second method of flow rate measurement which provides verification for the first one employs a vane anemometer located directly in combustion air pipe which has inner

diameter of 246 mm. Information from the anemometer is also automatically collected by the data acquisition system. The uncertainty provided by manufacturer is ±0.1 m/s and ±1.5 % of measured value. The readings from the vane anemometer are however biased due to natural non-uniformity of flow profile in the pipe and further due to slight non-symmetry of velocity profile at the location of measurement. This is caused by a 90° turn of the pipe, which precedes the probe by approximately 12 diameters. In order to provide a reliable correction function for the vane anemometer, the turbulent flow in the air supply pipe has been modelled using ANSYS FLUENT software system for several flow rates spanning the range corresponding to admissible burner duties. The results displayed in Figure 4 show that the following linear correction function is appropriate:

$$\dot{m}_{air} = 0.972 S v_{anem} \rho - 0.015, \tag{1}$$

where $\dot{m}_{air}$ [kg/s] is total air flow rate through the duct, S [m^2]is cross-sectional area, ρ [kg/m^3] is air density and v_{anem} [m/s] is the velocity measured by the anemometer. In the simulations was applied no-slip condition at the walls and wall roughness height equal to 0.1 mm. Table 3 provides a comparison of the corrected values from the anemometer with data based on the flue gas O_2 measurements.

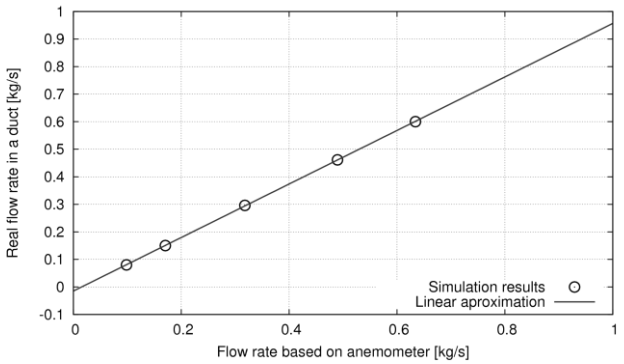

Figure 4: Vane anemometer air flow rate

Table 3: Mass flow rate of air in the supply air duct

Predicted by flue gas analyzer	kg/s	0.283	0.377	0.428	0.510	0.548
Predicted by anemometer	kg/s	0.273	0.393	0.434	0.512	0.585
Relative deviation	%	-3.49	4.31	1.38	0.57	6.74

6. Conclusions

Local wall heat fluxes were investigated in a cylindrical, water-cooled large experimental combustion chamber for non-premixed swirling natural gas flames.

Measured data are provided for two firing rates (745 kW and 1120 kW) together with a complete geometry of the fluid flow domain including air duct, staged-gas burner and combustion chamber. Error analysis is included to complete the data base. This validation benchmark is provided to the research community as a basis for the validation of combustion models and codes using a problem which is both well documented and practically relevant. The article also discusses air flow rate measurement issues when vane anemometry is utilized. Correction function for particular duct size is derived to account for in-duct velocity profile.

Acknowledgement

The authors gratefully acknowledge financial support of the Ministry of Education, Youth and Sports of the Czech Republic within the framework of research plan No. MSM 0021630502 "Waste and Biomass Utilization focused on Environment Protection and Energy Generation" and within the framework of Operational Programme "Research and Development for Innovations" – "NETME Centre – New Technologies for Mechanical Engineering".

References

Braembussche, V. D. (Ed.), 2001, Measurement Techniques in Fluid Dynamics: An Introduction, von Karman Institute for Fluid Dynamics, Rhode Saint Genése, Brussels, Belgium.

Dinesh, K. K. J. R., Jenkins, K. W., Kirkpatrick, M. P. and Malalasekera, W., 2010, Modelling of instabilities in turbulent swirling flames, Fuel, 89(1), 10-18.

EC 2001, Directive 2001/80/EC of the European Parliament and of the Council on the limitation of emissions of certain pollutants into the air from large combustion plants. Official Journal of the European Union, L309, 1-21.

Fureby, C., Grinstein, F., Li, G., and Gutmark, E., 2007, An experimental and computational study of a multi-swirl gas turbine combustor, Proceedings of the Combustion Institute, 31(2), 3107-3114.

Hayes, R. R., Brewster, S., Webb, B. W., McQuay, M. Q., and Huber, A. M., 2001, Crown incident radiant heat flux measurements in an industrial, regenerative, gas-fired, flat-glass furnace, Experimental Thermal and Fluid Science, 24(1-2), 35-46.

James, S., Zhu, J., and Anand, M., 2007, Large eddy simulations of turbulent flames using the filtered density function model, Proceedings of the Combustion Institute, 31(2), 1737-1745.

Kermes, V., Bělohradský, P., and Stehlík, P., 2008, Influence of burner geometry with staged gas supply on the formation of nitrogen oxides, in Proc of 8th European Conference on Industrial Furnaces and Boilers, Vilamouria, Portugal.

Khelil, A., Naji, H., Loukarfi, L., and Mompean, G., 2009, Prediction of a high swirled natural gas diffusion flame using a PDF model, Fuel, 88(2), 374-381.

Kobayashi, H., Ito, Y., Tsuruta, N., and Yoshikawa, K., 2002, Performance of High Temperature Air Combustion Boiler with Low NOx Emission, JSME International Journal Series B Fluids and Thermal Engineering, 45(3), 481-486.

Sadiki, A., Maltsev, A., Wegner, B., Flemming, F., Kempf, A., and Janicka, J., 2006, Unsteady methods (URANS and LES) for simulation of combustion systems, International Journal of Thermal Sciences, 45(8), 760-773.

Ströhle, J., 2004, Spectral Modelling of Radiative Heat Transfer in Industrial Furnaces, PhD Thesis, Shaker Verlag GmbH, Germany, Aachen, Germany.

Appendix F Experimental and numerical investigation of swirling non-premixed gas flames in industrial-scale furnace

This appendix contains author's paper published at 9th European Conference on Industrial Furnaces and Boilers, held in Estoril, Portugal, 26 April 2011.

Bibliographic citation:

VONDÁL, J. and HÁJEK, J. Experimental and numerical investigation of swirling non-premixed gas flames in industrial-scale furnace. In: *Proceedings of the 9th European Conference on Industrial Furnaces and Boilers*. Estoril, Portugal: 26 April 2011.

Experimental and numerical investigation of swirling non-premixed gas flames in industrial-scale furnace

Jiří Vondál, Jiří Hájek*
Brno University of Technology, Faculty of Mechanical Engineering, Institute of Process and Environmental Engineering, Technická 2, 616 69 Brno, Czech Republic
tel.: +420 541 142 331, e-mail: vondal@upei.fme.vutbr.cz, hajek@fme.vutbr.cz

The present work addresses a difficult problem often encountered in industrial furnaces and fired heaters, which is the prediction of swirling non-premixed gas flames in a large-scale furnace. The focus is on a practically very relevant parameter, i.e. the distribution of local wall heat fluxes. The studied burner is equipped with gas staging nozzles firing natural gas and a guide vane swirl generator acting as a flame holder. The combustion chamber consists of 7 water cooled segments and enables the measurement of local wall heat fluxes on the water-side. Two firing rates included in the work are 745 kW and 1120 kW. The measured data include detailed information necessary to set up boundary conditions including fuel and air flow rates, pressures and temperatures as well as distributions of wall heat fluxes extracted by the cooling water in individual segments.

The computational part unfolds from a central problem of predicting the swirling flow generated by guide vane swirler. Due to the non-symmetry of the flow in the swirler caused by air duct geometry and bad access for detailed measurement of velocity field in the burner inlet, it was decided to include the air supply duct in the simulation. However, it is well known that prediction of the action of swirl generator is extremely difficult and thus a validation of the code is carried out using published measurements in a similar laboratory-scale device.

Simulation of the non-premixed combustion is performed using unsteady RANS turbulence model coupled with simple eddy-dissipation chemistry model and discrete ordinates radiative heat transfer model. Two options for the calculation of absorption coefficient by a weighted sum of grey gases are discussed. Results confirm that a domain-based path length calculation is more appropriate for the prediction of wall heat fluxes than a cell-based option.

Keywords: Heat flux, Swirling flow, Combustion, CFD, Turbulence.

1. Introduction

Study of flame structure is the subject of long-lasting interest of the combustion modelling community. Detailed in-flame measurements of temperature, velocity and species concentrations have served for the validation of all existing combustion models. Unlike the in-flame properties, wall heat fluxes have been used for model validation only rarely. Heat flux measurements reported in the literature are either spot measurements or global heat transfer rates. Spot measurements however mostly provide just the thermal irradiation flux, not the actual radiative or total heat transfer rate (e.g. in the study of industrial furnaces and boilers (Kobayashi et al., 2002; Ströhle, 2004; Hayes et al., 2001)). Likewise, global heat transfer rates calculated from the total hot water (steam) production are insufficient for the validation of detailed predictions.

In contrast to that, the interest of engineering community focuses primarily on local heat fluxes and pollutant emissions. Emissions are studied namely to ensure compliance with legislative regulations (e.g. directive (EC 2001)), while heat fluxes are required to check proper furnace design and to ensure safe operation. It is thus apparent that the correct prediction of local heat fluxes on heat transfer surfaces is one of the most important aspects of practical combustion simulations that should receive adequate attention.

Swirl-stabilised non-premixed flames are frequently used in industrial burners, but they present one of the most difficult problems to predict computationally. Only with the advances in large eddy simulations (LES), successful predictions of in-flame properties were reported (Fureby et al., 2007; Sadiki et al., 2006; James et al., 2007). The LES approach is unfortunately still too computationally expensive for the simulation of large-scale fired heaters due to their huge dimensions (on the order of 10 m) and the need to resolve fine features like gas nozzles with diameters on the order of 1 mm. The

only viable alternative for practical predictions in the present as well as for a number of years to come thus consists of models based on first or second-order turbulence closures.

The key question in predicting swirling diffusion flames however is, whether the prediction of swirl using geometry of swirl generator is dependable. In the literature, only scarce instances may be found of measurements suitable for the validation of such swirl generation predictions (Mak and Balabani, 2007; Fernandes et al., 2005). In most cases of advanced predictions of swirling flows including those mentioned above, boundary conditions on the inlet are typically specified using measured velocities and velocity fluctuations. Predictions validated by experimental data are almost nonexistent in peer-reviewed journals. Occasionally, swirl is even specified by geometric swirl number, i.e. by inclination of swirl generator vanes (helixes) (So et al., 1985). Neither of these approaches is however suitable for most cases of practical predictions of swirl-stabilised gas and liquid fuel burners, due to the large variety of swirl generator designs used by burner vendors and due to the unavailability of detailed measurements. This work therefore includes a simulation of swirl generator validated by an experiment recently published in a peer-reviewed journal.

2. Swirl prediction and validation

For the validation of swirl prediction capability was used a recently published work (Mak and Balabani, 2007). The geometry of experimental setup was further clarified in personal communications with one of the authors (Balabani, 2010). Here we include only a brief summary of the experiment and its results.

The measurements were performed for a vane swirl generator by optical method (particle image velocimetry, PIV). Geometry of the computational domain including the swirl generator is displayed in Figure 1. Inclination of the guide vanes in the present case is 45°. The experimental work was focused on analyzing flow features in a sudden expansion and its deeper analysis by proper orthogonal decomposition (POD), but they measured also velocity components just above the expansion ($x/D = -0.44$) in order to determine accurately the amount of swirl in the expanding flow. These velocity measurements above the expansion were used in the present work to validate computational predictions. Working medium was water.

Commercial CFD code ANSYS Fluent 12.1 was used for all computations. The computational grid was unstructured polyhedral with more than 10^6 cells. The computations did not converge in a time-independent formulation, therefore it was necessary to run the case in unsteady mode. Turbulence was modelled using a two-equation model SST k-ω, which is a well-established alternative of the standard k-ε model, but it doesn't require wall functions to define wall boundary conditions for the turbulence model variables. Discretization of convective terms was done using second-order upwind method.

The results of simulations (Figures 2-4) display a notable non-symmetry of velocity profiles in the reference cross-section. Such non-symmetry has not been expected although some deviations were observed also in the measured data. Grid independence study of the predictions is the subject of present ongoing work. Unsteadiness of the flow has been removed from simulation results by averaging over a time period significantly longer than residence time in the flow domain (several seconds). Shown below are plots comparing the predicted and measured velocity components in the reference cross section as well as contour plots displaying the non-symmetry of computed flow mentioned above. The agreement of predictions with measurements is not convincing, but encouraging to continue the present efforts by further computations. Swirl number given by the experimenters (geometrical, therefore not calculated from the measured velocities) was 0.6, whereas the predictions yielded swirl number 0,8.

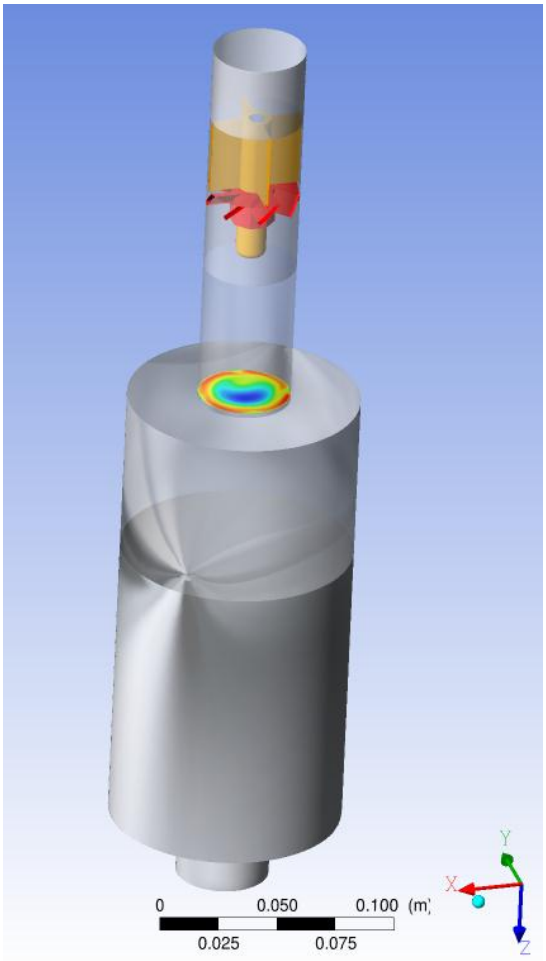

Figure 1: Experimental expansion chamber with guide vane swirl generator

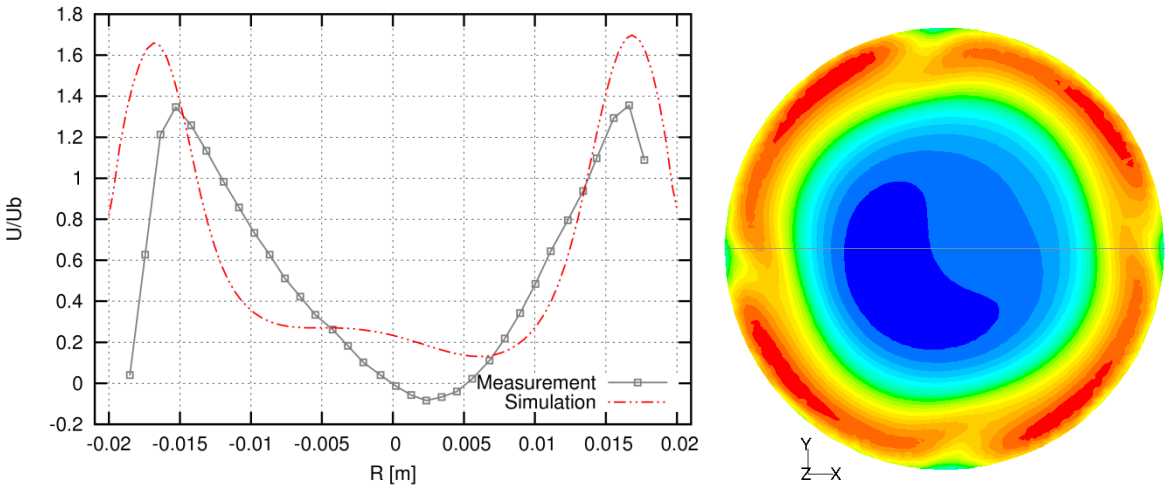

Figure 2: Axial velocity in the reference cross section; comparison of measurement and prediction and its contour plot with a line in the position of the plotted data

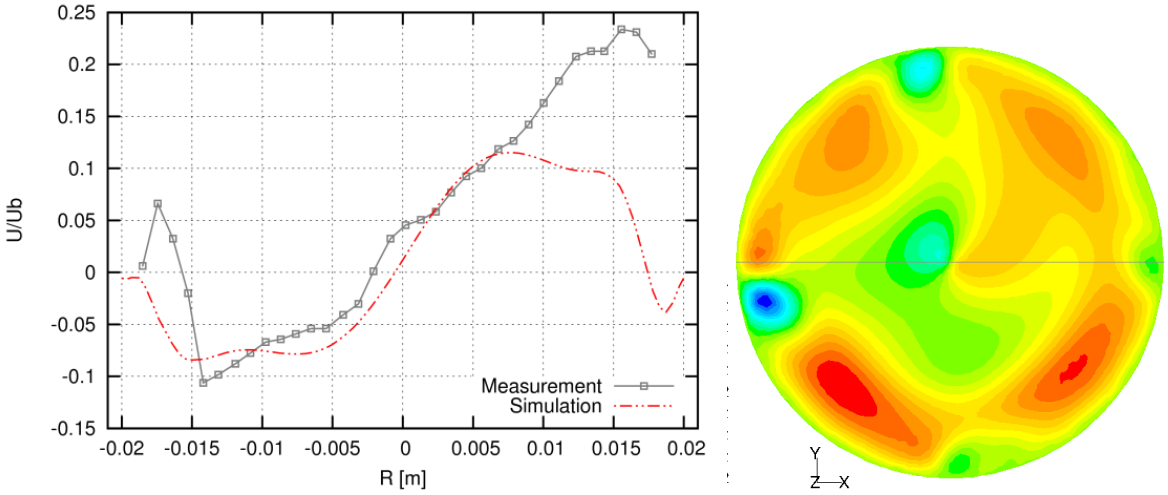

Figure 3: Radial velocity in the reference cross section; comparison of measurement and prediction and its contour plot with a line in the position of the plotted data

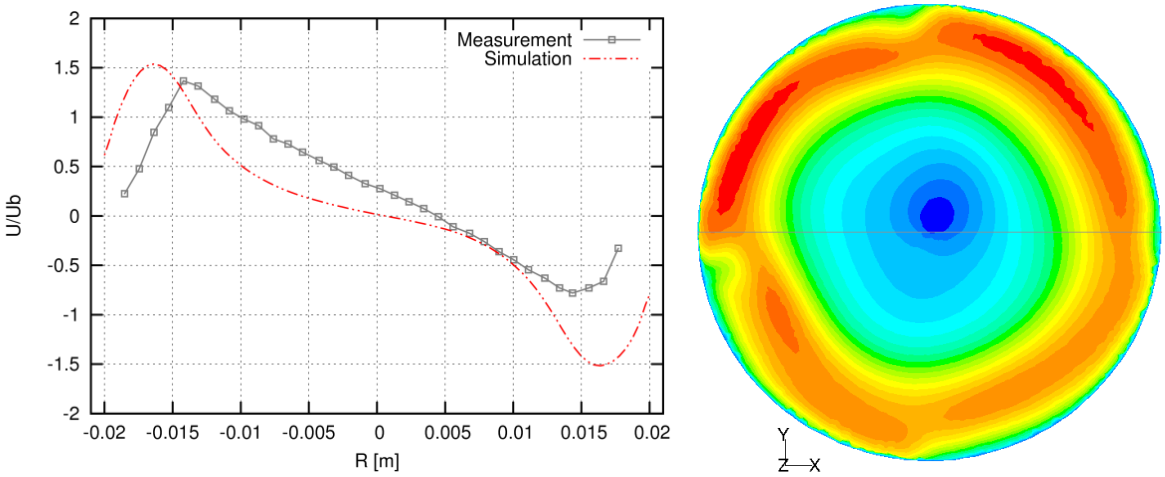

Figure 4: Tangential velocity in the reference cross section; comparison of measurement and prediction and its contour plot with a line in the position of the plotted data

3. Burner testing facility

The construction of the semi-industrial experimental facility for burners up to 2 MW was aimed at providing variable length of combustion chamber and accurate heat flux and emission measurements. The main feature distinguishing the test facility at Brno University of Technology from others is the ability to measure local heat transfer rates to the cooled walls, which is enabled by segmental design of the combustion chamber. There are up to seven water cooled segments of the combustion chamber, see Figure 6. All internal segments have the same flame-facing area of 1.57 m^2, whereas the first and seventh section has 1.26 m^2 and 3.14 m^2, respectively. The last three segments are removable which allows adjustment of the combustion chamber length.

The burner was a low-NOx design with staged gas supply (Figure 5) and axial swirl generator, fired by natural gas. Swirl generator with diameter 240 mm consisting of 8 vanes acts as a flame holder. Gas inlet consists of twelve primary nozzles and eight secondary nozzles. Eight of the primary nozzles have diameter 2.6 mm and the other four 3.0 mm. All the primary nozzles are drilled in a nozzle head located on the burner axis.

Secondary gas injection is performed by four additional nozzle heads located in regular intervals around annular air channel which surrounds the primary nozzle head. Each of the four secondary nozzle heads has two nozzles with a diameter of 3.3 mm.

Flame ignition and stabilization is performed by a small (25 kW) premixed natural-draft pilot burner. Its thermal duty was included in the total thermal duty.

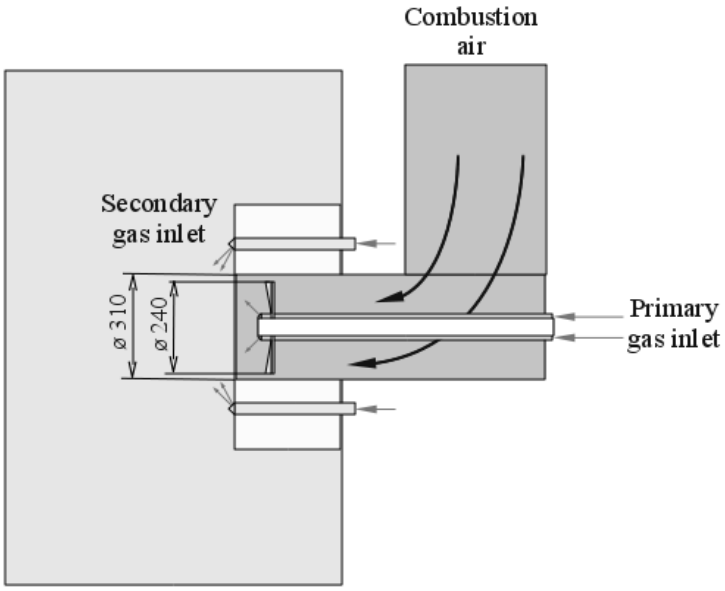

Figure 5: Swirl burner with two gas stages

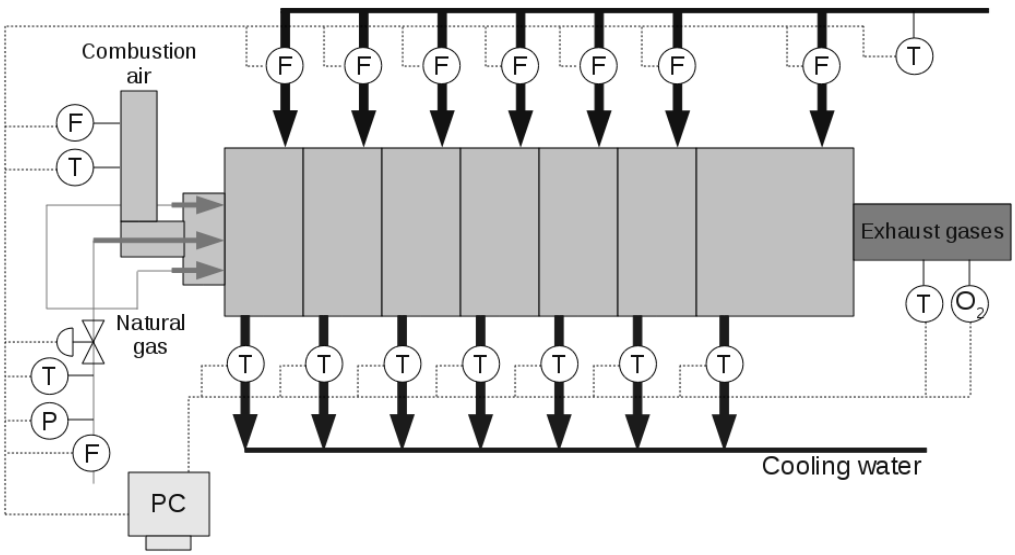

Figure 6: Combustion chamber and main parts of the data acquisition system

The burner performance was set to 745 kW (Case 1) and 1120 kW (Case 2) with excess air ratio 1.1. Several measurements previously performed at the same testing facility, although with different objectives than in this work, were described in (Bělohradský et al., 2008; Kermes, Bělohradský, and Stehlík, 2008; Kermes, Bělohradský, Oral, et al., 2008).

4. Heat flux measurements

Each of the two studied regimes (Case 1 and 2) was measured twice to test repeatability. Operating conditions during stabilization time are shown in Table 1. It can be seen that reproducibility is good even though conditions were slightly changed e.g. air temperature 19.3 °C vs. 4.3 °C in Case 1. The deviation in the total extracted heat flux into the water was 0.16 % for the Case 1 and 0.88 % in the Case 2. The maximum load difference was in 3rd section 2.7 % for the Case 2 and 2.4 % in 5th section for the Case 1. The total extracted heat from flame (Q_{total}) was evaluated from natural gas flow rate, temperature and pressure. Equivalent methane mass flow rate (m_{CH4}) is calculated from natural gas flow rate using the ratio of heating values of natural gas and methane. Air flow was calculated based on oxygen concentration in exhaust gases and the fuel flow rate. The data displayed in the tables and graphs are averaged values over 5 minutes (Case 1) and 15 minutes (Case 2). Averaging was applied to remove random fluctuations in the measured values.

Measured heat fluxes (extracted heat rates in each of the seven sections along the combustion chamber) are shown in Table 2. The displayed data are averages from the two repeated measurements for each of the cases. The averaging period was the same for measured data as for operating conditions. Mean fluctuations during the averaging period are shown as well. All of the fluctuations are under 1 % of measured heat fluxes.

Table 1: Operation conditions of the measurements

Case 1		Measurement 1	Uncertainty [%]	Measurement 2	Uncertainty [%]
Q_{total}	[kW]	746	1,62	748	2,7
m_{CH4}	[kg/s]	0,015	1,62	0,015	2,7
m_{air}	[kg/s]	0,289	9,8	0,290	10,1
T_{fuel}	[°C]	20,1	1,5	12,5	2,6
T_{air}	[°C]	19,2	1,5	4,3	1,9
Q_{water}	[kW]	438	4,3	438	5,27
RH	[%]	42		90	
Case 2		Measurement 1	Uncertainty [%]	Measurement 2	Uncertainty [%]
Q_{total}	[kW]	1115	1,6	1124	2,4
m_{CH4}	[kg/s]	0,022	1,6	0,022	2,4
m_{air}	[kg/s]	0,435	9,8	0,438	10
T_{fuel}	[°C]	20,6	1,5	13,1	2,3
T_{air}	[°C]	20,6	1,4	8,5	1,6
Q_{water}	[kW]	592	3,3	597	4,2
RH	[%]	41		81	

The fuel distribution among primary and secondary nozzles was determined from numerical simulation of gas distributor based on total fuel flow rate since only the gas main is equipped with flow

meter. Fuel flow rate in Case 1 was 3.84 10^{-3} kg/s for primary and 1.1 10^{-2} kg/s for secondary nozzles. In Case 2 the distribution was 5.79 10^{-3} kg/s to the primary and 1.65 10^{-2} to the secondary nozzles.

Using the information from sensor manufacturers, maximum error of heat fluxes was calculated and results are shown as uncertainties in Table 2. To do this, the theory of error propagation (Braembussche, 2001) was utilized.

Table 2: Measured heat fluxes

Case 1	Heat flux	Mean fluctuation	Uncertainty	**Case 2**	Heat flux	Mean fluctuation	Uncertainty
	[kW/m^2]	[kW/m^2]	[%]		[kW/m^2]	[kW/m^2]	[%]
Section 1	17,25	0,15	8,4%		21,88	0,21	6,4%
Section 2	25,57	0,16	4,8%		34,05	0,27	3,5%
Section 3	40,17	0,14	2,9%		53,28	0,26	2,3%
Section 4	46,41	0,15	2,8%		63,58	0,24	2,0%
Section 5	47,87	0,16	2,6%		65,45	0,27	1,9%
Section 6	42,33	0,17	2,8%		58,9	0,29	2,0%
Section 7	31,4	0,21	2,0%		42,74	0,19	1,6%

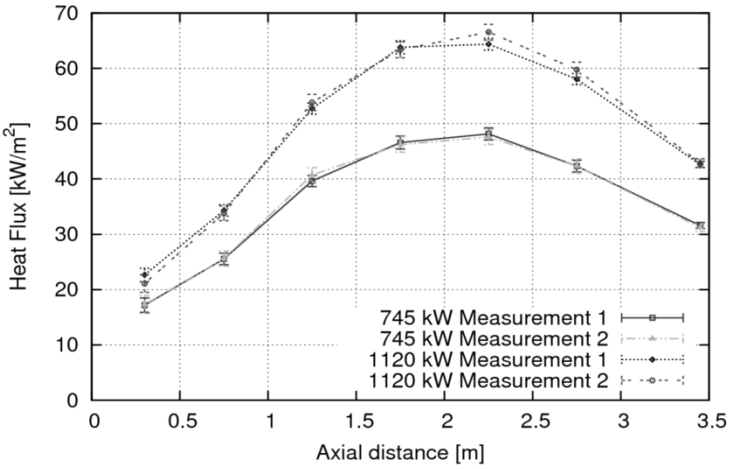

Figure 7: Comparison of measured heat fluxes in seven sections

Geometry of the flow domain in STEP format has been prepared for researchers interested in making their own computational analysis of the present flames. It will be provided upon request by the corresponding author.

5. Verification of air flow rate measurement

An additional procedure for the measurement of air flow rate has been implemented to provide verification of the primary method. The primary indirect measurement based on oxygen concentration in the flue gas has a long response time and rather large uncertainty as documented in Table 1. The calculation of air flow rate is in the primary method based on the measured O_2 content in flue gas and

measurement of natural gas flow rate, which itself depends on the readings of three sensors as described above.

The second method of flow rate measurement which provides verification for the first one employs a vane anemometer located directly in combustion air pipe which has inner diameter of 246 mm. Information from the anemometer is also automatically collected by the data acquisition system. The uncertainty provided by manufacturer is ±0.1 m/s and ±1.5 % of measured value. The readings from the vane anemometer are however biased due to natural non-uniformity of flow profile in the pipe and further due to slight non-symmetry of velocity profile at the location of measurement. This is caused by a 90° turn of the pipe, which precedes the probe by approximately 12 diameters. In order to provide a reliable correction function for the vane anemometer, the turbulent flow in the air supply pipe has been modelled using ANSYS FLUENT software system for several flow rates spanning the range corresponding to admissible burner duties. The results displayed in Figure 8 show that the following linear correction function is appropriate:

$$\dot{m}_{air} = 0.972 S v_{anem} \rho - 0.015 , \tag{1}$$

where $\dot{m}_{air}$ [kg/s] is total air flow rate through the duct, S [m^2] is cross-sectional area, ρ [kg/m^3] is air density and v_{anem} [m/s] is the velocity measured by the anemometer. In the simulations was applied no-slip condition at the walls and wall roughness height equal to 0.1 mm. Table 3 provides a comparison of the corrected values from the anemometer with data based on the flue gas O_2 measurements.

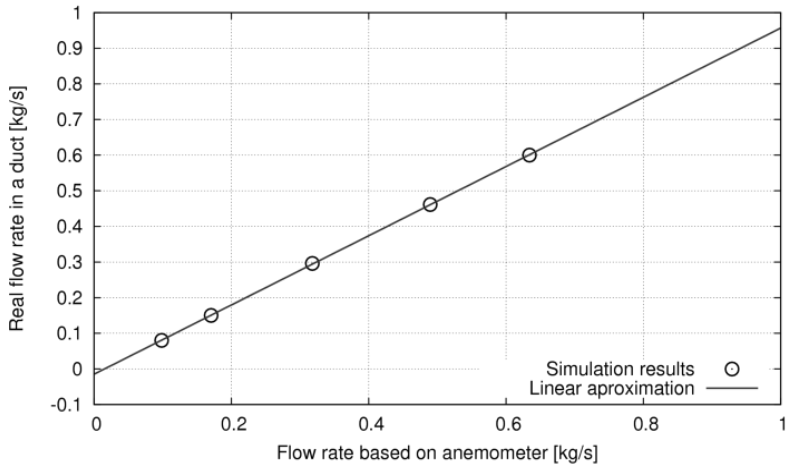

Figure 8: Vane anemometer air flow rate

Table 3: Mass flow rate of air in the supply air duct

Predicted by flue gas analyzer	kg/s	0.283	0.377	0.428	0.510	0.548
Predicted by anemometer	kg/s	0.273	0.393	0.434	0.512	0.585
Relative deviation	%	-3.49	4.31	1.38	0.57	6.74

6. Conclusions

Local wall heat fluxes were investigated in a cylindrical, water-cooled large experimental combustion chamber for non-premixed swirling natural gas flames. Measured data are provided for two firing rates (745 kW and 1120 kW) together with a complete geometry of the fluid flow domain

including air duct, staged-gas burner and combustion chamber. Error analysis is included to complete the data base. This validation benchmark is provided to the research community as a basis for the validation of combustion models and codes using a problem which is both well documented and practically relevant. The article also discusses air flow rate measurement issues when vane anemometry is utilized. Correction function for particular duct size is derived to account for in-duct velocity profile.

Acknowledgement

The authors gratefully acknowledge financial support of the Ministry of Education, Youth and Sports of the Czech Republic within the framework of research plan No. MSM 0021630502 “Waste and Biomass Utilization focused on Environment Protection and Energy Generation” and within the framework of Operational Programme “Research and Development for Innovations” – “NETME Centre – New Technologies for Mechanical Engineering”.

References

Balabani S. Personal communications, 2010

Bělohradský, P., Kermes, V., and Stehlík, P., 2008, Design and analysis of experiment for low-NOx burners design for process industries, in 8th European Conference on Industrial Furnaces and Boilers, Vilamouria, Portugal.

Braembussche, V. D. (Ed.), 2001, Measurement Techniques in Fluid Dynamics: An Introduction, von Karman Institute for Fluid Dynamics, Rhode Saint Genése.

EC 2001, Directive 2001/80/EC of the European Parliament and of the Council on the limitation of emissions of certain pollutants into the air from large combustion plants. Official Journal of the European Union, L309, 1-21.

Fernandes, E.C., M.V. Heitor, and S.I. Shtork. 2005. An analysis of unsteady highly turbulent swirling flow in a model vortex combustor. Experiments in Fluids 40, no. 2 (8): 177-187. doi:10.1007/s00348-005-0034-4.

Fureby, C., Grinstein, F., Li, G., and Gutmark, E., 2007, An experimental and computational study of a multi-swirl gas turbine combustor, Proceedings of the Combustion Institute, 31(2), 3107-3114.

Hayes, R. R., Brewster, S., Webb, B. W., McQuay, M. Q., and Huber, A. M., 2001, Crown incident radiant heat flux measurements in an industrial, regenerative, gas-fired, flat-glass furnace, Experimental Thermal and Fluid Science, 24(1-2), 35-46.

James, S., Zhu, J., and Anand, M., 2007, Large eddy simulations of turbulent flames using the filtered density function model, Proceedings of the Combustion Institute, 31(2), 1737-1745.

Kermes, V., Bělohradský, P., Oral, J., and Stehlík, P., 2008, Testing of gas and liquid fuel burners for power and process industries, Energy, 33(10), 1551-1561.

Kermes, V., Bělohradský, P., and Stehlík, P., 2008, Influence of burner geometry with staged gas supply on the formation of nitrogen oxides, in 8th European Conference on Industrial Furnaces and Boilers, Vilamouria, Portugal.

Kobayashi, H., Ito, Y., Tsuruta, N., and Yoshikawa, K., 2002, Performance of High Temperature Air Combustion Boiler with Low NOx Emission, JSME International Journal Series B Fluids and Thermal Engineering, 45(3), 481-486.

Mak, H., and S. Balabani. 2007. Near field characteristics of swirling flow past a sudden expansion. Chemical Engineering Science 62, no. 23 (December): 6726-6746. doi:10.1016/j.ces.2007.07.009.

Sadiki, A., Maltsev, A., Wegner, B., Flemming, F., Kempf, A., and Janicka, J., 2006, Unsteady methods (URANS and LES) for simulation of combustion systems, International Journal of Thermal Sciences, 45(8), 760-773.

So, R.M.C., S.A. Ahmed, and H.C. Mongia. 1985. Jet characteristics in confined swirling flow. Experiments in Fluids 3, no. 4: 221-230.

Ströhle, J., 2004, Spectral Modelling of Radiative Heat Transfer in Industrial Furnaces, Ph.D. Thesis, Shaker Verlag GmbH, Germany, Aachen, Germany.

Appendix G Prediction of flow through swirl generator and validation by measured data

This appendix contains author's paper published at 13th European Turbulence Conference, ETC13 held in Warsaw, Poland 12 – 15 September 2011.

Bibliographic citation:

VONDÁL, J. and HÁJEK, J. Prediction of flow through swirl generator and validation by measured data. In: *Journal of Physics: Conference Series*. 2011, Vol. 318, no. 2, pp. 022026. DOI 10.1088/1742-6596/318/2/022026.

Journal of Physics: Conference Series **318** (2011) 022026 doi:10.1088/1742-6596/318/2/022026

Prediction of flow through swirl generator and validation by measured data

Jiří Vondál & Jiří Hájek

Institute of Process and Environmental Engineering, Faculty of Mechanical Engineering, Brno University of Technology, Czech Republic

E-mail: vondal@upei.fme.vutbr.cz

Abstract. It is a well-recognized fact that reliable predictions of turbulent swirling nonpremixed flames are very difficult, especially for practical cases where application of LES methods is not feasible. It is also clear that detailed measured data of inlet velocity profiles for swirling combustion air are unavailable in practical applications. Therefore there is a need for validation of industry-standard codes for the prediction of flow through swirl generators. In this work are predictions validated by published experimental data for a swirler with guide vanes, which is similar to a typical flame holder in a staged-gas low-NO_x burner. Computations are done in ANSYS Fluent v12 code using a range of frequently used moment-closure turbulence models. Impact of grid type and quality is investigated. Discussion of the results is confronted with previously published observations on this topic. The aim is to critically evaluate the applicability of computations to determine inlet boundary conditions for swirling air in industrial combustors.

1. Introduction

Swirler (swirl generator, flame holder) is a key burner design element that significantly influences the flow pattern in combustion chambers. The purpose of a swirler is to convert part of axial momentum of the flow to a tangential momentum. This type of fow is required in many burners and also in other applications, including e.g. separation of particulate emissions in cyclones. In burners, swirling flow is important for flame stabilization and as a primary measure to decrease NO_x emissions. Swirler generates a low pressure zone in the flame core, which for confined flames leads to two recirculation zones that dilute reacting fuel and air by inert combustion products (flue gas). This desirable process can in cases with increased tangential momentum lead to unstable oscillations called precessing vortex core (PVC). The phenomenon may cause undesirable acoustic emissions and in extreme cases it may even destabilize the combustion process. Swirling flows and PVC are both the subject of a significant research activity as documented e.g. by (Nicholas Syred 2006), (Ranga Dinesh & Kirkpatrick 2009)).

For the quantitative description of the relative strength of tangential momentum is used a nondimensional swirl number (S), which is defined as the ratio of axial flux of tangential momentum over axial flux of axial momentum (Gupta, D. G. Lilley, et al. 1984). In most cases published works provide values of swirl number calculated on the basis of swirl generator geometry as proposed by (Claypole & N. Syred 1981). The geometric swirl number must however be used thoughtfully, as it is suitable only for specific swirler geometries, e.g. when guide vanes cover the whole cross-section of air flow tube and there are no short-cut currents. In spite of this, number of authors provides geometry-based swirl number as the only information about swirl intensity, e.g. (Cortés & Gil 2007), (Fernandes et al. 2006). Swirl number calculated from measured velocity profiles is encountered less frequently in the literature, e.g. in (Khezzar 1998) or (Coghe et al. 2004), but it is essential in the case of this work, as measured data are necessary for the validation of predictions.

There are two basic types of swirling flow – low swirl flows typically with swirl number lower than 0.6 and strongly swirling flows with higher value of swirl number. Precessing vortex core is encountered mainly in the case of strong swirl flows, with the exception of flow through sudden expansion (which is the case also in most burners), where PVC has been observed even with lower swirl numbers (Ranga Dinesh & Kirkpatrick 2009).

Lately, research in the area of swirling combustion has concentrated mainly on the flame itself with much activity centered around two specific burners, namely the TECFLAM burner (Schmittel et al.

2000), (Landenfeld et al. 1998), (Meier et al. 2000) and the Sydney burner (Kalt et al. 2002), (Al-Abdeli et al. 2006). In research works, the prevailing practice is to use measured velocity profiles at the inlet of a combustion chamber, i.e. on a plane after the swirler. The simulation then develops from the measured velocity inlet conditions, e.g. in (Escue & Cui 2010). Some authors in the past even used guessed velocity profiles at the inlet (flat, parabolic, etc.) like in (Dong & David G. Lilley 1994) However, as pointed out in (Roux et al. 2005) or (Sadiki et al. 2006) the practice of using measured velocity profiles may not be always suitable for computational predictions and in practical applications where measured data are not available it is simply infeasible.

This is why recent efforts aim to replace the measurement of inlet velocity profiles by modeling flow through the swirler (Selle et al. 2004; Moureau et al. 2007; Sadiki et al. 2006). Such approach leads to increased computational requirements, which is however becoming acceptable. In the case of Large Eddy Simulations (LES) which have increased demands on the quality of data for inlet boundary conditions, such treatment is almost a necessity.

LES is already quite widely used, but application to more complex geometries is still very difficult. The reason due to which LES of most practically relevant swirling nonpremixed flames is not feasible, is the excessive number of computational cells in a discretized model. This is caused by the great span of scales inherent to practical fired heaters, where gas nozzles are few millimeters in diameter, while combustion chambers have dimensions in meters or tens of meters. Due to the necessity to use uniform mesh cell size for the whole computational model in LES, such applications currently may be simulated only by moment closure turbulence models or by hybrid approach which combines RANS models at the walls with LES in the rest of the flow.

It could seem that RANS models are in decline due to the rising popularity of more advanced methods (LES, DES) but they still dominate in practical industrial applications ((Pallarés et al. 2009), (Stefanidis et al. 2006)). In the area of swirling nonpremixed combustion, several turbulence models are used that have been validated with relative success by measured velocity profiles. Specifically, it has been shown that the RNG k-ε turbulence model is acceptable for the prediction of low-swirl flows (up to 0.6), where it performs even better than the RSM model (Escue & Cui 2010). For the modeling of higher-swirl flows, it has been shown that solving the anisotropic Reynolds stresses directly by RSM is a more fitting option. The work (Wegner et al. 2004) even shows that unsteady RANS model based on RSM is applicable for the description of the precessing vortex core. The authors also report, that for a high-quality prediction it is necessary to include swirler in the simulated domain, otherwise velocity profiles may be deformed.

In validation studies of computational codes, authors often use their own measured data that are not provided in sufficient detail for others to use. It is also often necessary to communicate with the experimenters, as detailed geometry of the swirler is usually not included in publications. Typically, schematic drawing of the experimental setup and main dimensions of the combustor are just complemented by the value of swirl number in the text. After a longer period of time it becomes increasingly difficult to find all necessary specifications even for the authors of those experimental studies.

Below in a table is a summary of publications concerned with the measurements of swirling flows in combustors. The specifications for each case include type of the swirler, measurement method, as well as indication of whether the experiment was done in isothermal flow or reacting flow. The list covers only a selection of the most important works concerned with swirling flow in combustion chambers, with focus on recent publications.

Table 1. Summary of experiments on confined swirling flows

	Expansion ratio	Re	S – swirl number	Experimental technique	Swirl generation	Confined	Isothermal / reacting
(Yadav & Kushari 2010)	3	4095-8189	0-1.48	Hot wire	Axial guide vanes	y	Isothermal
(Raj & Ganesan 2009)	2.33	146 000		Five-hole pitot probe	8 guide vanes, angle 30°	y	Isothermal
(Mak & Balabani 2007)	2.5	10000	0-0.65	PIV	Axial guide vanes	y	Isothermal
(Fudihara et al. 2007)	oblique		0.2-3.2		Movable-Block	y	Isothermal
(Olivani et al. 2007)			0.82	PIV, LDV	Tangential air inlet	y	NG/air

(Meier, Weigand, et al. 2007)	2.1	35000	0,6	OH chemiluminescence, LDV, Raman scattering	Radial swirler	y	CH4/air
(Weigand, Meier, et al. 2006)	3,4	15000-58000	0.55-0.9	LDV, PLIF, Laser Raman Scattering	Radial swirlers – 8 for the central nozzle, 12 for the annular nozzle.	y	CH4/air
(Fernandes et al. 2006)		81 000	1,05	LDV, microphone, CCD camera for flow visualisation	Swirler with variable blade angles		Isothermal
(Pollard et al. 2005)		71000	0,89	LDV	Axial? guide vanes.		Isothermal
(Roux et al. 2005)				LDV	12 vanes tangential entry	y	CH4/air
(Wang et al. 2004)	1,94	10000-20000	0-0.43	LDV	Axial swirler with 8 vanes	y	Isothermal
(Coghe et al. 2004)		20700 – air jet; 5600 – fuel jet	0,82	LDV, thermocouple; emmision spectroscopy in visible range	Tangential air inlet	y	NG/air
(Grinstein et al. n.d.)		>70000	0.25-0.75	PIV, LDV, PDPA	TARS - axial and radial swirler	y	Isothermal
(Widmann et al. 2000)	8,0	10 000	S=0.49	Pitot tube	Vane-cascade	y	Isothermal
(Schmittel et al. 2000)	8,3		0-2.0	LDV, thermocouple	Movable-Block	y	NG/air
(A.R. Masri et al. 2000)	unconfined	12800	0-1.6	LDV	Tangential air inlet + bluff body at the outlet	n	NG/air
(Zhou et al. 2000)	2	47600	1 – 2.1	PDPA	Tangential air inlet into the main flow	y	Isothermal
(Landenfeld et al. 1998)		Regas=8000 ; Reair=42900	0.95; 2	LDV, LIF, Rayleigh scattering	Movable-Block	y	CH4/air
(Khezzar 1998)	1,82	15000	1,5	LDA	Radial swirler	y	Isothermal
(Ballester et al. 1997)	7,2	120000-160000	0.25, 0.75	Pitot tube, thermocouples	Axial swirler	y	NG/air
(Dellenback et al. 1988)	1,94	30000, 60000, 100000	0-1.23	LDA	Tangential air inlet	y	Isothermal
(Escudier & Keller 1985)	2	7000		LDA	Radial guide vanes	y	Isothermal
(Rhode et al. 1983)				Pitot tube	Guide vanes	y	Isothermal

There are basically three types of swirlers (Gupta, D. G. Lilley, et al. 1984) – axial guide vane swirler, tangential inlet swirler and rotating pipe swirler. The rotating pipe swirler has not found wide application in practice and it is not used in combustion applications. The tangential inlet swirler is used relatively often especially thanks to its clearly defined swirl intensity and low pressure loss. It is also used in the two popular research projects, centered around the Sydney burner (Karpetis & R.S. Barlow 2002) and around the TECFLAM burner (Schmittel et al. 2000)) although with some modifications. Axial swirler, which is studied in this work, is popular in industrial burners mainly for its operational reliability and simple design.

2. Model validation

It is necessary to use data measured in a similar configuration to validate models that could provide prediction of swirling flow at a combustion chamber inlet. Published model validations (Fudihara et al. 2007; Widmann et al. 2000) were done for very specific swirl generator geometries, so in this work are used data published by (Mak & Balabani 2007) who used PIV method to analyze flow field in a model of combustor (see Fig. 1) with an axial guide vane swirler.

Simulations are in this work performed with moment closure turbulence models and a transient formulation (URANS). The tested turbulence models include mainly variants of the popular k-ε model previously validated for different swirl generators e.g. in (Escue & Cui 2010; Fudihara et al. 2007; Widmann et al. 2000). The RNG k-ε model has in those works displayed some superiority over the

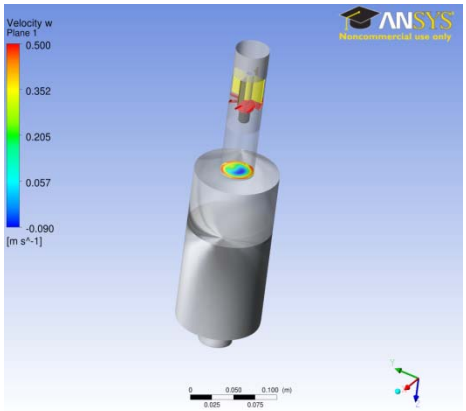

Figure 1. Flow domain geometry adopted from (Mak & Balabani 2007)

standard k-ε model since it predicted more accurately recirculation zones in the combustors. Another model applied in this work is the shear stress transport (SST) k-ω model (Menter 1994), which removes the need for wall functions and was previously applied for isothermal flow in a vortex combustor simulation in (Ridluan et al. 2007). Reynolds stress model (RSM) was also included in the analysis, which is more computationally intensive but handles anisotropy of turbulence and has been reported to outperform two-equation eddy-viscosity models in highly swirling flows. Finally, the realizable variant of the k-ε model (Shih et al. 1995) was tested as well. All simulations were done with discretization of second order for momentum.

All the simulations were performed using a commercial code ANSYS Fluent v12 (ANSYS 2009). Reynolds number at the inlet (before swirl generator) was 10,000 and swirl number calculated from the measured velocity data was 0.64. Two meshes were created for the simulation. One used simplified geometry, taking advantage of the rotational periodicity of the flow domain, which covered 90° section of the whole domain. This simplified geometry was meshed with a high-quality all-hexahedral mesh with 1,138,000 cells. The second model included the whole flow domain and it was meshed by a more coarse mesh containing 621,000 polyhedral cells.

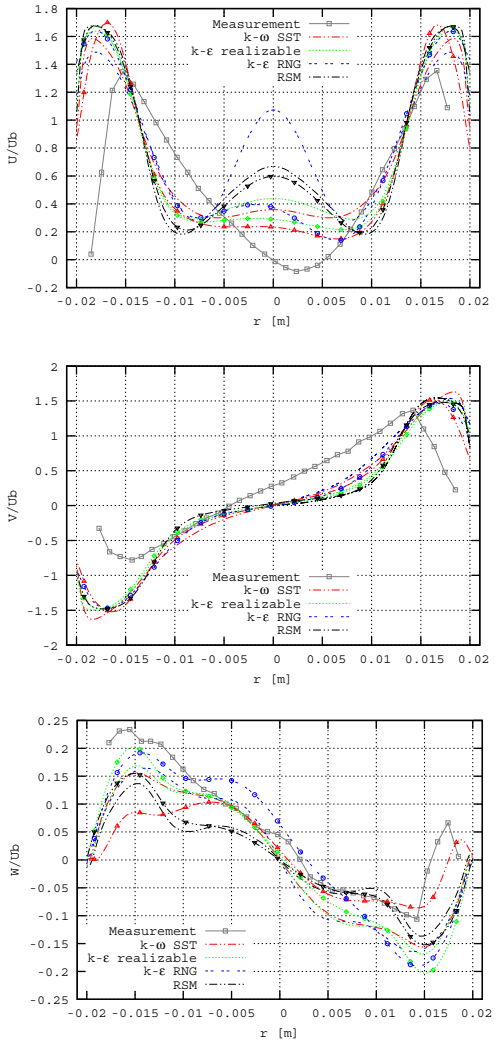

Figure 2. Comparison of measured and calculated velocity profiles for several turbulence models. Lines with symbols are for full model and lines without symbols for the quarter model with the periodic conditions.

3. Conclusion

Results from the simulation are displayed in Fig. 2. The plots show averaged velocity over sufficient time period normalized with the average velocity magnitude. Position of the reporting cross-section lies downstream from the swirl generator but still upstream from the sudden expansion (see Fig. 1). The results of simulations display consistent local disagreements with measured data. While simulation suggests no reverse flow, the measurement contradicts it. The most consistent result among two grid sizes gives the RSM model. The biggest grid type sensitivity shows RNG k-ε. Generally the full model predicts lower axial velocity at the r = 0 m than the quarter model.

4. Acknowledgements

The authors gratefully acknowledge financial support of the Ministry of Education, Youth and Sports of the Czech Republic within the framework of project CZ.1.07/2.3.00/20.0020, research plan MSM 0021630502 and within the framework of Operational Programme "Research and Development for Innovations" – "NETME Centre – New Technologies for Mechanical Engineering".

5. References

ANSYS Academic Research, Release 12.1, 2009. Help System, Users's Guide.

AL-ABDELI, Y.M. et al., 2006. Time-varying behaviour of turbulent swirling nonpremixed flames. *Combustion and Flame*, 146(1-2), pp.200-214.

BALLESTER, J.M. et al., 1997. Investigation of low-NOx strategies for natural gas combustion. *Fuel*, 76(5), pp.435-446.

CLAYPOLE, T.C. & SYRED, N., 1981. The effect of swirl burner aerodynamics on NOx formation. *Symposium (International) on Combustion*, 18(1), pp.81-89.

COGHE, A., SOLERO, G. & SCRIBANO, G., 2004. Recirculation phenomena in a natural gas swirl combustor. *Experimental Thermal and Fluid Science*, 28(7), pp.709-714.

CORTÉS, C. & GIL, A., 2007. Modeling the gas and particle flow inside cyclone separators. *Progress in Energy and Combustion Science*, 33(5), pp.409-452.

DELLENBACK, P.A., METZGER, D.E. & NEITZEL, G.P., 1988. Measurements in turbulent swirling flow through an abrupt axisymmetric expansion. *AIAA J.*, 26(6), pp.669-681.

DONG, M. & LILLEY, David G., 1994. Inlet velocity profile effects on turbulent swirling flow predictions. *J. of Propulsion and Power*, 10(2), pp.155-160.

ESCUDIER, M.P. & KELLER, J.J., 1985. Recirculation in swirling flow: a manifestation of vortex breakdown. *AIAA journal*, 23(1), pp.111-116.

ESCUE, A. & CUI, J., 2010. Comparison of turbulence models in simulating swirling pipe flows. *Applied Mathematical Modelling*, 34(10), pp.2840-2849.

FERNANDES, E.C., HEITOR, M.V. & SHTORK, S.I., 2006. An analysis of unsteady highly turbulent swirling flow in a model vortex combustor. *Experiments in Fluids*, 40(2), pp.177-187.

FUDIHARA, T., GOLDSTEIN, L. & MORI, M., 2007. A numerical investigation of the aerodynamics of a furnace with a movable block burner. *BRAZILIAN JOURNAL OF CHEMICAL ENGINEERING*, 24(2), pp.233-248.

GRINSTEIN, F. et al., Flow dynamics in a swirl combustor. *J. of Turbulence*, 3(June 2001), pp.1-19.

GUPTA, A.K., LILLEY, D. G. & SYRED, N., 1984. *Swirl Flows*, Abacus Press.

KALT, P.A.M. et al., 2002. Swirling turbulent non-premixed flames of methane: Flow field and compositional structure. *Proceedings of the Combustion Institute*, 29(2), pp.1913-1919.

KARPETIS, A.N. & BARLOW, R.S., 2002. Measurements of scalar dissipation in a turbulent piloted methane/air jet flame. *Proceedings of the Combustion Institute*, 29(2), pp.1929-1936.

KHEZZAR, L., 1998. Velocity measurements in the near field of a radial swirler. *Experimental Thermal and Fluid Science*, 16(3), pp.230-236.

LANDENFELD, T. et al., 1998. Laser-diagnostic and numerical study of strongly swirling natural gas flames. *Symposium (International) on Combustion*, 27(1), pp.1023-1029.

MAK, H. & BALABANI, S., 2007. Near field characteristics of swirling flow past a sudden expansion. *Chemical Engineering Science*, 62(23), pp.6726-6746.

MASRI, A.R., POPE, S.B. & DALLY, B.B., 2000. Probability density function computations of a strongly swirling nonpremixed flame stabilized on a new burner. *Proceedings of the Combustion Institute*, 28(1), pp.123-131.

MEIER, W. et al., 2000. Investigations in the TECFLAM swirling diffusion flame: Laser Raman measurements and CFD calculations. *Applied Physics B: Lasers and Optics*, 71(5), pp.725-731.

MEIER, W., WEIGAND, P., et al., 2007. Detailed characterization of the dynamics of thermoacoustic pulsations in a lean premixed swirl flame. *Combustion and Flame*, 150(1-2), pp.2-26.

MENTER, F.R., 1994. Two-equation eddy-viscosity turbulence models for engineering applications. *AIAA J.*, 32, pp.1598-1605.

MOUREAU, V., BÉRAT, C. & PITSCH, H., 2007. An efficient semi-implicit compressible solver for large-eddy simulations. *J. of Computational Physics*, 226(2), pp.1256-1270.

OLIVANI, A. et al., 2007. Near field flow structure of isothermal swirling flows and reacting non-premixed swirling flames. *Experimental Thermal and Fluid Science*, 31(5), pp.427-436.

PALLARÉS, J. et al., 2009. Numerical study of co-firing coal and Cynara cardunculus in a 350 MWe utility boiler. *Fuel Processing Technology*, 90(10), pp.1207-1213.

POLLARD, A., OZEM, H.L.M. & GRANDMAISON, E.W., 2005. Turbulent, swirling flow over an axisymmetric, constant radius surface. *Experimental Thermal and Fluid Science*, 29(4), pp.493-509.

RAJ, R.T.K. & GANESAN, V., 2009. Experimental study of recirculating flows induced by vane swirier. *Indian J. of Engineering and Materials Sciences*, 16(1), pp.14-22.

RANGA DINESH, K.K.J. & KIRKPATRICK, M.P., 2009. Study of jet precession, recirculation and vortex breakdown in turbulent swirling jets using LES. *Computers & Fluids*, 38(6), pp.1232-1242.

RHODE, D.L., Lilley, D. G. & MCLAUGHLIN, D.K., 1983. Mean Flowfields in Axisymmetric Geometries with Swirl Combustor. *AIAA J.*, 21(4), pp.593-600.

RIDLUAN, A., EIAMSA-ARD, S. & PROMVONGE, P., 2007. Numerical simulation of 3D turbulent isothermal flow in a vortex combustor. *International Communications in Heat and Mass Transfer*, 34(7), pp.860-869.

ROUX, S. et al., 2005. Studies of mean and unsteady flow in a swirled combustor using experiments, acoustic analysis, and large eddy simulations. *Combustion and Flame*, 141(1-2), pp.40-54.

SADIKI, A. et al., 2006. Unsteady methods (URANS and LES) for simulation of combustion systems. *International J. of Thermal Sciences*, 45(8), pp.760-773.

SCHMITTEL, P. et al., 2000. Turbulent swirling flames: Experimental investigation of the flow field and formation of nitrogen oxide. *Proceedings of the Combustion Institute*, 28(1), pp.303-309.

SELLE, L. et al., 2004. Compressible large eddy simulation of turbulent combustion in complex geometry on unstructured meshes. *Combustion and Flame*, 137(4), pp.489-505.

SHIH, T.-H. et al., 1995. A new k-[epsilon] eddy viscosity model for high reynolds number turbulent flows. *Computers & Fluids*, 24(3), pp.227-238.

STEFANIDIS, G.D. et al., 2006. CFD simulations of steam cracking furnaces using detailed combustion mechanisms. *Computers & Chemical Engineering*, 30(4), pp.635-649.

SYRED, Nicholas, 2006. A review of oscillation mechanisms and the role of the precessing vortex core (PVC) in swirl combustion systems. *Progress in Energy and Combustion Science*, 32(2), pp.93-161.

WANG, P. et al., 2004. Large eddy simulation and experimental studies of a confined turbulent swirling flow. *Physics of Fluids*, 16(9), p.3306.

WEGNER, B. et al., 2004. Assessment of unsteady RANS in predicting swirl flow instability based on LES and experiments. *International J. of Heat and Fluid Flow*, 25(3), pp.528-536.

WEIGAND, P., MEIER, W., et al., 2006. Investigations of swirl flames in a gas turbine model combustor: I. Flow field, structures, temperature, and species distributions. *Combustion and Flame*, 144(1-2), pp.205-224.

WIDMANN, J.F., RAO CHARAGUNDLA, S. & PRESSER, C., 2000. Aerodynamic study of a vane-cascade swirl generator. *Chemical Engineering Science*, 55(22), pp.5311-5320.

YADAV, N.P. & KUSHARI, A., 2010. Effect of swirl on the turbulent behaviour of a dump combustor flow. *Proceedings of the Institution of Mechanical Engineers, Part G: J. of Aerospace Engineering*, 224(6), pp.705 -717.

ZHOU, L.X. et al., 2000. Studies on the effect of swirl numbers on strongly swirling turbulent gas-particle flows using a phase-Doppler particle anemometer. *Powder Technology*, 112(1-2), pp.79-86.

Appendix H Software: Experimental data processing (TepToky)

Due to the size of source code it is attached only on DVD. Bellow are attached header files only.

File: fluent.h

```
#ifndef FLUENT_H
#define FLUENT_H
#include <wx/wx.h>
#include "PlotSort.h"
#include <vector>

extern wxTextCtrl *m_log;
class Vzduch: public Data
{
   float O2_mer;
   float airFuelRatio;
   float fuel, airFlow, fuelFlow;
   //kg/Nm3    kJ/Nm3  kJ/kg
   float ngDensity, ngHeatValueWeight, fluentHeatValueWeight;
   float nitr, argon, oxcarb, ox, water;
   Senzory *OxAnalyzator, *FuelFlow, *FuelPressure, *FuelTemp;

   //Vnořená třída - pro odlišení stavů pro které se provádí výpočet
   class Stav   {
   public:
      //Vnořená třída - pro odlišení fyzikálních jednotek
      class Units {
      public:
         float N2,Ar,Co2,O2,H2o,sum;
      } vol,weight,mol,kgPerKmol;
      } mol,air,stechioExho, unburntAirDry, dryExho, wetExho, unburnAirReal, stechioReal, stechioAir, airReal;

public:
```

```
    Vzduch(){};
    //Objemová %
     Vzduch (Senzory *ox_meas, Senzory *fuel_fl, Senzory *fuel_pres, Senzory *fuel_temp, float nitrogen=0.7735,float argon1=0.00942,float oxycarb=0.0003,float oxygen=0.20808,float water_h2o=0.00867);
    //Objemová %
        void SetVzduch (Senzory *ox_meas, Senzory *fuel_fl, Senzory *fuel_pres, Senzory *fuel_temp, float nitrogen=0.7735,float argon1=0.00942,float oxycarb=0.0003,float oxygen=0.20808,float water_h2o=0.00867);
    void ComputeVzduch ();
     void setCompWeight (float ox_mer, double fuelFlow, float nitr,float argon,float oxcarb,float ox,float water);
    double setCompVol (float ox_mer, double fuelFlow);
    float GetNgDensity(){return ngDensity;};
    float GetNgHeatValueWeight(){return ngHeatValueWeight;};
    float GetFluentHeatValueWeight(){return fluentHeatValueWeight;};
    float GetAirWeightN2(){return air.weight.N2;};
    float GetAirWeightAr(){return air.weight.Ar;};
    float GetAirWeightCo2(){return air.weight.Co2;};
    float GetAirWeightO2(){return air.weight.O2;};
    float GetAirWeightH2o(){return air.weight.H2o;};
};
#endif
```

file: PlotApp.h

```
#ifndef PLOTAPP_H
#define PLOTAPP_H
#include <wx/app.h>

class PlotApp : public wxApp
{
   public:
      virtual bool OnInit();
};
#endif // PLOTAPP_H
```

file: PlotMain.h

```
#ifndef PLOTMAIN_H
#define PLOTMAIN_H

#include "mathplot.h"
#include "fluent.h"
//Headers(PlotFrame)
#include "wx/listctrl.h"
#include <wx/menu.h>
#include <wx/frame.h>
#include <wx/statusbr.h>
#include "wx/sizer.h"
#include <wx/string.h>
#include <wx/spinbutt.h>
#include "timespin.h"
#include <wx/aui/aui.h>
#include <wx/event.h>

extern wxTextCtrl *m_log;
extern wxString directoryName;
extern Senzory F52,F53,F54,F55,F56,F57,F58,F59; //Průtoky vody sekcemi
extern Senzory F60,F61; //Průtok plynu a průtok vzduchu
extern Senzory T01,T02,T03,T04,T05,T06,T07,T08; //Teploty na výstupu z jednotlivých sekcí
extern Senzory T12,T15,T16; //Teplota plynu, teplota vzduchu a teplota vody na vstupu do sekcí
extern Senzory P35,P48; //Tlak v plynovém potrubí a v přívodním vzduchovém potrubí
extern Senzory Q92; //Množství kyslíku ve spalinách
extern Sekce s1,s2,s3,s4,s5,s6, s7;
extern HeatFlux power;
extern Info meas1;
extern Vzduch airFluent;
extern AirFlow fuelFl, vrtulkaFl;
extern wxTextCtrl *m_log;
```

```
class PlotFrame: public wxFrame {
public:
    PlotFrame(wxWindow* parent,wxWindowID id = -1);
    mpWindow *m_plot;
    wxButton *btn1;
    wxButton *btn2;
    wxButton *btn3;
    wxButton *refresh_btn;
    virtual ~PlotFrame();
    wxString fileName;
    void OnOpenF(wxCommandEvent& event);
    wxTextCtrl *InputFrom;
    wxTextCtrl *InputTo;
    wxButton *AirButton;
    wxButton *FluentButton;
    wxButton *MvAverButton;
    wxButton *WaterFlowButton;
    wxButton *HeatFluxButton;

    std::vector<double> xs,ys, xs2,ys2,xs3,ys3,xs4,ys4,xs5,ys5,xs6,ys6,xs7,ys7;
private:

    //Handlers(PlotFrame)
    void OnQuit(wxCommandEvent& event);
    void OnAbout(wxCommandEvent& event);
    void OnRange(wxCommandEvent& event);
    void OnAir(wxCommandEvent& event);
    void OnFluent(wxCommandEvent& event);
    void OnMvAver(wxCommandEvent& event);
    void ChangePlot1(wxCommandEvent& event);
    void ChangePlot2(wxCommandEvent& event);
    void ChangePlot3(wxCommandEvent& event);
    void OnRefreshClick(wxCommandEvent& event);
```

```
    void OnWaterFlow(wxCommandEvent& event);
    void OnHeatFluxButton(wxCommandEvent& event);
    void OnInFromLooseFocus(wxFocusEvent& event);
    void OnInToLooseFocus(wxFocusEvent& event);

    wxAuiManager m_mgr;

    //Identifiers(PlotFrame)
        static const long idMenuQuit;
        static const long idMenuAbout;
        static const long idMenuOpenF;
        static const long idMenuRange;
        static const long idMenuAir;
        static const long idMenuFluent;
        static const long idMenuMvAver;
        static const long idMenuWaterFlow;
        static const long ID_STATUSBAR1;
        static const long ID_BUTTON1;
        static const long ID_BUTTON2;
        static const long ID_BUTTON3;
        static const long ID_REFRESH;
        static const long idAirButton;
        static const long idFluentButton;
        static const long idMvAverButton;
        static const long idWaterFlowButton;
        static const long idHeatFluxButton;

        static const long idInputFrom;
        static const long idInputTo;
    mpFXYVector *plot1;
    mpFXYVector *plot2;
    mpFXYVector *plot3;
    mpFXYVector *plot4;
```

```
    mpFXYVector *plot5;
    mpFXYVector *plot6;
    mpFXYVector *plot7;
    wxStatusBar* StatusBar1;
    DECLARE_EVENT_TABLE()
};

class CustomDialog : public wxDialog {
public:
    CustomDialog(const wxString& title);
    wxTextCtrl *tc1;
    wxTextCtrl *tc;
     wxSpinButton *spinB1;
     wxSpinButton *spinB2;
     wxTimeSpinCtrl *t_spinB1;
     wxTimeSpinCtrl *t_spinB2;

private:
    void OnClose(wxCommandEvent& event);
    void OnOK(wxCommandEvent& event);
    void OnSP1_Up(wxCommandEvent& event);
    void OnSP1_Down(wxCommandEvent& event);
    void OnSP2_Up(wxCommandEvent& event);
    void OnSP2_Down(wxCommandEvent& event);

    static const long ID_BUTTON_OK;
    static const long wxID_CANCEL;
    static const long ID_SPIN1;
    static const long ID_SPIN2;
};

class AirDialog : public wxDialog {
public:
```

```
    AirDialog(const wxString& title);
    wxTextCtrl *tc1;
    wxTextCtrl *tc;

private:
    void OnClose(wxCommandEvent& event);
    void OnOK(wxCommandEvent& event);
    static const long ID_BUTTON_OK;
    static const long wxID_CANCEL;
};

class AverDialog : public wxDialog {
public:
    AverDialog(const wxString& title);
    wxTextCtrl *tc;
private:
    void OnClose(wxCommandEvent& event);
    void OnOK(wxCommandEvent& event);
    static const long ID_BUTTON_OK;
    static const long wxID_CANCEL;
};
#endif // PLOTMAIN_H
```

File: Plot_sort_new.h

```
#ifndef PLOTSRT_H
#define PLOTSRT_H
#include <vector>
#include <wx/wx.h>

//-------Hlavičkový soubor PlotSort.h------------
class Data {
  time_t range_from, range_to;
  time_t get_time(string);

  public:
  Data(vector<time_t> &cas_all, vector<double> &temp_all, string name);
  Data();
  void Set_range(string from, string to) {range_from = get_time(from); range_to = get_time(to)};
  double Average(string from, string to);
  double Stability (string from, string to);
  double Error(string from, string to);
};

class Sensors  {

  }F60,F35,T12,T16,T01,T02,T03,T04,T05,T06,T07,F52,F53,F54,F55,F56,F57,F58;

class Measurement :protected Sensors {
  public:
    set_fileTime(wxString fileTime);
}

void Data::Average(string from, string to) {
  time_t cas_start, cas_end;
  string cas_file = filename;
  double allv;
```

```
 int count, start_pozice, end_pozice, n;
 vector<time_t>::iterator start_poz;

 cas_file.erase(10);
 //Určení počátku pro průměrování
  cas_start = get_time(cas_file+" "+from);

  for (n=0; n<cas.size() && cas[n] <= cas_start; n++) //puvodne bylo != cas_start_i
     start_pozice = n+1;

  //Určení konce pro průměrování
  cas_end = get_time(cas_file+" "+to);
  for (n=0;n<cas.size() && cas[n] <= cas_end; n++)
     end_pozice = n+1;

  for (n=start_pozice, count=0; n<variable.size() && n<=end_pozice; n++)  {
     allv += variable[n];
     count++;
  }
  return allv/count;
}

void sortier(std::vector<std::vector <double> > &sekce, std::string cesta);
void refresh (wxTextCtrl* m_log);
int get_new_data(std::vector<time_t> &cas_all, std::vector<double> &temp_all, std::string
filename, int *pos);
int calc_sekce(std::vector<std::vector<time_t> > &cas_p_all, std::vector<std::vector<double> >
&perf_all, std::vector<std::vector<double> > &flow_all,std::vector<std::vector<double> >
&temp_all, std::vector<std::vector<double> > &sekce);
void print_aver_sekce(std::string, std::string);
void print_aver_sekce(void);
float get_aver(std::string cas_start, std::string cas_end, std::vector<time_t> &cas_v,
std::vector<float> &data);
double get_aver(std::string cas_start, std::string cas_end, std::vector<time_t> &cas_v,
std::vector<double> &data);
```

```
int get_data(std::vector<time_t> &cas_all, std::vector<float> &temp_all, std::string filename);
int get_data2(std::vector<time_t> &cas_all, std::vector<double> &temp_all, std::string filename);
void mv_aver(int av_count, int start_p, std::vector <double> &source_v, std::vector <double> &aver_v);

extern std::vector<std::vector<double> > temp_all;
extern std::vector<std::vector<double> > flow_all;
extern std::vector<std::vector<time_t> > cas_t_all;
extern std::vector<std::vector<time_t> > cas_f_all;
extern std::vector<std::vector<time_t> > cas_p_all;
extern std::vector<std::vector<double> > perf_all;
extern std::vector<time_t> cas_O2;
extern std::vector<float> vol_O2;
extern std::vector<time_t> cas_oxi;
extern std::vector<float> oxi_vol;
extern bool yes_comm;
extern bool rangeLoaded;
extern bool averLoaded;
extern bool oxiLoaded;
extern bool fileLoaded;
extern std::vector<std::vector <double> > sekce;
extern std::vector<std::vector <double> > sekce_aver;
extern std::string cas_file;
extern wxString cas_start, cas_end;
time_t get_time(std::string);
std::string get_time(time_t*);
extern wxString time_period;
extern std::vector<time_t> cas_O2;
extern std::vector<float> vol_O2;
extern time_t now;

//Slouží pro převod mezi string a wxString a naopak
inline wxString convStr(const std::string& s) {
```

```
  return wxString(s.c_str(), wxConvUTF8);
 }

 inline std::string convStr(const wxString& s)  {
  return std::string(s.mb_str(wxConvUTF8));
 }

#endif
```

Appendix I Software: CFD Energy Balance for Combustion Applications

This addon software is written in C language with the use of ANSYS Fluent® macros. It monitors overall energy balance.

Header file bilance_v1.4.h

```
#include "udf.h"
#include "sg_mem.h"
#include "string.h"

#define SIZE_OF_ARRAY(array) (sizeof(array)/sizeof(array[0]))

/*Formation enthalpy*/
#define HFORM_CH4 -7.489518e+07
#define HFORM_O2 0
#define HFORM_CO2 -3.935324e+08
#define HFORM_H2O -2.418379e+08
#define HFORM_N2 0
#define HFORM_CO -1.10539600e+08
#define MOLAR_WEIGHT_CH4 16
#define MOLAR_WEIGHT_CO 28
#define NUM_SPEC_UNBURN_WATCH 2

void get_mass_fraction(int num, int *thready, real
*mass_fraction, real *mass_flux, Domain *domain);
real get_enthalpy(int num, int *thready, real *flux, Domain
*domain);
real energy_imbalance(real *el, real *enth, real *mass, Domain
*domain);
real walls_heat_flux(int num, int thready[], Domain *domain);
/*real fuel_enthalpy(int num, int *thready, real *fuel_flux);*/
real radiation(int num, int *thready, real *radiation_each,
Domain *domain);
/*real air_enthalpy(int num, int *thready, real *air_flux);*/

/*If you don't want to use any of following threads put zero to
the array*/
int wall_thread[] =
{32,33,34,29,30,31,19,20,28,16,17,18,13,14,15,10,11,12,7,8,9}; /
*w_d1_side, w_d1_down, w_d1_up, ..... ,w_d7_side, w_d7_down,
w_d7_up*/
int inlet_thread[] = {53} /*a_air_inlet = 53*/;
int outlet_thread[] = {52};
int fuel_thread[] = {26,35,36}; /*a_gas_primary_higher = 26,
a_gas_secondary = 35, a_gas_primary_lower = 36*/
int rad_thread[] = {26,35,36,53,52};
```

Source code file Bilance_v1.4.c

```
/*
Pozor p  i zm  n   verze Fluentu:
funkce - species_name() - musí vracet  et  zec "invalid specie"
p  i p  ekro  ení po  tu dotazovaných složek
*/
#include "bilance_v1.4.h"
#include "species.h"

int aa=0;

#define NUM_ELEMENTS_ARRAY 12
#define NUM_ENTHALPY_ARRAY 3
#define NUM_MASS_FL_ARRAY 3

DEFINE_ON_DEMAND(bilance)
{
  #if !RP_HOST
  Domain *domain;
  real Heat_imbalance;
  /*----------------------*/
  real elements[NUM_ELEMENTS_ARRAY],
enthalpy[NUM_ENTHALPY_ARRAY], mass_flux[NUM_MASS_FL_ARRAY];
  /*----------------------*/

  domain = Get_Domain(ROOT_DOMAIN_ID);

  Heat_imbalance = energy_imbalance(elements, enthalpy,
mass_flux, domain);

  Message0("\n\n--------Vypocet bilance----------\n");
  Message0("\nEntalpie:\n Vzduch \t= %9.1f kJ/kg\n Palivo \t=
%9.1f kJ/kg\n Spalinovod \t= %9.1f
kJ/kg",enthalpy[0]/mass_flux[0], enthalpy[1]/mass_flux[1],
enthalpy[2]/mass_flux[2]
);
  Message0("\nHmotnostni tok:\n m_air \t\t= %9f kg/s\n m_fuel
\t= %9f kg/s\n m_out \t\t= %9f kg/s\n",mass_flux[0],
mass_flux[1], mass_flux[2]);

  Message0("\nLHV_CH4\t\t = %9.1f kJ/kg\nLHV_CO\t\t = %9.1f
kJ/kg\n"
  "\nAir\t\t = %11.6f kW\nFuel\t\t = %11.6f kW\nCombust\t\t =
%11.6f kW\nOut\t\t = %11.6f kW\nWalls\t\t = %11.6f
kW\nUnbur_CH4\t = %11.6f kW\nUnbur_CO\t = %11.6f kW"
```

```
  "\nRad_f_in\t = %11.6f kW\nRad_a_in\t = %11.6f kW",
elements[10], elements[11], elements[0], elements[1],
elements[2], elements[3], elements[4], elements[5], elements[6],
element
s[7], elements[8]);
  Message0("\nRad_out\t\t = %11.6f kW"
  "\n---------------------------------\n"
  "Imbalance\t = %11.6f kW\n", elements[9], Heat_imbalance);

  Message0("\n-------------Konec---------------");
  /*
  for(i=0,species_n=specie_name(domain,0);
(strncmp(species_n,"invalid specie",14) != 0) && (i <
MAX_SPE_EQNS) ;i++,species_n=specie_name(domain,i))
  {
    Message("\nNazev %d = %s",i,species_n);
  }*/

  /*char *name_ch4 = "ch4\n"
  ch4_id = mixture_specie_index(Material *m, char *name_ch4);*/
  #endif /*!RP_HOST*/
}

DEFINE_EXECUTE_AT_END(bilance_calc)
{
  real Heat_imbalance;
  real elements[NUM_ELEMENTS_ARRAY],
enthalpy[NUM_ENTHALPY_ARRAY], mass_flux[NUM_MASS_FL_ARRAY];

  #if !RP_HOST
  Domain *domain;

  domain = Get_Domain(ROOT_DOMAIN_ID);
  Heat_imbalance = energy_imbalance(elements, enthalpy,
mass_flux, domain);
  #endif /*!RP_HOST*/

  /*Sends data from node-0 to host, doesn't do anything in
serial*/
  node_to_host_real_1(Heat_imbalance);
  node_to_host_real(elements,NUM_ELEMENTS_ARRAY);
  node_to_host_real(enthalpy,NUM_ENTHALPY_ARRAY);
  node_to_host_real(mass_flux,NUM_MASS_FL_ARRAY);

  #if !RP_NODE
  FILE *soubor;
  aa++;
```

```
  if((soubor = fopen("_balance.out", "at")) == NULL) /*Opens
file _balance.out for appending data at the end ("a") in the
text mode ("t")*/
   Message("\n\nSoubor se neotevrel!!!!\n\n");

  /*First run & Unsteady*/
  if (aa==1 && rp_unsteady)
    fprintf(soubor, "\n#Flow time [s]  Imbalance [kW]  Heat to
walls [kW]  Spec. out enthalpy [kJ/kg]");
  /*First run & Steady*/
  if (aa==1 && !rp_unsteady)
    fprintf(soubor, "\n#Iteration  Imbalance [kW]  Heat to walls
[kW]  Spec. out enthalpy [kJ/kg]");
  /*Unstedy*/
  if (rp_unsteady)
    fprintf(soubor, "\n%g %g %g %g",CURRENT_TIME,
Heat_imbalance, elements[4], elements[3]);  /*Prints variables
into the file "soubor"(it is pointer) */
  else
    fprintf(soubor, "\n%d %g %g %g",N_ITER, Heat_imbalance,
elements[4], elements[3]);  /*Prints variables into the file
"soubor"(it is pointer) */

  if (fclose(soubor) == EOF)
    Message("\n\nNeco je se zavrenim souboru\n\n");
  #endif /*RP_!NODE*/
}

real energy_imbalance(real *el, real *enth, real *mass, Domain
*domain)
{
  real Heat_imbalance;
  real m_air = 0, m_out = 0, mass_flux_fr = 0;
  real enth_fuel = 0, enth_air = 0, enth_out = 0;
  real m_fuel = 0, lhv_CH4, lhv_CO;
  real Fuel=0, Air=0, Combust=0, Out=0, Walls=0, Unburnt_CH4=0,
Unburnt_CO = 0, Rad_f_in=0, Rad_a_in=0, Rad_out=0;
  real Radiation_all = 0;
  real mass_fraction[NUM_SPEC_UNBURN_WATCH]={0,0}; /*CH4, CO*/
  int num_rad = SIZE_OF_ARRAY(rad_thread);
  real rad_parts[num_rad];
  # if RP_NODE
  real mass_fl_work[NUM_SPEC_UNBURN_WATCH];
  real rad_work[num_rad];
  # endif
  int i;

  /*Goes in:
```

```
  - pointer to the array of threads on which to perform
evaluation
  - pointer to the array of mass fraction to be filled
  - reference to the over all mass flux (for all inserted
threads)
  - pointer to the domain
  */
  if (SIZE_OF_ARRAY(outlet_thread)>1 || outlet_thread[0] !=0)
    get_mass_fraction(SIZE_OF_ARRAY(outlet_thread),
outlet_thread, mass_fraction, &mass_flux_fr, domain);
  else
  {
    mass_flux_fr = 0;
    for(i=0; i<NUM_SPEC_UNBURN_WATCH; i++)
      mass_fraction[i] = 0;
  }

  /*Zjisteni hmotnostniho toku na vstupu vzduchu - pozor vraci
zapornou hodnotu pro tok smerem do domeny!!! */
  if (SIZE_OF_ARRAY(outlet_thread)>1 || outlet_thread[0] !=0)
    enth_out = get_enthalpy(SIZE_OF_ARRAY(outlet_thread),
outlet_thread, &m_out, domain);
  else  {
    enth_out = 0;
    m_out = 0;
    }

  if (SIZE_OF_ARRAY(inlet_thread)>1 || inlet_thread[0] !=0)
    enth_air = get_enthalpy(SIZE_OF_ARRAY(inlet_thread),
inlet_thread, &m_air, domain);
  else  {
    enth_air = 0;
    m_air = 0;
    }

  if (SIZE_OF_ARRAY(fuel_thread)>1 || fuel_thread[0] !=0)
    enth_fuel = get_enthalpy(SIZE_OF_ARRAY(fuel_thread),
fuel_thread, &m_fuel, domain);
  else  {
    enth_fuel = 0;
    m_fuel = 0;
    }

  /*mixture_species_loop(THREAD_MATERIAL(t),sp,i)
      {
        prop = (MATERIAL_PROPERTY(sp));
        ktc = generic_property(c,t,prop,PROP_hform,C_T(c,t));
        sum += C_YI(c,t,i)*ktc;
```

```
      }*/
  # if RP_NODE
  if I_AM_NODE_ZERO_P  {
  # endif /*RP_NODE*/
  lhv_CH4 = (-1*HFORM_CH4+HFORM_CO2+2*HFORM_H2O) /
MOLAR_WEIGHT_CH4/1000.0;
  lhv_CO = (-1*HFORM_CO+HFORM_CO2)/MOLAR_WEIGHT_CO/1000.0;
  # if RP_NODE
  }
  # endif /*RP_NODE*/

  /*Hodnoty v kW!*/
  if (SIZE_OF_ARRAY(rad_thread)>1 || rad_thread[0] !=0)
    Radiation_all = radiation(SIZE_OF_ARRAY(rad_thread),
rad_thread, rad_parts, domain)/1000;
  else   {
    Radiation_all = 0;
    for(i=0; i<num_rad; i++)
      rad_parts[i] = 0;
    }

  if (SIZE_OF_ARRAY(wall_thread)>1 || wall_thread[0] !=0)
    Walls =
walls_heat_flux(SIZE_OF_ARRAY(wall_thread),wall_thread,
domain)/1000;
  else
     Walls = 0;

  # if RP_NODE
  enth_out = PRF_GRSUM1(enth_out);
  enth_air = PRF_GRSUM1(enth_air);
  enth_fuel = PRF_GRSUM1(enth_fuel);
  m_out = PRF_GRSUM1(m_out);
  m_air = PRF_GRSUM1(m_air);
  m_fuel = PRF_GRSUM1(m_fuel);
  Radiation_all = PRF_GRSUM1(Radiation_all);
  Walls = PRF_GRSUM1(Walls);
  PRF_GRSUM(rad_parts,num_rad,rad_work);
  PRF_GRSUM(mass_fraction,NUM_SPEC_UNBURN_WATCH,mass_fl_work);
  # endif /*RP_NODE*/

  # if RP_NODE
  if I_AM_NODE_ZERO_P  {
  # endif /*RP_NODE*/
  Rad_f_in = (rad_parts[0]+rad_parts[1]+rad_parts[2])/1000;
  Fuel = enth_fuel/1000;
  Air = enth_air/1000;
  Combust = -lhv_CH4 * m_fuel;
```

```
  Out = enth_out/1000;
  Unburnt_CH4 = mass_fraction[0] * lhv_CH4;
  Unburnt_CO = mass_fraction[1] * lhv_CO;
  Rad_a_in = rad_parts[3]/1000;
  Rad_out = rad_parts[4]/1000;
  # if RP_NODE
  }
  # endif /*RP_NODE*/

  mass[0]=m_air; mass[1]=m_fuel; mass[2]=m_out;
  enth[0]=enth_air; enth[1]=enth_fuel; enth[2]=enth_out;
  el[0]=Air; el[1]=Fuel; el[2]=Combust; el[3]=Out; el[4]=Walls;
el[5]=Unburnt_CH4; el[6]=Unburnt_CO; el[7]=Rad_f_in;
el[8]=Rad_a_in; el[9]=Rad_out; el[10]=lhv_CH4; el[11]=lhv_CO;

  return Heat_imbalance = Fuel + Air + Combust + Out + Walls +
Unburnt_CH4 + Rad_f_in + Rad_a_in + Rad_out;
}

void get_mass_fraction(int num, int *thready, real
*mass_fraction, real *mass_flux, Domain *domain)
{
  Thread *thr[num];
  face_t f;
  real mass_flux1=0;
  int i;
  int ch4_pos = -1, co_pos = -1;
  char *species_n;

  *mass_flux = 0;
  /*RP_Get_Integer("variable-name")*/
   for(i=0,species_n=specie_name(domain,0);
(strncmp(species_n,"invalid specie",14) != 0) && (i <
MAX_SPE_EQNS) ;i++,species_n=specie_name(domain,i))
    {
      if(strncmp(species_n,"ch4",3)==0)
        ch4_pos=i;
      if(strncmp(species_n,"co",2)==0 && strlen(species_n)==2)
        co_pos=i;
    }

  for(i=0;i<num;i++)
  {
    thr[i] = Lookup_Thread(domain,thready[i]);
    /*Zjisteni koncentrace na vystupu a entalpie*/
    begin_f_loop(f,thr[i])
    {
      mass_flux1 = -F_FLUX(f,thr[i]);
```

```
      *mass_flux += mass_flux1;

      if (ch4_pos >= 0)
        mass_fraction[0] += F_YI(f,thr[i],ch4_pos)*mass_flux1;
/*CH4*/
      if (co_pos >= 0)
        mass_fraction[1] += F_YI(f,thr[i],co_pos)*mass_flux1;
/*CO*/

    /*enth_c += F_H(f,thr[i])*mass_flux_c;*/
    }
    end_f_loop(f,thr[i])
  }

  mass_fraction[0] = mass_fraction[0];  /*CH4*/
  mass_fraction[1] = mass_fraction[1];  /*CO*/
}

real get_enthalpy(int num, int *thready, real *flux, Domain
*domain)
{
  Thread *thr[num];
  face_t f;
  real enth_c=0;
  real mass_flux1=0, mass_flux=0;
  int i;

  for(i=0;i<num;i++)
  {
    thr[i] = Lookup_Thread(domain,thready[i]);

    begin_f_loop(f,thr[i])
    {
      mass_flux1 = -F_FLUX(f,thr[i]);
      mass_flux += mass_flux1;
      enth_c += F_H(f,thr[i])*mass_flux1;
    }
    end_f_loop(f,thr[i])
  }

  *flux = mass_flux;

  return enth_c/*/mass_flux*/;
}

real walls_heat_flux(int num, int thready[], Domain *domain)
{
  Thread *t_d[num];
```

```
  face_t f;
  int k,i;
  real flux[num/3+1];
  real h_flux = 0;

  domain = Get_Domain(ROOT_DOMAIN_ID);

  for(k=0;k<num/3+1;k++)
    flux[k] = 0;
  for(i=0;i<num;i++)
    t_d[i] = Lookup_Thread(domain,thready[i]);

  for(i=0,k=i/3;i<num;i++,k=i/3)
  {
    begin_f_loop(f,t_d[i])
    {
      flux[k] += WALL_HEAT_FLUX(f,t_d[i]);
      }
      end_f_loop(f,thread)
   }

   for(k=0;k<num/3;k++)
    h_flux += flux[k];

    return h_flux;
}

real radiation(int num, int *thready, real *radiation_each,
Domain *domain)
{
  Thread *t_rad[num];
  face_t f;
  real rad_flux=0,rad_flux_all = 0;
  int i;

  domain = Get_Domain(ROOT_DOMAIN_ID);

  for(i=0;i<num;i++,rad_flux=0)
  {
    t_rad[i] = Lookup_Thread(domain,thready[i]);

   begin_f_loop(f,t_rad[i]) {
     rad_flux += WALL_RAD_HEAT_FLUX(f,t_rad[i]);
   } end_f_loop(f,t_rad[i])

   radiation_each[i] = rad_flux;
   }
```

```
  for(i=0;i<num;i++)
    rad_flux_all += radiation_each[i];

  return rad_flux_all;
}
```

Appendix J Software: New WSGGM implementation

Header file wsggm_new.h

```
#include "udf.h"

#define MOLAR_WEIGHT_H2O 18.01528
#define MOLAR_WEIGHT_CO2 44.01 /*g/mol = kg/kmol*/

struct coeff {
  float k[4], be[4][4];
} /*Pw_0, Pw_01, Pw_03, PwPc_0125, PwPc_025, PwPc_05,PwPc_075,
PwPc_1, PwPc_2, PwPc_4*/;
struct coeff Ps[10];
int init_coeff();
```

Source code file wsggm_new.c

```
 #include "wsggm_new.h"

DEFINE_ON_DEMAND(pokus)
{
  float promen;
  init_coeff();
  promen = Ps[0].be[0][1];

  real P_w=0.0158465, P_c=0.00648669;
  int i,j, v;
  real a_eps=0,pred1=0, eps=0;
  real Tref = 1200, L=1, Tg=351.734;

   v=0;
    for (i=0;i<4;i++) {
      for(j=0;j<4;j++) {
        pred1 = Ps[v].be[j][i]*pow(Tg/Tref,j);
        a_eps+=pred1;
        Message("\nPS[%d].be[%d][%d]=%g; pred1 = %g; a_eps =
%g",v,j,i, Ps[v].be[j][i],pred1, a_eps);
      }
      eps += a_eps  * (1 - exp(-Ps[v].k[i] * (P_w+P_c) * L));
        Message("\nTg= %g; a_eps = %g; eps = %g\n",Tg,a_eps,
eps);
      a_eps=0;
    }
}
DEFINE_PROPERTY(abs_coeff,c,t)
{
  Domain *domain;
  Material *sp;
  char *species_n;
  real P_w, P_c;
  int i,j, v;
  real abs_c=0;
  real a_eps=0, eps=0;
  real Tref = 1200, L=1, Tg;
  int SecondRun=0;
  int co2_pos=-1;
  int h2o_pos=-1;

  domain = Get_Domain(ROOT_DOMAIN_ID);
    if (SecondRun == 0) {
    mixture_species_loop(THREAD_MATERIAL(t),sp,i) {
      species_n=specie_name(domain,i);
      if(strncmp(species_n,"co2",3)==0)
        co2_pos=i;
```

```
      if(strncmp(species_n,"h2o",3)==0 && strlen(species_n)==3)
      h2o_pos=i;
    }
    init_coeff();
    SecondRun = 1;
    }

    P_c= UNIVERSAL_GAS_CONSTANT*C_T(c,t)*C_R(c,t)*C_YI(c,t,
co2_pos)/MOLAR_WEIGHT_CO2; /*partial pressure [Pa]*/
    P_w= UNIVERSAL_GAS_CONSTANT*C_T(c,t)*C_R(c,t)*C_YI(c,t,
h2o_pos)/MOLAR_WEIGHT_H2O; /*partial pressure [Pa]*/

    Tg=C_T(c,t);
    P_c = P_c/101325.0;
    P_w = P_w/101325.0;
    L=3.6*2.9481/13.798;

  if (P_w+P_c <= 0.1) {
    v=0;
    for (i=0;i<4;i++) {
      for(j=0;j<4;j++)
        a_eps += Ps[v].be[j][i]*pow(Tg/Tref,j);
      eps += a_eps * (1 - exp(-Ps[v].k[i] * (P_w+P_c) * L));
       a_eps=0;
    }
  }
  else if (P_w+P_c <= 0.3)  {
    v=1;
    for (i=0;i<4;i++)
    {
      for(j=0;j<4;j++)
        a_eps += Ps[v].be[j][i]*pow(Tg/Tref,j);

      eps += a_eps * (1 - exp(-Ps[v].k[i] * (P_w+P_c) * L));
      a_eps=0;
    }
  }
  else if (P_w+P_c <= 0.5) {
    v=2;
    for (i=0;i<4;i++)
    {
      for(j=0;j<4;j++)
        a_eps += Ps[v].be[j][i]*pow(Tg/Tref,j);

      eps += a_eps * (1 - exp(-Ps[v].k[i] * (P_w+P_c) * L));
      a_eps=0;
    }
  }
```

```
  else if (P_w<=0.2*P_c) {
    v=3;
    for (i=0;i<4;i++)
    {
      for(j=0;j<4;j++)
        a_eps += Ps[v].be[j][i]*pow(Tg/Tref,j);

      eps += a_eps * (1 - exp(-Ps[v].k[i] * (P_w+P_c) * L));
      a_eps=0;
    }
  }
  else if (P_w<=0.4*P_c) {
    v=4;
    for (i=0;i<4;i++) {
      for(j=0;j<4;j++)
        a_eps += Ps[v].be[j][i]*pow(Tg/Tref,j);

      eps += a_eps * (1 - exp(-Ps[v].k[i] * (P_w+P_c) * L));
      a_eps=0;
    }
  }
  else if (P_w<=0.6*P_c) {
    v=5;
    for (i=0;i<4;i++) {
      for(j=0;j<4;j++)
        a_eps += Ps[v].be[j][i]*pow(Tg/Tref,j);

      eps += a_eps * (1 - exp(-Ps[v].k[i] * (P_w+P_c) * L));
      a_eps=0;
    }
  }
  else if (P_w<=0.9*P_c) {
    v=6;
    for (i=0;i<4;i++) {
      for(j=0;j<4;j++)
        a_eps += Ps[v].be[j][i]*pow(Tg/Tref,j);

      eps += a_eps * (1 - exp(-Ps[v].k[i] * (P_w+P_c) * L));
      a_eps=0;
    }
  }
  else if (P_w<=1.1*P_c) {
    v=7;
    for (i=0;i<4;i++) {
      for(j=0;j<4;j++)
        a_eps += Ps[v].be[j][i]*pow(Tg/Tref,j);

      eps += a_eps * (1 - exp(-Ps[v].k[i] * (P_w+P_c) * L));
```

```
      a_eps=0;
    }
  }
  else if (P_w<=2.5*P_c) {
    v=8;
    for (i=0;i<4;i++) {
      for(j=0;j<4;j++)
        a_eps += Ps[v].be[j][i]*pow(Tg/Tref,j);

      eps += a_eps * (1 - exp(-Ps[v].k[i] * (P_w+P_c) * L));
      a_eps=0;
    }
  }
  else {
    v=9;
    for (i=0;i<4;i++) {
      for(j=0;j<4;j++)
        a_eps += Ps[v].be[j][i]*pow(Tg/Tref,j);

      eps += a_eps * (1 - exp(-Ps[v].k[i] * (P_w+P_c) * L));
      a_eps=0;
    }
  }
  abs_c = -1/L*log(1-eps);

  if (abs_c!=abs_c)
    abs_c=0;
  else if (abs_c < 0)
    abs_c = 0;
  else if (abs_c > 1)
    abs_c = 1;

  return abs_c;
}
```

Source code wsggm_new_coeff.c

```
#include "wsggm_new.h"

int init_coeff()
{

/*Pw    0 atm; Pc    0 atm*/
Ps[0].k[0]=0.009422; Ps[0].be[0][0]=0.778969; Ps[0].be[1][0]=-
1.342848; Ps[0].be[2][0]=0.964858; Ps[0].be[3][0]=-0.195747;
Ps[0].k[1]=0.415646; Ps[0].be[0][1]=-0.011449; Ps[0].be[1]
[1]=0.343754; Ps[0].be[2][1]=-0.234886; Ps[0].be[3][1]=0.044008;
Ps[0].k[2]=11.617018; Ps[0].be[0][2]=-0.007627; Ps[0].be[1]
[2]=0.242233; Ps[0].be[2][2]=-0.173738; Ps[0].be[3][2]=0.033868;
Ps[0].k[3]=319.911168; Ps[0].be[0][3]=0.080082; Ps[0].be[1][3]=-
0.04928; Ps[0].be[2][3]=0.001861; Ps[0].be[3][3]=0.002232;

/*Pw = 0.1 atm; Pc = 0.1 atm*/
Ps[1].k[0]=0.256738; Ps[1].be[0][0]=0.492304; Ps[1].be[1][0]=-
0.433789; Ps[1].be[2][0]=0.279329; Ps[1].be[3][0]=-0.05777;
Ps[1].k[1]=3.108033; Ps[1].be[0][1]=0.082686; Ps[1].be[1]
[1]=0.486294; Ps[1].be[2][1]=-0.369752; Ps[1].be[3][1]=0.070509;
Ps[1].k[2]=52.585782; Ps[1].be[0][2]=0.144385; Ps[1].be[1][2]=-
0.083662; Ps[1].be[2][2]=0.002003; Ps[1].be[3][2]=0.003902;
Ps[1].k[3]=440.845718; Ps[1].be[0][3]=0.079515; Ps[1].be[1][3]=-
0.110361; Ps[1].be[2][3]=0.051379; Ps[1].be[3][3]=-0.007983;

/*Pw = 0.3 atm; Pc = 0.1 atm*/
Ps[2].k[0]=0.132242; Ps[2].be[0][0]=0.478371; Ps[2].be[1][0]=-
0.608643; Ps[2].be[2][0]=0.475098; Ps[2].be[3][0]=-0.109044;
Ps[2].k[1]=14.660767; Ps[2].be[0][1]=0.101065; Ps[2].be[1]
[1]=0.204118; Ps[2].be[2][1]=-0.202202; Ps[2].be[3][1]=0.042771;
Ps[2].k[2]=1.750654; Ps[2].be[0][2]=0.185155; Ps[2].be[1]
[2]=0.299794; Ps[2].be[2][2]=-0.240346; Ps[2].be[3][2]=0.046968;
Ps[2].k[3]=165.763926; Ps[2].be[0][3]=0.191665; Ps[2].be[1][3]=-
0.277448; Ps[2].be[2][3]=0.133514; Ps[2].be[3][3]=-0.02128;

/*Pw/Pc = 1:8; Pw + Pc = 1 atm (corresponding to dry flue gas
recycling)*/
Ps[3].k[0]=0.051237; Ps[3].be[0][0]=0.515415; Ps[3].be[1][0]=-
0.618162; Ps[3].be[2][0]=0.430921; Ps[3].be[3][0]=-0.092082;
Ps[3].k[1]=0.688383; Ps[3].be[0][1]=0.199807; Ps[3].be[1]
[1]=0.298581; Ps[3].be[2][1]=-0.265758; Ps[3].be[3][1]=0.05291;
Ps[3].k[2]=13.763205; Ps[3].be[0][2]=0.138767; Ps[3].be[1][2]=-
0.001851; Ps[3].be[2][2]=-0.049353; Ps[3].be[3][2]=0.013012;
Ps[3].k[3]=289.841885; Ps[3].be[0][3]=0.087511; Ps[3].be[1][3]=-
0.067295; Ps[3].be[2][3]=0.013489; Ps[3].be[3][3]=-5.54e-6;

/*Pw/Pc = 1:4; Pw + Pc = 1 atm*/
```

```
Ps[4].k[0]=0.052694; Ps[4].be[0][0]=0.486247; Ps[4].be[1][0]=-
0.644137; Ps[4].be[2][0]=0.485654; Ps[4].be[3][0]=-0.107808;
Ps[4].k[1]=0.752776; Ps[4].be[0][1]=0.213959; Ps[4].be[1]
[1]=0.306543; Ps[4].be[2][1]=-0.264417; Ps[4].be[3][1]=0.051889;
Ps[4].k[2]=11.543306; Ps[4].be[0][2]=0.181991; Ps[4].be[1][2]=-
0.02046; Ps[4].be[2][2]=-0.053791; Ps[4].be[3][2]=0.015058;
Ps[4].k[3]=252.938841; Ps[4].be[0][3]=0.10618; Ps[4].be[1][3]=-
0.096088; Ps[4].be[2][3]=0.028114; Ps[4].be[3][3]=-0.002443;

/*Pw/Pc = 1:2; Pw + Pc = 1 atm*/
Ps[5].k[0]=0.052378; Ps[5].be[0][0]=0.383225; Ps[5].be[1][0]=-
0.510937; Ps[5].be[2][0]=0.442201; Ps[5].be[3][0]=-0.106398;
Ps[5].k[1]=0.712283; Ps[5].be[0][1]=0.251481; Ps[5].be[1]
[1]=0.161562; Ps[5].be[2][1]=-0.150405; Ps[5].be[3][1]=0.028982;
Ps[5].k[2]=8.067637; Ps[5].be[0][2]=0.208239; Ps[5].be[1]
[2]=0.070697; Ps[5].be[2][2]=-0.135668; Ps[5].be[3][2]=0.03209;
Ps[5].k[3]=195.892573; Ps[5].be[0][3]=0.147259; Ps[5].be[1][3]=-
0.156339; Ps[5].be[2][3]=0.057698; Ps[5].be[3][3]=-0.007266;

/*Pw/Pc = 3:4; Pw + Pc = 1 atm*/
Ps[6].k[0]=0.051639; Ps[6].be[0][0]=0.255953; Ps[6].be[1][0]=-
0.276222; Ps[6].be[2][0]=0.311285; Ps[6].be[3][0]=-0.084903;
Ps[6].k[1]=0.617739; Ps[6].be[0][1]=0.340392; Ps[6].be[1][1]=-
0.126902; Ps[6].be[2][1]=0.051357; Ps[6].be[3][1]=-0.010259;
Ps[6].k[2]=6.05177; Ps[6].be[0][2]=0.160253; Ps[6].be[1]
[2]=0.289548; Ps[6].be[2][2]=-0.284144; Ps[6].be[3][2]=0.060344;
Ps[6].k[3]=150.875915; Ps[6].be[0][3]=0.201452; Ps[6].be[1][3]=-
0.233937; Ps[6].be[2][3]=0.095159; Ps[6].be[3][3]=-0.013302;

/*Pw/Pc = 1:1; Pw + Pc = 1 atm (corresponding to wet flue gas
recycling)*/
Ps[7].k[0]=0.051487; Ps[7].be[0][0]=0.164048; Ps[7].be[1][0]=-
0.087793; Ps[7].be[2][0]=0.195253; Ps[7].be[3][0]=-0.063573;
Ps[7].k[1]=0.571797; Ps[7].be[0][1]=0.412652; Ps[7].be[1][1]=-
0.33981; Ps[7].be[2][1]=0.197886; Ps[7].be[3][1]=-0.038963;
Ps[7].k[2]=5.398936; Ps[7].be[0][2]=0.112364; Ps[7].be[1]
[2]=0.450929; Ps[7].be[2][2]=-0.388486; Ps[7].be[3][2]=0.079862;
Ps[7].k[3]=130.622859; Ps[7].be[0][3]=0.238339; Ps[7].be[1][3]=-
0.288619; Ps[7].be[2][3]=0.121962; Ps[7].be[3][3]=-0.017651;

/*Pw/Pc = 2:1; Pw + Pc = 1 atm*/
Ps[8].k[0]=0.05448; Ps[8].be[0][0]=-0.002188; Ps[8].be[1]
[0]=0.286129; Ps[8].be[2][0]=-0.048594; Ps[8].be[3][0]=-
0.016243;
Ps[8].k[1]=0.555304; Ps[8].be[0][1]=0.546857; Ps[8].be[1][1]=-
0.714799; Ps[8].be[2][1]=0.452812; Ps[8].be[3][1]=-0.088841;
Ps[8].k[2]=5.040174; Ps[8].be[0][2]=-0.001911; Ps[8].be[1]
[2]=0.764177; Ps[8].be[2][2]=-0.581819; Ps[8].be[3][2]=0.115069;
```

```
Ps[8].k[3]=100.372663; Ps[8].be[0][3]=0.317219; Ps[8].be[1][3]=-
0.41547; Ps[8].be[2][3]=0.18657; Ps[8].be[3][3]=-0.028335;

/*Pw/Pc = 4:1; Pw + Pc = 1 atm*/
Ps[9].k[0]=0.0608; Ps[9].be[0][0]=-0.053999; Ps[9].be[1]
[0]=0.434975; Ps[9].be[2][0]=-0.152413; Ps[9].be[3][0]=0.005094;
Ps[9].k[1]=5.608831; Ps[9].be[0][1]=-0.094953; Ps[9].be[1]
[1]=0.95201; Ps[9].be[2][1]=-0.696161; Ps[9].be[3][1]=0.136316;
Ps[9].k[2]=0.67604; Ps[9].be[0][2]=0.606525; Ps[9].be[1][2]=-
0.853216; Ps[9].be[2][2]=0.545562; Ps[9].be[3][2]=-0.107328;
Ps[9].k[3]=84.540632; Ps[9].be[0][3]=0.369661; Ps[9].be[1][3]=-
0.517493; Ps[9].be[2][3]=0.244011; Ps[9].be[3][3]=-0.038451;

return 0;
}
```

Appendix K Software: High Temperature Data Acquisition

The source code bellow allows to read from serial line or usb incoming data strings and print them out on standard output with time stamp in millisecond resolution. Most of the source code is taken from the following site:

http://tldp.org/HOWTO/Serial-Programming-HOWTO/index.html

accessed online on 29th March 2012 and modified for our purpose.

Copyright Information


```
#include <stdio.h> /* Standard input/output definitions */
#include <string.h> /* String function definitions */
#include <unistd.h> /* UNIX standard function definitions */
#include <fcntl.h> /* File control definitions */
#include <errno.h> /* Error number definitions */
#include <termios.h> /* POSIX terminal control definitions */
#include <cstdlib>
#include <time.h>
#include <math.h>

#include <sys/types.h>
#include <sys/stat.h>
#include <sys/time.h>



        #define BAUDRATE B9600
        /* change this definition for the correct port */
```

```
        #define MODEMDEVICE "/dev/ttyUSB0"
        #define _POSIX_SOURCE 1

        #define FALSE 0
        #define TRUE 1

        volatile int STOP=FALSE;


        void time_withMiliSeconds(char *s_cas)
        {
          time_t cas;
          struct timeval t;
          struct tm *current;

          cas = time(0);
          current = localtime(&cas);

          gettimeofday(&t,NULL);

          sprintf(s_cas, "%02d:%02d:%02d.%d", current-
>tm_hour,current->tm_min, current->tm_sec,
int(round(t.tv_usec/1000.0)));
        }


        int main()
        {
          int fd, res;
          struct termios oldtio,newtio;
          char buf[255];
        /*
          Open modem device for reading and writing
        */
         fd = open(MODEMDEVICE, O_RDWR | O_NOCTTY );
         if (fd <0) {perror(MODEMDEVICE); exit(-1); }

         tcgetattr(fd,&oldtio); /* save current serial port
settings */
         bzero(&newtio, sizeof(newtio)); /* clear struct for new
port settings */

         newtio.c_cflag = BAUDRATE | CS8 | CLOCAL | CREAD |
PARODD;
          newtio.c_iflag = IGNPAR | ICRNL;
          newtio.c_oflag = 0;
          newtio.c_lflag = ICANON;
          newtio.c_cc[VMIN]=1;
```

```
          newtio.c_cc[VTIME]=0;

         tcflush(fd, TCIFLUSH);
         tcsetattr(fd,TCSANOW,&newtio);


        time_t cas;
        char s_cas[50];
        struct tm *current;


        cas = time(0);
        current = localtime(&cas);
        time_withMiliSeconds(s_cas);

        res = read(fd,buf,255);
        if (res > 0)
        {
          buf[res]=0;
//          printf("%d:%d:%d %s",current->tm_hour,current-
>tm_min, current->tm_sec, buf);
          printf("%s %s", s_cas, buf);
//        printf ("Res = %d\n", res);
        }
        else
          printf("\nError: Neni co cist! Zkontroluj pripojene
zarizeni a cislo portu.\n");
         /* restore the old port settings */

         tcsetattr(fd,TCSANOW,&oldtio);

         return 0;
        }
```

Appendix L Software: High Temperature Data Processing and Visualization

Inhouse code for input data correction and various averaging such as exponential, backward and central moving average and Gaussian filter. Data needs to be corrected due to unreliable transfer from Omega iSeries ® DPi8 monitor over the serial line. Correction is in multiple writing within 1 second and on the other side missing data for particular time range. This code enables direct data processing during measurement without requirement to install complex and expensive software such as Matlab®.

Example below illustrates the process of calibration against other thermocouples of type K.

```
#include <iostream>
#include <fstream>
#include <sstream>
#include <string>
#include <vector>
#include <cmath>
#include <ctime>
#include <algorithm>

using namespace std;

struct C_hodnoty {
 float cas;
 float teplota;
 bool operator ==(const float &val) //Slouží pro vyhledávací
funkci find(), aby prohledávala a porovnávala hodnotu "cas"
  {
    return (cas == val);
  }
};

class Senzory
{
  bool Nacteno, Averaged; //Možná nebude pot  eba
  string file_lab, file_nase;

  int chyby; //Po  et chyb nalezených v souboru (zápis 2x za
sekundu, chyb  jící data v sekund  )
  int pozice; //Hodnota konce na  tného souboru (jeho velikosti)
získaná pomocí myfile.tellg()
  int DefaultRange; //Rozsah pro pr  m  rování
  double AverageVal, FluctuationVal;

  int LoadData(void); //Na  te data ze souboru
  int LoadDataNase(void); //Na  te data ze souboru
```

```
  int CheckData(); //Vrací po  et opravených hodnot; Vykoná se
automaticky po na  tení dat ze souboru
  //N  jakým zp  sobem zajistit i porovnání s ostatními senzory!


  public:
    vector<C_hodnoty> hodnotyT1;
    vector<C_hodnoty> hodnotyT2;
    vector<C_hodnoty> hodnotyT3;
    vector<C_hodnoty> hodnotyTok;
    vector<C_hodnoty> hodnoty_nase;
    Senzory(const string fnmLab="", const string fnmNase="")
{file_lab = fnmLab; file_nase = fnmNase;
LoadData();LoadDataNase();};
    void tisk();
    void OpravData(vector<C_hodnoty> &data, const int oprava);
    void GaussianFilter(vector<double> &data, vector<double>
&vysledky, int sirka);
    void GaussianFilter(vector<C_hodnoty> &data, vector<double>
&vysledky, int sirka);
    double Average(const string from,const string to);
    double Average();
    double Fluctuation();
    double Fluctuation(const string from,const string to);
    double Uncertainty(const double err, const char typ);
    void mvAverBackward(const int av_count, int start_p, const
vector <double> &source_v, vector <double> &aver_v); //Klouzavý
pr  m  r
    //Parametry jsou: po  et hodnot v pr  m  ru, pozice kde za  ít
pr  m  rovat, ukazatel na zdrojový vektor, ukazatel na vektor s
pr  m  ry
    void mvAverCentral(const int av_count, int start_p, const
vector <C_hodnoty> &source_v, vector <double> &aver_v);
    void mvAverExponential(const int av_count, int start_p,
const vector <C_hodnoty> &source_v, vector <double> &aver_v);

    vector<C_hodnoty> &GetDataL(void){return hodnotyT1;};
//Vrací odkaz na vektor hodnot lze použít: F60.GetData() v
fun(vector<double> &data);
    vector<C_hodnoty> &GetDataN(void){return hodnoty_nase;};
//Vrací odkaz na vektor hodnot lze použít: F60.GetData() v
fun(vector<double> &data);
//     void SetRange(const string from,const string to);
};

void Senzory::tisk()
{
}
```

```
//Koriguje  as dle rozdílu zadaného v prom  nné "oprava" a
dopisuje desetinná místa pro více hodnot p  ipsaných pro stejnou
sekundu
void Senzory::OpravData(vector<C_hodnoty> &data, const int
oprava)
{
  float no[5];
  float aa=0;

  for (int i=0;i<data.size();i++)
  {
    //Korekce na posun  asu m    ení - náš versus jejich  as
    data.at(i).cas-=oprava;

    no[0]=data.at(i).cas;
    if(no[0]!=no[1])
      aa=0;
    else if(no[1]==no[0])
    {
      aa=1;
      if (no[2]==no[1]) {
        aa =2;
        if (no[3]==no[2]){
          aa=3;
          if (no[4]==no[3])
            aa=4;
        }
      }
    }

    if(aa!=0)
    {
      if(aa==1)
        data.at(i).cas=no[0]+1.0/(aa+1);
      else if (aa==2)
      {
        data.at(i-1).cas=no[0]+1.0/(aa+1);
        data.at(i).cas = no[0] + (1.0/(aa+1))*2;
      }
      else if (aa==3)
      {
        data.at(i-2).cas=no[0]+1.0/(aa+1);
        data.at(i-1).cas = no[0] + (1.0/(aa+1))*2;
        data.at(i).cas = no[0] + (1.0/(aa+1))*3;
      }
      else if (aa==4)
      {
```

```
        data.at(i-3).cas=no[0]+1.0/(aa+1);
        data.at(i-2).cas=no[0]+(1.0/(aa+1))*2;
        data.at(i-1).cas = no[0] + (1.0/(aa+1))*3;
        data.at(i).cas = no[0] + (1.0/(aa+1))*4;
      }
    }

    no[4]=no[3];
    no[3]=no[2];
    no[2]=no[1];
    no[1]=no[0];
  }
}

int Senzory::LoadData(void)
{
float sekunda, t1, t2, t3, t4;
C_hodnoty h1;
int pos;
string line;
ifstream myfile;
stringstream buffer1;

myfile.open(file_lab.c_str());

    if (myfile.is_open())
    {
        //Ur  í pozici konce souboru (jeho velikost)
        myfile.seekg (0, ios::end);
        pos = myfile.tellg();
        myfile.seekg (0, ios::beg);

        buffer1 << myfile.rdbuf(); //Na  tení celého souboru do
buffer1

        while (getline(buffer1,line))
        {
            if (line[0] != '#' && !iscntrl(line[0]))
            {
                //stringstream je prilis pomaly! proto se
pouziva sscanf()
//    stringstream(line) >> rok >>fuj >>mesic >>fuj >>den
>>hodina >>fuj >>minuta >>fuj >>sekunda >>var;
                sscanf(line.c_str(),"%f %f %f %f %f",&sekunda,
&t1, &t2, &t3, &t4);
                /*time_struct.tm_year=rok-1900;
                time_struct.tm_mon=mesic-1;
                time_struct.tm_mday=den;
```

```
                time_struct.tm_sec=sekunda;
                time_struct.tm_min=minuta;
                time_struct.tm_hour=hodina;
                time_struct.tm_isdst=-1;

                tim1 = mktime(&time_struct);
                if (tim1<0)
                {
                    cerr<<"Err.: Error getting time.\n"<<endl;
                    return -1;
                }*/
          h1.cas = sekunda;
          h1.teplota = t1;
          hodnotyT1.push_back(h1);
          h1.teplota = t2;
          hodnotyT2.push_back(h1);
          h1.teplota = t3;
          hodnotyT3.push_back(h1);
          h1.teplota = t4;
          hodnotyTok.push_back(h1);
            }
        }

        myfile.close();
        return pos;
        }
else
        cerr <<"\nUnable to open file " <<file_lab;
return -1;
}

int Senzory::LoadDataNase(void)
{
float cas1;
double t1;
int hodina,minuta,sekunda;
C_hodnoty h1;
int pos;
string line;
ifstream myfile;
stringstream buffer1;

myfile.open(file_nase.c_str());

    if (myfile.is_open())
    {
        //Ur  í pozici konce souboru (jeho velikost)
        myfile.seekg (0, ios::end);
```

```
        pos = myfile.tellg();
        myfile.seekg (0, ios::beg);

        buffer1 << myfile.rdbuf(); //Na  tení celého souboru do
buffer1

        while (getline(buffer1,line))
        {
            if (line[0] != '#' && !iscntrl(line[0]))
            {
                //stringstream je prilis pomaly! proto se
pouziva sscanf()
//    stringstream(line) >> rok >>fuj >>mesic >>fuj >>den
>>hodina >>fuj >>minuta >>fuj >>sekunda >>var;
                sscanf(line.c_str(),"%d:%d:%d %*s %lf",&hodina,
&minuta, &sekunda, &t1);

                /*
          cout << hodina <<":" << minuta <<":" << sekunda <<" "
<<t1 <<endl;

          time_struct.tm_year=0;
                time_struct.tm_mon=0;
                time_struct.tm_mday=0;
                time_struct.tm_sec=sekunda;
                time_struct.tm_min=minuta;
                time_struct.tm_hour=hodina;
                time_struct.tm_isdst=-1;

                tim1 = mktime(&time_struct);
                if (tim1<0)
                {

                    cerr<<"Err.: Error getting time.\n"<<endl;
                    return -1;
                }*/

          cas1 = hodina*3600+minuta*60+sekunda;
          h1.cas = cas1/*-56768*//*-(53520-38)*/;
          h1.teplota = t1;
          hodnoty_nase.push_back(h1);
           }
        }
        myfile.close();
        return pos;
        }
else
        cerr <<"\nUnable to open file " <<file_nase;
```

```
return -1;
}

//Gausuv filtr (rozsah 3 sigma dle
http://www.librow.com/articles/article-9) - na okrajích nejsou
data zpracována a pouze se do výsledk  nakopírují p  vodní
hodnoty
void Senzory::GaussianFilter(vector<double> &data,
vector<double> &vysledky, int sirka)
{
  vector<double> G1;
  vector<double> G2;
  double vysl=0, k=0, pom=0;
  int i,j;

  //Dopln  ní výsledk  o data ze za átku zdrojového vektoru
  for(i=0;i<sirka;i++)
    vysledky.push_back(data.at(i));

  //Výpo et Gaussových koeficient  nap : {0.011109, 0.606531, 1,
0.606531, 0.011109}
  for(j=0;j<(2*sirka+1);j++)
    {
      vysl=exp(-(pow(3*(j-sirka)/sirka,2)/2));
      G2.push_back(vysl);
      k+=G2.back();
    }

  //Výpo et váh
  for(j=0;j<(2*sirka+1);j++)
      G1.push_back(G2.at(j)/k);

  //Vlastní výpo et filtrovaných dat
  for(i=sirka;i<data.size()-sirka;i++)
  {
    for(j=-sirka;j<sirka+1;j++)
       pom += G1.at(j+sirka)*data.at(i+j);

    vysledky.push_back(pom);
    pom=0;
  }

  //Dopln  ní výsledk  o data z konce zdrojového vektoru
  for(i=data.size()-sirka;i<data.size();i++)
    vysledky.push_back(data.at(i));
}
```

```
//Gausuv filtr (rozsah 3 sigma dle
http://www.librow.com/articles/article-9) - na okrajích nejsou
data zpracována a pouze se do výsledk   nakopírují p  vodní
hodnoty
void Senzory::GaussianFilter(vector<C_hodnoty> &data,
vector<double> &vysledky, int sirka)
{
  vector<double> G1;
  vector<double> G2;
  double vysl=0, k=0, pom=0;
  int i,j;

  //Dopln  ní výsledk   o data ze za  átku zdrojového vektoru
  for(i=0;i<sirka;i++)
    vysledky.push_back(data.at(i).teplota);

  //Výpo  et Gaussových koeficient   nap  : {0.011109, 0.606531, 1,
0.606531, 0.011109}
  for(j=0;j<(2*sirka+1);j++)
    {
      vysl=exp(-(pow(3*(j-sirka)/sirka,2)/2));
      G2.push_back(vysl);
      k+=G2.back();
    }

  //Výpo  et váh
  for(j=0;j<(2*sirka+1);j++)
      G1.push_back(G2.at(j)/k);

  //Vlastní výpo  et filtrovaných dat
  for(i=sirka;i<data.size()-sirka;i++)
  {
    for(j=-sirka;j<sirka+1;j++)
       pom += G1.at(j+sirka)*data.at(i+j).teplota;

    vysledky.push_back(pom);
    pom=0;
  }

  //Dopln  ní výsledk   o data z konce zdrojového vektoru
  for(i=data.size()-sirka;i<data.size();i++)
    vysledky.push_back(data.at(i).teplota);
}


void Senzory::mvAverBackward(const int av_count, int start_p,
const vector <double> &source_v, vector <double> &aver_v)
{
```

```
    int divis=0, numer = 0;
    double var=0;

    if (start_p < 1 )
        start_p = 1;

    aver_v.push_back(source_v.at(0));
    for (int i=start_p; i<source_v.size(); i++)
    {
        if (i<av_count)
        {
            var = 0;
            divis = i+1;
            numer = i;
        }
        else
        {
            divis = av_count;
            numer = av_count;
            var = source_v.at(i-av_count); //Hodnota, která se
vy  azuje z pr  m  ru
        }

        aver_v.push_back((aver_v.at(i-1)*numer - var +
source_v.at(i))/divis);
    }
}

//Klouzavý pr  m  r - hodnoty jsou pr  m  rovány zp  tn   i dop  edn
(odstra  uje posun u pouze zp  tného pr  m  rování), celkový po  et
pr  m  rovaných bod   je 2*av_count+1
void Senzory::mvAverCentral(const int av_count, int start_p,
const vector <C_hodnoty> &source_v, vector <double> &aver_v)
{
    int divis=0, numer = 0, i;
    double var=0;

    if (start_p < av_count )
        start_p = av_count;

    for (i=start_p-av_count;i<=start_p;i++)
      aver_v.push_back(source_v.at(i).teplota);

    for (i=start_p+1; i<(source_v.size()-av_count); i++)
    {
        divis = 2*av_count+1;
        numer = 2*av_count+1;
        if ((i-av_count-1) < 0)
```

```
          var=0;
        else
          var = source_v.at(i-av_count-1).teplota; //Hodnota,
          která se vy  azuje z pr  m  ru

        aver_v.push_back((aver_v.at(i-1)*numer - var +
        source_v.at(i+av_count).teplota)/divis);
    }

    //Celý konec vektoru vyplní hodnotou z pozice
(source_v.size()-av_count) ==> hodnoty na konci jsou všechny
stejné
    for(i=source_v.size()-av_count; i<source_v.size(); i++)
      aver_v.push_back(aver_v.at(source_v.size()-av_count-1));
}

//Exponenciální klouzavý pr  m  r
void Senzory::mvAverExponential(const int av_count, int start_p,
const vector <C_hodnoty> &source_v, vector <double> &aver_v)
{
    double alpha;
    int i;

    alpha = 2.0/(av_count*2+1.0);

    if (start_p < 1 )
        start_p = 1;

      aver_v.push_back(source_v.at(start_p-1).teplota);

    for (i=start_p; i<source_v.size(); i++){
      aver_v.push_back(alpha*source_v.at(i).teplota+(1-
alpha)*aver_v.at(i-start_p));
//       cout << alpha <<"\t" << source_v.at(i).teplota <<"\t"
<<aver_v.back() <<endl;
    }

}



int main ()
{
  vector <double> vysledkyGaus_1;
  vector <double> vysledkyGaus_2;
  vector <double> vysledkyMvAver_1;
  vector <double> vysledkyMvAver_2;
  vector <double> vysledkyExpo_1;
```

```
  vector <double> vysledkyExpo_2;
  int width = 50;
  int i;
  Senzory s1("mereni1_T.txt", "data.txt");

  s1.GaussianFilter(s1.hodnoty_nase, vysledkyGaus_1, width);
  s1.mvAverCentral(width, 0, s1.hodnoty_nase, vysledkyMvAver_1);
  s1.mvAverExponential(width, 0, s1.hodnoty_nase,
vysledkyExpo_1);

  Senzory s2("mereni2_T.txt", "data900_final.txt");

  s1.OpravData(s1.hodnoty_nase, 53520-38);
  s2.OpravData(s2.hodnoty_nase, 56768);

  s2.GaussianFilter(s2.hodnoty_nase, vysledkyGaus_2, width);
  s2.mvAverCentral(width, 0, s2.hodnoty_nase, vysledkyMvAver_2);
  s2.mvAverExponential(width, 0, s2.hodnoty_nase,
vysledkyExpo_2);

  cout <<"Cas\tBez filtru\tGauss\tKl. prum. centr\tKl. prum.
expo" <<endl;

//Vytiskne rozdíly mezi hodnotami vždy v celou sekundu.
  vector<C_hodnoty>::iterator it;
  vector<C_hodnoty> tempDiff;
  C_hodnoty diff;

  for (i=0;i<s1.hodnotyT1.size();i+=3)
  {
    it=find(s1.hodnoty_nase.begin(), s1.hodnoty_nase.end(),
s1.hodnotyT1.at(i).cas);
    if (it != s1.hodnoty_nase.end()){
      diff.cas=it->cas;
      diff.teplota = s1.hodnotyT1.at(i).teplota - it->teplota;
      tempDiff.push_back(diff);
      cout <<tempDiff.back().cas <<"\t"
<<s1.hodnotyT1.at(i).teplota <<"\t" <<it->teplota <<"\t"
<<tempDiff.back().teplota <<endl;
    }
  }

  for (i=0;i<s2.hodnotyT1.size();i+=3)
  {
    it=find(s2.hodnoty_nase.begin(), s2.hodnoty_nase.end(),
s2.hodnotyT1.at(i).cas);
    if (it != s2.hodnoty_nase.end()){
      diff.cas=it->cas+2246;
```

```
      diff.teplota = s2.hodnotyT1.at(i).teplota - it->teplota;
      tempDiff.push_back(diff);
      cout <<tempDiff.back().cas+1006 <<"\t"
<<s2.hodnotyT1.at(i).teplota <<"\t" <<it->teplota <<"\t"
<<tempDiff.back().teplota <<endl;
    }
  }
 return 0;
}
```

Gnuplot source file for generation of approximate temperature contourplot from several measured positions.

```
set style line 1 lc -1 lw 2 ps 2
set title "Flame temperature [℃]"
set xlabel "Length of chamber [m]"
set ylabel "Diameter of chamber [m]"
set terminal png font arial 22 size 2000,600
set output "komora_plamen_en.png"
set palette maxcolors 50 color
set palette defined ( 500 "dark-blue", 680 "blue", 860 "green", 1040 "yellow", 1220 "red", 1400 "dark-red" )
set xrange [4:0]
set pm3d interpolate 50,50
set view map

splot "data_tisk.txt" u 2:1:3 w pm3d notitle, "" u 2:(1-$1):3 w pm3d notitle, "" u 2:1:3 w p ls 1 notitle
```

Appendix M Forced radiation convergence routine

Routine is written in Unix shell Bash (Bourne-again shell) [111]. It generates a journal file "`radiation_iter.jou`" which can be offered to ANSYS Fluent to control its run.

```
#! /bin/bash
#
#Usage: sh jougen_radiace_keps.sh case_file.cas.gz
data_file.dat.gz
#It assumes that you run this script from directory where are
all the monitors data stored, otherwise you have to set variable
monitno.
#

test $# -lt 2 && {
echo "Parameter missing - two parameters required!!"
echo "Usage: sh jougen_radiace_keps.sh case_file.cas.gz
data_file.dat.gz"
exit
}

test -a radiation_iter.jou && {
rm -f radiation_iter.jou
}

echo "Enter how many flow iterations to perform in total: "
read iter
echo "Enter how many flow iterations per radiation iterations: "
read fr
echo "Enter how many radiation iterations: "
read rn

echo "Enter number of iterations befor 1st save (from begining):
"
read sf
echo "Enter number of iterations befor 2nd save (from previous
save): "
read ssf
echo "Enter number of iterations befor 3rd save (from previous
save): "
read srf

echo "/file/read-case $1" >> radiation_iter.jou;
echo "/file/read-data $2" >> radiation_iter.jou;
echo "/file/set-batch-options y y n" >> radiation_iter.jou;
echo "/solve/set/equation/disco y"  >> radiation_iter.jou;
```

```
echo "/define/models/radiation/radiation-model-parameters $
(($fr+1))" >> radiation_iter.jou;  #Po  et flow iterací na
radia  ní iterace
echo "/solve/iterate $fr" >> radiation_iter.jou;

#Append monitors to existing files? = yes!!!
test -z "$monitno" && {
monitno=$(ls -l *.out |wc -l)
}
for ((i=1;i<=monitno;i++))
  do
    echo "yes" >> radiation_iter.jou;
  done

ff=$(($iter/$fr))
for ((i=1;i<=ff;i+=1));
  do
    echo "/define/models/radiation/radiation-model-parameters 1"
>> radiation_iter.jou;  #Po  et flow iterací na radia  ní iterace
    echo "/solve/set/equation/flow n" >> radiation_iter.jou;
    echo "/solve/set/equation/ke n" >> radiation_iter.jou;
    echo "/solve/set/equation/species-0 n" >>
radiation_iter.jou;
    echo "/solve/set/equation/species-1 n" >>
radiation_iter.jou;
    echo "/solve/set/equation/species-2 n" >>
radiation_iter.jou;
    echo "/solve/set/equation/species-3 n" >>
radiation_iter.jou;
    echo "/solve/set/equation/temperature n" >>
radiation_iter.jou;
    echo "/solve/set/equation/disco y"  >> radiation_iter.jou;
    #echo "/define/models/radiation/radiation-model-parameters
1" >> radiation_iter.jou;
    echo "/solve/iterate $rn" >> radiation_iter.jou;

    echo "/define/models/radiation/radiation-model-parameters $
(($fr+1))" >> radiation_iter.jou;  #Po  et flow iterací na
radia  ní iterace
    echo "/solve/set/equation/flow y" >> radiation_iter.jou;
    echo "/solve/set/equation/ke y" >> radiation_iter.jou;
    echo "/solve/set/equation/species-0 y" >>
radiation_iter.jou;
    echo "/solve/set/equation/species-1 y" >>
radiation_iter.jou;
    echo "/solve/set/equation/species-2 y" >>
radiation_iter.jou;
```

```
    echo "/solve/set/equation/species-3 y" >>
radiation_iter.jou;
    echo "/solve/set/equation/temperature y" >>
radiation_iter.jou;
    echo "/solve/set/equation/disco n"  >> radiation_iter.jou;
    #echo "/define/models/radiation/radiation-model-parameters $
(($fr+5))" >> radiation_iter.jou;
    echo "/solve/iterate $fr" >> radiation_iter.jou;

    if [ $i -eq $(($sf/$fr)) ]
     then
      echo "wd ./${2%.dat.gz}_1_$sf-it.dat.gz" >>
radiation_iter.jou;
    fi

    if [ $i -eq $((($sf+$ssf)/$fr)) ]
      then
      echo "wd ./${2%.dat.gz}_1_$ssf-it.dat.gz" >>
radiation_iter.jou;
    fi

    if [ $i -eq $((($sf+$ssf+$srf)/$fr)) ]
      then
      echo "wd ./${2%.dat.gz}_1_$srf-it.dat.gz" >>
radiation_iter.jou;
    fi

  done

echo "wd ./${2%.cas.gz}_$iter-it.dat.gz" >> radiation_iter.jou;
echo "exit yes" >> radiation_iter.jou;
exit 0
```

Appendix N A novel approach to the uniform distribution of liquid in multi-channel (electrochemical) flow-through cells

This appendix contains author's paper published in Journal Analytica Chimica Acta, Volume 727, 21 May 2012, Pages 41-46.

Bibliographic citation:

LACINA, K., VONDÁL, J. and SKLÁDAL, P. A novel approach to the uniform distribution of liquid in multi-channel (electrochemical) flow-through cells. In: *Analytica Chimica Acta*. 21 May 2012, Vol. 727, no. 0, pp. 41–46. DOI 10.1016/j.aca.2012.03.046.

Analytica Chimica Acta 727 (2012) 41–46

Contents lists available at SciVerse ScienceDirect

Analytica Chimica Acta

journal homepage: www.elsevier.com/locate/aca

A novel approach to the uniform distribution of liquid in multi-channel (electrochemical) flow-through cells

Karel Lacina[a,*], Jiří Vondál[b], Petr Skládal[a,c]

[a] Department of Biochemistry, Faculty of Science, Masaryk University, Kotlářská 2, 611 37 Brno, Czech Republic
[b] Institute of Process and Environmental Engineering, Faculty of Mechanical Engineering, Brno University of Technology, Technická 2, 616 69 Brno, Czech Republic
[c] CEITEC MU, Masaryk University, Kamenice 5, 625 00 Brno, Czech Republic

ARTICLE INFO

Article history:
Received 9 January 2012
Received in revised form 20 March 2012
Accepted 27 March 2012
Available online 3 April 2012

Keywords:
Flow injection analysis
Multi-channel electrochemical cell
Uniform liquid distribution
Amperometry

ABSTRACT

Four-channel flow-through electrochemical cell working in thin-layer regime was designed, fabricated and characterized experimentally and in computational fluid dynamics (CFD) simulations. The new principle of operation allows reproducible splitting of a stream of liquid into multiple flow channels. Systems comprising of 2-, 3-, 4- and 8-channels were tested. The proper function of the cell is given by the ratio of the cross-sections of the fluidic element collecting chamber and the particular flow paths among which the liquid is distributed. Suitable flow rates providing uniform liquid distribution were evaluated and the results were compared to CFD modeling. The flow-through cells designed according to the proposed principle can be simply incorporated in automated routine analysis as only one inlet and one common outlet are required.

1. Introduction

Analytical techniques combining several methods or measuring elements always result in a more powerful tool than the simple direct sum of its single parts. However, the combined techniques do not bring only advantages. For example, multi-channel electrochemical sensors linked to flow-through techniques provide more comprehensive analysis of the sample and the simplicity of automation; unfortunately, some 'minor' difficulties appear, too. Perhaps the most important is the uniformity in chemical (composition) and physical (liquid flow) properties of the analyzed solution above the individual sensing surfaces, which is required for comparable results from all channels. Furthermore, the sensing elements must not affect each other by cross-talks. These complications can be solved by absolute spatial separation of the electrodes to channels with uniformly flowing liquid. The realization of such simple conditions is not straightforward and various alternatives were proposed. Although reports on multiple working electrodes are not frequent [1,2] in comparison with single-channel set-ups, multi-electrode fluidic systems working either in thin-layer or wall-jet regimes operating in non-recycling modes [1,3] were considered.

The elegant solution for a pair of electrodes was introduced by Kurita et al. [4]; a fluidic element "microseparator" divided the main channel into two branches just in the location of the electrodes. Nevertheless, this simple and robust principle can hardly be applied for more than two channels. Electrodes can also be simply placed on the opposite walls of a channel [5]. Simultaneous data acquisition was achieved using microelectrode arrays based on 16-elements [6] and even 32-elements [7]. Being placed parallel with the flowing liquid, cross-talk effects were not significant [8]. On the other hand, realization, especially manufacturing and characterization of such defined microelectrodes and their further modification, is much more demanding in comparison with common screen-printed 'macro' electrodes [6,9]. Dock et al. [10] solved distribution of liquid among eight electrodes by integration of a stirring element; the screen-printed sensor with eight electrodes arranged in a circular layout formed the bottom of the cell and the stirrer with the inlet was placed above. However, this is strongly enhancing the cross-talk effects.

The dilemma of the uniform distribution is often solved by using the wall-jet regime [11]; liquid is driven directly against the circular electrode array and radial flow into all directions from the inlet is obtained. A large space behind the circle of the array and rather high flow rate are required, the latter results in high consumption of samples and reagents. Similar but transitional architecture was utilized for cells working in a thin-layer regime [12–14]. Nevertheless, at slow flow rates, these designs with shared working space exhibit cross-talk between neighboring electrodes and excessive dilution of the zone of sample limits reproducibility.

In this contribution, a novel principle of uniform liquid distribution into multiple channels was proposed. The incoming liquid

* Corresponding author. Tel.: +420 5 49 49 60 36.
E-mail address: lacinak@chemi.muni.cz (K. Lacina).

0003-2670/$ – see front matter © 2012 Elsevier B.V. All rights reserved.
http://dx.doi.org/10.1016/j.aca.2012.03.046

stream becomes split among n identical symmetrically arranged flow channels, each containing the disc-shaped working electrode. After splitting and passing through the channels, the divided streams are re-joined in the so-called collecting chamber; this is basically a large space with a single common outlet. Due to the large collecting volume compared to the channels, the output path can be placed anywhere without any relation to the array of channels.

The 4-channel electrochemical cell based on such design was developed for characterization of complex samples using the bioelectronic tongue format [15]. Properties of this cell were investigated using flow-through amperometric experiments considering the effects of different volumes of the collecting chamber and variable flow rates. The hydrodynamic properties of the cell were also simulated with the help of the computational fluid dynamics (CFD).

2. Experimental

2.1. Apparatus and electrochemical measurements

Electrochemical cell and forms for casting of sealing were cut from poly(methyl methacrylate) (PMMA, 10 mm thick squares, Panchim, Bulgaria) using the KOSY2-MCS CNC-milling machine (MAX Computer, Germany) operated under the NCCad7 version 7.0 software. The sealing was made from a silicone-based Lukopren N Super (Lucebni zavody Kolin, Czech Rep.).

The flow-through system consisted of the peristaltic pump Minipuls 3 (Gilson, Villeurbanne, France), six-position switching valve (VICI Valco Instruments, Houston, USA), multi-channel electrochemical cell and either the 4-channel potentiostat ImmunoSMART (SMART Brno, Czech Rep.) or the 8-channel potentiostat (J. Kitlicka, Brno, Czech Rep.) linked to the data acquisition card PCI-6251 (National Instruments, Austin, USA). Amperometric detection in the two electrode set-up was carried out at 400 mV against the Ag/AgCl pseudoreference/counter electrode. The gold-based 4- and 8-channel screen printed sensors (SPE, BVT Technologies, Czech Rep.) were used. Sampling time for measurements was 0.2 s, otherwise it is mentioned in the text. Changes of current due to the introduction of the zone of sample (1 mM potassium ferrocyanide) into the carrier stream (50 mM phosphate buffer pH 7.4, 100 mM KCl, 0.1% Tween 20) were recorded and visualized with the program LabTools (developed in-house). Data evaluation was done using Origin 7.0 (Microcal, Northampton, USA) as discussed below.

2.2. Computational fluid dynamics simulation (CFD)

Virtual simulation experiments were carried out utilizing CFD with the final volume method in the program ANSYS Fluent ver. 12.1 [16]. The fluid cell model consisted of 960,000 cells, mostly polyhedral elements in the channels and hexahedral elements in the straight parts. The Reynolds number Re was calculated from flow velocity and liquid viscosity:

$$Re = \frac{\upsilon D}{\nu}$$

where parameters included hydraulic diameter $D = 4S/o$, S represents area, o wetted perimeter, υ velocity and ν kinematic viscosity. Re varied between 0.11 and 4.76 for flow rates 24 and 1000 μL min^{-1}, respectively. Hence the laminar flow regime was assumed [17]. The liquid was assumed to be incompressible, isothermal and without chemical reactions. The only equations to be solved were continuity equation and momentum transport (Navier–Stokes equations [18]).

3. Results and discussion

3.1. Principle of the flow cell

The uniform splitting of the primary flow stream into several separated channels containing the sensing element should provide the same flow velocities in all channels. The proposed principle is based on the assumption that all channels, among which the liquid should be distributed, must possess the highest possible similarity. If all channels are equivalent or at least the differences among them are negligible, the flowing liquid would not prefer any of them. The similarity of channels is expressed by the pressure loss, which denotes that flow rate (the most important parameter describing distribution of liquid) will be higher in the channel offering the smallest change of pressure in the system. The meaning of the pressure loss in fluidics can be analogously compared to resistance in electronics, the higher resistance (pressure loss) leads to the lower current (flow rate) at the given voltage (initial static pressure). This system offers also limited flow regulating behavior driven by a feedback mechanism. If the liquid is flowing towards the place with originally lower pressure loss, the local flow rate becomes increased, but the pressure loss grows up as well. If there is another channel for liquid to flow, it chooses this one and pressure loss in the previous place is lowered back. The basic rule is that the pressure loss must be identical in all channels between common inlet and common outlet. Therefore, the flow rate is established to reach the same pressure loss along every channel under steady-state conditions.

The obvious conditions influencing the system are thus the cross-section, shape and length of the channels and their arrangement with respect to the inlet (material of the walls is supposed to be the same in structure and composition). Providing that the channels should be similar as much as possible, the easiest way is to fabricate them as short as possible while not affecting the diffusion layer of the sensing surface. Hence the influence of the fabrication inaccuracy becomes minimized. Generally, the suitable arrangement of channels stems from their combination in the simplest symmetrical and regular shape (a line for 2 channels, n-branched stars for n channels) with the inlet in the center.

For possible automation, the detection cell should be easily mounted to the flow path, so it must be equipped with one inlet and preferably with one outlet. Rejoining of the split liquid streams represents the second and even more complicated condition. To obtain the fluidic system with equal pressure losses, *i.e.* all channels are absolutely interchangeable, the best possibility are short channels with direct opening to the waste. Nevertheless, this solution is not straightforward and easily applicable, especially when dangerous, infectious or odorous materials are analyzed. The collection of the analyzed liquid in a (closed) container is naturally advantageous for handling. All potential arrangements combining several channels and one common outlet are facing the same problem represented by different pressure loss between at least pair of channels. One principal solution offers possibility to circumvent or neglect this difference – incorporation of the collecting chamber to the output path of the fluidic system.

The collecting chamber represents a fluidic element, where all channels are terminated by direct openings. The purpose of the collecting chamber can be demonstrated as follows: if *e.g.* four channels arranged in a cross should be combined with the single outlet, it is impossible to place this outlet symmetrically to all channels. In the most symmetrical arrangement, two of the channels will always be closer to the outlet (see Fig. 1C). The flow rate in the closer channels outperforms the others to equilibrate pressure loss differences. The role of the collecting chamber is to lower significance of this difference through the elimination of the pathway dissimilarities. In fact, the difference of pressure

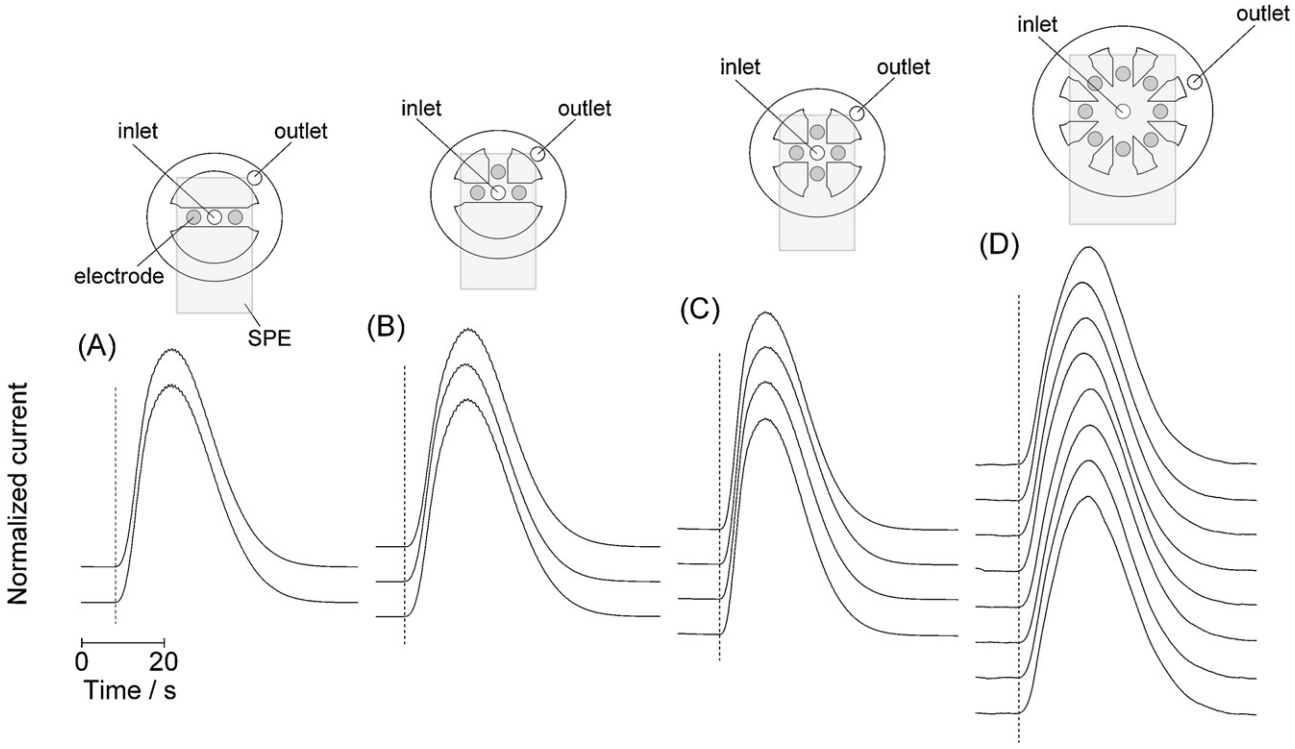

Fig. 1. Normalized record of measured current for selected *n*-channel electrochemical flow-through cells. Fluidic system is visualized above the corresponding curve. Experimental conditions: 20 s injection of 1 mM ferrocyanide, flow rate 150 μL min^{-1}, working potential 400 mV *vs.* Ag/AgCl.

loss between two channels becomes negligible in comparison to the difference between collecting chamber and any single channel. Therefore in the general case, flow channels combined with the collecting chamber represent inseparable parts of the whole fluidic system.

3.2. Multi-channel flow cells and the cell architecture

The proposed principles were tested on 2-, 3-, 4- and 8-channel electrochemical cells designed and fabricated to be compatible with the commercial screen-printed electrodes. In Fig. 1, the recorded smoothed curves (10 points adjacent averaging) of normalized current from individual channels can be seen together with fluidic pathways. The normalization of the signal was performed as division of the particular set of data representing one curve by its highest value, so the maximum always reached the value of 1. The highest symmetry of the channels combination was advantageous, but if the similarity among individual channels is sufficient, also less symmetrical (Fig. 1B) or even irregular shapes can be employed.

The architecture of the cell common for all variants is described for the 4-channel version. It consists of four parts (Fig. 2), the upper PMMA part (1) with inlet (5), collecting chamber (12) and outlet (6), sealing (2) with a system of four flow channels (10), SPE array (3) with four disc electrodes (9) representing bottom of the cell and the lower PMMA part (4) serving for precise placement of SPE. The whole cell is held together by four screws (7). The specific and reproducible diameter of channels (defined by the sealing made from soft silicone material) is achieved due to the end-stops (13) located around each screw hole. When the electrochemical cell becomes assembled, liquid is flowing through the inlet in the upper PMMA part directly against SPE, then reaching center of the fluidic system (8) formed by the sealing and SPE itself. The stream of liquid becomes divided among channels. In the end of each channel, liquid enters the collecting chamber in the upper PMMA part through a particular channel outflow (11). The flow is gathered up from all channels in the collecting chamber and aims to the single outlet, as shown in animation (Supporting Information).

Reference electrode (REF) (14) can be with advantage placed in the opposite side of the collecting chamber with respect to the common outlet. In this region (as visualized by computational modeling) there are no convective forces, no liquid is flowing and biased voltage is thus not influenced. Measurement for 2 and 3 channels was realized with the identical equipment, but with different sealing elements employing only 2 or 3 electrodes from SPE according to fluidic pathways. The 8-channel SPE array possessed its own REF/AUX electrodes.

For the proper function of the multi-channel cell, flow rates in the channel and in the collecting chamber must be in some specific relation, which is given by the ratio of their cross-section areas. This relation was considered in experiments and in the CFD modeling as well.

Simple amperometry providing peak of current in the course of experiment was employed. The liquid distribution among multiple flow channels can be evaluated from the peaks separation in time and their height as well. An expectable peak height difference caused by unequal liquid flow in the multiple channels system could be disturbed by possible differences in the electroactive surface of each electrode given by the fabrication of SPE. If the geometric (not electroactive) area of all electrodes is the same, the zone of sample in the optimal case reaches the electrodes at the same time and the shape of each peak is same as well. However, if the electroactive area is different, in spite of the liquid uniformly flowing in all channels, peak heights and shapes might not be the same. For this reason, the contributions from the slightly different electroactive surfaces were zeroed by normalization and only the time separation was utilized for further evaluation.

The 4-channel cell provides four peaks as a response to the sample injection. The mutual time separation for this quartet of the peaks was taken as a measure of the uniformity of flow rates – the bigger time difference among peaks, the worse distribution.

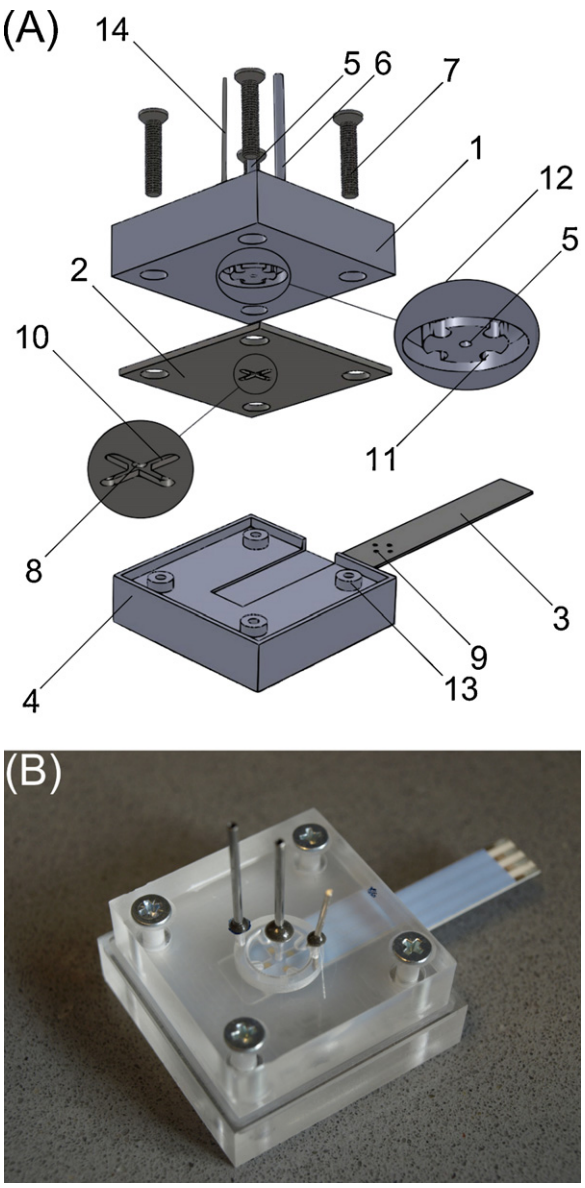

Fig. 2. (A) Detail of the 4-channel flow-through electrochemical cell with its components: upper PMMA part (1), sealing (2), screen-printed sensor (3), lower PMMA part (4), inlet (5), outlet (6), screw (7), fluidic system (8), disc electrode (9), flow channel (10), channel outflow (11), collecting chamber (12), end-stop (13) and reference electrode (14). (B) Photography of the assembled cell (for sectional view of the cell and detail photo of the fluidic system see Supporting Information).

Each peak was normalized, the background current was zeroed by baseline subtraction and characterized by three time parameters t_1, t_2 and t_3 (Fig. 3). The parameter t_1 was obtained as an intersection of the slope of the growing current of the peak with the level of signal corresponding to the background (here considered as zero current); t_3 was obtained similarly, but using the slope of the peak tail. Finally, t_2 was determined as the x-axis coordinate of the intersection of both slopes.

3.3. Interpretation of data and role of the collecting chamber

The uniformity of the liquid distribution was expressed as a percent difference of flow rates in channels. The flow rate in each channel was calculated according to the derived equations considering that flow rate in the channel m was higher than flow rate in the channel n, $v_m > v_n$, thus time for liquid to travel some constant

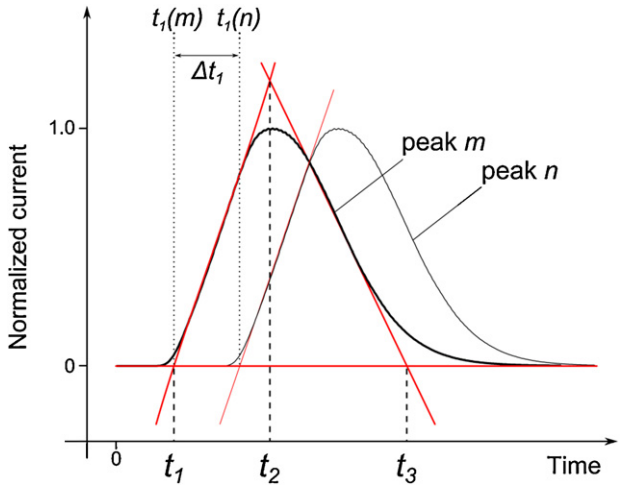

Fig. 3. Data analysis – meaning of the t_i parameters, obtaining of t_i parameters from the highlighted peak of current m and Δt_i values as a difference between $t_i(m)$ and $t_i(n)$.

distance s was higher for channel n, $t_n > t_m$. The difference in flow rates was:

$$\Delta v = \frac{s}{t_m} - \frac{s}{t_n} \quad (1)$$

and based on the assumption that the flow rate is distributed linearly over the multiple channels:

$$v_{opt} = \frac{v_m + v_n}{2} \quad (2)$$

where v_{opt} represents flow rate in any channel at optimal conditions, when flow rate in all channels is the same. The combination of Eqs. (1) and (2) provides:

$$0 = t_n^2 - t_n(t_{opt} - \Delta t) + \frac{t_{opt}\Delta t}{2} \quad (3)$$

together with

$$t_m = \frac{t_{opt} t_n}{2t_n - t_{opt}} \quad (4)$$

where Δt stands for the Δt_i parameters determined experimentally (Fig. 3) and t_{opt} is time value corresponding to v_{opt}. With these known parameters (time difference and distance) all flow rates and their following differences can be calculated and properties of the cell evaluated.

The collecting chamber represents crucial part of the fluidic system. Its cross-section area must be in a specific ratio to the cross-section area of flow channels for proper function of the whole cell. From the viewpoint of the liquid distribution, the outlet from the collecting chamber divides four flow channels into two equal groups in our case. Hence it divides the fluidic system into two mirror parts and the function of the chamber affects flow parameters in both branches in a similar way, but separately. If the collecting chamber does not work properly, the channel closer to the outlet becomes preferred. On the other hand, the more distant channel is not preferred since its pressure loss is higher and therefore its flow rate becomes lower. This complication can be solved by careful adjustment of the cross-section area of the chamber.

The assumption of the preferred and non-preferred channels was also confirmed by the data analysis. Results measured with collecting chamber not working properly indicated that the four electrodes formed two pairs of preferred and non-preferred channels according to the outlet location (data not shown). The cross-section of both channels forming fluidic pathway of the particular system (one half of the 4-channel flow system) were taken

as a standard, to which cross-section of the collecting chamber was rationalized.

The proposed behavior was probed by the CFD modeling and by the experiment with six different cross-section areas of the chamber. The experimental error represents standard deviation obtained from two sets of three sample injections including disassembling and re-assembling of the electrochemical cell. Fig. 4A presents the data obtained from flow-through experiments with the cross-section areas of the collecting chamber equal to 0.50, 1.00 and 5.79 mm^2. The cross-section of the individual flow channel was constant 0.58 mm^2. Slight differences between peaks within preferred and non-preferred channels were caused by fabrication imperfections. It is clearly visible that the fluidic system with smaller collecting chamber did not work properly. In Fig. 4B, there are presented results from the experiments and from the analytical calculation of the flow rate difference between preferred/non-preferred channels. These data are plotted against the dimensionless cross-section areas ratio. The meaning of the percent difference of the flow rates in channels can be expressed on the example of two channels. If the difference is 100% – liquid is flowing only through one of them, if the difference is 0% – liquid is divided into both at equal flows (more details in Supporting Information).

As it can be seen from a plot in Fig. 4B, three t_i parameters were utilized for calculation of percent difference of the flow rates. The influence of the collecting chamber was apparent until the chamber/channels cross-section ratio reached the value of 1.55. Further increase of the chamber cross-section area above this limit did not provide detectable improvement of the behavior and the position of the common outlet did not influence the liquid distribution. A high agreement of the experimental data with CFD simulations was achieved, especially for the t_1 value as it is less burdened by the error of random diffusion. For further expression of experimental data only results based on the t_1 parameter were considered.

The final architecture of the cell consisted of collecting chamber and single channel cross-sections of 5.79 mm^2 and 0.58 mm^2, respectively (ratio 4.98). The employed dimensions were chosen from the region where no evident effect on the liquid distribution was observed. The behavior of the fluidic system was modeled in detail at flow rate of 150 $\mu L\,min^{-1}$. In Fig. 5, the outputs obtained from the program ANSYS are presented. The wall shear at Fig. 5A refers to the shear stress in fluids defined by Newton, which is proportional to the strain rate. The constant of proportionality in

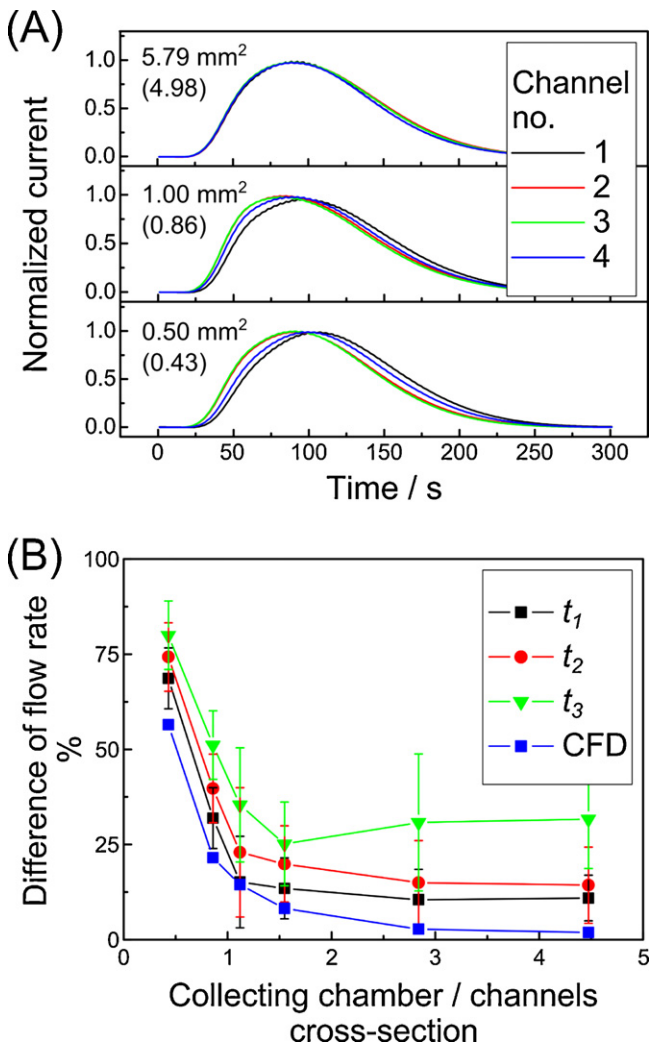

Fig. 4. Difference among flow rates in particular channels visible from the peak separation is influenced by the used collecting chamber. The values of its absolute cross-sectional area and the ratio of collecting chamber/channels cross-section (in brackets) are indicated for each set of traces (A). Plot of the percent difference of flow rates in preferred and non-preferred channels in dependence on the ratio of the collecting chamber/flow path cross-sections (B).

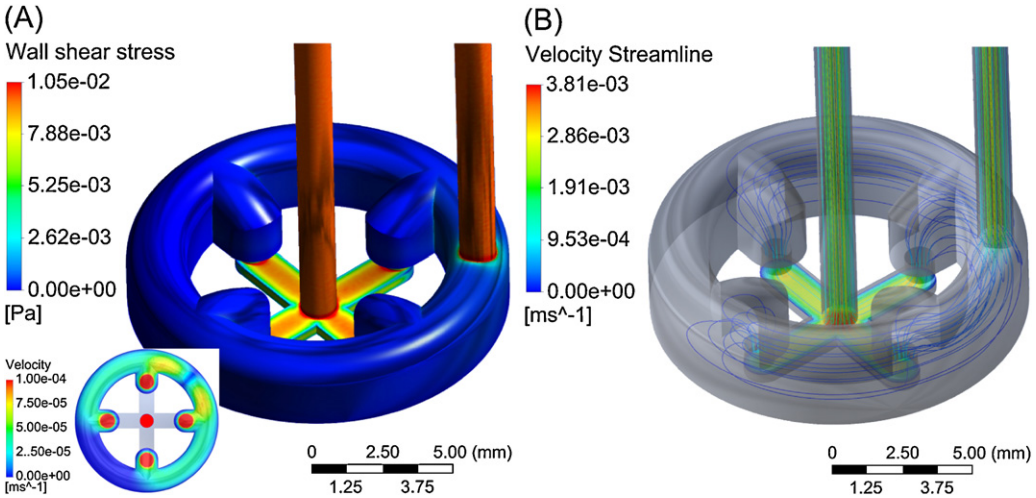

Fig. 5. CFD simulation of the final fluidic cell with 4 measuring channels at flow rate 150 $\mu L\,min^{-1}$; wall shear stress in the fluidic system (A); inset – plan view with the visualization of the flow rates in channel termini and the collecting chamber; modeling of streamlines (B).

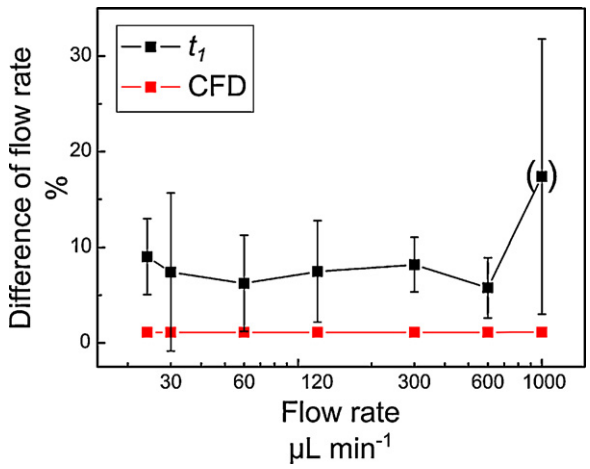

Fig. 6. Plot of differences of flow rates among four channels in dependence on the total flow rate through the system (*x*-axis in log scale for better visualization).

this case of Newtonian fluid is viscosity. The no-slip condition was defined for all walls, *i.e.* velocity at the wall equals to zero. Velocity of the flow in the collecting chamber is depicted in the inset of Fig. 5A. The similar fluidic behavior is expressed as a similar color in all channels. In Fig. 5B, there can be seen results of simulation of streamlines, *i.e.* lines that are at all points tangent to the velocity vector of the fluid. In the course of the modeling, the difference of 1.11% between preferred and non-preferred channels was found. The experimental performance of the cell with the final architecture can be seen in Fig. S-3 (Supporting Information).

3.4. Effect of flow rate on performance of the cell

Although the architecture of the introduced electrochemical cell was similar to cells working in the wall-jet regime, the principle is not the same. The 4-channel cell was working in the thin-layer regime, therefore the interval of applicable liquid velocities was widened, especially towards the slower values. This influence was tested in order to find the interval of utilizable flow rates (Fig. 6). Simulation with CFD modeling revealed that none of the employed flow rates affected distribution of liquid and the obtained differences were below 1.12%. A higher experimental differences for the flow rate of 1000 $\mu L\,min^{-1}$ were attributed to the inappropriate usage of sampling times utilized for 600 $\mu L\,min^{-1}$ (see Table S-1 for details) and to limitations of the instrumentation.

Compared to Fig. 4B, the percent difference in this case means rather the random error among channels than systematic difference between preferred/non-preferred channels. No systematic preference of some channel was found as in the case of probing of an influence of the collecting chamber.

4. Conclusions

The principle of the uniform liquid distribution for the multichannel systems was proposed, experimentally studied and modeled and the optimized 4-channel flow-through electrochemical cell was developed on its basis. The introduced fluidic solution with collecting chamber enables to construct the cell with the single inlet and single outlet and thus simplifies its incorporation into automated analysis. The unique design absolutely eliminates cross-talk. The crucial ratio of collecting chamber to flow path cross-section was determined as 1.55. This is generally applicable for any dimensions (macro to microfluidic systems) and for laminar flow regimes, *i.e.* Reynolds number less than 400 [19]. The range from 24 to 1000 $\mu L\,min^{-1}$ was tested without detecting any deviation from the ideal behavior. When minimal volume of liquid in the system is required and therefore the collection chamber with low cross-section area cannot work properly, the compensation of the irregular flow distributions has to be performed. The cross-section area of the channels should be modified proportionally to the overflow or underflow in the particular channel. However, this approach demands precise fabrication of all components and cannot be realized without additional preliminary tests.

Furthermore, the fluidic system allowed simple change of disposable SPE sensors (rejection of any electrode fouling effects, change of the electrode modification layer). These findings seem promising for the bioelectronic tongue constructed in our laboratory. Electrodes as a part of the wall of channel were used in this study, but it is important to note that the proposed system is equally useful for alternative applications with various designs and principles of detectors.

Acknowledgments

This work was supported by the projects "CEITEC – Central European Institute of Technology" (CZ.1.05/1.1.00/02.0068) from European Regional Development Fund, NPV II No. 2B08035 and the research plan MSM 0021630502 provided by the Ministry of Education (Prague, Czech Rep.).

Appendix A. Supplementary data

Supplementary data associated with this article can be found, in the online version, at http://dx.doi.org/10.1016/j.aca.2012.03.046.

References

[1] P.T. Kissinger, W.R. Heineman, Laboratory Techniques in Electroanalytical Chemistry, second ed., Marcel Dekker, New York, 1996.
[2] D.A. Roston, R.E. Shoup, P.T. Kissinger, Anal. Chem. 54 (1982) 1417A.
[3] S.A. Brooks, R.T. Kennedy, J. Electroanal. Chem. 436 (1997) 27.
[4] R. Kurita, H. Tabei, K. Hayashi, T. Horiuchi, K. Torimitsu, O. Niwa, Anal. Chim. Acta 441 (2001) 165.
[5] J. Wang, G.D. Rayson, L. Ziling, H. Wu, Anal. Chem. 62 (1990) 1924.
[6] A. Aoki, T. Matsue, I. Uchida, Anal. Chem. 64 (1992) 44.
[7] M. DeAbreu, W.C. Purdy, Anal. Chem. 59 (1987) 204.
[8] N. Kasai, T. Matsue, I. Uchida, Electroanalysis 8 (1996) 748.
[9] A. Aoki, T. Matsue, I. Uchida, Anal. Chem. 62 (1990) 2206.
[10] E. Dock, A. Christenson, S. Sapelnikova, J. Krejci, J. Emnéus, T. Ruzgas, Anal. Chim. Acta 531 (2005) 165.
[11] Q. Chen, J. Wang, G. Rayson, B. Tian, Y. Lin, Anal. Chem. 65 (1993) 251.
[12] B.P. Solomon, H. Long, Y. Zhu, C. Gunaratna, L. Coury, Curr. Sep. 4 (2000) 118.
[13] P.R. Fielden, T. McCreedy, Anal. Chim. Acta 273 (1993) 111.
[14] J.C. Hoogvliet, J.M. Reijn, W.P. van Bennekom, Anal. Chem. 63 (1991) 2418.
[15] J. Zeravik, A. Hlavacek, K. Lacina, P. Skladal, Electroanalysis 21 (2009) 2509.
[16] ANSYS Academic Research, Release 12.1, 2009, Help System, Users's Guide, ANSYS, Inc.
[17] S.B. Choi, R.F. Barron, R.O. Warrington, Micromechanical Sensors, Actuators and Systems, vol. 32, ASME DSC, Atlanta, GA, 1991, pp. 123–134.
[18] D.J. Acheson, Elementary Fluid Dynamics, Oxford Applied Mathematics and Computing Science Series, Oxford University Press, New York, 1990.
[19] G.L. Morini, Microscale Thermophys. Eng. 8 (2004) 15–30.